THE KINEMATIC AND MICROSTRUCTURAL DEVELOPMENT OF SOME SHEAR ZONES

by

Michael G. Norton

A thesis submitted for the degree of Doctor of Philosophy in the University of London

Department of Geology
Royal School of Mines
Imperial College of Science and Technology
London, S.W.7.

February, 1982

Abstract

An area of well-exposed shear zones has been studied in detail in order to obtain information about shear zone development. Samples from various stages of deformation were taken and detailed mapping of sampled areas was carried out; along with specific parts of the shear zone network of particular interest. The samples obtained were studied in thin section by optical microscopy to provide a general picture of the progressive deformation. Two contrasting suites of samples from deformed microgranites were prepared for transmission electron microscopy (TEM). TEM was used to identify deformation mechanisms in feldspars and micas, and particularly to record microstructural variations with increasing strain. It was found possible to subdivide quartz mylonites on textural grounds and, with the aid of TEM this variation was identified as being due to a varying component of grain-boundary sliding. Exsolution in the sodic plagioclases was found to be significantly enhanced by strain. Relatively pure quartz samples were studied using the chemical etching of polished sections, and variation of dislocation density, sub-grain size and recrystallized grain size were recorded. The various empirical and theoretical relationships between these parameters and stress have been critically reviewed, criteria for their practical use developed, and the observations in this study interpreted. A combination of these field and microstructural observations, with theoretical considerations from geology and other related disciplines have been used to develop a physical model of a propagating shear zone. This model has been used to predict aspects of shear zone behaviour and the shear zones at Cap de Creus have been re-evaluated in the light of these predictions in terms of both their kinematic and microstructural development. Shear zones are found to propagate at a rate faster

than their rate of displacement, and shear zone networks tend to form during a relatively short period at the beginning of their active life. Shear zone networks are seen to be related to the bulk strain state with the development of domains of coaxial and non-coaxial deformation. Strain softening (s.l.) in the shear zones of Cap de Creus is thought to be controlled by fabric softening, but combined with a variable degree of structural softening due to the operation of grain-boundary sliding as a contributory deformation mechanism.

CONTENTS

		Page No.
Abstract		(i)
Contents		(ii)
List of Plates		(viii)
List of Figures		(x)
List of Tables		(xiv)
Chapter 1	Introduction	3
1.1	Aims	3
1.2	Methods	4
1.3	Thesis structure	5
Chapter 2	Shear zones - a literature review	6
2.1	Occurrence	6
2.2	Shear zone networks	7
2.3	Rocks characteristic of shear zones	7
2.4	Fabrics in shear zones	8
2.5	Strain states in shear zones	9
2.5.1	Pure shear v. simple shear	9
2.5.2	Strain profiles	10
2.6	Changes in chemistry in shear zones	11
2.7	Shear localization and deformation stability	12
2.7.1	Localization	13
2.7.2	Mechanisms of strain softening (s.l. - sensu lato)	16
2.7.2.1	Geometrical softening/hardening	16
2.7.2.2	Structural softening/hardening	17
2.7.2.3	Strain softening (s.s.)/hardening	18

2.7.2.5 Shear heating 19

2.8 Theories of shear zone formation 23

2.8.1 Localization models 23

2.8.2 Propagation models 24

Chapter 3 Fieldwork 28

3.1 Regional setting 28

3.2 The geology of the Cap de Creus 29

3.2.1 Geometrical aspects of the mylonite belt 30

3.2.2 The mylonites 31

3.2.3 Structures within the mylonites 32

3.2.4 Relationship of mylonite zones to the regional structures 33

3.3 Fieldwork carried out 34

3.3.1 The Cala Sardina network 34

3.3.1.1 Minor shear zones 35

3.3.1.1.1 Shear zone orientation 35

3.3.1.1.2 Shear zone junctions and terminations 37

3.3.1.1.3 Control by earlier structures 38

3.3.1.2 The main shear zone 39

3.3.1.2.1 High strain/low strain mylonites 39

3.3.1.3 Sampling in the Cala Sardina area 40

3.3.1.4 Discussion 41

3.3.2 The Portixol (Cala Serena) network 41

3.3.2.1 Minor shear zones 42

3.3.2.2 Major shear zones 42

3.3.2.3 The effect of earlier structures 44

3.3.2.4 Brittle structures 45

3.3.2.5 Sampling carried out 45

3.3.2.6 Discussion

3.3.3 Other areas studied 46

3.3.3.1 Punta del Moli 46

3.3.3.2 Constriction zone 47

3.3.3.3 Shear zone termination, Cala Prona 48

3.3.4 General observations 48

Chapter 4 Microstructural studies 50

4.1 Quartz 50

4.1.1 Literature review 50

4.1.1.1 Strain features 51

4.1.1.2 Preferred orientation 52

4.1.1.3 Deformation mechanisms 53

4.1.1.4 Recrystallization mechanisms 56

4.1.2 Optical observations 57

4.1.2.1 Preferred orientations 57

4.1.2.2 Recrystallization 58

4.1.2.3 Grain shapes/boundaries 59

4.1.2.4 Second phase effects 60

4.1.3 T.E.M. observations 60

4.1.3.1 Dislocation structures 61

4.1.3.2 Grain-boundary structures 61

4.1.3.3 Heated fractures 62

4.1.4 Discussion 63

4.2 Feldspars 64

4.2.1 Microcline 64

4.2.1.1 Review of previous work 64

4.2.1.1.1 Ordering phenomena 65

4.2.1.1.2 Perthites 66

4.2.1.2 Optical observations 67

4.2.1.3 TEM observations 68

4.2.1.4 Discussion 73

4.2.2 Albite - Oligoclase 76

4.2.2.1 Literature review, plagioclase microstructures 77

4.2.2.1.1 Strain features 77

4.2.2.1.2 Recrystallization 79

4.2.2.1.3 Peristerites 81

4.2.2.2. Optical microscopy 82

4.2.2.2.1 Sample series PCM 01-03 83

4.2.2.2.2 Sample series CSE 01-03 84

4.2.2.2.3 Sample series RDS 01-03/CSC01-03 85

4.2.2.3 TEM observations 86

4.2.2.3.1 Deformation features, sample series PDM 01-03 86

4.2.2.3.2 Deformation features, sample series CSE 01-03 88

4.2.2.3.3 Exsolution phenomena 90

4.2.2.4 Discussion 94

4.3 Micas 101

4.3.1 Review of previous work

4.3.2. Optical strain features 102

4.3.3. TEM of micas 102

4.4 Assessment of use of feldspars and micas in palaeostress estimation 103

Chapter 5 The Estimation of palaeostresses 105

5.1 Palaeostress estimation, a literature review 105

5.1.1 Dislocation density 105

5.1.2 Subgrain size 109

5.1.3 Recrystallized grain size 112

5.1.4 The effect of intrinsic and extrinsic variables 114

5.2 Internal consistency of stress estimates 116

5.3 Effect of a change in recrystallization mechanism 122

5.4 The practical use of microstructures in the estimation of palaeostresses 125
Examples of use 128

5.5 Observations from Cap de Creus 131

5.6 Stresses associated with the shear zones at Cap de Creus 133

Chapter 6 Shear zone development 138

6.1 The physical model 138

6.2 Shear zone propagation rates 141

6.2.1 Assumptions of the analysis 141

6.2.2 Analysis 142

6.2.3 Results 143

6.2.4 Discussion 145

6.3 The development of shear zones within a system subject to constraints 147

6.3.1 Approach adopted 147

6.3.2 The system 147

6.3.3 The effects of progressive strain on the system 148

6.4 Shear zone terminations 150

6.5 Shear zone networks at Cap de Creus 153

6.5.1 The Cala Sardina network 153

6.5.1.1 Low-strain mylonites 155

6.5.2 The Portixol (Cala Serena) area 156

6.6 Strain-softening in the shear zones at Cap de Creus 157

6.6.1 Geometrical softening 157

6.6.2 Structural softening 158

6.6.3 Strain, and strain-rate softening? 160

6.6.4 Shear-heating 160

6.6.5 Relative importance of softening mechanisms at Cap de Creus 162

6.7 A history of part of the shear zone network at Cap de Creus 162

Chapter 7 Conclusions 167

7.1 Suggestions for further work 167

Acknowledgements 168

References 169

Appendix 190

List of Plates

Plate 3.1 Field photographs of the Cap de Creus shear zones

3.2 Field photographs of the Cap de Creus shear zones (cont.)

4.1 Optical micrographs of quartz microstructures

4.2 Quartz mylonite textures

4.3 TEM micrographs of quartz microstructures

4.4 TEM micrographs of quartz grain boundaries and healed fractures

4.5 Optical micrographs of alkali feldspar

4.6 TEM micrographs of alkali feldspar

4.7 TEM mosaic of perthite

4.8 TEM mosaic of recrystallized zone between K feldspars

4.9 TEM micrographs of areas within Plate 4-8

4.10 Optical micrographs of plagioclase feldspar (PDM01-03, CSE01-03)

4.11 Optical micrographs of plagioclase feldspar (CSE01-03, RDS01-03, CSC01-03)

4.12 TEM micrographs of deformation microstructure in oligoclase (PDM01-03)

4.13 TEM micrographs of plagioclase microstructures, PDM03.

4.14 TEM mosaic of 'core and mantle' structure

4.15 TEM micrographs of deformation microstructures in oligoclase (CSE01-03)

4.16 TEM micrographs of deformation microstructure in oligoclase, CSE02.

4.17 TEM mosaic of heterogeneous exsolution microstructure

4.18 TEM micrographs of exsolution microstructures in CSE01-03 plagioclases

4.19 Optical micrographs of white micas

4.20 TEM micrographs of micas

5.1 Example of bad specimen preparation, SEM micrograph

5.2 Well-etched dislocations, SEM micrograph

5.3 Mosaic of reflected light micrographs showing sub grain network

List of Figures

Figure 2.1 Shear strain profile (Ramsay and Graham, 1970)

2.2 Response of a material to deformation (Bowden, 1970)

2.3 Detail of surface in Fig. 2.2 (Bowden, 1970)

2.4 Reference system for shear-heating models

2.5 Solutions to steady-state shear-heating equations (Brun and Cobbold, 1980)

2.6 Initial stages of shear zone formation (Coward, 1976)

3.1 Geological map of north-eastern Spain

3.2 Geological map, and section of Cap de Creus (Carreras, 1975)

3.3 Stereoplot of mylonite foliation and lineations, Cap de Creus (Carreras, 1979)

3.4 Minor structures developed within mylonite

3.5 Map of shear zones between Cala Taballera and Cala Portaló (Carreras et al., 1975)

3.6 Shear zone orientation data from the Cala Sardina area

3.7 Types of shear zone termination observed

3.8 Complex termination zone

3.9 Shear zone orientation data from the Portixol area

3.10 Schematic diagram of sinistral zone, Portixol

3.11 Shear zone boundary, Portixol area

3.12 Shear zone localized in minor fold limb

3.13 Stages of formation of shear zone in Fig. 3.12

3.14 Model for development of shear zone network at Portixol

3.15 Sketch map of Punta del Moli zone

3.16 Sketch map of Constriction zone, Cala sa Caixa

3.17 Minor dextral zone with termination, Cala Prona

3.18 Tracing of Plate 3.2 (e)

3.19 Variation of width with displacement and shear strain in minor shear zones

4.1 C-axis, a-axis orientation diagrams for quartz mylonites, Cap de Creus

4.2 Alternative exsolution paths for alkali feldspar

4.3 Schematic diagram of mosaic on Plate 48

4.4 Example of trace analysis to find direction of dislocation line

4.5 Schematic diagram of recrystallized zone showing exsolution traces

4.6 Stereographic projection illustrating exsolution trace measured in this study

4.7 Steographic projection showing all exsolution traces in plagioclase

4.8 Variation in exsolution lamellar spacing

4.9 Alternative explanations for persterite exsolution

4.10 G-X diagrams illustrating the effect of a conditional spinodal (Carpenter, 1981)

5.1 Normalized plot of stress v. dislocation density

5.2 Formation of strain-free nucleus (Mercier, 1977)

5.3 Log-log plot of σ_f v. d_{SG}, olivine

5.4 Data of Matsui et al. 1980

5.5 Synoptic plot of published relationships of stress with subgrain size olivine

5.6 Log-log plot of σ_f v d_{SG} quartz

5.7 Comparison of calculated relationship, with published relationships, quartz

5.8 Log-log plot of d_{SG} v. d_{RG}, olivine

5.9 Synoptic plot of published relationships of stress with grain size, olivine

5.10 Log-log plot of d_{SG} v. d_{RG}, quartz

5.11 Empirical and theoretical relationships of stress with grain size, quartz

5.12 Fields of SGR, GBM recrystallization in stress temperature space

5.13 Fields of SGR, HMGBM, and LMGBM, and effect of impurity content

5.14 The effect of a change in mechanism on the grain size for a constant stress

5.15 Map and strain profile of the Woodroffe thrust (Bell and Etheridge, 1976)

5.16 Variation of d_{RG} across the Woodroffe thrust (Bell and Etheridge, 1976)

5.17 Variation of stress estimated across the Woodroffe thrust

5.18 Variation of stress estimated (taking account of change in mechanism)

5.19 Possible temperature profile across the Woodroffe thrust

5.20 Variation of d_{RG} across the Woodroffe thrust (Etheridge and Wilkie, 1979)

5.21 Subgrain network in a remnant quartz grain

5.22 Frequency distribution of subgrain size

5.23 Measurement of inequant grains

5.24 Stress profiles estimated for zone at Cala Sardina

6.1 Schematic diagram of propagating shear zone

6.2 Stress and strain distribution around a propagating zone

6.3 Stress and strain profiles in direction of propagation

6.4 Stress and strain profiles across a propagating zone

6.5 Published shear strain profiles

6.6 Response of a system to displacement at its boundaries

6.7 Change in stress in the system with time

6.8 Fabric softening in incipient p- and s- bands

6.9 Networks of shear zones due to pure and simple shear

6.10 Expected shear zone orientations for different bulk strain ellipsoids

6.11 Predicted and observed shear zone orientations, Cala Sardina

6.12 Effects of structural control on resultant shear zone network

6.13 Result of overlap of strain fields from adjacent shear zones

6.14 Areas of strain overlap at a shear zone junction

6.15 Mode of evolution of complex junction at Cala Sardina

6.16 Temperature profile for zone of constant width with varying strain-rate

6.17 Temperature profile for zone at constant strain-rate of varying width

6.18 Temperature rise at the centre of a 20 m wide zone

6.19 Block diagram of area between Portixol and Cala Sa Caixa, prior to shear zones

6.20 Stages in the evolution of the network between Portixol and Cala sa Caixa

List of Tables

Table 2.1 Fault rock classification

3.1 Chronology of Hercynian events in the Pyrenees

4.1 List of slip systems in quartz

4.2 Deformation mechanisms and related flow laws

4.3 Variation in quartz grain size with mylonite textural types

4.4 Variation of albite twin spacing with width of Na feldspar

4.5 K feldspar analyses using STEM

4.6 Observed burgers vectors and slip planes in plagioclase

4.7 Chemical changes with recrystallization in plagioclase

4.8 Plagioclase analyses using probe

4.9 Degree of development of exsolution in plagioclase

5.1 Variation in microstructural parameters and stresses (after White, 1979(b))

5.2 Measurements of microstructural parameters from Cap de Creus

5.3 Stress estimated for samples from Cap de Creus

5.4 Variation of estimated stresses with bulk strain

6.1 Calculated shear zone propagation rates

6.2 Time for propagation to final size

6.3 Time for propagation compared to total shear zone life

6.4 Relative contributions of softening mechanisms in Cap de Creus mylonites

Chapter 1 INTRODUCTION

The recent, rapid increase in interest in shear zones since the classic paper by Ramsay and Graham (1970) has in part been due to their use as 'testing grounds' for theoretical predictions concerning the response of geological materials to progressive deformation. Such studies assume that samples taken across a shear zone boundary show a progressive strain history that approximates to the incremental strain history of the most highly strained rocks themselves. However, without a clearer understanding of shear zone initiation, propagation, and subsequent development, the true significance of such microstructural variations must remain in doubt.

1.1 Aims

One of the initial aims of this study was to look at the progressive deformation of feldspar and mica-bearing rocks in the shear zones of the Cap de Creus area of north-eastern Spain. In particular it was intended to look for systematic variations of those parameters that have been considered to be related to flow stresses, in feldspars and micas, by comparison with relatively pure quartz 'control' samples. It was, however, considered important that the reason for any such variations in these parameters was understood as fully as possible. This led both to a critical re-assessment of the use of these parameters in estimating differential stress levels during deformation, and to an attempt to provide a physical model of shear zone initiation and propagation.

The aims of this study may then be summarized as:-

1. To record microstructural variations with strain in feldspars and micas.
2. To critically reassess the use of microstructural parameters in the estimations of palaeostresses.

3. To develop a physical model of shear zone initiation and propagation combining theoretical considerations with field observations of individual shear zones, and shear zone networks.

1.2 Methods

In part fieldwork was undertaken in order to provide the samples for microstructural work. It was also used to study individual shear zones in an effort to obtain information on initiation, propagation and possible controls on localization. Additional evidence was sought from shear zone networks, involving detailed mapping of part of the area; detailed maps were also prepared of all areas sampled in order to establish their precise geological context.

Thin sections of all the samples were studied by optical microscopy, and, of these, two contrasting sets of samples from deformed microgranites were prepared for transmission electron microscopy (TEM). TEM was used to study detailed microstructural variations in feldspars and micas. A minimum of control on chemistry in the feldspars was provided by electron microprobe and scanning transmission electron microscope (STEM) microanalysis, the former giving information on general compositional ranges in each section, the latter being used on particular TEM specimens to provide analyses on the scale of a few microns.

Measurements of recrystallized grain size for use in palaeostress estimation were made initially from standard thin sections and a computer program was written allowing the true mean of the distribution to be calculated. In order to provide measurements of sub-grain size and dislocation density in quartz, etched polished sections were prepared and studied by reflected light microscopy or scanning electron microscopy (SEM). These

results were combined with published data for quartz and olivine and used to test the validity of theoretical and empirical relationships between these parameters and stress, leading finally to criteria for their practical use for naturally deformed geological materials.

A theoretical basis for a model of shear zone initiation and propagation was sought not only in the geological literature but also in the related disciplines of metallurgy, materials science, soil mechanics and engineering fracture mechanics. A physical model of a propagating shear zone was developed combining field observations with aspects of a number of different theoretical models. This was used to predict certain aspects of shear zone development, and these were compared with the shear zones observed in this study.

1.3 Thesis structure

After this brief introductory chapter the thesis continues by reviewing the literature on shear zones and associated structures (Chapter 2). The third chapter briefly reviews previous work on the Cap de Creus area of north-eastern Spain and describes the investigation carried out, the observations made, and the rocks sampled in the present study. Chapter 4 looks at quartz, the feldspars and the micas, in each case with reviews of the literature followed by observations using optical microscopy and TEM, of variations in microstructure with strain.

The fifth chapter reviews the theoretical and empirical relationship between microstructural parameters and stress, provides criteria for their practical use, and finally interprets the measurements made in this study. Chapter 6, on shear zone development, draws on all of the previous four chapters to provide a physical model for a propagating shear zone; both field and microstructural observations are then interpreted in the light of this model. Finally, the conclusions of this study are presented in Chapter 7 with suggestions for further work.

SHEAR ZONES - A LITERATURE REVIEW

This review is intended to cover all of the most relevant of the previous work done on the many aspects of shear zones.

2.1 Occurrence

Before discussing the occurrence of shear zones, it is necessary to present a working definition of the term. Shear zone is used here in the sense of a tabular region of heterogeneously high deformation, the strain state being one of dominant simple shear, in which ductile deformation mechanisms have predominated at the grain scale. Attempts have been made (Ramsay, 1980) to widen the definition to include brittle fault zones. Although cataclastic deformation is a ductile mechanism on the scale of the fault zone it is considered that 'shear zone' should carry the implication of a continuous deformation; if a more general term is required to cover all such structures, perhaps the S-band of Cobbold (1977(a)) would suffice.

The accommodation of bulk strain by zones of heterogeneous simple shear is a characteristic feature of rocks in the ductile deformation regime in which there is no mechanically active layering likely to lead to buckling, such as; igneous bodies (e.g. gabbro (Ramsay and Graham, 1970), granodiorite (Burg and Laurent, 1978) or granite (Bossière and Vauchez, 1978; Ramsay and Allison, 1979; Simpson, 1980), or certain metamorphic terrains (e.g. the Pre-Cambrian basement of West Greenland (Bak et al. 1975) and the Hercynian basement of Brittany (Berthé et al, 1979; Watts and Williams, 1979). Shear zones may also be found marking the ductile levels of major crustal fault zones e.g. the Outer Hebrides Thrust (Sibson,1977), the Laxford front, Beach et al. (1973). In addition to the above occurrences, small finite strains at high crustal levels may be accommodated by the so-called 'en-echelon tension-gash' shear zones, which involve both brittle and ductile mechanisms, generally in folded, massive, limestone or sandstone units, e.g. Beach (1975), Knipe and White (1979).

2.2 Shear Zone Networks

Shear zones tend to form continuous networks except in those cases where they occur as a single isolated structure such as the Lochseitenkalk mylonite on the movement plane of the Glarus overthrust (Briegel and Goetze, 1978), or where a planar nature is forced upon them as in shear zones developed along dyke boundaries (Escher et al., 1975). Even if all the shear zones in an area are all of the same sense, they commonly form three-dimensional anastomosing networks enclosing less-deformed lozenge-shaped blocks or 'augen', at all scales from a few metres (Coward, 1976; Ramsay and Allison, 1979) to several hundred metres (Sibson, 1977).

This tendency to form networks has been regarded as evidence for the non-planar propagation of the shear zones (Coward, 1976, see section 2.82), although Sibson (1979) has suggested that initial material heterogeneities may be important in this respect and cites examples from the Outer Hebrides Thrust Zone of control of shear zones by metabasite pods in otherwise homogeneous gneiss.

Two or more sets of shear zones of different movement sense may be developed in an area, all apparently active at the same time, forming a continuous network (Ramsay, 1979; Mitra, 1979). Coward, (1976) and Mitra (1979) have suggested that the progressive deformation of such a network may be possible by a mechanism akin to that of grain boundary sliding as developed in polycrystalline aggregates.

2.3 Rocks characteristic of Shear Zones

The main rock types found in shear zones (as defined in 2.1) are mylonites. The exact usage of the term mylonite is, however, still a subject of controversy amongst geologists. This is due to a change in understanding of the deformation mechanisms responsible for the textures observed in mylonites (see sections 4.1.1 , 4.2.2.1). Thus the original mylonites described by Lapworth (1885) from the Moine Thrust Zone were named from the Greek word mylos,

a mill, to describe a texture also known as 'mortar' or porphyroclatic that he thought due to the milling down of original grains. This texture that he called 'fluxion structure' has been identified in many other zones of intense deformation which has led to the widespread use of the term 'mylonite' for any foliated fault rock (e.g. Sibson, 1977). The 'fluxion structure' has been found in more recent studies to be principally a result of ductile deformation at the grain scale (for a review see White et al. 1980).

White (1981) has examined samples from Lapworths original locality and found that both brittle and ductile mechanisms were involved in the initial grain-size reduction mechanism but that further deformation was dominantly ductile. He has proposed that the terms r- and c- type mylonite should be used depending on whether the initial grain-size reduction was respectively dominantly ductile or brittle. A further problem in the terminology is due to the recent recognition of certain brittle fault rocks with strong foliations and textures reminiscent of Lapworth's 'fluxion structure', termed fault gouges (Hall & Rutter, 1981; Higgs and Friedman, 1981). Bell and Etheridge (1973) have suggested that the term 'mylonite' should not carry a genetic connotation and Sibson's 1977 fault-rock classification adopted this approach. Table 2.1 shows this classification slightly modified to include fault gouges (in the sense of Hall and Rutter, 1981). The term blastomylonite has also been removed as, although it had at one time a generally accepted usage, it has suffered from constant misuse. The classification shown in Table 2.1 has been used throughout the present study.

2.4 Fabrics in shear zones

The relationship between the crystallographic preferred orientations developed in shear zones and their kinematic framework have been extensively reviewed by Lister and Williams (1979). Fabrics in shear zones have been used to measure shear strains (Laurent and Etchecopar, 1976), to determine

TABLE 2.1

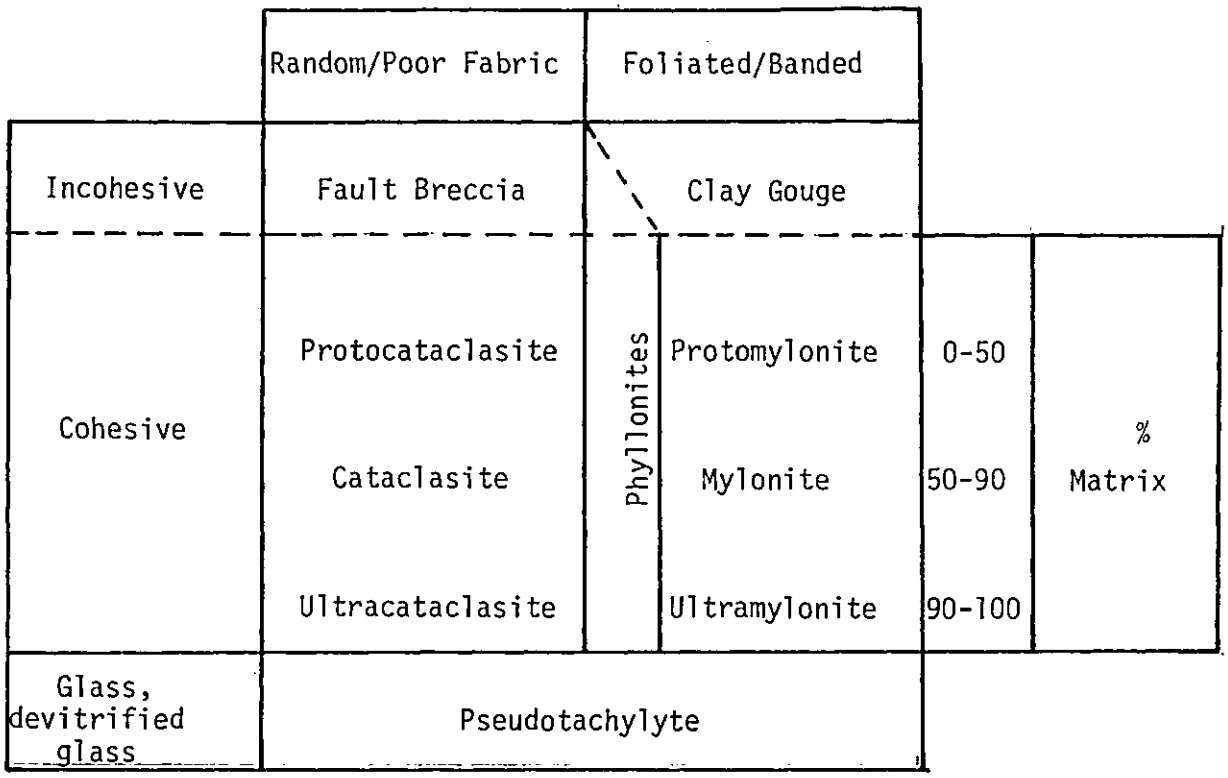


Table 2.1 Fault rock classification as used in this study (after Spry, 1969; Sibson, 1977).

the sense of shear (Bouchez and Pecher, 1978) and to infer the strain-state (Christie, 1965; Johns on, 1967).

2.5 Strain states in shear zones

As shear zones often form a significant component of the bulk deformation it is important that both the amount, and type of strain developed is known, in order to characterise the strain state of the whole system.

2.5.1. Pure Shear v. Simple Shear

It is commonly assumed that both the incremental and finite strain states in shear zones are heterogeneous simple shear (e.g. Ramsay, 1980). There is, however, a considerable amount of evidence that at least a component of pure shear is present in most zones. Some workers (e.g. Bell, 1980) have even gone so far as to suggest that heterogeneous flattening is the dominant strain state in many mylonite zones. Evidence as to the nature of the finite strain state in shear zones has come from two principal sources; strain analysis and preferred orientation studies (Section 2.4).

Johnson (1967) considered that mylonite foliation was analagous to slaty cleavage, and represented heterogeneous flattening. He quoted evidence from the Moine Thrust Zone, but most of this is equivocal. Dalziel and Bailey (1968) described garnets from mylonites along the Grenville Front, Canada, that are oblate spheroids, $o \leqslant k \leqslant 1$ in the terms of Flinn (1962). They show the garnets to be deformed from Laue X-ray photographs, but also mention garnets from the same vicinity that are significantly elongated in the z-direction of the finite strain ellipsoid. Similar arguments have been employed by Ross (1973), for a similar area; he also noted that the geometry and symmetry of the deformation were the same within and without the mylonite zone.

Coward (1976) has looked at the strain states in a variety of shear

zones using various methods of strain analysis; Rf/ϕ, centre-centre method, and magnetic susceptibility anisotropy. All of the zones studied show a significant component of pure shear. However, he proposed that the pure shear component relates to the propagation event (see section 2.82) and cannot subsequently be removed. Goldstein (1980) found moderately to severely oblate ellipsoids using magnetic susceptibility anisotropy in mylonites from the Lake Char mylonite zone, and suggested that it was due to an initial simple shear related to propagation followed by a flattening event. Bell (1981) has presented a model for deformation by 'heterogeneous flattening' but the zones of intense deformation shown appear to be related to dominantly simple shear rather than 'inhomogeneous shortening.'

2.5.2 Strain Profiles

In the measurement of strain profiles the assumption is normally made of heterogeneous simple shear (but see previous section). The first investigation of the strain profiles from shear zones was carried out by Ramsay and Graham (1970), who showed that they could be used in computing displacements. They show strain profiles to be approximated by normal distributions across the zone (Fig. 2.1). Many other published profiles, however, have flat tops (Watterson, 1979; Means, 1981) and some of the profiles shown in Ramsay and Graham (1970) show this tendency quite strongly.

Although the strain profiles reported in the literature are commonly symmetrical about the centre of a shear zone asymmetric profiles have been published, but these are normally confined to those zones which form along lithological boundaries, such as the Woodroffe Thrust between granulite, and amphibolite gneisses (Bell and Etheridge, 1976).

Not all shear zones have simple strain profiles and this is particularly true of large scale zones where the strain within is often markedly hetero-

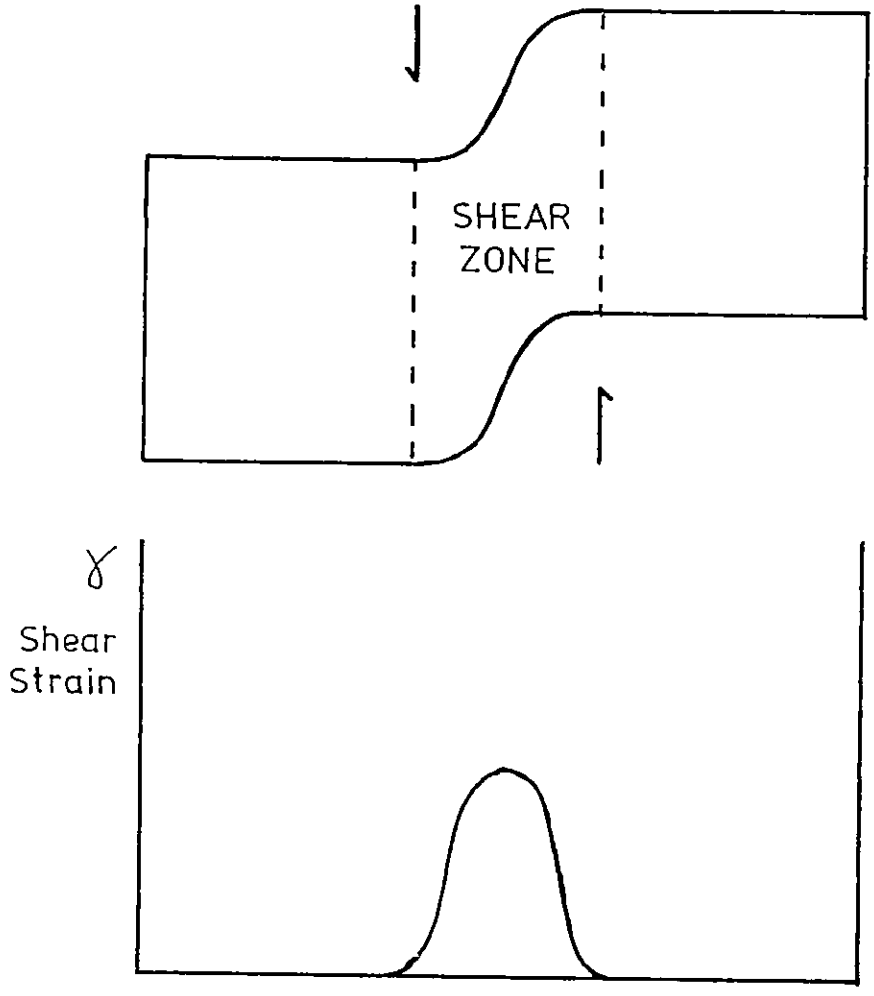


Fig. 2.1 Variation of shear strain (γ) across a shear zone (after Ramsay and Graham 1970).

geneous. Grocott and Watterson (1980) have described the strain profile across part of the Ikertoq shear belt in the Nagssuqtoqidian of West Greenland. The strain varies between about $\gamma = 1$ to $\gamma > 14.5$, and this variation seems fairly typical of zones developed at deep crustal levels.

2.6 Changes in chemistry in shear zones

Chemical changes in shear zones have been recognized since the work of Teall (1885) on a heterogeneously deformed Scourie dyke, from the Lewisian of north-west Scotland. The detailed analysis of both bulk chemical changes and changes in mineral chemistry were first carried out by Boyle (1961) and Beach and Fyfe (1972). Beach and Fyfe (op.cit.) (see also Beach 1973, 1976, 1980) looked at shear zones in Scotland similar to those described by Teall, associated with retrogression of granulite facies gneisses to amphibolite facies. The main observed changes in chemistry were; an increase in H_2O, K, Na, coupled with a loss of Fe, Ca, Mg. They interpreted this as due to the interaction with a very large volume of aqueous fluid of low pH moving upwards through the crust, either derived originally from the mantle or from relatively cold Laxfordian granites into hot Scourian granulites.

Bridgewater (1979), Dostal et al. (1980) and Kerrich et al. (1977) all report bulk chemical changes, in zones which vary from a few tens of centimetres, to several hundreds of metres in width. Kerrich et al. (op.cit.) also describe the chemical changes in a 1cm wide zone within an adamellite from Laghetti in the Swiss Alps and from mass-balance calculations found the deformation to be isochemical; Brodie (1981) similarly used mass-balance considerations and found that a 5m wide zone in a metagabbro from Valle d' Ossola was deformed isochemically. Kerrich et al. (1980) present the only example so far reported of a major (100m → 1km wide) shear zone in which the deformation is considered to have been isochemical, also, from stable isotope data, they conclude that little or no fluid flow occurred.

Chemical changes in shear zones may be summarized as: changes in mineral chemistry due to requilibration with prevailing P/T conditions with or without bulk chemical changes depending on whether the system was open or closed. This last effect appears to depend on the particular shear zone; many zones seem to have remained as open systems and to have acted as major pathways for fluid flow, while others have apparently acted as closed systems with no fluid flow at all.

2.7 Shear localization and deformational stability

Before moving on to review theories of shear zone formation it is necessary to consider the relationship between deformation that involves localization and that which becomes formally unstable. Various criteria have been put forward for the onset of instability, Hill (1950) uses the 'loss of load carrying capacity under controlled boundary displacement'; Bowden (1970) defines instability in compression in terms of the negative slope of the stress-strain curve, i.e. $\frac{\partial \sigma}{\partial \varepsilon} < 0$ in tension this becomes (Argon, 1973) $\frac{dp}{dt} \leqslant 0$ (where P is the load); the difference in criteria being due to the effect of localization in tension which is always to increase the stress in the localized zone due to the consequent volume reduction. Biot (1965) talks in terms of deformation becoming unstable through loss of 'uniqueness' but as pointed out by Argon (1973) this is in fact due to localization by inhomogeneous deformation and the two conditions differ except in the case of plastic rigid rheology.

It is unfortunate that the concept of instability is so strongly tied to the failure of engineering materials, as the geologist interested in ductile flow is attempting to relate it to deformation for which the term failure is meaningless.

Rudnicki (1979) has discussed two types of instability, localization

and runaway. In the terms of the model presented, of a weak zone embedded in a rock mass, the former relates to an instability in the constitutive description of homogeneous deformation, leading to the development of concentrated non-uniform deformation in a narrow band within the weakened zone itself. Runaway instability occurs when a remote boundary strain increment induces an unbounded strain increment in the weakened zone; that is, there is no static solution for the next increment of deformation.

2.71 Localization

Bowden (1970) developed an analysis for the inhomogeneous deformation of materials that exhibit strain-softening. Fig. 2.2 shows the typical form of a surface in stress, strain, strain-rate space for such a material. Strain-softening, that is a reduction in flow stress with increasing strain, is a necessary requirement for the development of shear instabilities (Argon, 1973) (the possible cause of strain softening will be considered in a later section).

Taking a model of a material deforming homogeneously in shear at an imposed shear strain rate ($\dot{\gamma}_o$) Bowden (1970) looked at the effect of the development of embryonic bands, representing a certain volume fraction (f) of the material, in which the strain was 'fortuitously' larger than the rest of the material by a small amount $\Delta\gamma$. If no material heterogeneities were present the deformation would clearly remain homogeneous. Fig. 2.3 shows a small part of the flow-stress surface shown in Fig. 2.2 projected onto axes of strain v. strain-rate; the broken lines are contours of constant stress.

The strain-rate on the bands ($\dot{\gamma}_b$) will increase instantaneously from $\dot{\gamma}_o$ to $\dot{\gamma}_b'$ and that in the matrix ($\dot{\gamma}_m$) will decrease to $\dot{\gamma}_m'$ such that both regions still fall n the same stress contour. For the small part of the flow-stress surface shown in Fig. 2.3 the gradient of the stress contours

FIG. 2.2

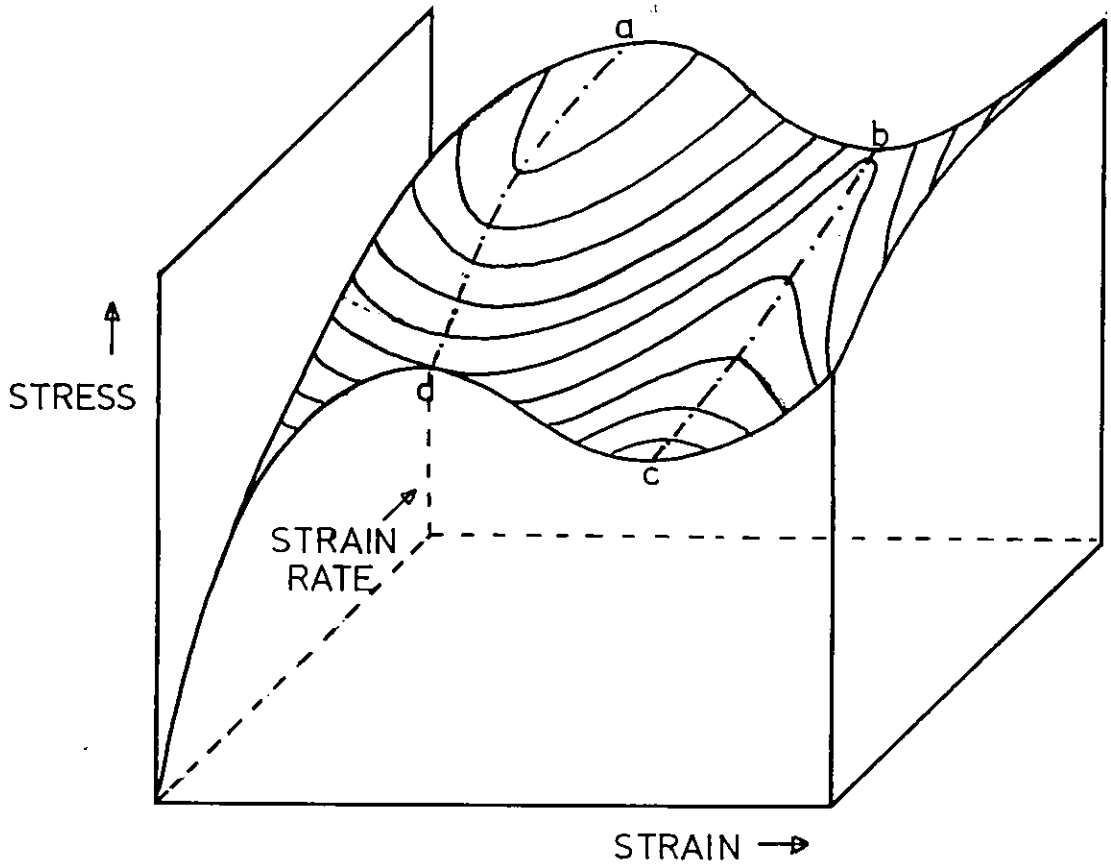

a
b
c
d
STRESS
STRAIN RATE
STRAIN

FIG. 2.3

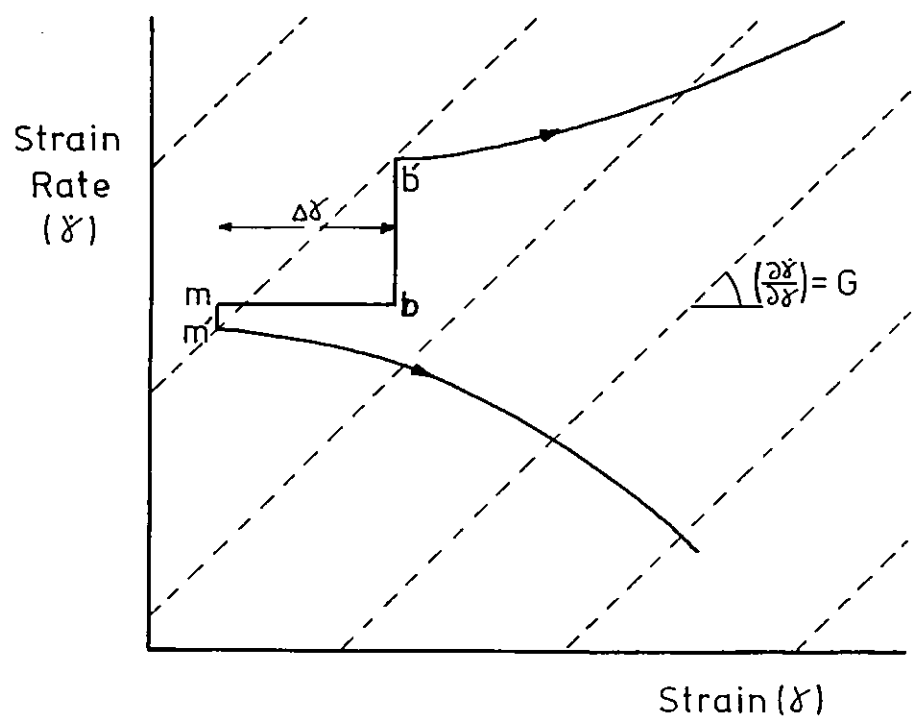

Strain Rate ($\dot{\gamma}$)
$\Delta\dot{\gamma}$
b'
m
m'
b
$\left(\frac{\partial\dot{\gamma}}{\partial\gamma}\right)$ = G
Strain (γ)

Fig. 2.2 The response of material to deformation represented as a surface in stress, strain, strain-rate space (after Bowden, 1970). Such a diagram may be constructed by combining stress-strain curves for different strain-rates . The contours are lines of equal stress .

Fig. 2.3 Part of the surface shown in Fig. 2.2 , in the region of negative slope abcd , projected onto strain, strain-rate axes (after Bowden (1970)).

$(\frac{\partial\sigma}{\partial\gamma})_\sigma$ is taken to be a constant G. The equation

$$f\dot{\gamma}_b + (1-f)\dot{\gamma}_m = \dot{\gamma}_o \qquad (2.1)$$

must always be satisfied, so it therefore follows that the strain-rate on the band must increase to $(\dot{\gamma}_o + G(1-f)\Delta\gamma)$ and that on the matrix decrease to $(\dot{\gamma}_o - Gf\Delta\gamma)$.

From this Bowen (op.cit.) derives equations for the change of strain rate with strain in bands and matrix

$$\frac{d\dot{\gamma}_b}{d\gamma_b} = G(1-f)(\dot{\gamma}_b - \dot{\gamma}_m)/\dot{\gamma}_b \qquad (2.2)$$

$$\frac{d\dot{\gamma}_m}{d\gamma_m} = -Gf(\dot{\gamma}_b - \dot{\gamma}_m)/\dot{\gamma}_m \qquad (2.3)$$

which may be integrated to give,

$$\gamma_b = {}^1/G(\dot{\gamma}_b - \dot{\gamma}_o + \dot{\gamma}_o \ln(\frac{\dot{\gamma}_b - \dot{\gamma}_o}{G(1-f)\Delta\gamma})) \qquad (2.4)$$

$$\gamma_m = {}^1/G(\dot{\gamma}_m - \dot{\gamma}_o + \dot{\gamma}_o \ln(\frac{\dot{\gamma}_o - \dot{\gamma}_m}{Gf\Delta\gamma})) \qquad (2.5)$$

For various values of the strain inhomogeneity ($\Delta\gamma$) and the volume fraction (f) of bands it is possible to draw a family of curves on the flow-stress surface. For small values of $\Delta\gamma$ the divergence in strain rate is very small, for larger values the matrix strain rates become very slow and the band strain rate approaches a value of $\dot{\gamma}_b = \dot{\gamma}_{o/f}$.

Argon (1973) presented a somewhat generalized version of Bowden's (1970) analysis for a material deforming by the general deformation equation

$$\frac{d\dot{\gamma}}{d\gamma} = m\frac{\dot{\sigma}}{\sigma} - m\left(\frac{\partial \ln\tau}{\partial \ln p}\right)_{\gamma p}\frac{\dot{p}}{p} + \frac{-m}{\tau}\left(\frac{\partial\tau}{\partial\gamma}\right)_p + \frac{\Delta H}{kT}\cdot\frac{\beta\sigma\dot{\gamma}h^2}{k_t\gamma T}\dot{\gamma} \qquad (2.6)$$

where m is the strain-rate sensitivity (from $\dot{\varepsilon} = A_\sigma^{1/m}\exp(^{-Q}/RT)$)

τ is the plastic shear resistance

p is the pressure

ΔH is the activation enthalpy characteristic of the deformation process

β is the fraction of work done dissipated in the form of heat

k is the Boltzmans constant

k_t is the thermal conductivity

h is the thickness of the zone of concentrated deformation

σ is the shear stress

In this analysis he includes the criteria for instability in shear, $\dot{\sigma} = 0$. The predictions of this analysis are essentially similar to those of Bowden (1970) except that Argon (1973) has tried to link the effects of localization more directly to the various mechanisms of strain-softening.

Poirier (1980) in an analysis based on that of Dillamore et al. (1979) has used a similar deformation equation to that of Argon (1973) but in a more useful and general form. He began with the flow law

$$\sigma = k\tau o\varepsilon^{n}\dot{\varepsilon}^{m}\exp(^{mQ}/RT) \qquad (2.7)$$

where $K = M^{(1+n+m)}$ and M is the Taylor factor which depends on the orientation of the active slip system with respect to the principal stress and represents the effects of geometric softening.

$n = \frac{\partial \ln\sigma}{\partial \ln\dot{\varepsilon}}$ is the strain rate sensitivity of stress

$m = \frac{\partial \ln\sigma}{\partial \ln\varepsilon}$ is the strain sensitivity of stress

(N.B. this is the reciprocal of the m used by Argon (op.cit.)

τ_o represents the effect of structural changes (e.g. phase changes, recrystallization); this gives the differential equation for deformation in shear,

$$\frac{(1+n+m)}{M}\frac{dM}{d\gamma} + \frac{1}{\tau_o}\cdot\frac{d\tau_o}{d\gamma} + \frac{n}{\dot{\gamma}} + \frac{m}{\dot{\gamma}}\cdot\frac{d\dot{\gamma}}{d\gamma} - \frac{mQ}{RT}\cdot\frac{dT}{d\gamma} = \frac{1}{\tau}\frac{d\tau}{d\gamma} \qquad (2.8)$$

this may be re-arranged to give

$$\frac{d\dot{\gamma}}{d\gamma} = \frac{1}{m}\frac{\dot{\tau}}{\tau} - \frac{(1+n+m)}{m.M}\dot{M} - \frac{1}{m}\frac{\dot{\tau o}}{\tau o} - \frac{n}{m}\frac{\dot{\gamma}}{\gamma} + \frac{Q}{RT^2}\dot{T} \qquad (2.9)$$

which is very similar to equation(2.6)due to Argon (op.cit.)

2.7.2 Mechanisms of Strain-Softening (s.l - sensu lato)

Mechanisms of strain-softening, that is mechanisms by which deformation may become localised, have been reviewed by Poirier (1980), and White et al. (1980). They may be subdivided into the following types, all except the last may be in the right circumstances either softening or hardening mechanisms. The different mechanisms are correlated with the terms in the general deformation equation of Poirier (1980).

1.	Geometrical softening/hardening	$\frac{(1+n+m)}{M}.\frac{dM}{d\gamma}$
2.	Structural softening/hardening	$\frac{1}{\tau o}.\frac{d\tau o}{d\gamma}$
3.	Strain softening (S.S.)/hardening	$\frac{n}{\gamma}$
4.	Strain-rate softening/hardening	$\frac{m}{\dot{\gamma}}.\frac{d\dot{\gamma}}{d\gamma}$
5.	Shear heating	$\frac{-mQ}{RT^2}.\frac{dT}{d\gamma}$

The requirement for instability is that the combined effect of all this makes $\frac{d\tau}{d\gamma} \leqslant 0$ in equation (2.8).

2.7.2.1 Geometrical softening/hardening

Two types of geometrical softening may be important in the evolution of shear zones rotation softening related to the bulk anisotropy of a rock (Cobbold, 1977(a),(b)) and fabric softening caused by the rotation of slip plane towards the XY plane of the finite strain ellipsoid giving increasingly easy slip in the case of simple shear (Nicolas et al. 1971).

The development of kink-bands is thought to be due to the effects of rotation-softening (Cobbold, 1977(a),(b); Summers, 1979) but the effect is only important in a rock containing a strong planar anisotropy, such as a phyllite. The shear bands commonly found in phyllonites (White et al. ,1980), and quartz (Gapais and White, 1982) or calcite (White et al., 1980) ribbon mylonites, are micro-shear zones that only seem to be developed when such a planar anisotropy is present. Similar structures have also been described from clay fault gouges with a strong foliation (Hall and Rutter, 1981).

Fabric softening was considered by Dillamore et al. (1979) to be the dominant softening process associated with the formation of 'shear-bands' in rolled cubic metals. In their analyses they showed that shear bands would form along planes of maximum resolved shear stress if there was no pre-existing fabric, but that a strong initial fabric caused other orientations to be favoured. The tendency of a fabric to soften or harden a material will depend on the number of independent slip systems available and their relative ease of slip. If a material meets Von Moses criterion with five independent slip systems, all of approximately the same strength, then fabric softening will be negligible. Most geological materials however, have only one or two dominant (i.e. weak) slip systems operating at any particular temperature, and this will therefore favour fabric softening (Reid, 1973). White et al. (1980) have suggested that fabric softening is the controlling factor in the strain-softening associated with the formation of mylonites.

2.7.2.2 Structural softening/hardening

Structural softening occurs whenever the structure changes with strain towards a more deformable state. The structural change may be due to; a phase transformation, e.g. α-quartz to β-quartz, a metamorphic reaction, e.g. the sericitization of a feldspar, or dynamic recrystallization. The possible softening effects due to a phase transformation include transfor-

mation to a more deformable phase, and volume changes due to production of more or less dense phases. Metamorphic reactions may soften by replacing a strong mineral (e.g. olivine) by a relatively weak one (e.g. serpentine) or by acting as a grain size reduction mechanism (as in the sericitization of feldspar phenocrysts to a fine-grained aggregate of white micas). Dynamic recrystallization acts in two ways, firstly as a mechanism of recovery (White, 1977), if the recrystallization involves the production of strain-free new grains that are therefore more deformable, and secondly as a grain size reduction mechanism. The grain size reduction associated with dynamic recrystallization and metamorphic reactions softens the material by enhancing any process that involves diffusive mass transfer; pressure solution, Coble creep and Nabarro Herring creep or by increasing the contribution to the overall strain-rate due to grain boundary sliding (White, 1976).

2.7.2.3 Strain softening (s.s.)/hardening

Strain softening, sensu stricto, occurs for $n<0$ in the third factor of equation (2.9). Generally n is positive, although commonly very small and, when recovery balances the effect of dislocation multiplation (Nicolas and Poirier, 1976), $n \simeq 0$, i.e. it has no effect on the softening. There may be some true softening in the very early stages of deformation caused by the avalanching of dislocations once a critical stress has been reached, either freeing dislocations pinned at impurities or allowing adjacent dislocations to pass one another (Poirier, 1980), but it is not thought that this will contribute much to the overall softening.

2.7.2.4 Strain-rate softening/hardening

The term $\frac{m}{\dot{\varepsilon}}\frac{d\dot{\varepsilon}}{d\varepsilon}$ is invariably positive, however, the value of m, the strain rate sensitivity, is important in that, for values of $m<1$ (i.e. for non-Newtonian rheologies), localization of deformation is much more likely. (Poirier, op.cit.) Values of m for geological materials vary between 0.15 -

0.5 (see Kirby, 1980, for recent review), and they are therefore liable to localization.

2.7.2.5 Shear heating

The effect of shear heating is always to soften a material, but there is considerable controversy as to how important this effect is in naturally occurring shear zones. Brun and Cobbold (1980) have recently reviewed the various approaches that have been used to study the effects of shear heating.

They all use the general equation of Carslaw and Jaeger (1959)

$$C\frac{\partial T}{\partial t} = K\nabla^2 T + \dot{E} \qquad (2.10)$$

which refers to the situation shown in Fig. 2.4.

The term on the L.H.S. of the equation represents the rate of temperature (T) increase with time (t) and is governed by the volumetric specific heat (C). On the R.H.S. the first term represents the rate of heat loss due to conduction and depends on the thermal conductivity (K) and the temperature distribution ($\nabla^2 T \equiv \frac{\partial^2 T}{\partial x^2} + \frac{\partial^2 T}{\partial y^2} + \frac{\partial^2 T}{\partial z^2}$). The final term $\dot{E}$ is rate of energy dissipation per unit volume of material and is given by

$$\dot{E} = \sigma ij \dot{\varepsilon} ij$$

which becomes, for simple shear, $\dot{E} = \tau xy.\dot{\gamma} = \tau xy\frac{\partial u}{\partial y}$ (2.11)

In order to make the solution of (2.10) tractable certain simplifying assumptions are normally made. For a steady-state solution (i.e. $\frac{\partial T}{\partial t} = 0$) the equation reduces to

$$-K\frac{\partial^2 T}{\partial y^2} = \dot{E} = \tau\frac{\partial u}{\partial y} \qquad (2.12)$$

N.B. the R.H.S. has also been simplified by assuming that the temperature varies only in the y-direction, that is normal to the shear zone boundaries.

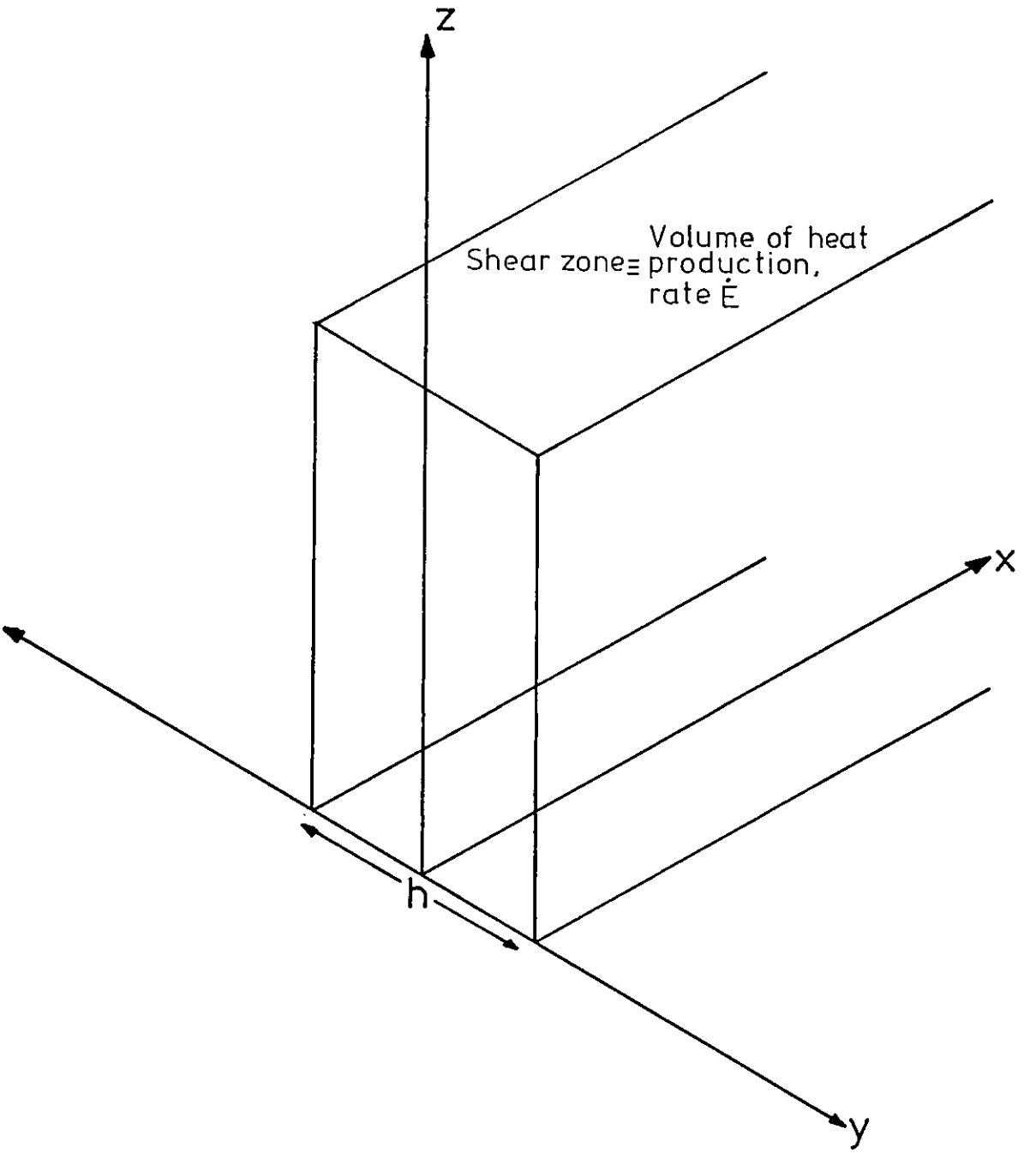


Fig.2.4 Reference system used in the mathematical modelling of shear heating problems. A vertical semi-infinite slab, thickness h, with rate of heat production Ė.

Although it is uncertain as to whether such a steady-state is ever achieved geologically, equation (2.12) has been much used in the study of shear-heating.

For a steady-state the stress (τ) is constant with time and, in the absence of body forces, this allows (2.12) to be integrated giving (Yuen et al., 1978)

$$K \frac{dT}{dy} + \tau u = 0 \qquad (2.13)$$

However, the rheological properties must be included before further integration. The flow law

$\dot{\gamma} = \frac{\partial u}{\partial y} = (2B/T)\exp(-H/RT)\tau^n$ when combined with (2.13) gives

$$K \frac{d^2T}{dy^2} + (\tau)^{n+1}(2B/T).\exp(-H/RT) = 0 \qquad (2.14)$$

Solutions covering a variety of particular cases have been developed by Gavis and Lawrence (1968); Yuen and Schubert (1977); Yuen et al. (1978) and Clark et al. (1977). The main conclusion is that the solution has three branches, known as the cold or subcritical branch, the intermediate or supercritical branch, and the hot branch (see Fig. 2.5). If the G parameter (a sort of normalized stress $G = \frac{a h^2 \tau^2}{k\mu o}$ where a is a constant, h is the slab thickness and μo the viscosity) exceeds a certain critical value, thermal runaway occurs.

On the cold branch, at low shear-rates, heat production is negligible and the strain-rate increases simply with stress. At higher shear-rates the heat production becomes significant, although strain-rate still increases with stress until, at a critical shear-rate, heat is produced faster than it can be conducted away, the material softens and the stress drops. At the higher temperatures experienced with higher shear-rates still the Arrhenius factor in the flow-law tends to a limiting value, and the strain-rate again

Fig. 2.5 Sketch of steady-state solutions to equation (2.14). H = hot branch , I = intermediate or supercritical branch , C = cold or subcritical branch .

Fig. 2.6 Model showing growth of a shear zone (after Coward, 1976). A. Undeformed state . Line a–b marks the initial shear zone surface . B. Deformed grid showing curvature of original shear surface . C. Flow cell for the shear zone . D. Variations in foliation orientation (long axes of strain ellipsoid) within the shear zone .

FIG. 2.5

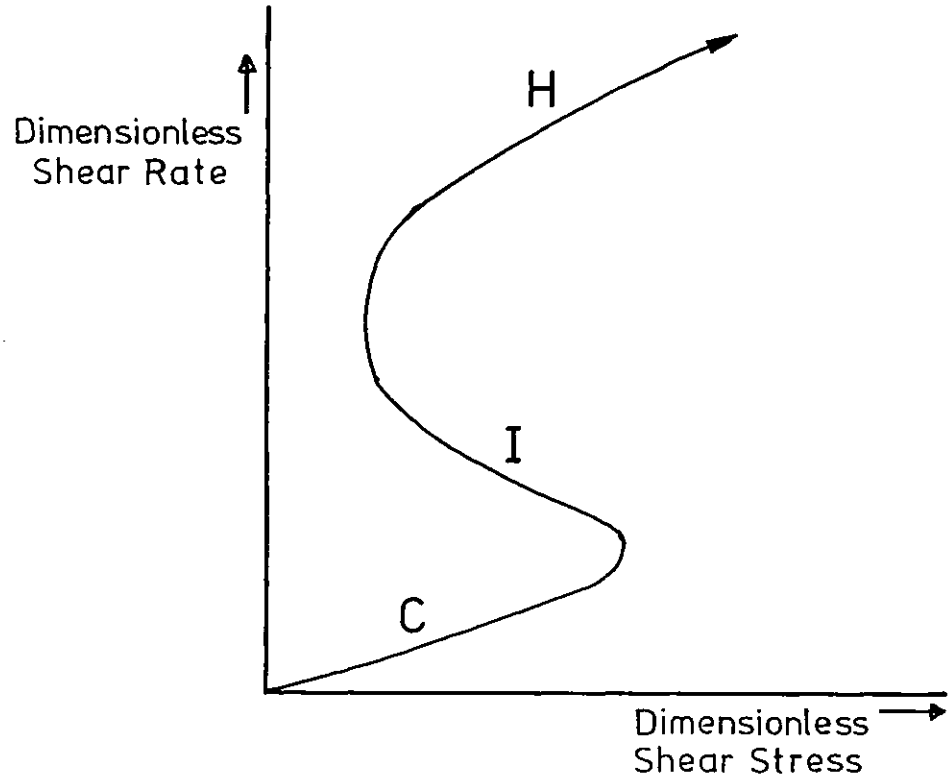
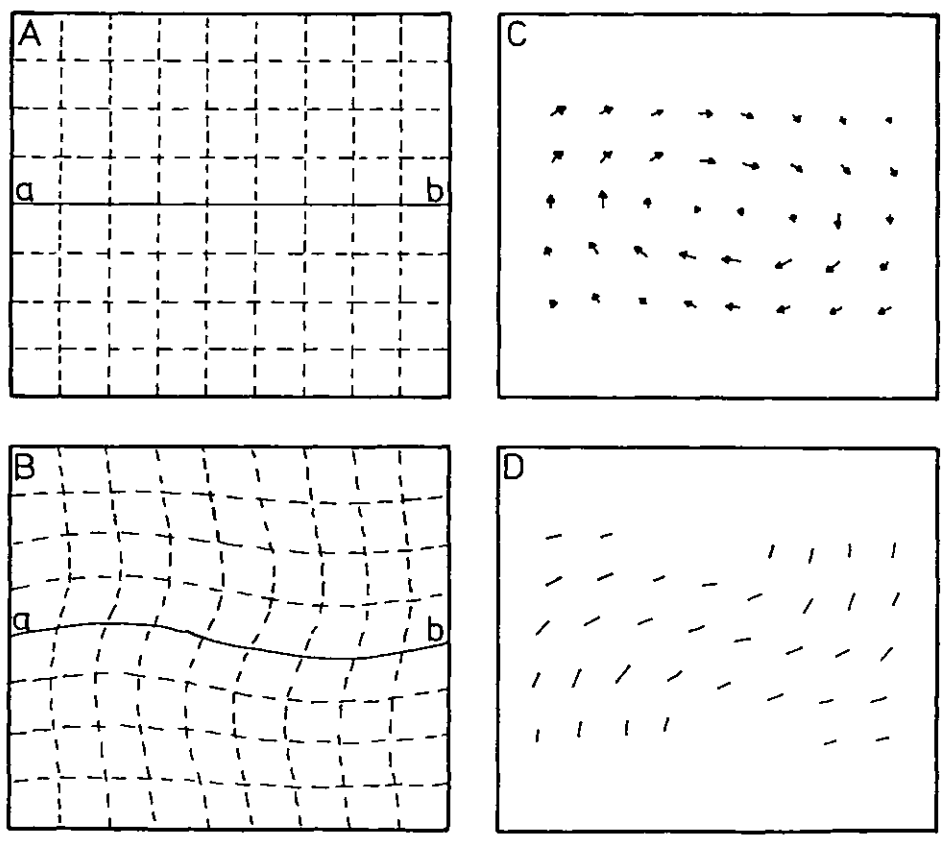

Dimensionless
Shear Rate
H
I
C
Dimensionless
Shear Stress

FIG. 2.6


A
a
b
C
B
a
b
D

increases with stress, this is the 'hot' branch. The existence of the 'cold' (subcritical) and 'intermediate' (supercritical) branches have been confirmed experimentally by Sukanek and Lawrence (1974).

The stability with time of the steady-state solutions may be investigated either by using the fully time-dependent equations (e.g. equation (2.10)), or else by determining the effect of a small perturbation of the steady-state flow, that is to see if it grows or decays.

The effect of small one or two-dimensional perturbations on the steady-states in the sub- and super-critical branches have been studied by Melosh (1976); Clark et al. (1977); Yuen and Schubert (1977) and Schubert and Yuen (1978). Of these, only the analysis of Melosh (1976) predicts unstable flow, due to an infinitesimal perturbation on a supercritical branch steady-state, but only at constant stress; all the other analyses indicate that the basic states are stable to perturbation.

Using equation (2.12) combined with the flow-law, Yuen et al. (1978) studied the evolution of an initial disturbance in an infinitely thick slab at constant boundary velocity and temperature. They found that if the disturbance was confined to a narrow zone, the temperature of the zone rapidly approached the maximum value predicted by the steady-state solution, whilst outward conduction of the heat caused the zone to broaden slowly.

Fleitout and Froidevaux (1980) have looked at the effect of a relatively broad (10 km), but weak thermal anomaly upon a 100 km wide 'shear zone' in a non-newtonian material. The initial effect is to localize the deformation in the central two kilometres, although this broadens with time; the lower the initial temperature, the greater the rate and degree of localization.

Another simplified form of equation (2.10) is made by assuming that no heat is conducted away, i.e. the system is at all points adiabatic, giving

$$C\frac{\partial T}{\partial t} = \dot{E} \qquad (2.15)$$

This approach has been used by Poirier et al. (1979), who justify this approximation from their results which indicate no significant shear heating for either fast, narrow zones, or slow, broad zones; the assumption of adiabatic heating can only lead to an overestimation of the resultant temperature rise(Brun and Cobbold, 1980).

The last simplification that has been made, is that the rate of heat production remains constant i.e. $\dot{E}$ = Const. The analysis may then proceed using the equations of Carslaw and Jaeger (1959). Such analyses assume a zone on constant width, imply linear viscous rheology and ignore the effects of positive thermal feedback. This approach is, however, useful as a preliminary study, allowing a relatively simple analysis to get an approximate estimate of the importance of shear heating.

The following conclusions may be drawn from the published literature,

1. Thermal runaway is only possible under constant stress, for large zones ($\sim$1 - 10 km) and/or high differential stresses ($\sigma_1 - \sigma_3 \geqslant$ 100MPa), conditions that may never occur naturally.

2. Large shear zones are expected to show some shear-heating effects, particularly the localization of deformation at the centre of the zone.

3. Shear heating in small ($\leqslant$ 100 m) shear zones is not thought to be significant.

4. The evidence for shear heating is both scanty and equivocal.

2.8 Theories of shear zone formation

In reviewing the literature on shear zone formation, it is necessary to look at the literature in many other related fields, as shear zones are the common mode of heterogeneous ductile deformation in materials. The development of shear zones as instabilities has already been considered in Section (2.7) and theories of shear zone formation tend to fall into two categories depending on whether they are treated as localisation or propagation instabilities. In the former case, analyses proceed from the assumption that a planar zone of weaker material is already present, and then look at the localization of deformation within the zone. Alternatively shear zones may be considered to have formed from instabilities that have propagated through the system, leaving the shear zone behind.

2.8.1 Localization models

This phenomenon has already been treated in a general way in Section 2.7 (e.g. Bowden, 1970; Poirier, 1980), and in Section 2.7.2.5 specifically with regard to localization by thermal softening (e.g. Yuen et al., 1978; Fleitout and Froidevaux, 1980). Recent analyses have been applied to the specific problem of the localization of deformation within a zone of simple shear, Poirier et al. (1979) and Casey (1980).

Poirier et al. (1979) modelled their shear zone as, a zone of finite, constant width whose boundaries are subjected to a constant strain-rate (i.e. a constant displacement rate). They assumed the material inside the zone to have an almost perfectly rigid plastic rheology and to deform by the sort of flow-law used in Poirier (1980) (Equation 2.7). They looked at the effect of an initial strength defect, $^{\Delta K}/K$ (where K represents the combined effects of structural and geometric softening) on the resultant evolution of strain in the zone under both adiabatic and isothermal conditions, using rheological data from the experimental deformation of granite (Goetze,

1971; Goetze and Brace, 1972).

The principal conclusions of Poirier et al. (1979) are; shear heating is unimportant as regards shear localization, stresses in shear zones should be ∿1 - 25 MPa, an initial transient unstable period is replaced by a stable growth regime with the strain-rate in the shear zone proportional to that at its boundaries, this transient period may be increased by structural softening, leading to further localization.

Casey (1980) also used a model of a planar zone of weakened material to look at the development of both brittle and ductile shear zones. For the brittle case he used an elastic analysis to predict the orientations, and relative magnitudes of the principal stresses based on the minimization of the elastic strain energy. This analysis is generalized to the ductile case by using the normal strain - strain-rate, bulk modulus - viscosity, equivalence (see for example, Biot, 1965), and looking for the minimization in the rate of energy dissipation. The analysis predicts observed orientations of second order fractures and is also used to explain the development of the semi-brittle en echelon 'tension-gash' shear zones. The application to purely ductile zones is completely restricted to the possibilities of phase changes caused by increases in the mean stress (see also White and Knipe, 1978).

2.8.2 Propagation models

All the preceding analyses assume the initial presence of a weak zone in which deformation may localize. It seems clear, however, that shear zones form in areas in which no planar zones of weakness previously existed. Coward (1976) and Cobbold (1977(a),(b)) have both provided continuum models of shear zone propagation.

Coward (1976) looked briefly at the initial stage of shear zone devel-

opment in a homogeneous continuum. He showed that for constant boundary conditions, a shear displacement at the centre must be accompanied by a rotation of the zone leading to a sygmoidal shape. Associated with the ends of the zone are areas subject to incremental strains that depart considerably from simple shear (Fig. 2.6)(see also Ramsay, 1980). Coward suggests that the form of a shear zone will be controlled by the rate of displacement compared to that of propagation; if the propagation rate is of the same order as the displacement he argues that the resulting zones will be curviplanar, and of low aspect ratio, and that only if the propagation rate is comparatively high will long planar zones result.

Cobbold (1977(a)(b)) presented a general analysis of the development of banded perturbations. He divided them into P, P and S, and S bands, depending on the relative contributions of pure and simple shear to the finite strain state within the band. He discussed the possible importance of strain-softening, and hardening associated with a variety of deformation mechanisms, both brittle and ductile. He shows that the effect of strain-softening is to cause the deformation to accelerate under constant stress, and to become locally perturbed; strain-hardening has the opposite effect.

Cobbold (op.cit.) also addressed himself to the problem of how banded deformation structures evolve from initial perturbations that are very unlikely to be of the same form or size as the resultant structure. He considered two ways in which deformation could spread from the initial perturbations into unperturbed regions; terminal propagation, and lateral propagation. Terminal propagation occurs by continued deformation softening at the ends of an original lens-like perturbation induced by the presence of the perturbation during progressive regional deformation; this process has been observed in the experimental formation of kink-bands. The lateral

propagation of kinks has also been observed experimentally (Cobbold et al. 1971) and Cobbold (1977(b)) gives secondary strain-hardening within the band as the most likely cause of this widening.

Rice (1973) was the first to apply models developed for crack propagation including the effects of crack-tip plasticity (for a general review see Lawn and Wilshaw, 1975, Chapter 4), to the problem of propagation of shear-zone like structures, 'shear-bands' developed in overconsolidated clays (Palmer and Rice, 1973). They used the J-integral technique, developed from fracture mechanics (Rice, 1968(a), (b)) to derive the conditions for the propagation of a shear-band. The analysis is elastic/viscoelastic and is not therefore strictly applicable to ductile shear zones. However the concept of a shear zone as a type of shear fracture is a very useful one.

Ball (1980) presented a theory for shear zones based on a shear-crack model. He considered a disc-shaped crack embedded in a volume of rock with a toroidal volume of plastic deformation at the leading edge, with the rest of the volume deforming elastically. He gives an expression for the stress at the shear-zone tip (τc)

$$\tau c = \tau o(c/2r)^{0.5} \quad \text{where } \tau o \text{ is the initial stress} \qquad (2.16)$$

c is the 'crack' length

r is the distance from the tip

This equation assumes that the deformation is effectively discontinuous due to the material within the shear zone having a negligible shear resistance, analagous to a fluid-filled crack. The extreme weakness of the mylonites within the zone envisaged by Ball follows from the use of a characteristic 10μm grain size, and particular flow-laws for the material inside and outside the zone. These give strain-softening of at least seven orders of magnitude during mylonite formation.

The degree of strain-softening determined above seems likely to be an overestimate. The grain size of 10μm is at odds with published mylonite grain sizes, with grains of d $\leqslant$10μm being the exception rather than the rule (see for instance Fig. 5.9 for olivine, Table 5 from this study for quartz, also Etheridge and Wilkie, 1979). For grain boundary study homologous temperatures of T/Tm $\geqslant$ 0.6 are assumed ($\sim$750^{o}C for quartz, $\sim$1200^{o}C for olivine) conditions unlikely to be met within the lithosphere outside anatectic regions. Finally, equation (2.16) predicts ever increasing stresses as the length of the crack increases. This change should be reflected in major variations in grain size along the length of any shear zone, with the grain size decreasing away from the point of initiation; such distributions of grain size have not been reported although it is not clear if any study has been carried out in sufficient detail to find such an effect.

CHAPTER 3

In this chapter the general geology of the eastern Pyrenees will be briefly outlined to provide the regional setting, previous work on the Cap de Creus will be reviewed, and the fieldwork carried out during the present study will be described.

3.1 Regional setting

The Cap de Creus area forms part of the eastern margin of the Pyrenees mountain range. This orogenic belt is commonly divided (e.g. Ager 1980) into; the central axial zone, consisting of strongly deformed Palaeozoic and earlier schist, gneisses and granitoids; two internal zones, composed of folded Mesozoic and Caenozoic sediments with occasional massifs of Palaeozoic basement, and two external zones, marginal troughs of relatively undeformed Mesozoic and Caenozoic sediments; the area studied falls within the axial zone.

The sequence of events in the Hercynian complex of the Pyrenees is shown in Table 3.1. (from Read and Watson, 1975). A distinction is made between a metamorphic infrastructure, and a non-metamorphic suprastructure with a marked change in tectonic styles occurring across this boundary. Related to this is the unusually high geothermal gradients associated with the metamorphism, which is of high temperature, low pressure type; locally the gradient is thought to have been as high as $150^{o}C\ km^{-1}$, as at Bosost (Zwart, 1962).

The fourth phase of deformation shown in Table 3.1. was followed in many places by the development of mylonite zones in the infrastructure, with trends approximately parallel to the dominant E-W folds (Carreras et al. 1980). The exact age of these mylonites is a matter of some controversy (Carreras et al. op. cit.), but most workers agree that the majority are late Hercynian, with varying degrees of reactivation during the Alpine

TABLE 3.1 HISTORY OF THE HERCYNIAN COMPLEX OF THE PYRENEES (based on de Sitter, Zwart and others)

		Sedimentation	Deformation and Metamorphism		Granite-emplacement
CARBONIFEROUS	Stephanian (locally late Westphalian)	post-tectonic non-marine sediments including coals	Phases of deformation		
			4	E-W folding in supra- and infrastructure; migmatisation continues in infrastructure	intrusive granodiorites
			3	conjugate folds and crenulations in infrastructure, sillimanite-bearing assemblages and migmatites	intrusive granites
			2	infrastructure only, N-S axes, new schistosity, with andalusite-cordierite assemblages	
			1	main E-W folding, with steep axial-plane cleavage in suprastructure, flat schistosity and greenschist facies assemblages in infrastructure	
	Dinantian (locally includes early Westphalian)	sandy shales, often with a dark chert group at the base, usually less than 1km			
DEVONIAN		shales and limestones, including griottes, up to 1km			?early granites now transformed to orthogneisses
SILURIAN		black slates			
CAMBRO-ORDOVICIAN		psammites, pelites, conglomerates, rare limestones, thickness unknown			
PRECAMBRIAN		crystalline basement			

FIG. 3.1

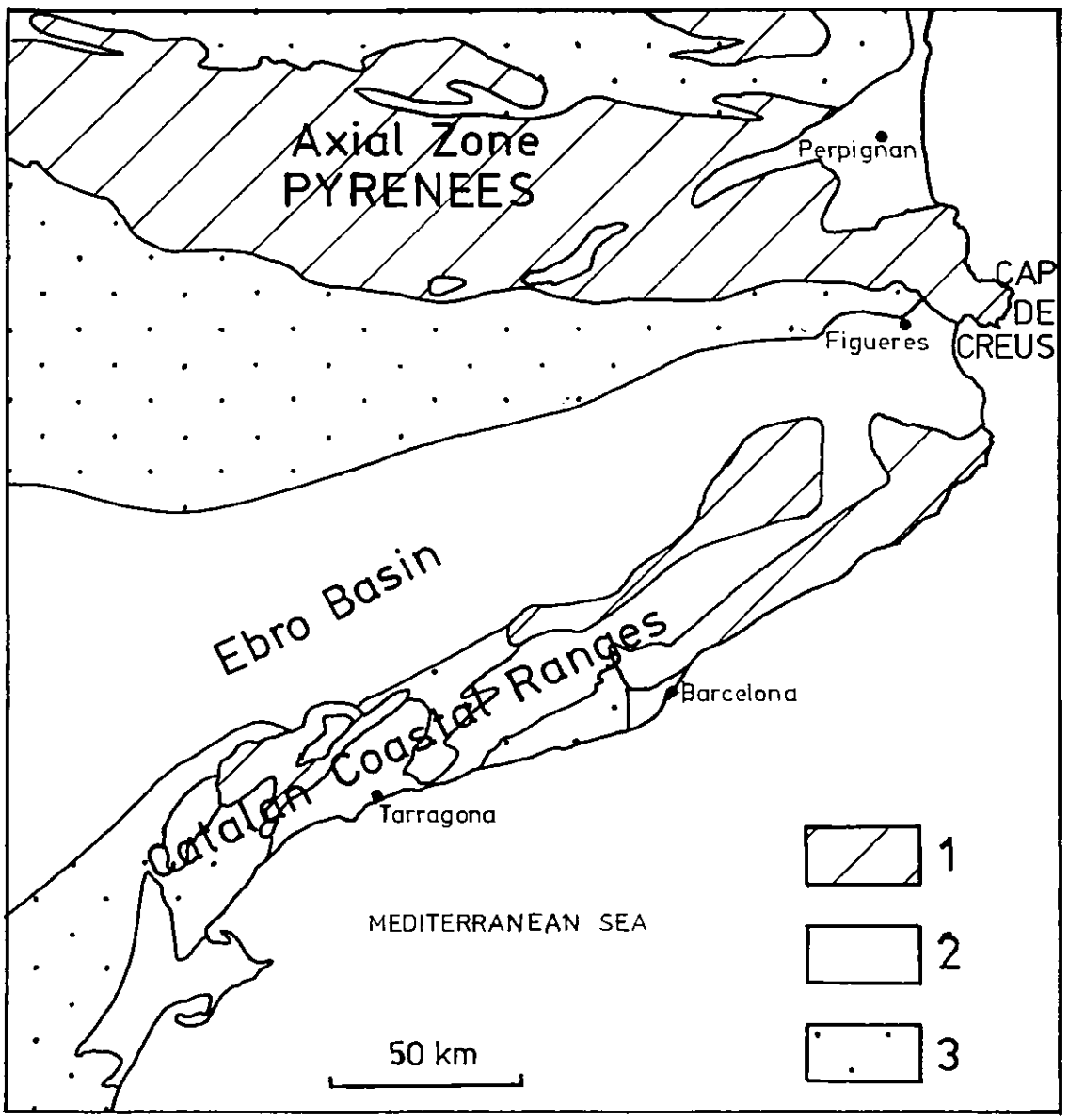


Fig. 3.1 The main litho-structural units of Catalonia (NE Spain)
1. Hercynian basement 2. Mesozoic and Caenozoic sediments
3. Post-alpine sediments.

movements. The stretching lineation in the mylonites of the eastern Pyrenees show a variation from near horizontal i.e. dominantly strike-slip, to moderately steeply plunging towards the north-west, i.e. dip slip ≈ strike slip. Carreras et al. (op. cit.) have shown that these mylonite zones may be related genetically to the E-W folding, especially in the 'pinched-in' synforms developed at the edges of the gneissic domes commonly found in the axial zone.

3.2 The geology of the Cap de Creus

Until the last decade the geology of the Cap de Creus area was not studied in anything more than a superficial manner. However, in the last ten years, the geology has become known in considerable detail, principally through the efforts of Carreras and his colleagues from the University of Barcelona.

On the peninsula of the Cap de Creus (for location see Fig. 3.1.), two main lithological units can be delimited (Carreras, 1979).

1) A monotonous series of psammitic and pelitic sediments, attributed to the Cambro-Ordovician, which underwent varying degrees of metamorphism during the Hercynian orogeny.

2) Two small (and possibly connected) granitoid massifs, partly transformed into gneisses.

The distribution of these is shown in Fig. 3.2(a), which also shows the development of the metamorphic zones within the sediments. The zones dstinguished are; I) Chlorite-muscovite zone, II) Biotite zone, III) Cordierite-andalusite zone. The last of these zones is confined to a narrow strip running along the north-eastern coast, and parallel to it, and is also known as the Perianatectic zone (Carreras et al. 1975). In this region the schists are cut by a number of granitoid sheets of varying chemistry from granite s.s. to quartz-diorite. The latter type locally forms anatectic migmatites,

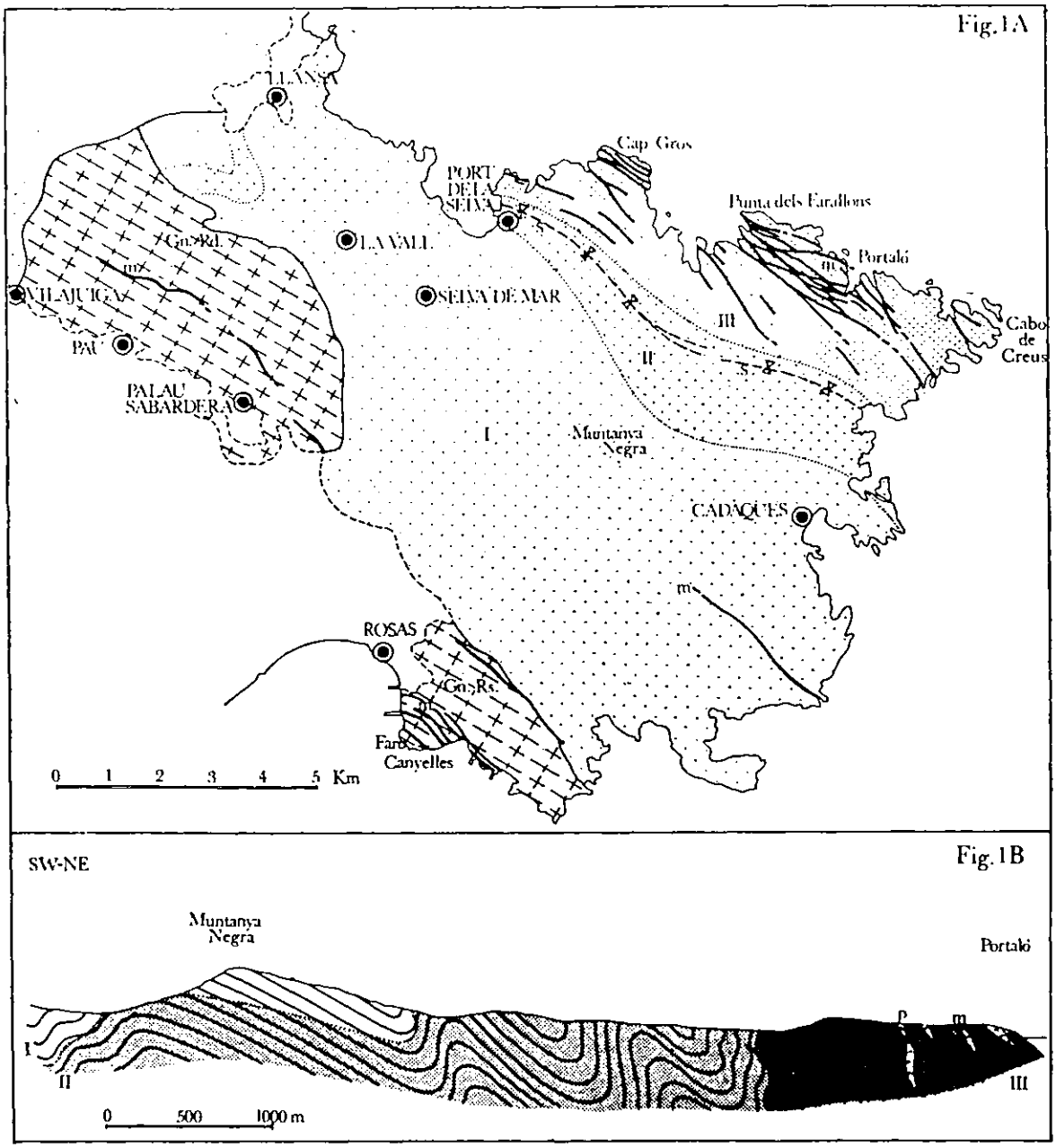


Fig. 3.2 Geological map (a), and section (b) of the peninsula of Cap de Creus. Gn.Rd. Roda gneissic granodiorite ; Gn.Rs. Roses gneissic granodiorite. I. Chlorite-muscovite zone II. Biotite zone III. Cordierite-andalucite zone including the perianatectic zone. m : mylonites , s : synform axial trace. (from Carreras, 1975)

whereas the granitic dykes and pegmatites show only intrusive relationships with the schists.

The structural history of the Cap de Creus area may be divided into two main deformation episodes. During the first, a major phase of folding, the main S1 schistosity was developed under prograde metamorphic conditions. The second was characterized by folding of the S1 schistosity under retrograde conditions. In this later episode, more than one phase of folding may be recognised, but, in general, the dominant folds are the last, and have north-west-south-east axial plane traces, with axes subhorizontal or gently plunging towards the south-east.

The last ductile deformation in the area is that which produced the mylonite zones. These occur as anastomosing curviplanar bands of very high shear strain, almost completely confined to the cordierite-andalusite zone of the metasediments. The assignment of these particular zones to the late Hercynian is based on the cutting of one zone by an undeformed lamprophyre dyke (Carreras, 1975(a)). This dyke is correlated with very similar dykes found at Begur, and Patamos, c. 30km to the south, that have been dated by Chessex et al. (1965) as late Triassic - early Jurassic.

3.2.1. Geometrical aspects of the mylonite belt

The deformation within the mylonite zones is assumed to be one of dominant simple shear, from the consistent sense, and magnitude of displacements suffered by originally continuous markers of varying initial orientation (Carreras, 1979). By making the above assumption it is then possible to measure shear strains by observing the rotation of markers into the mylonite foliation (Carreras, 1975 (b)), and shear strains of $\gamma>10$ have generally been observed (Carreras, 1979).

The individual shear zones vary in width from several millimetres up to a few tens of metres. Locally they form dense concentrations of anastomosing bands giving rise to complex shear zones of up to hundred metres in

width. Between the separate bands in such a zone, relatively undeformed country rock augen are developed (Carreras, and Santanach, 1973). The overall trend of the zones is north-west - south-east, but due to the anastomosing pattern, this varies from east-west, to north-north-west - south-south-east (Carreras, 1979). Fig. 3.3 (after Carreras, op.cit.) shows both the variations in orientation of the mylonite foliation, and the associated stretching lineations, which plunge shallowly towards the north-west.

The sense of displacement on most of the zones is seen to be dextral which, together with the orientation data shown above, and the assumption that the stretching lineation is approximately the movement direction (Carreras, and Santanach, 1973), indicates dextral strike-slip displacement with a small component of reverse dip slip, for the mylonite belt as a whole.

3.2.2. The mylonites

Rock types affected by mylonitization include; psammitic to pelitic schists, with quartz lenses, chlorites, quartz-diorites, microgranites, garnetiferous pegmatites, and tourmaline pegmatites. Deformation of this lithologically heterogeneous country rock produces well banded mylonites.

Three main types of mylonite have been recognized (Carreras, 1979):

i) Schist-derived mylonites (Phyllonites)

These rocks are dominated by fine, new or recrystallized, micas giving the very strong planar fabric typical of a phyllonite. Porphyroclasts of strongly bent mica, feldspar, garnet, andalucite, cordierite remain relatively undeformed. Any quartz present is completely recrystallized to grains whose size is similar to that of the fine micas.

ii) Quartzo-feldspathic mylonites

These are derived from granitoid rocks and tend to form very well-

FIG. 3.3

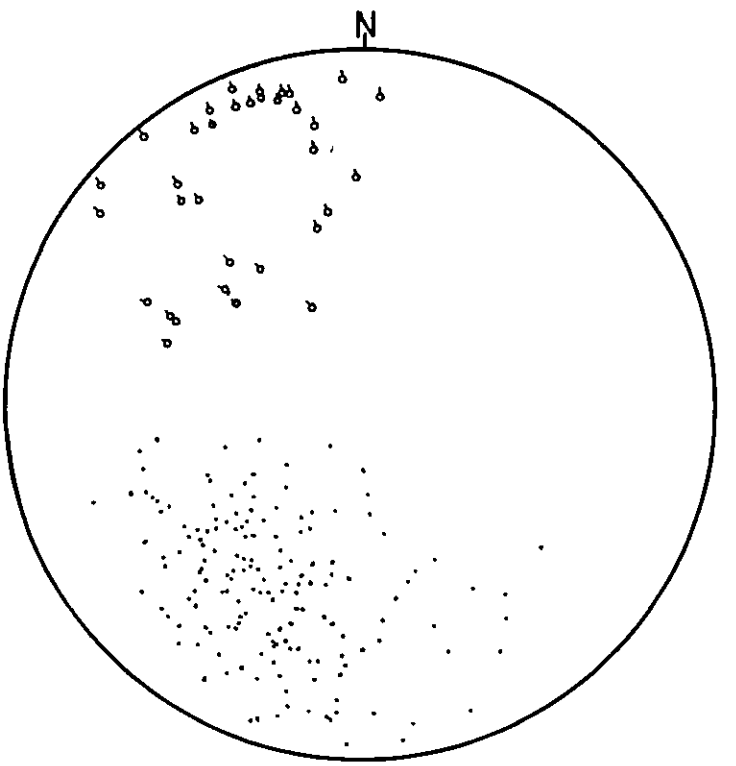


Fig. 3.3 Lower hemisphere stereoplot of mylonite foliation poles (•) and associated stretching lineations (b) in the shear zones at Cap de Creus. (after Carreras, 1979)

banded mylonites on the grain scale. Quartz forms very elongate ribbons of completely recrystallized grains; micas and feldspars show some internal deformation with recrystallization at grain boundaries.

iii) Quartz mylonites

These result from the deformation of quartz veins within the schist, or locally in the granitoids, and rarely from single quartz megacrysts in pegmatites. The quartz is completely recrystallized to an aggregate of sub-equant grains ranging in size from 50μm to 500μm. The quartz grains show a very well-defined c-axis preferred orientation, consisting of two maxima lying on the plane perpendicular to both foliation and lineation, symmetrically disposed at between 20^{o}-30^{o} to the foliation plane. The progressive development of this fabric has been studied by Carreras et al. (1977), who showed that a stable c-axis pattern was already present at a shear strain of $\gamma \sim 2$.

3.2.3. Structures within the mylonites

The mylonite foliation, particularly in quartz rich bands is affected by small asymmetric folds (Plate 3.1(a)) These folds have an asymmetry that is usually consistent with the sense of movement (see Fig. 3.4)(Carreras and Santanach, 1973). Commonly the hinge lines of these folds are curved, sometimes very strongly so as to give the tongue-like structures that have been termed 'sheath folds' (Carreras et al. 1977). These folds have been interpreted as being due to the modification, by simple shear, of folds formed due to some sort of buckling instability related to the strong, planar, mechanical anisotropy of the mylonites (Carreras et al. op.cit.).

Plate 3.1 Field photographs of the Cap de Creus shear zones

(a) Asymmetric folds in quartz mylonite bands developed in a shear zone of dextral sense. Field of photograph = 0.5m.

(b) Shear bands developed in dextral sense shear zone in phyllonite layers.

(c) Shear zone formed at contact between microdiorite dyke (bottom left) and psammitic schist (top right). Note the sigmoidal foliation developed within the dyke.

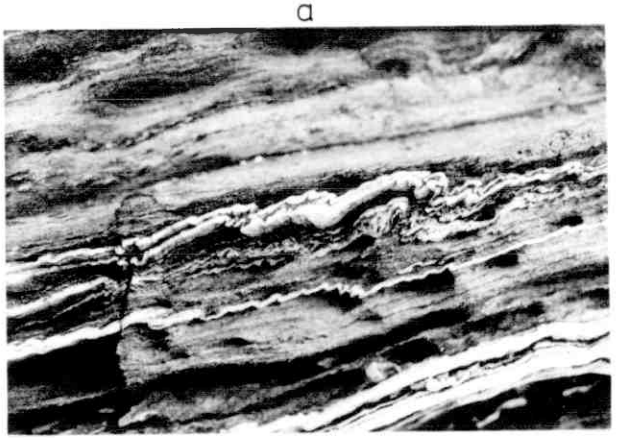
(d) View of the junction between the main dextral zone (the gully running from top right to bottom left) with a minor sinistral zone (small gully to left).This is the area marked (D) on Map 1.

(e) Ultramylonite zone developed within quartz-diorite migmatite.

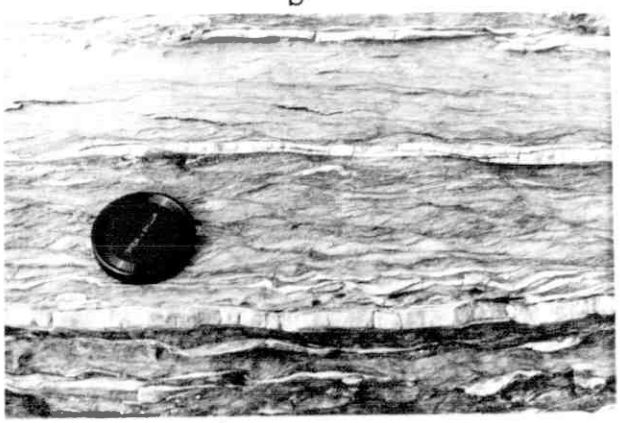
(f) Original quartz vein in quartz-diorite now a mylonite while the adjacent rock remains virtually undeformed.

PLATE 3.1

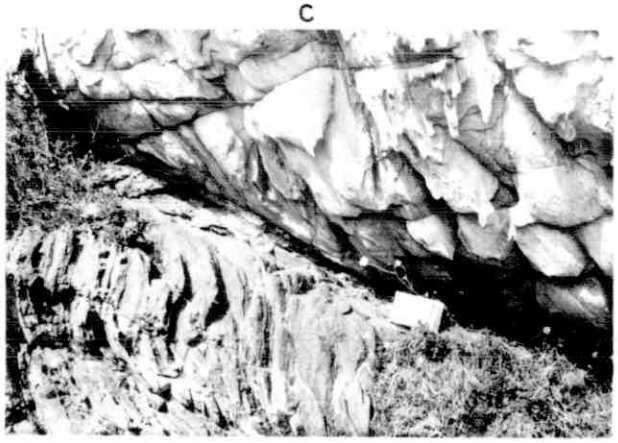
a



b



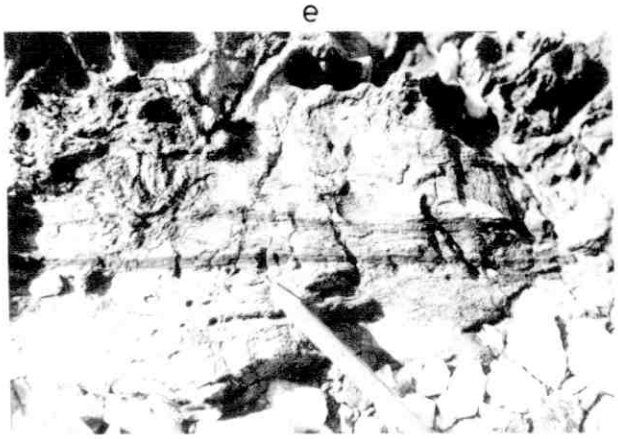
c



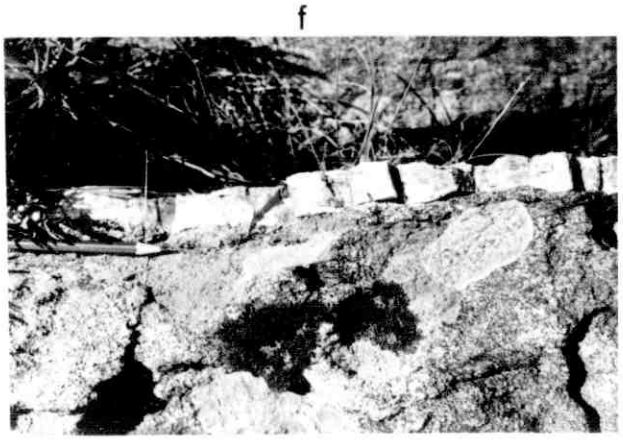
d



e



f



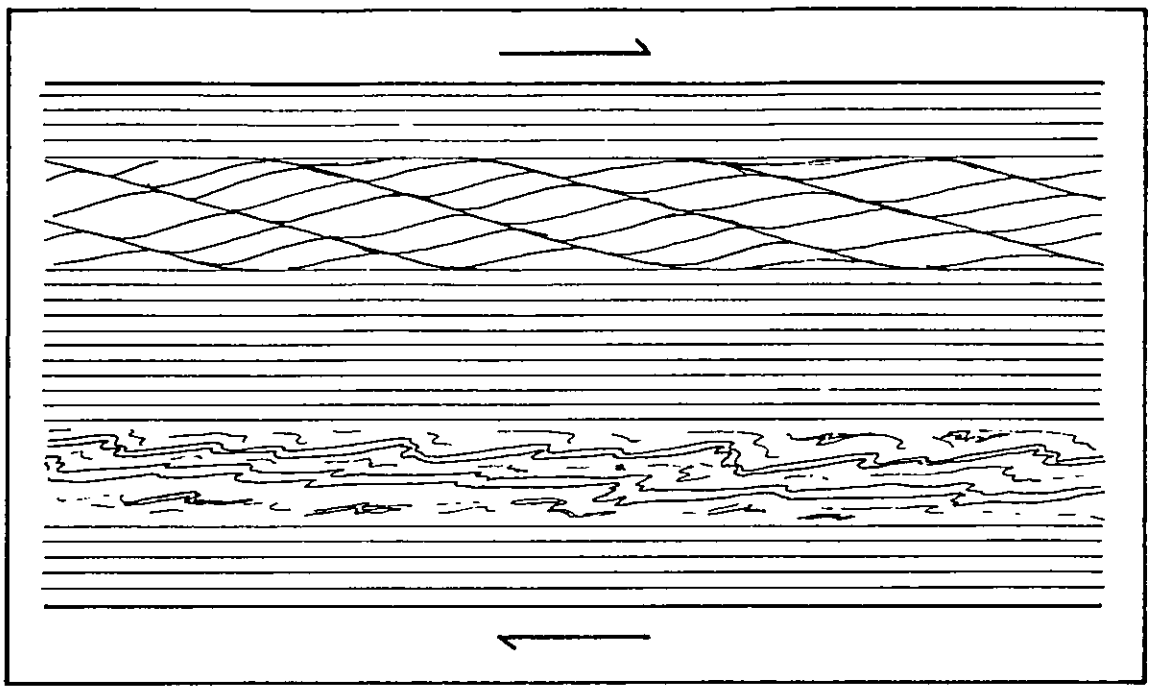


Fig. 3.4 Schematic diagram showing the geometric relationship between minor structures within the mylonites and the overall sense of shear, with shear-bands in the phyllonite layers and folds in the quartz bands.

In the phyllonites, a secondary foliation is commonly developed, with a concomitant rotation of the mylonite foliation (Plate 3.1(b)) The foliation is developed as fine-scale bands showing shear displacement that have been termed shear-bands (White et al. 1980), due to their geometrical similarity to the secondary shear structures observed in rolled metals (e.g. Dillamore et al. 1979). The mylonite foliation rotates due to the constraints on movement along the shear bands provided by the planar boundary conditions. The shear bands have always been observed to show the same sense of shear as the mylonite zone in which they are developed (Fig. 3.4) but as they are thought to be a very late event in the ductile history of the shear zone (White et al. 1980) they may reflect only the last period of movement within the mylonites.

3.2.4. Relationship of mylonite zones to the regional structure

The relationship between the shear zones, and the late fold phases have already been mentioned in section 3.1. In the Cap de Creus area it is possible to trace the shear zones into the lower grade, and more aniso-

tropic schists to the south-west. In these rocks the shear zones grade into the thinned and stretched limbs of asymmetric folds (Carreras,1979). From Fig. 3.2. (b) it can be seen that the mylonite zones are preferentially developed on the steep limb of a tight synform, and Carreras op. cit. has suggested that the shear zones may be associated with the deformation of the most crystalline rocks, which resisted folding during the flattening that occurred at an advanced stage in the development of the main fold.

3.3. Fieldwork carried out

The aims of the fieldwork may be summarized as follows:-

(i) To provide samples for microstructural observations and for palaeostress work.

(ii) To look at individual shear zones, particularly their terminations with respect to shear zone propagation.

(iii) To map in detail a few areas, to observe the kinds of network set-up, and to check for evidence that pre-shear zone structures were important in localizing the deformation.

In the following section the areas mapped in detail will be described, and observation relating to aims (i) → (iii) reported, finishing with general observations not restricted to individual areas.

3.3.1. The Cala Sardina Network

This area was chosen because of the excellence of the exposure, in many places ∿ 100%, combined with an extensive network of minor shear zones developed in an area lacking any dominant foliation, or significant lithological variation.

The area consists entirely of pelitic/psammitic schists with the exception of a single, ca. 1m wide, microdiorite dyke, which cuts all the

pre-shear zone structures. The region mapped is bounded to the south by the southern edge of a major shear zone of the main set of roughly equal normal dip-slip, and dextral strike-slip components of movement, and to the north by the Mediterranean coast.

Mapping in this case concentrated almost entirely on the minor shear zone network, no attempt being made to decipher the complex structure and resultant outcrop pattern of pelitic and psammitic layers caused by up to three phases of superimposed folding. Blank areas on the map signify that no shear zones at all are developed there. Sketch maps were drawn of relatively small areas, without any base or exact scale, but with the orientation accurately recorded. Later these individual sections were pieced together and drawn onto a base map produced by photographic enlargement of part of the map shown in Fig. 3.5., giving rise to Map 1.

3.3.1.1 Minor Shear Zones

Outside the major shear zone, the network at Cala Sardina may be divided into three types, that will be termed sinistral, dextral and thrust. These minor shear zones vary in width from a few millimetres up to about half a metre, and have lengths ranging from a few metres up to at least fifty metres.

3.3.1.1.1 Shear zone orientations

Fig. 3.6(a) is a π-pole diagram, showing the variation in orientation of the three types of shear zone. (The data recorded is that of mylonitic foliation planes within the zone which, for the shear strains of $\gamma \sim 50$ developed is taken to be the same as that of the shear zone planes themselves). The individual sets define separate concentrations with only a small degree of overlap. The dextral data falls approximately along a great circle, with trends from ESE/WNW - SSE/NNW, the greatest concentration being to the latter end of the range; dips are generally very steep towards the north-east. The

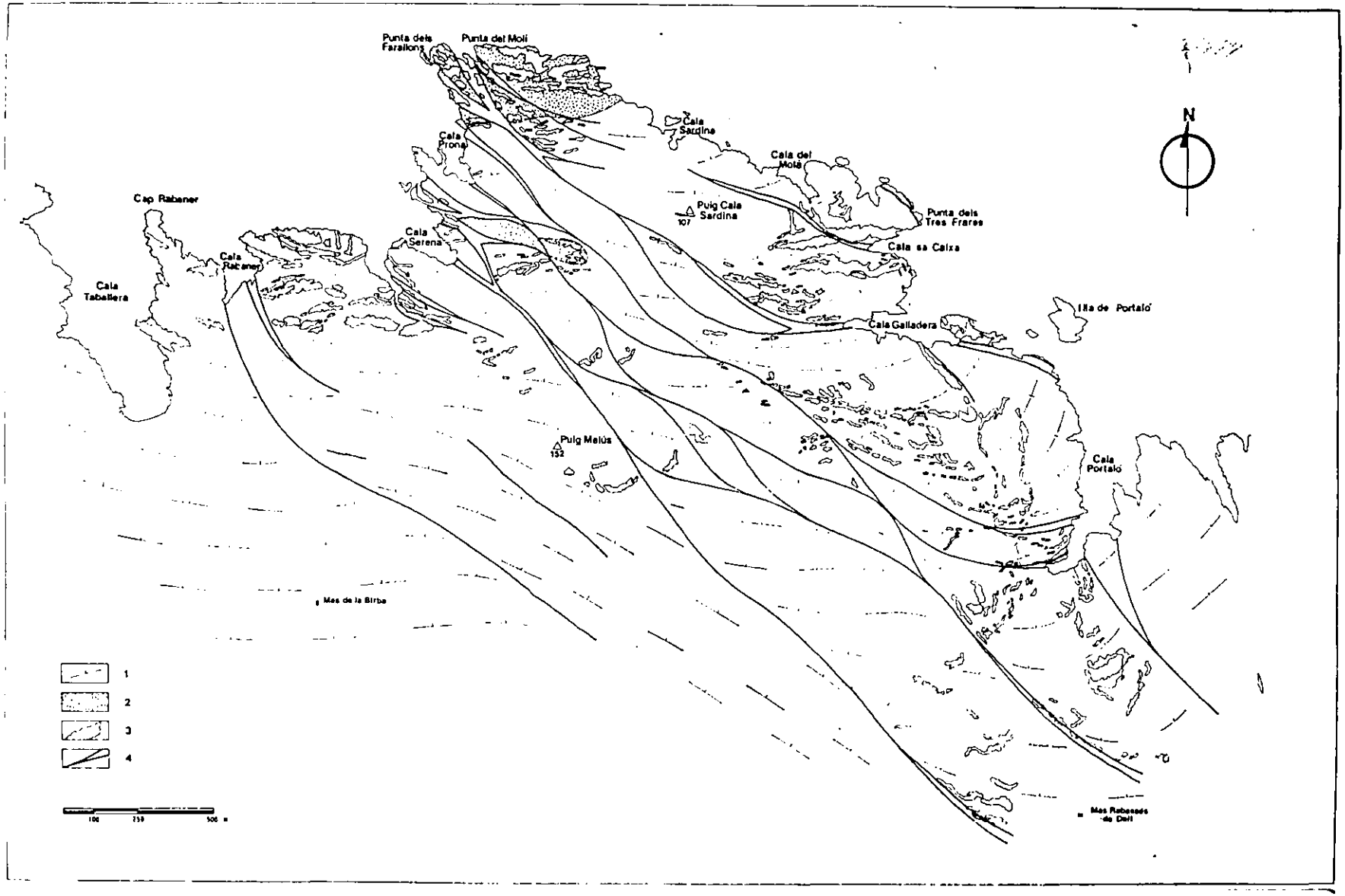


Fig. 3.5 The Cap de Creus shear zones in the area located between Cala Taballera and Cala Portalό. 1. Schists with trace of foliation. 2. Migmatites and quartz-diorites. 3. Pegmatites 4. Mylonites .

Fig. 3.6 Lower hemisphere. equal area, steroplots from the Cala Sardina area.

(a) π-poles to planes of minor shear zones

(b) Quartz grain elongation lineations in minor shear zones

(c) π-poles to mylonite foliation in main dextral shear zone Cala Sardina

(d) Quartz grain elongation lineations in main shear zone

KEY

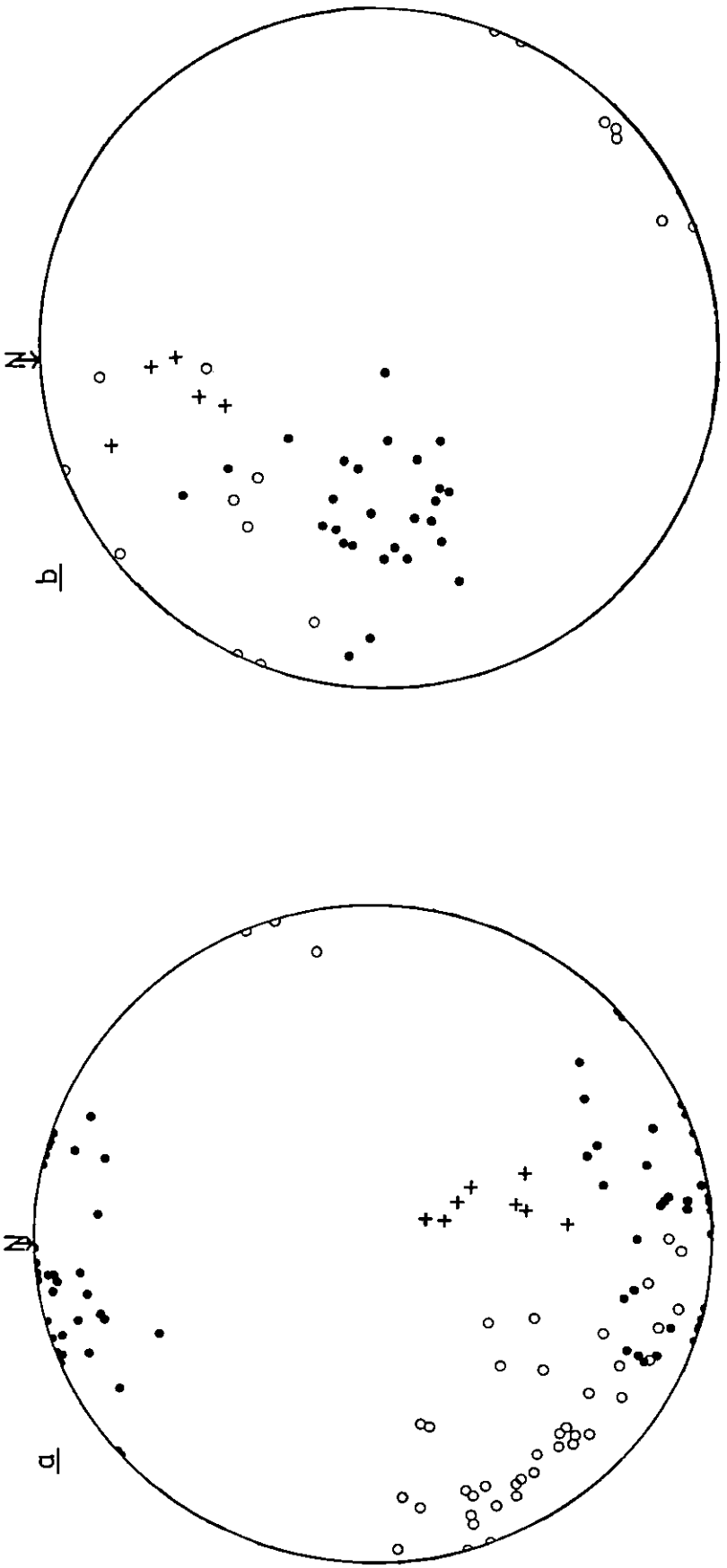
minor shear zones

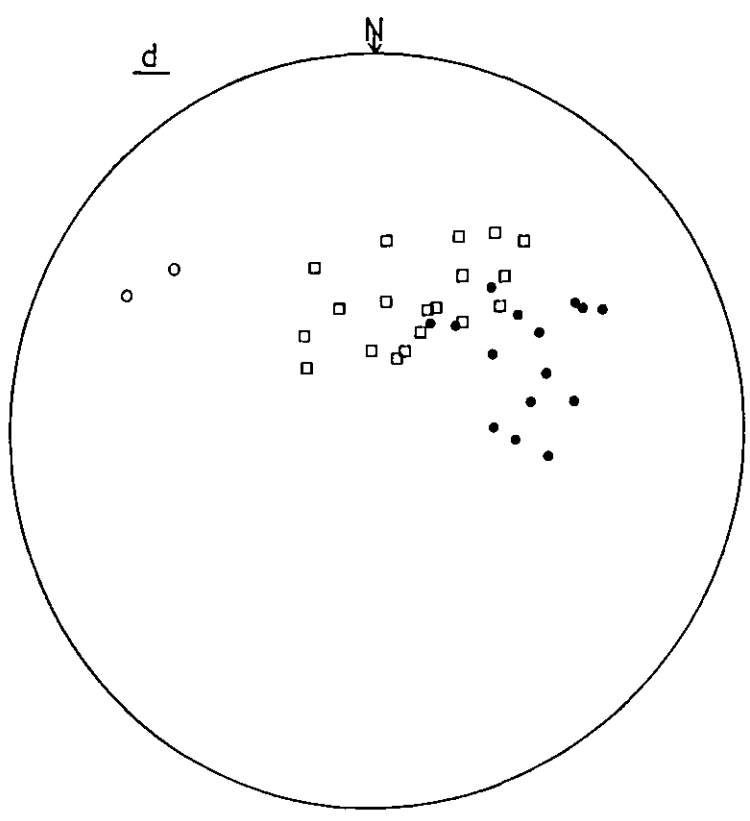
- ● sinistral
- O dextral
- + thrust

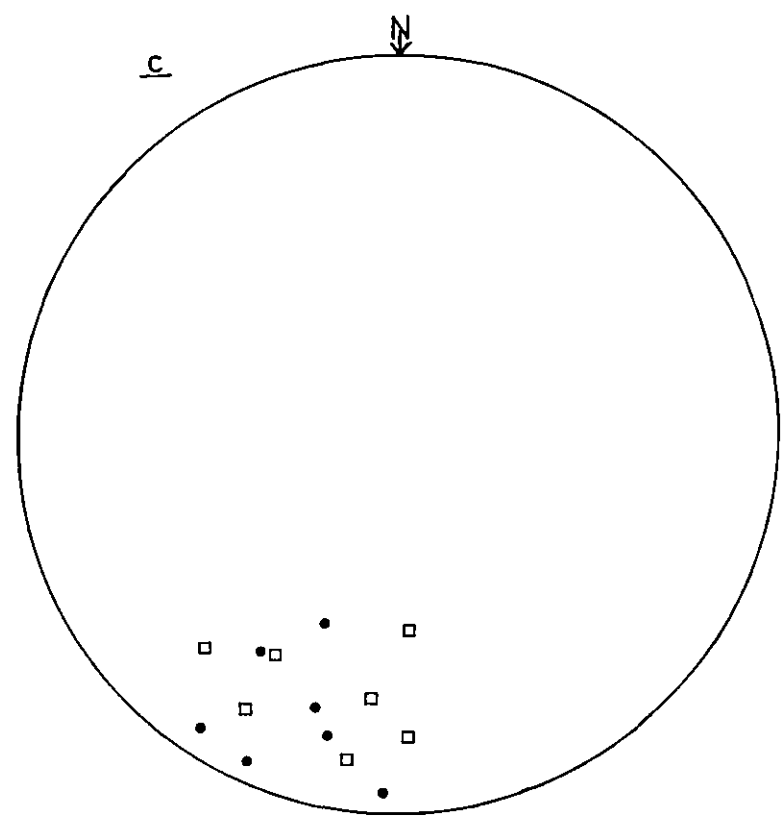
main zone

- ● high-strain mylonite
- □ low-strain mylonite
- O inherited sinistral

FIG. 3.6




d
N


c
N

sinistral data form a less well-defined pattern, with trends from ESE/WNW - ENE/WSW, the highest concentrations being towards the latter end of the range; dips vary from steeply to the north, through vertical, to steeply towards the south. Thrust zones trend ENE-WSW, and dip shallowly towards the north. The region, on the stereogram , in which the data overlap is approximately the same as shown in Fig. 3.6 (c) for π-poles to mylonite foliation from within the main shear zone. In areas where two sets are equally well-developed, the dihedral angle between the shear zone planes, facing the direction of maximum shortening, varies from 90^{o} - 160^{o}.

In Fig. 3.6. (b), lineations, as defined by quartz grain elongation within mylonite foliation are plotted for all the minor shear zones. Most dextral zones have a sub-horizontal lineation, but a significant number show moderate plunge towards the north-west. The sinistral data is more consistent, with lineations generally showing moderate plunge towards the west. All the thrust zones have lineations shallowly to moderately plunging towards the north.

The combined orientation and lineation data for the three sets may be summarized as:-

(i) dextral: NW-SE trending, steeply dipping to NE, dominantly dextral strike slip with varying amounts of reverse dip-slip.

(ii) sinistral: E-W trending, sub-vertical, equal sinistral strike-slip, vertical dip-slip (downthrow to the north).

(iii) thrust: E-W trending, shallowly dipping to the north, essentially reverse dip-slip.

3.3.1.1.2 Shear zone junctions and terminations

In this area there are junctions between shear zones of all types, but in no case is there any evidence that one zone is offset by another, as would be expected if the zones were of different ages. These junctions, as elsewhere in Cap de Creus, show smooth gradations from one zone to another. This is taken to imply that they all moved contemporaneously for the majority of their active lives, no matter which set developed first.

Another aspect of shear zones which can be well-observed in this area is their terminations. From observations here it has proved possible to identify a series of types of terminations, which are shown schematically in Fig. 3.7. Some zones simply end cleanly, with no splays, curvature or interaction with other zones, type 1. The second type is similar, except that the end may be curved, generally in a consistent sense, with respect to the sense of displacement, often with the development of secondary shear zones, or splays (by analogy with the terminology used for brittle faults, e.g. Chinnery, 1966).

In all other cases, shear zones are seen to terminate due to their interaction with other zones; in detail, however, terminations are either type 1 or 2. In a type 3 termination, the zone has apparently originated by branching from another zone, and this is termed a 'failed branch.' In a type 4, two shear zones of opposite sense propagate so as to encounter each other tip to tip, this is termed 'opposite sense cancellation.' Type 5 is similarly termed 'same-sense cancellation' which occurs when shear zones of the same sense, but of opposite propagation direction meet. Finally, a type 6 termination is due to the encounter between a propagating zone, and a well established and still active zone.

All of these types may be illustrated by reference to just two small

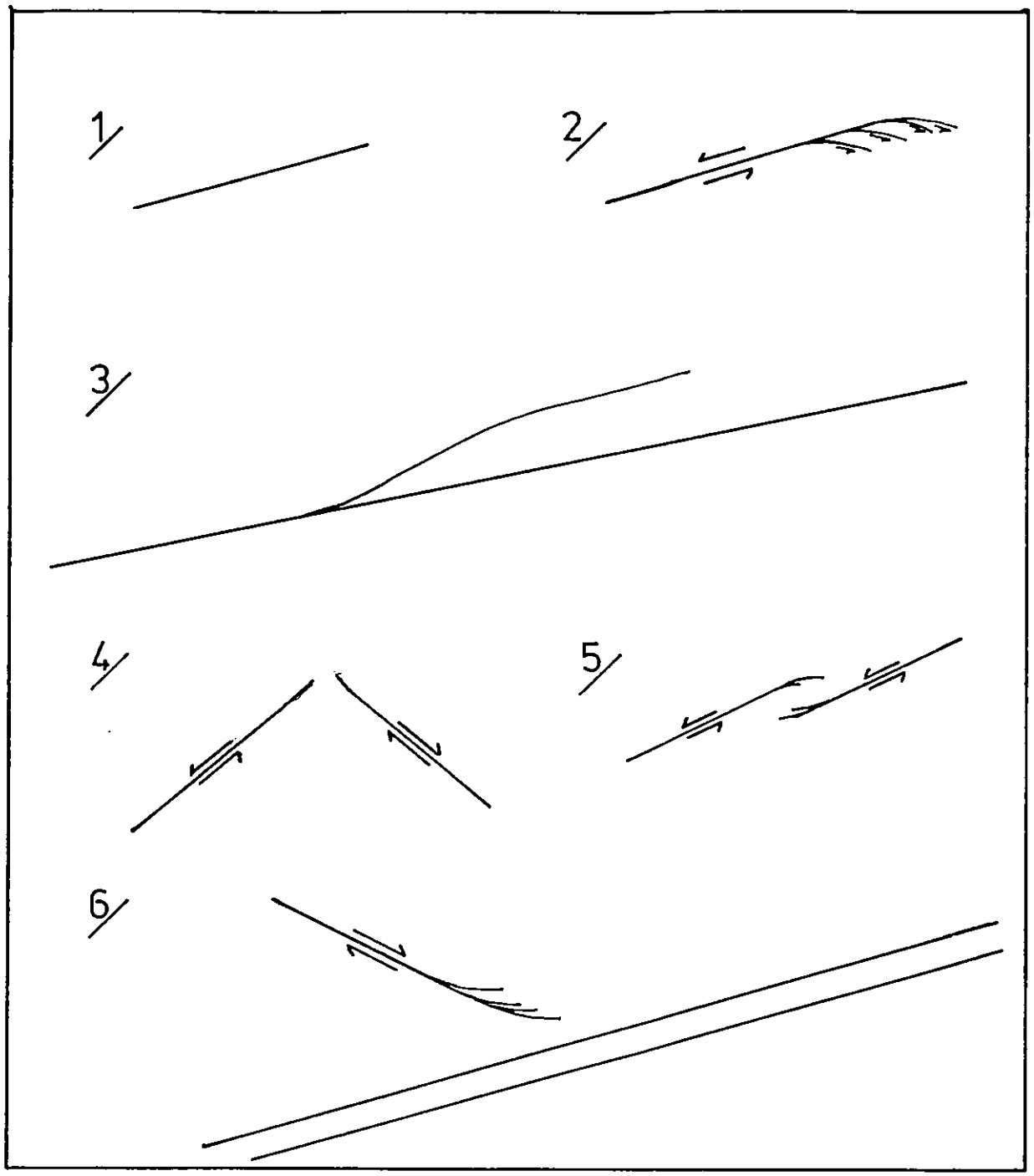


Fig. 3.7 Types of shear zone termination observed.

parts of the network, marked A and B on the enclosed map (1). In area A, a number of sinistral zones show type 4 terminations, the smaller dextral zones involved themselves terminating at their other ends by type 1 or 2 terminations. One of the sinistral zones is also involved in an interaction of type 5. On a still smaller scale, Fig. 3.8 shows a complex junction from within the area, and in this case the terminations involve the interaction between three or four zones.

In the area marked B, the network is dominated by a single dextral zone which terminates in a complex fashion by a type 6 interaction with the main shear zone. This zone splits up into a number of irregular splays of the same sense, the northernmost of which ends in a type 4 interaction.

3.3.1.1.3 Control by earlier structures

The only definite example in the area of control by an earlier structure upon shear localization is provided by the dextral shear zones developed along the microdiorite dyke on both of the dyke/wall-rock contacts (Plate 3.1(c)). The orientations of these shear zones fall within the dextral scatter shown in Fig. 3.6(a).

One other area in which control on localization is suspected, is in the area marked C on the map. Here a series of sinistral zones, all with orientations and lineations typical of that set, deviate strongly from their ENE/WSW trend to form a series of curved segments of zone trending approximately ESE/WNW, with very variable lineations, which line up over a distance of ca. 40 metres. This behaviour would suggest the existence of some sub-planar heterogeneity prior to shear zone development, however, no such structure has been identified.

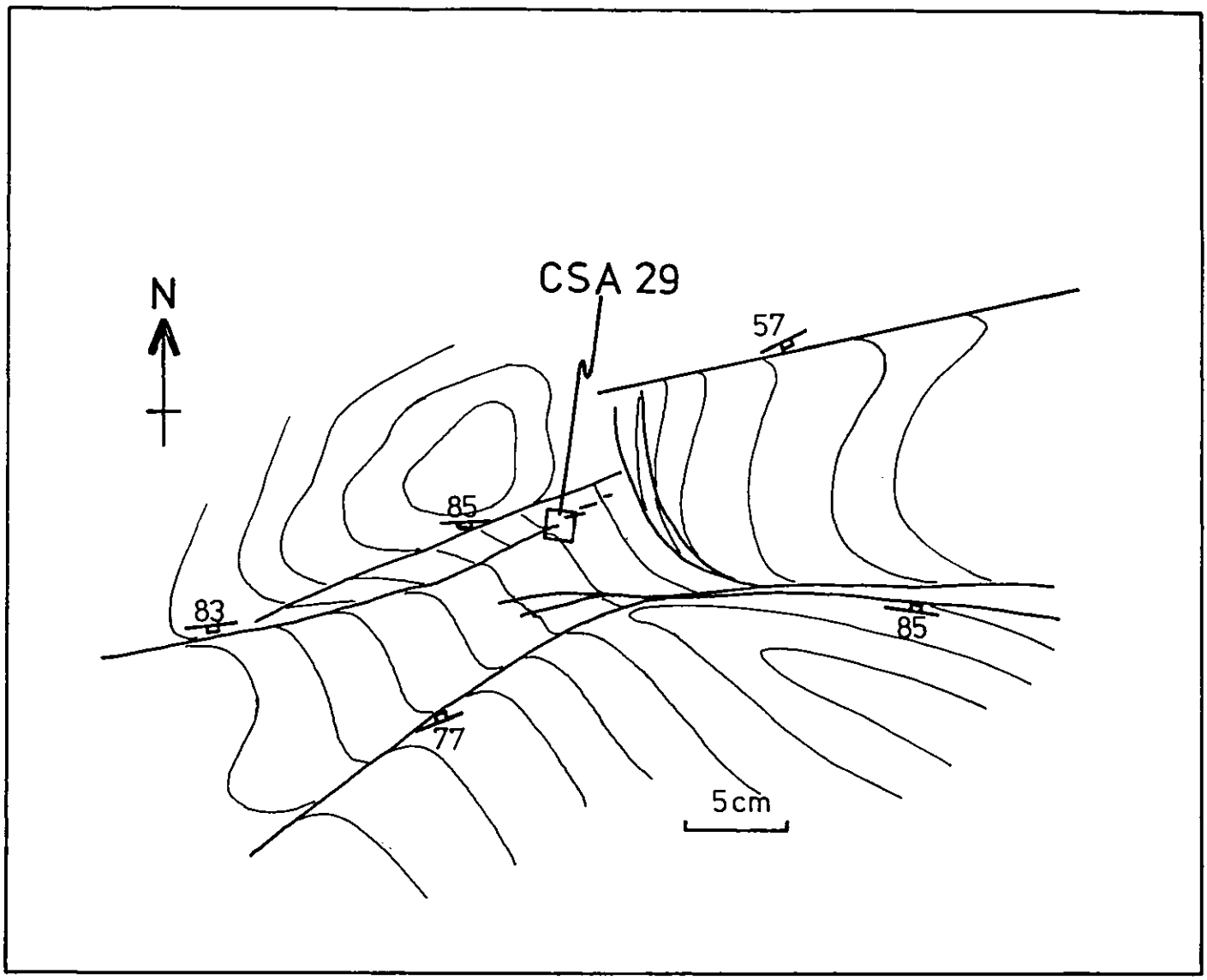


Fig. 3.8 Complex termination caused by the interaction of several shear zones. The sampling point of CSA 29 is indicated.

3.3.1.2 The main shear zone

From its orientation and size this dextral zone would automatically be included in the main set of dextral shear zones at Cap de Creus, except that, in contrast to their small reverse component, this zone has a very large component of normal sense movement. The dip of the shear zone plane varies from ca. 45^{o} to the north at the western end of the area, to ca. 80^{o} at the eastern end (see also Fig. 3.6(c)).

3.3.1.2.1 High strain/low strain mylonites

It can be seen from the map that at various points along the main shear zone, its boundaries 'bulge' into the surrounding schists. These areas in the mylonite are characterized by lineations plunging down foliation, suggesting a purely normal sense of movement, comparatively low shear strains, with the preservation of some original structures; these areas are often partly bounded by other shear zones. These low-strain mylonites appear to have suffered a rather different deformation history to the areas of high shear strain. This is also indicated by the quite different lineations developed in the two types of mylonite, as in Fig.3.6(d).

A particular area of interest (marked (D) on the map, see also Plate 3.1(d)) is the junction of one of the largest sinistral zones with the main zone. The mylonite here resolves itself into three separate high-strain zones; the two to the south both being zones characterized by normal sense dip-slip movement with a large component of dextral strike-slip separated by a low strain mylonite of similar character. The other zone is a continuation of the sinistral zone, but now brought into parallelism with the main zone, and which may be traced for a distance of ca. 30 metres. The sinistral nature of this mylonite is not in doubt; it carries both a lineation plunging ca. 30^{o} towards the north-west and shear bands (see

section 3.23) of consistent sinistral sense. The area of low-strain mylonite between sinistral and dextral mylonite is characterized by a lineation varying smoothly from that characteristic of the dextral mylonite round to that characteristic of the sinistral mylonite. This is considered to represent the country rock schists between the sinistral shear zone, and dextral main zone that have been progressively included in the main zone, as the sinistral zone has been brought into parallelism.

3.3.3 Sampling in the Cala Sardina area

The majority of the sampling carried out in this area has been of quartz veins, lenses etc. for use in Palaeostress work (see Chapter 4) (the location of all samples is shown in Map 1). Apart from minor shear zones (CSA04, CSA10) the main effort was directed at differences between high strain, and low strain mylonites. This was done in area (D), CSA15, 16 from either side of a low strain mylonite/country-rock boundary, CSA17, 18 from adjacent low and high strain mylonites. In the area marked (E), the series CSA 20-25, 28 was taken from the sinistral zone to the north, across the low strain mylonite to the main dextral zone, also CSA26, 27 were taken from either side of a low strain mylonite/country-rock boundary. CSA19 was obtained from the 'bulge' of low strain mylonite at the western-most end of the main shear zone.

Attempts were made to obtain samples of the microdiorite being progressively deformed into several of the sinistral minor shear zones, but the material samples has always proved to be too weathered to be of use. Another aim of sampling was to obtain samples containing shear zone terminations of such a scale that they could be studied on one thin section. A number of samples were taken for this purpose, but only one, CSA29 (for locality see Fig. 3.8) was successfully prepared.

3.314 Discussion

For any network of shear zones operating simultaneously in response to the same constraints, for plane strain, it would be expected that all displacement vectors (which in this case it is assumed are represented by mineral elongation lineations) would lie approximately within a plane i.e. as a great circle on the stereonet. Taking Figs.3.6 (a), 3.6(c) together it is clear that this does not apply. Therefore, in this area, it is possible that constraints varied across the area, and that overall deformation departed significantly from plane strain.

Evidence for this interpretation is that only rarely are more than two sets developed in any one area, and only two of the possible pairings occur, i.e. sinistral + dextral, or thrust + dextral; also shear zone orientations are generally consistent within such areas.

3.32 The Portixol (Cala Serena) network

In the light of preliminary results gained from the Cala Sardina network, described in the previous section, it was decided to map another area, in detail, for comparison. The area at Portixol (Cala Serena) (shown in Fig. 3.5) was selected because the exposure was generally very good, and, in contrast to the Cala Sardina area, both a strong and consistent foliation in the country-rock schists and considerable lithological variation are present. (This area was also the site from which many of the samples in this study were obtained).

Lithological contrast is provided by; thin, (ca. 0.5m) but laterally continuous garnetiferous schist bands, discordant pegmatites and micro-granites, and quartz-diorite with associated migmatized schists. The map (see Map 2(a)) was prepared without a base, using pacing and triangulation, the area of quartz diorite with migmatistic schist was not mapped in detail.

Fig. 3.9 Lower hemisphere, equal area, stereoplots from the Portixol (Cala Serena) area.

(a) π-poles to planes of minor shear zones and lines of intersection of conjugate pairs

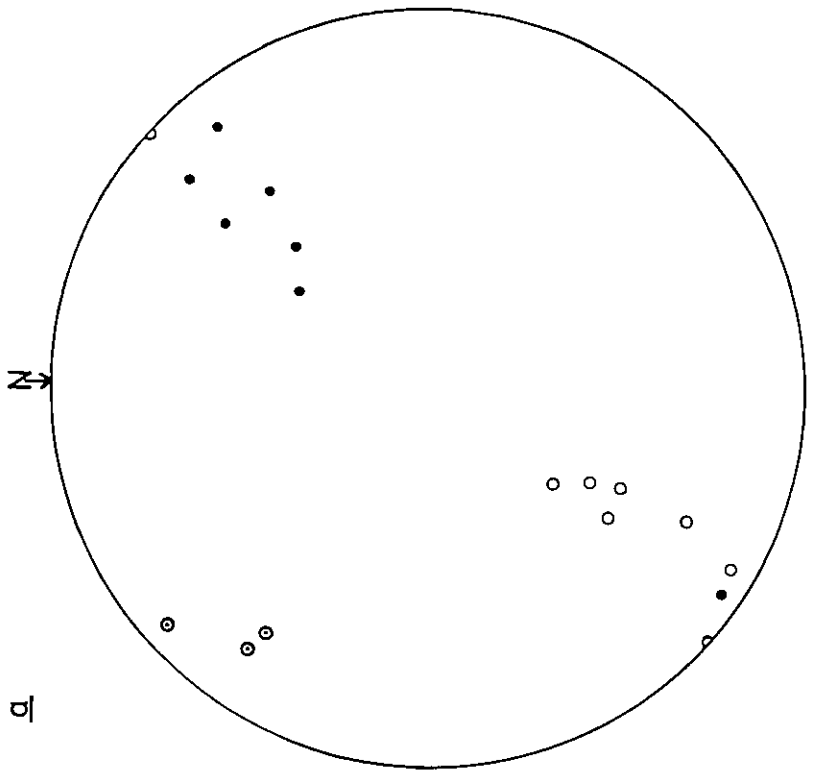
(b) Quartz grain elongation lineations in minor shear zones

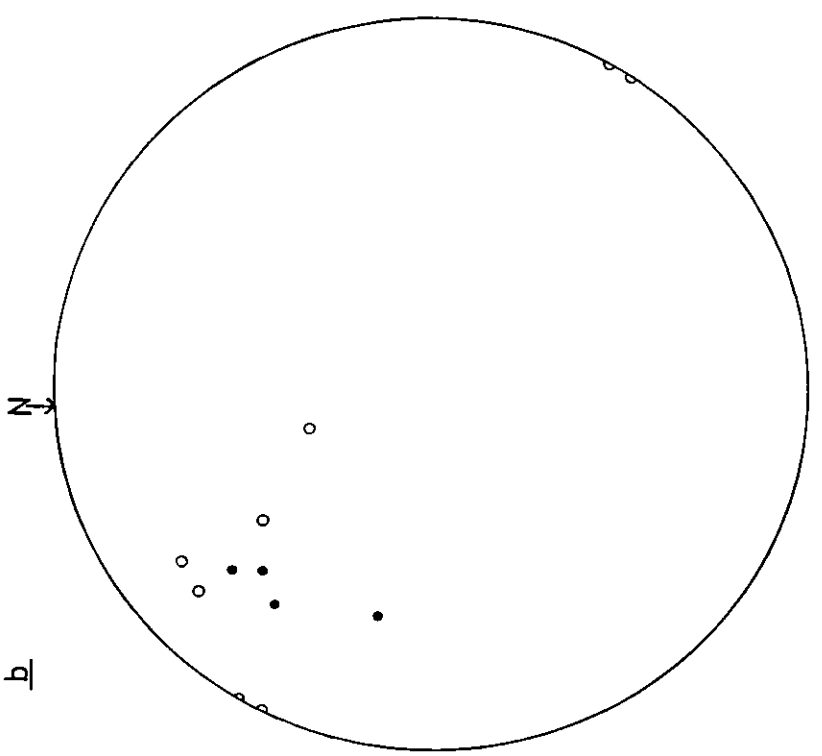
(c) π-poles to mylonite foliation in the main dextral zone, Portixol, including data from the area where its outcrop runs parallel to the main sinistral zone. (indicated by dashed line)

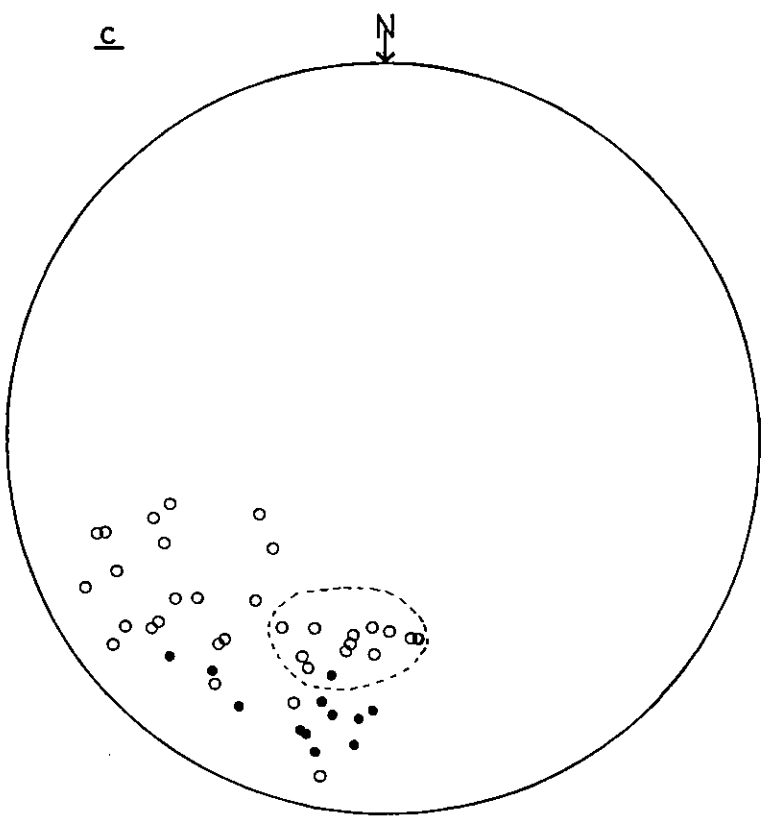
KEY

- O dextral
- ● sinistral
- ⊙ intersection line of conjugate pairs of shear zones

FIG. 3.9






c
N

3.321 Minor shear zones

In the south western part of the area, between the coast and the main dextral zone, there are country rock schists in which minor shear zones are developed, similar to those already described from Cala Sardina (section 3.311.). All these zones trend NW-SE, but the dextral zones dip towards the NE, while the sinistral zones dip towards the SW (Fig. 3.9(a)); the lineations for both sets plunge moderately to shallowly towards the NW (Fig. 3.9(b)).

In this small area, therefore, the minor shear zones have consistent orientations, and movement directions. However, lines of intersection for pairs of zones of opposite sense have approximately the same plunge as the movement direction. From the classic explanation of conjugate shear sets, it would be expected that these two directions would be perpendicular.

Within the quartz diorite areas a large number of minor shear zones are developed; they are commonly in the form of either ultramylonite in the quartz diorite itself (Plate 3.1(e)), or as quartz mylonites along originally planar quartz veins within the quartz diorite (Plate 3.1(f)).

3.322. Major shear zones

There are three major shear zones in the area mapped; one sinistral zone trending E-W, forming the northern boundary of the migmatite/quartz diorite block, and two dextral zones; one trending NW-SE forming the south-western boundary of the migmatite, the other trending WNW-ESE and meeting with the former at the southern end of the area mapped.

The sinistral zone (actually sinistral strike slip with a component of normal dip-slip) shows several unusual features which are summarized in Fig. 3.10. The shear zone is not symmetrical about its centre, and in

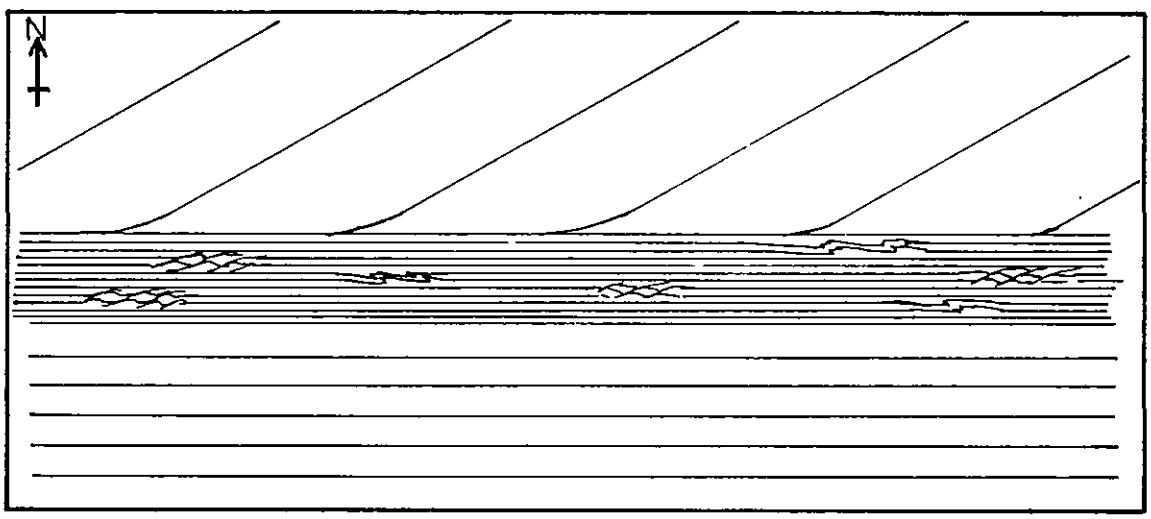


Fig. 3.10 Schematic diagram of main sinistral shear zone at Portixol (Cala Serena), showing the assymetry of foliation, and the minor structures indicating sinistral sense movement in apparent contradiction to the sense of rotation of foliation on the north side.

fact the sense of rotation of country-rock foliation on the northern boundary would indicate a dextral sense for this zone. However, the sinistral nature is deduced from very consistent minor fold asymmetry, and the sense of shear bands within the mylonite (see section 3.23).

Both dextral zones (dominantly dextral strike slip with a small component of reverse dip-slip) are composite, that is they are made up of a series of sub-parallel mylonite bands, with septa of more or less deformed country rock between (see Map 2(b)). Locally these septa are deformed sufficiently to become low strain mylonites, they may also be cut by higher strain zones to give the characteristic 'augen' structure.

In the north-western corner of the area both dextral and sinistral zones change in trend, although the parallel outcrop patterns shown on the map are partly due to the effect of topography. In fig. 3.9(c) a composite plot of all mylonite foliation from the major shear zone, the change in orientation of the dextral zone is clearly visible. The two zones are only separated by a septum of partly deformed quartz diorite, migmatite, and pegmatite that may be traced a further 150 metres to the coast, with mylonites of opposite sense still clearly developed on either side; Plate 3.2(a) shows a view looking north-west from the point at which the two zones come into near contact.

The dihedral angle between the two zones is in the range 150^{o} - 130^{o}, which reduces to 160^{o} - 150^{o} in the area mentioned above (Fig. 3.9(c)). This difference in orientation is much smaller than either that generally observed, or predicted by theory (Ramsay, 1980). Also, although the minor dextral zones have orientation in close agreement with those of the major zones, the minor sinistral zones have orientations apparently unrelated to that of the minor dextral zones (Figs. 3.9 (a)(c)).

Plate 3.2 Field photographs of the Cap de Creus shear zones (contd.).

(a) View of part of the main Portixol shear zone showing the area in which the dextral zone converges with the sinistral zone. The sinistral zone runs roughly along the path on the right and is relatively steeply dipping, while the dextral zone is more shallowly dipping and forms the extreme bottom left of the picture; the ground in between is strongly deformed quartz-diorite.

(b) Shear zone localized within the limb of a minor fold in a less-deformed septum of country-rock schist in the main dextral zone at Portixol.

(c) Microgranite deformed by minor dextral sense shear zone that provided the sample series CSE 01-04.

(d) General view of the complex shear zone at Punta del Moli, see Fig. 3.15.

(e) Termination of minor dextral sense shear zone at Cala Prona; a tracing of this forms Fig. 3.18.

PLATE 3.2

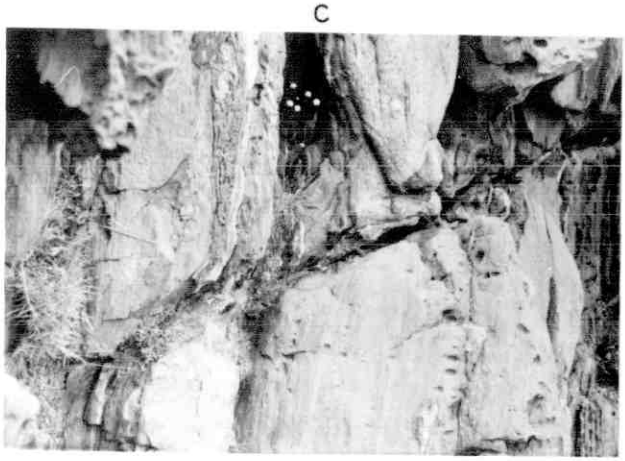
a



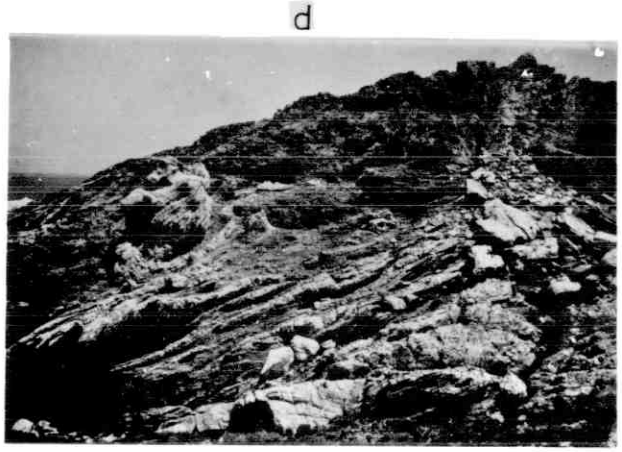
b



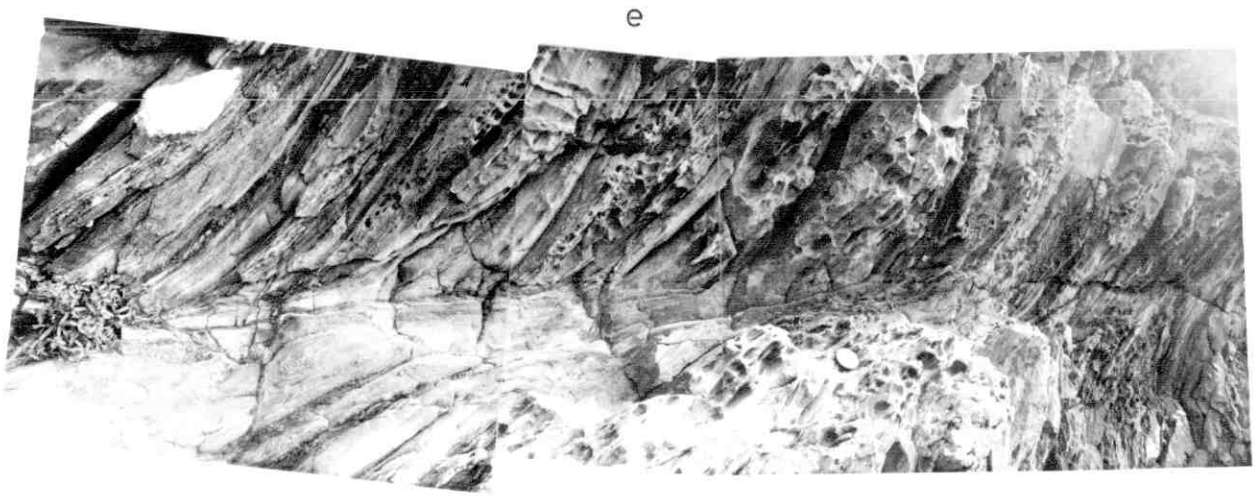
c



d



e



3.323 The effect of earlier structures

In the Portixol region there is good evidence that shear localization has been to some extent, controlled by either pre-existing structures, or by lithological changes, each of which will be dealt with below.

The composite nature of the dextral zones is characteristic of those zones developed within areas of country rock schist with a strong and relatively consistent foliation. Structures of the type shown schematically in Fig. 3.11(a) are common on the boundaries of the dextral zones where the country rock is schist rather than migmatite. A schematic shear strain profile of such a boundary is shown in Fig. 3.11(b); obtained from the qualitative assessment of schistosity orientation; the increase in strain, within the low strain septa, away from the boundary is thought to be original. The earlier structure represented by this would be similar to a kink-band, within which the shear zones later localized (Fig.3.11(c)).

Moving to a somewhat smaller scale, clear evidence for localization controlled by a pre-existing fold was found within a less deformed septum on the lower part of the dextral shear zone, just south of the area mapped, where the two zones become one. Fig.3.12 taken from a field sketch, shows a shear zone found within a fold limb (Plate 3.2(b)), but which then cuts across the same fold's axial plane. This zone is thought to have formed by the localization of shear in the thinned limb of the minor fold, followed by propagation away, and a change in direction to that of sub-parallel to main zone as the fold amplitude decreased (see Fig. 3.13).

An excellent small scale example of lithological control has already been mentioned (see section 3.321) in which deformation within the quartz-diorite body has been taken up, whenever possible, by the quartz veins within it. In some cases the quartz vein may become a thoroughgoing quartz-mylonite, while no deformation is visible within the adjacent quartz-

Fig. 3.11 Shear zone boundary structure at Portixol, with possible mode of formation.

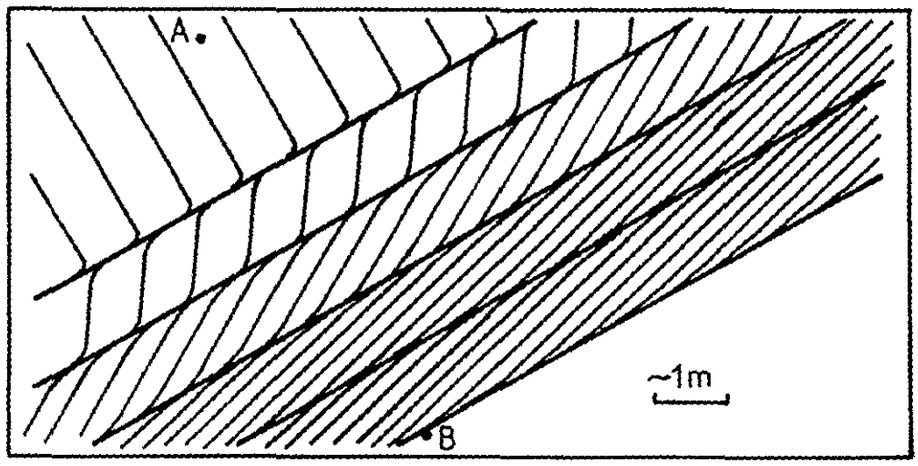
(a) Schematic diagram of shear zone boundary

(b) Strain profile across the boundary shown in (a)

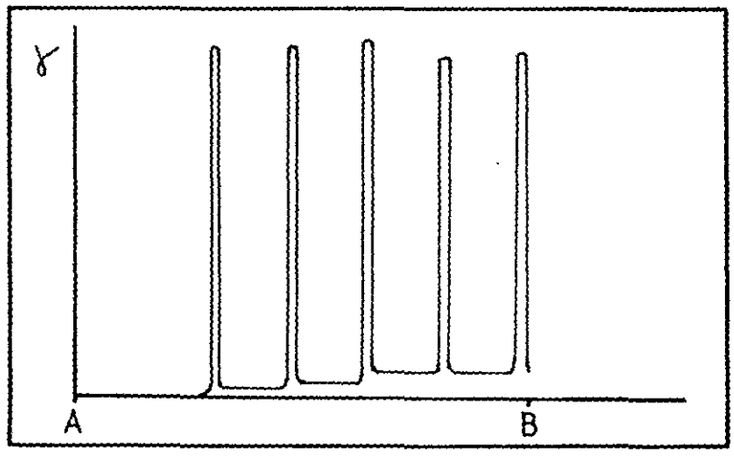
(c) Formation of boundary by shear localization in existing kink-like structure

FIG. 3-11

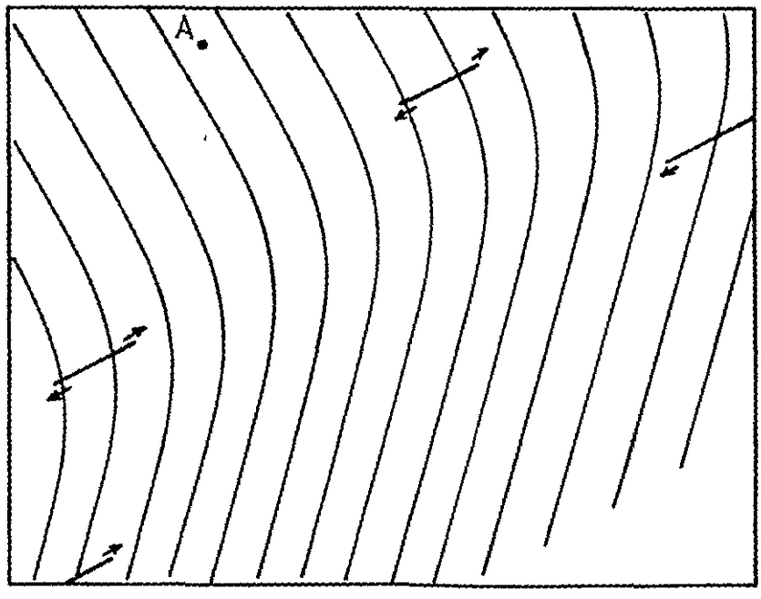
a



b



c



diorite (e.g. as in Plate 3.1(f)).

On a much larger scale the contrast in 'competence' between the migmatite, pegmatite and quartz diorite, on one hand, and the schists on the other, has had a considerable influence on the development of shear zones in this area. The migmatite complex was more 'competent' probably due both to a larger initial grain size, and a relatively high feldspar content, and would therefore act as a less-deformable block within the schists. It is not surprising, therefore, to find the block bounded on it northern, north-eastern and south-western sides by shear zones.

In Fig. 3.14 a tentative model is proposed to explain the development of the present configuration, especially with regard to the sinistral zone. The rotation of the migmatite is explained in terms of the response of this more competent block to a flattening component between the shear zones.

3.324 Brittle structures

Brief mention will now be made of the brittle structures found in this area during the mapping, including kink-bands, fault gouges, cataclasites and pseudotachylytes; their distribution as shown in Map 2(c)). The cataclasites are unusual, being very thin (ca.2mm) and parallel to mylonite foliation. This also describes the development of the pseudotachylyte faults, which are almost all generation surfaces (in the terminology of Sibson, 1977). In the sinistral zone, at least three separate and parallel pseudotechylyte faults may be distinguished. In a few places offsets were observed on these faults at points where they cut across mylonite foliation, all the offsets showed a sinistral component of ca. 15cm.

3.325 Sampling carried out

Map 2(c) also shows the places from which samples were obtained. Sets

Fig. 3.12 Shear zone within minor fold Portixol (Cala Serena) (from field sketch).

Fig. 3.13 Various stages in the formation of the structure shown in Fig. 3.12 and Plate 3.2(b).

(i) Fold nucleates at heterogeneity

(ii) Fold propagates

(iii) Shear localizes in thinned limb of minor fold

(iv) Shear zone propagates out of fold, deforming fold axial plane

FIG. 3·12

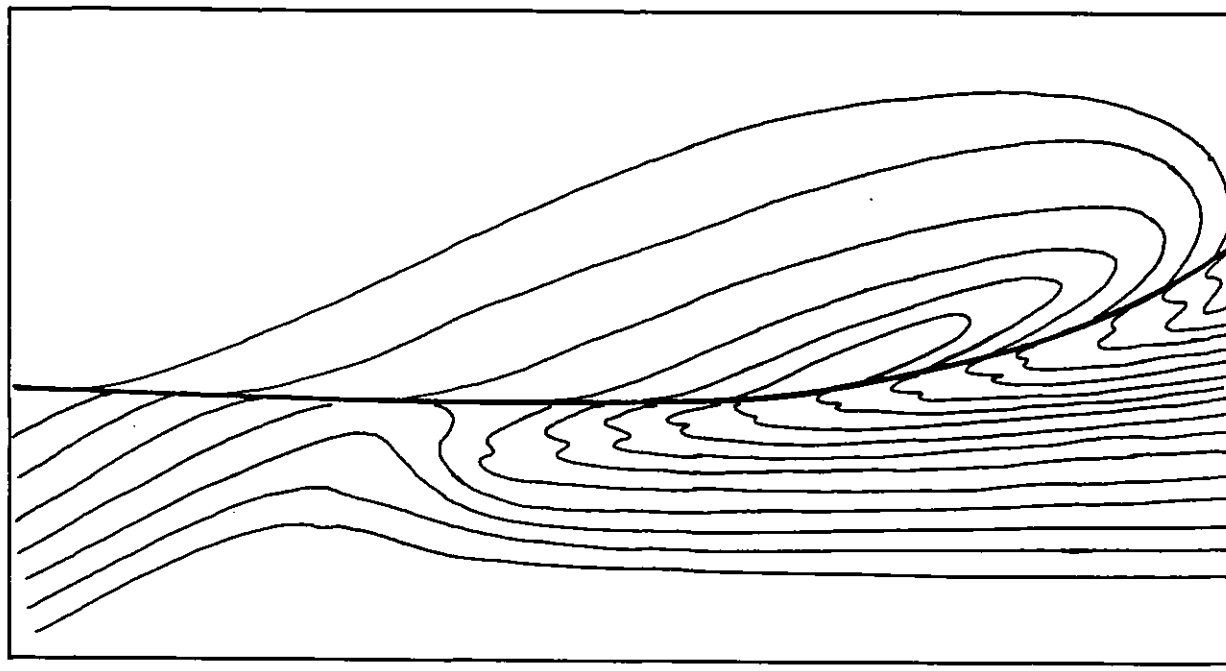
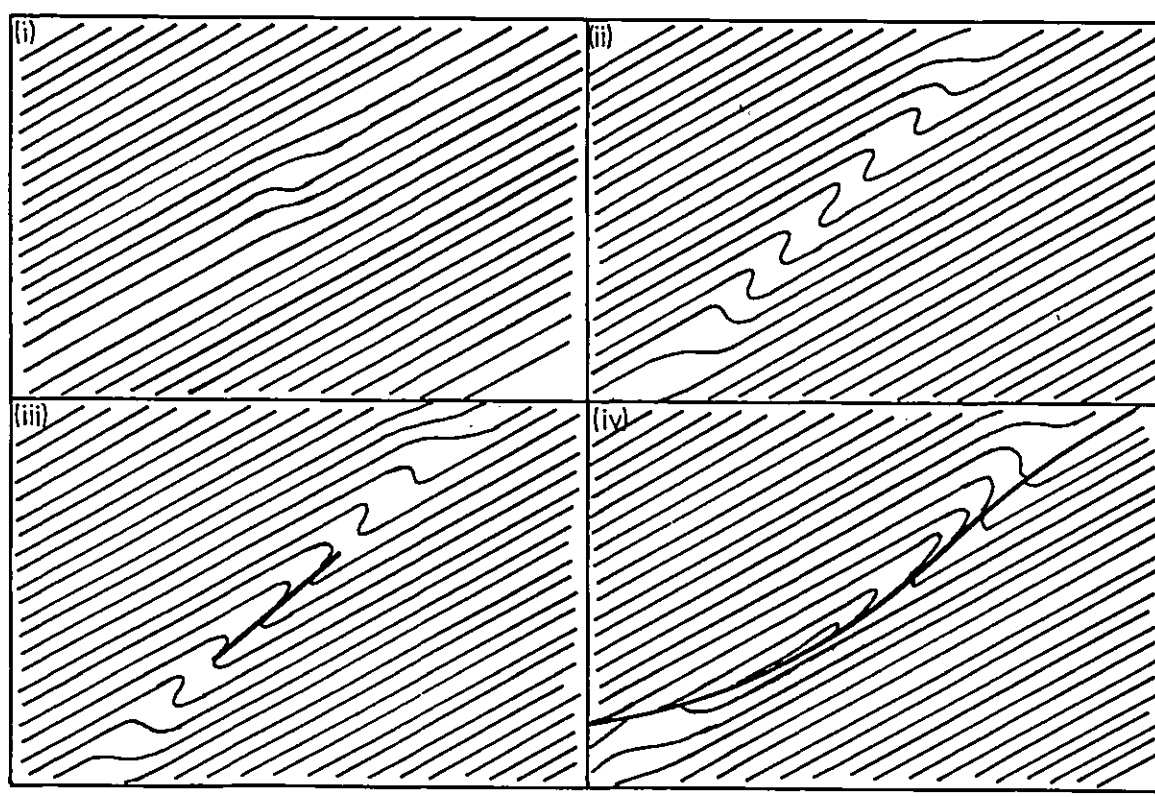


FIG. 3·13



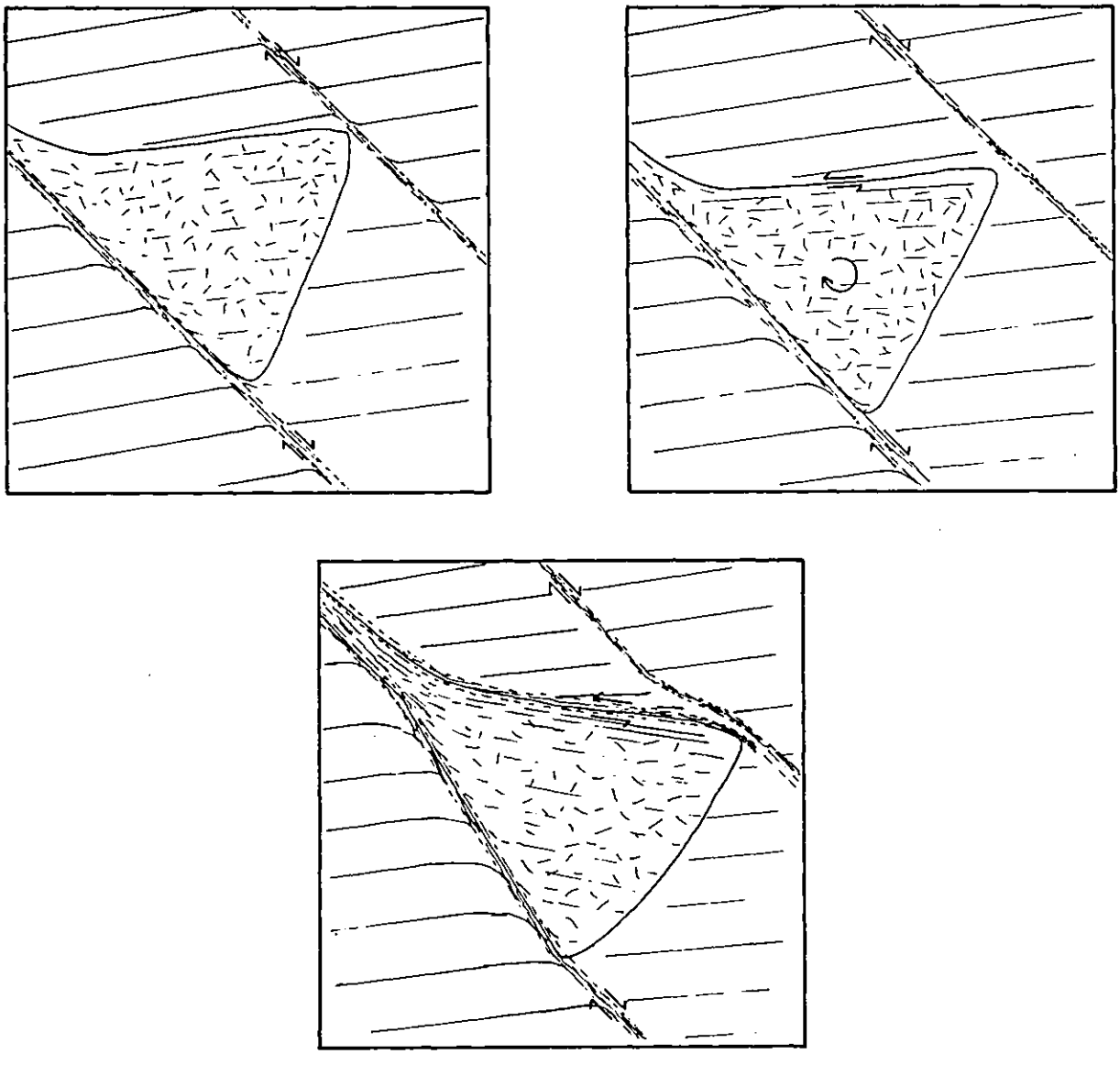


Fig. 3.14 Model for the formation of the main sinistral zone Portixol (Cala Serena). The less-deformable block of migmatite (with ornament) rotates due to the component of flattening between the two main dextral sense shear zones.

of samples of progressively deformed pegmatites, microgranites, quartz-diorites, psammites and pelitic schists were all taken; in addition quartz samples were taken adjacent to them. Apart from those shown on the map, one other set of samples was taken from this area, from a minor dextral zone, slightly above, and parallel to, the main dextral zone, just south-east of the area mapped. In this example, a pegmatite could be traced completely from one side of the shear zone to the other (Plate 3.2c); from the reduction in thickness of the pegmatite, a shear strain of $\gamma \sim 55$ was deduced for this zone.

3.3.2.6 Discussion

From the previous sections it is quite clear that, in complete contrast to the Cala Sardina area, shear localization in the Portixol area has been almost entirely controlled by pre-existing structures and lithological variation. It may, therefore, be deduced that the existence of earlier structures while strongly controlling shear zone development if present, are not essential for shear zone formation. Fig. 3.14 shows a suggested sequence of events in the Portixol area during the period from the peak of metamorphism.

3.3.3 Other areas studied

In addition to the areas mapped in detail, a number of small areas were studied briefly, with a specific end in view, such as defining the local context of a suite of samples.

3.3.3.1 Punta del Molí

In this area (see Fig. 3.15) two adjacent bands of, one quartz diorite, the other a microgranite could be traced through a very well exposed shear zone, from one side to the other (Plate 3.2d). The area as a whole marks the 'confluence' of a series of shear zones which are affected by a group

FIG. 3.15

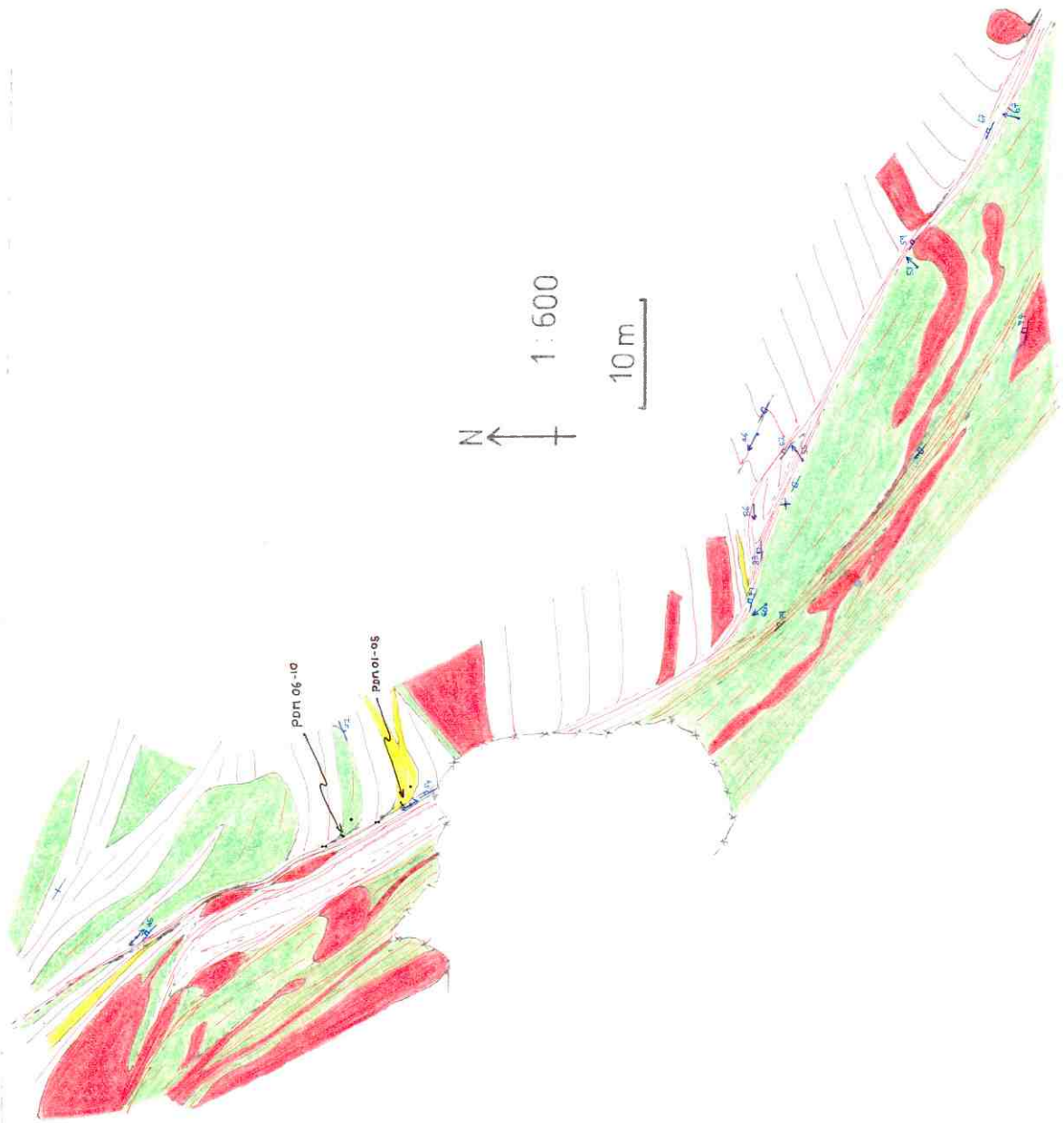


Fig. 3.15 Sketch map of part of the complex zone at Punta del Moli showing sampling points. (Key as for Maps 1 and 2)

of resistant quartz diorite and pegmatite blocks. The zone from which the samples came marks the uppermost boundary of this composite zone; no shear zones at all are found in the area to the north of this. This shear zone is also thought to mark the western continuation of the main zone at Cala Sardina.

Fig. 3.15 shows the sketch map of the zone and adjacent areas, with sampling points marked. The shear strain at the point of sampling was measured by two different methods, $\gamma_1 = d/w$ where d is displacement, and w is width and by $\gamma_2 = to/t$ where to is the original separation of two markers and t is the separation within the shear zone. The values obtained were $\gamma_1 = 13.3$ and $\gamma_2 = 11.5$; fairly consistent and implying a shear zone of unusually low strain for Cap de Creus (c.f. values in section 3.34). The distance t was found to be essentially constant from one edge of the zone to the other, suggesting that the shear strain profile would be 'flat-topped.'

3.332 Constriction zone

The main shear zone at Cala Sardina continues ESE, reaching the coast at Cala sa Caixa. Just before it reaches this point the zone passes between two large pegmatite bodies (for location see Fig. 3.5), and the width of the zone drops from $w \sim 8m$ to $w \sim 1m$ (Fig. 3.16). In the centre of this constriction, it is possible to find a traverse across the zone, along which no schist-derived mylonite is visible, implying that the pegmatite was once continuous across the zone.

The orientation of the mylonite foliation is similar to that found at Cala Sardina but the plunge of the lineations towards the NE becomes gradually shallower as the zone is followed to the east (M. Drury, Pers. Comm.), becoming locally sub-horizontal. At the constriction however, the lineation steepens, then becomes horizontal in the centre and finally on the eastern side plunges moderately towards the NW.

FIG. 3·16

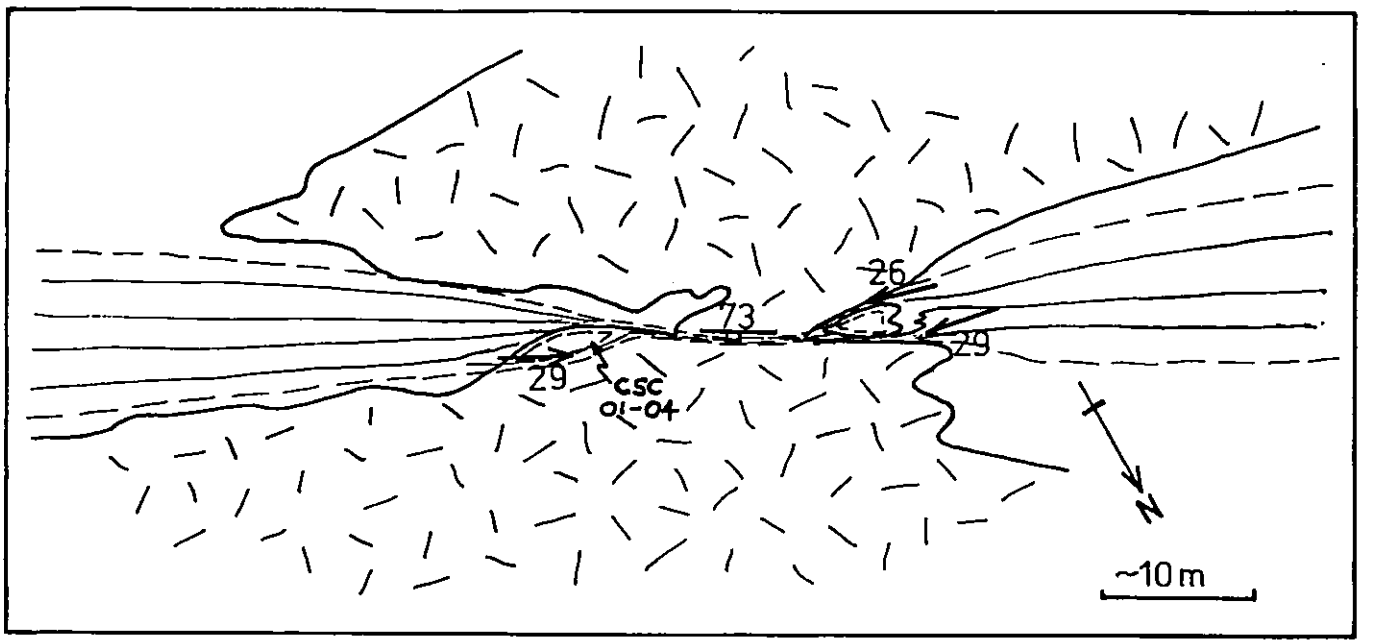


Fig. 3.16 Sketch map of constriction in major dextral sense shear zone, near, Cala sa Caixa, showing sampling points.

FIG. 3·17

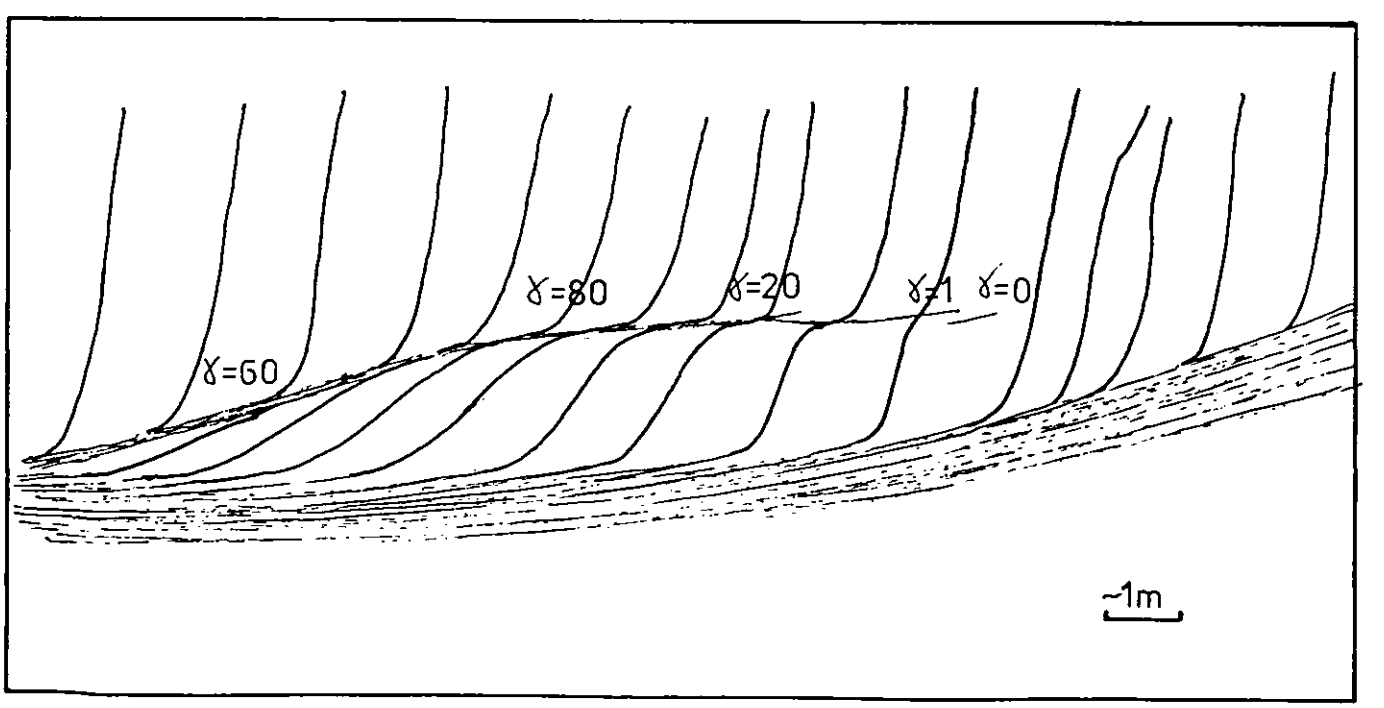


Fig. 3.17 Sketch showing relationship of minor dextral shear zone to major shear zone (Cala Prona) with approximate values of shear strain marked.

A series of samples of deformed pegmatites were obtained from just east of the constriction zone, the sampling points are shown in Fig. 3.16.

3.333 Shear zone termination, Cala Prona

At Cala Prona (see Fig. 3.6 for location) a shear zone termination of type 3 (failed branch) is very well exposed. Fig. 3.17 shows the relationship between this zone, and the other dextral zone from which it has branched, and also shows the variation in shear strain. Plate 3.2(e) shows the detail of the termination itself, and Fig. 3.18 shows the interpretation of this. The displacement dies out, with a simultaneous increase in the width of the zone affected by shear, and this causes the shear strain to fall off quite dramatically.

In detail it can be seen that the shear zone termination may be resolved into a number of small shear zones, which help to take up the deformation.

3.34 General Observations

Whereever possible the overall shear strain was measured for all the shear zones studied by one of the methods already mentioned (Section 3.331). Fig. 3.19(a) shows a plot of width (w) against displacement (d), which was plotted to check for any variation of shear strain with width. The data is very scattered, especially for the smaller zones which, combined with the paucity of data from larger zones, does not allow any definite conclusions to be drawn. In fig. 3.19(b) a frequency distribution is presented of shear strains for all zones. The data show a unimodal distribution, skewed towards the larger shear strains and a mean strain of $\bar{\gamma} = 54$, has been obtained. No significant variation has been found for shear zones of different sets.

Some workers have attempted to distinguish between continuous and

discontinuous shear zones (Burg and Laurent, 1978). All the observations made in this area, during the present study, suggest that no matter how sharp the boundary is, there is no discontinuity. The sharpness of these boundaries increase with increasing shear strain, but even for zones of equal shearstrain there may still be a large variation in strain gradient.

FIG. 3·18

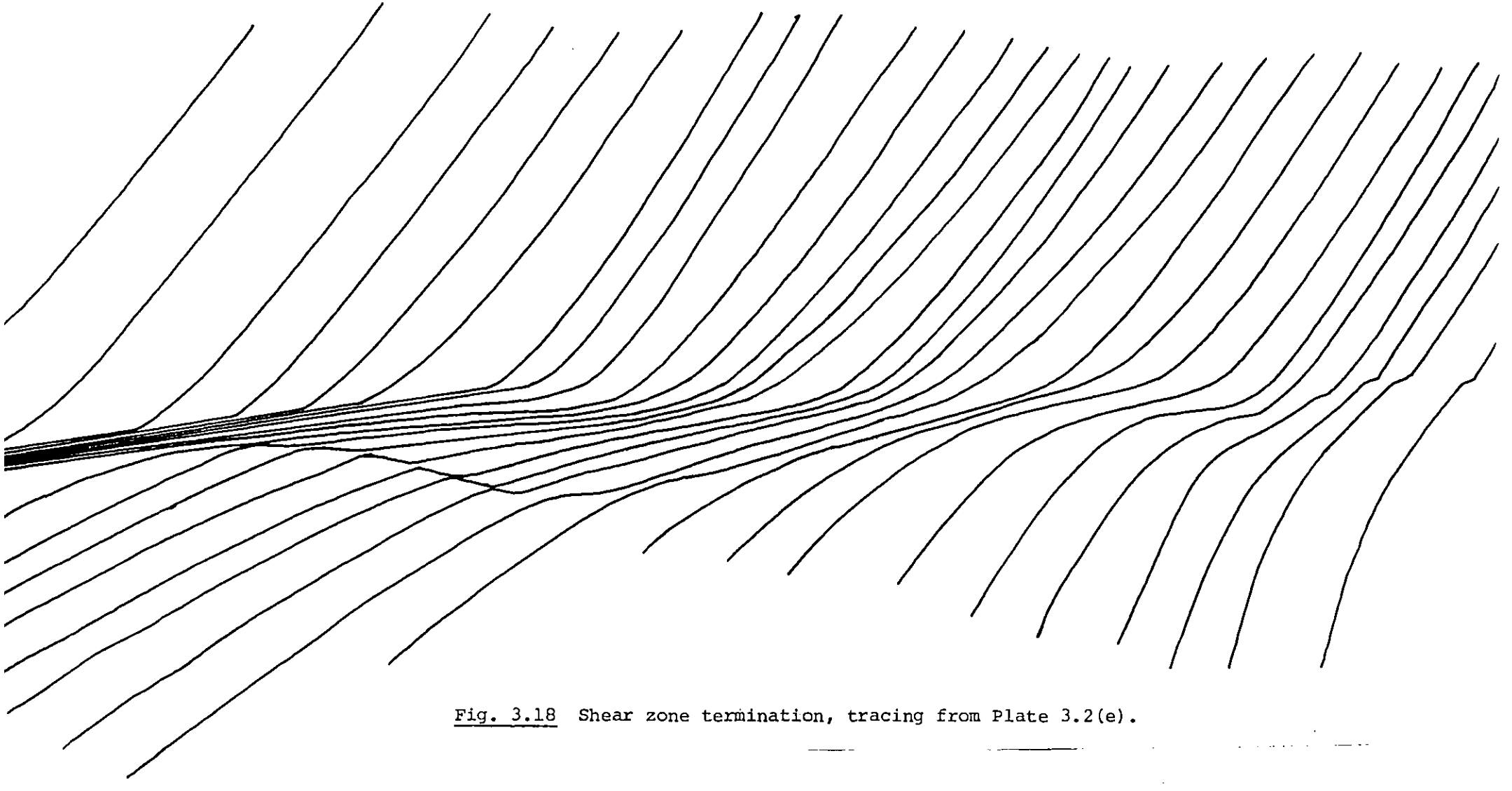
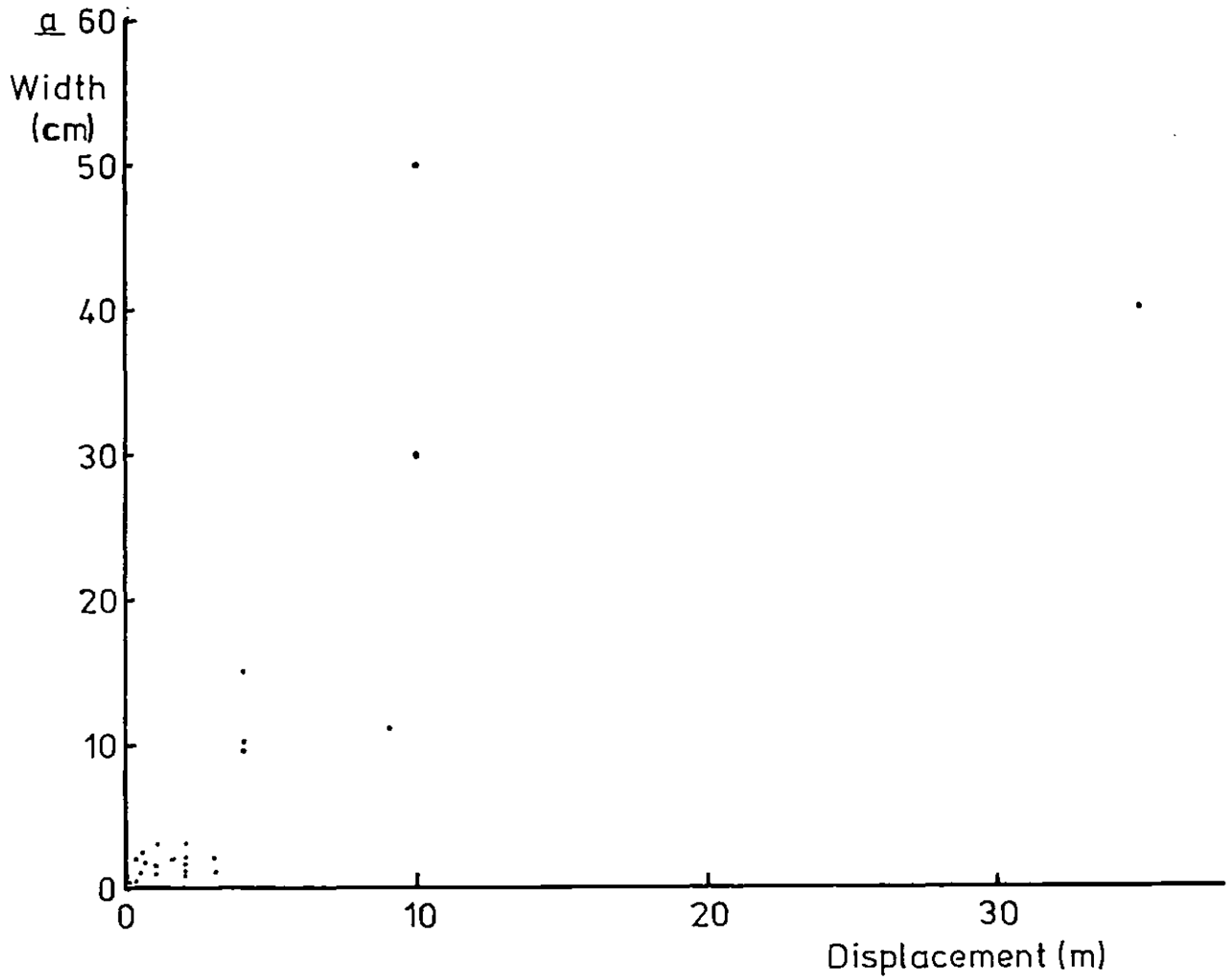


Fig. 3.18 Shear zone termination, tracing from Plate 3.2(e).

FIG. 3.19



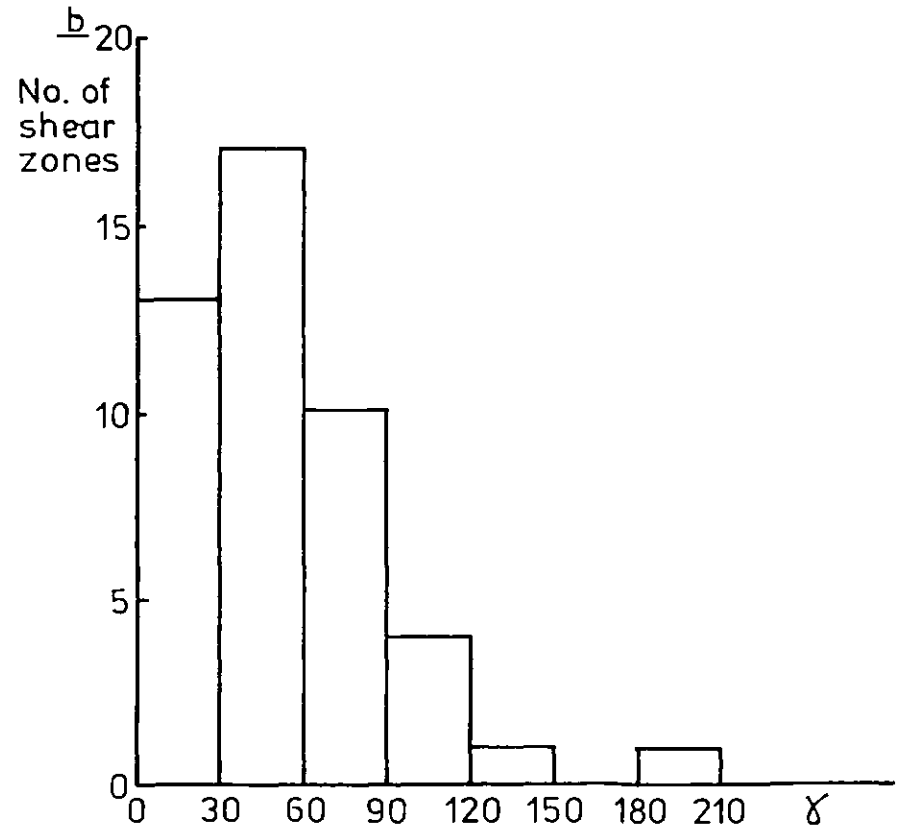


Fig. 3.19 (a) Plot of width v. displacement for all minor shear zones.

CHAPTER 4 - Microstructural Studies

In this chapter, the microstructures revealed by both optical and electron microscopy are described for the various minerals that constitute the rocks studied. Each mineral is dealt with individually with, a review of previous work, observations from the present study, and finally a discussion with comments on the relevance of these to mylonite formation, and palaeostress estimation.

4.1 Quartz

Quartz is a significant constituent of most of the rocks studied, and in all the cases it appears to have, at least in part, influenced their deformation. A large number of nearly pure quartz samples were studied by the etching of polished sections, however, these observations and results are not discussed here, and will be described in Chapter Five with reference to palaeostress measurements. The quartz described in this chapter was taken from both quartz vein, and polyphase aggregates.

4.1.1 Literature Review

The literature on the deformation of quartz extends back to the earliest studies involving the use of a petrological microscope.(e.g. Rosenbüch – Iddings,1888; Teall, 1888). Perhaps the greatest amount of work in the first half of this century was directed towards the measurement of crystallographic preferred orientations, and attempts to relate these to the deformation itself, e.g. the tectonic axes of Sander, 1930. In the past twenty years geologists have increasingly adopted the approach of physical metallurgy, a process that has in part been due to the development of electron microscopy, and its use in mineralogy. The methods employed by a modern structural petrologist have much in common with those used by a material scientist.

4.1.1.1 Strain Features

Harker in his "Petrology for Students" (1895) in the section on "Dynamic Metamorphism" mentions undulatory extinction or strain shadows, where the extinction position varies throughout the grain, and healed fractures, which he describes as rows of fluid pores, passing across grain boundaries formed parallel to actual planes of faulting. In 1930, Sander, in a review of previous work, also included 'deformation lamellae', closely-spaced planar features and 'ruptured quartz', described as consisting of discrete fragments with a slight misorientation relative to one another.

By 1947, Riley had noted the similarity between the common elongate 'fragments' within a grain of 'ruptured quartz', and 'deformation bands' due to ductile deformation in metals; in 1960, Voll used another metallurgical term 'sub-grain' for the sub-equant type of structure.

Spry (1969) distinguished two types of 'deformation lamellae'; the 'normal lamellae', thin, planar to curviplanar features similar to those of Sander (1930) and "Boehm lamellae", planar arrays of minute cavities or inclusions, sometimes appearing brown or red as described by Harker (1895). Shelton and Orville (1980) have shown experimentally that inclusion arrays may be produced by heating fractured quartz in the presence of water.

The crystal structures responsible for the observed deformation features were a matter of speculation until electron microscope studies allowed these to be viewed directly. Undulatory extinction has been shown (White, 1973) to result from the lattice distortion caused either by the progressive misorientation due to regular arrays of sub-parallel low angle sub-grain walls or to the strain induced by forests of dislocations in those grains that have undergone little or no recovery. Optically visible sub-grains may be related to those seen in electron micrographs that are bounded by walls with misorientations across them $\sim 4^{o}$ (White, op.cit.); further

sub-grains, with low angle $\leq 1^{o}$ walls are commonly found within them, a fact which has important implications for the use of sub-grain size in palaeostress estimation (see Chapter 5).

Deformation lamellae (the 'normal lamellae' of Spry, 1979) have been shown to be due to a whole variety of sub-microscopic structures, the type depending on temperature, strain-rate, water content etc. McLaren et al. (1967) found thin Brazil twin bands parallel to (0001) in experimentally deformed synthetic quartz. White (1973) has described lamellae from naturally deformed quartz due to, slip planes related to late high strain-rate deformation and also to closely-spaced dislocation walls forming very narrow basal sub-grains, thought to be formed during recovery. Christie and Ardell (1974) used TEM to look at two types of lamellae - basal in experimentally deformed Brazilian quartz, and non-rational lamellae (i.e. not parallel to a rational crystallographic plane) in naturally deformed quartz. The former were identified as thin zones of glass sometimes associated with festoons of dislocations on one side of the lamellae; the latter were found to be zones of differing dislocation density and, therefore, by implication, recovery.

4.1.1.2. Preferred Orientation

As already mentioned above many studies of c-axis preferred orientation were undertaken before their true significance was understood. More recent studies have used models developed in metallurgy and materials science to explain the origin of 'textures' in polycrystalline aggregates. The model commonly used, known as the Taylor Bishop Hill model (Taylor, 1938; Bishop and Hill, 1951), allows predictions to be made of the fabric produced by any given deformation, depending on the activity of the various slip systems. (For a review of this model see Lister et al., 1978). Central to this model are the assumptions of homogeneous strain, and that the material

possesses five independent slip systems, that is that it fulfills Von Mises Criteria.

In the case of quartz, Lister et al. (op. cit.) have listed the possible slip systems; the common ones are shown in Table 4.1. Of these the most active in both natural and experimental deformation are the basal <a>, prism <a>, and rhomb <a> systems (Carreras et al.1977; Morrison-Smith, 1978). These, however, only provide three independent systems and for Von Mises criterion to be fulfilled, one of the systems with a <c+a> burgers vector must operate. Evidence for the operation of such systems comes mainly from experiments (Morrison-Smith, op.cit.) suggest minor activity on <c+a> systems. Carreras et al. (1977) observed dislocation in naturally deformed quartz that could not be made to go out of contrast but could not determine whether they had <c+a> burgers vectors or were mixed dislocation for which the g.b xu criterion could not be satisfied. A possible way of relaxing Von Mises criterion is through dislocation climb (Ball & White, 1978), or by allowing heterogeneous strain (Spiers, 1982).

In the quartz mylonites of Cap de Creus Carreras et al. (1977) Carreras (1974) Schmid et al. (1981) have all published c-axis diagrams, and in the case of Schmid et al. also an a-axis diagram. Fig. 4.1(a)(b). All of these diagrams are consistent with competition between basal <a>, prism <a> and rhomb <a>. The symmetrical nature of the fabric diagram (i.e. symmetric about the foliation) is caused by the two possible stable orientations for a grain such that the combined slip activity is balanced. The population within which each grain will fall, will depend on the initial orientation.

On recrystallization these two types of grain will give rise to bands of new grains of differing preferred orientation (e.g. Eisbacher, 1970).

4.1.1.3. Deformation Mechanisms

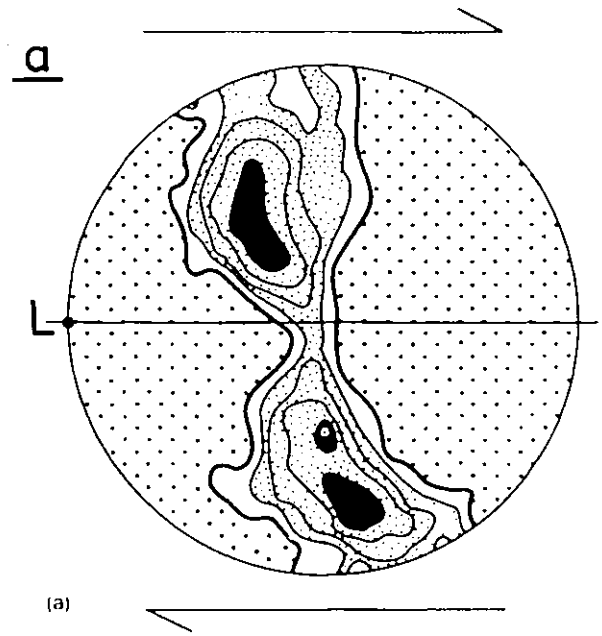
In the previous section the assumption has been made that dislocation

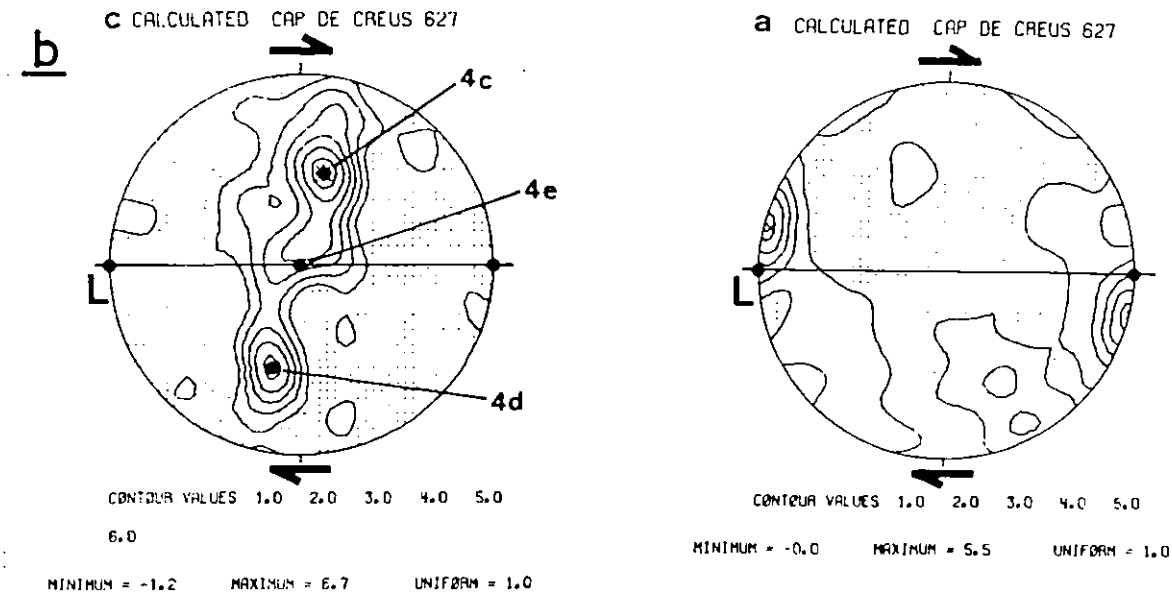
TABLE 4.1

Glide Plane	Glide direction	Multiplicity	Opposite senses equivalent
(0001) basal	$\langle\bar{1}2\bar{1}0\rangle$ a	3	yes
$\{10\bar{1}0\}$ prism	$\langle 12\bar{1}0\rangle$ a $\langle 0001\rangle$ c $\langle 12\bar{1}3\rangle$ c + a	3 3 6	yes no no
$\{10\bar{1}1\}$(+)rhomb	$\langle\bar{1}2\bar{1}0\rangle$ a $\langle\bar{1}\bar{1}23\rangle$ c + a	3 6	yes no
$\{01\bar{1}1\}(\dot{-})$rhomb	$\langle\bar{1}2\bar{1}0\rangle$ a $\langle\bar{1}\bar{1}23\rangle$ c + a	3 6	yes no

Table 4.1 Potential glide systems for α-quartz (Lister et al. 1978)

FIG. 4.1





Pole figures for c and a, calculated from the ODF. Foliation trace E-W; L = Lineation

Fig. 4.1 Stereoplots of c-axis, a-axis orientation data from quartz mylonites at Cap de Creus.

(a) c-axis plot from Carreras et al. (1977)

(b) c- and a-axis plots from Schmid et al. (1981)

glide is the dominant deformation in quartz. The existence of strongly developed preferred orientations in most deformed quartz suggests that this is in general a valid assumption. There may, however, be contributory mechanisms, which have a significant effect on the deformation. Dynamic recrystallization does have such an effect but it is not a deformation mechanism as such, and will be discussed in the next section.

Dislocation creep is the result of the simultaneous operation of dislocation glide and dislocation climb, the latter mechanism allowing the continued operation of the former by preventing dislocation pile-ups either through the annihilation of dislocations of opposite sense, or the incorporation of dislocations into networks. Evidence for the operation of this mechanism is the development of regular dislocation networks, and a lack of dislocation tangles or forests . White (1977) has discussed the role of climb in quartz tectonites and concludes that it only occurs as a subsidiary process, but that as climb is diffusion-controlled it may be the rate-limiting process causing a marked effect on the rheology.

Three types of diffusive mass transfer have been suggested as deformation mechanisms; Coble creep, intergranular diffusion, Pressure solution as for Coble creep but using an interstitial fluid phase, and Nabarro-Herring creep, intragranular diffusion either through the lattice, or along dislocation cores. Pressure solution in quartzite has been described from many low-grade environments, for a review see Kerrich (1978). Evidence for Coble and Nabarro-Herring creep in quartz is no more than circumstantial, and these mechanisms are only expected to operate for fine-grained rocks at moderate to high homolog ous temperatures ($T/Tm \sim 0.5$-1.0) and low normalized stresses.

In 1971 White suggested that grain boundary sliding (GBS) would be a contributory mechanism in the development of high strains in quartz. During the past he and many authors have equated the operation of such a

mechanism as evidence for superplasticity (e.g. Boullier and Gueguen, 1975). However, the metallurgical definition for such a deformation; that is tensile extension without necking, cannot be immediately applied to geological deformation. Tensile extension is an inherently unstable mode of extension (see Section 2.7), and the conditions for stable extension are very restricted. In geological examples, in zones of very high strain, the deformation generally approximates to simple shear, plane strain, a comparatively stable mode of deformation. Therefore, regions of very high strain, even with evidence of grain-boundary sliding do not imply superplastic behaviour.

Grain-boundary sliding cannot occur as an isolated mechanism, but it may operate in cooperation with any of the previously mentioned mechanisms (for a review see Gifkins, 1976). For quartz Etheridge & Wilkie (1979) have considered the following combinations; (After regions identified by Gifkins 1976), II_A, GBS + Coble Creep, II_B, GBS and Dislocation creep confined to grain mantles, III GBS and Dislocation creep throughout the grains. Table 4.2 shows flow laws theoretically or empirically derived for the various mechanisms.

Boullier and Guegen (1975) have set criteria for the recognition of 'superplastic' behaviour (and by implication GBS). However, these seem unnecessarily restrictive for application to geological materials. GBS in quartz has been identified by White (1977) in the fine-grained pipe rock mylonite, Eribol, N.W. Scotland, on the basis of microstructures; high dislocation densities at triple points, grain boundary voids, especially at triple junctions, and the blocky grain shape with grain boundaries aligned parallel to the foliation (for dominant simple shear). The operation of some grain size sensitive mechanism has also been suggested by White (1981) and Evans et al. (1981) from variation in strain correlated with variation in grain size, and the relative development of grain boundary

TABLE 4.2

Mechanism	Flow Law
1. Dislocation Glide	No steady-state flow, only transient creep.
2. Dislocation Creep	$\dot{\varepsilon} = \text{Const. Exp}(B\sigma)$ or $\dot{\varepsilon} = \text{Const.}\left(D_L/T\right)\sigma^n$
3. Coble Creep	$\dot{\varepsilon} = \text{Const.}w\left(D_{GB}/d^3T\right)\sigma$
4. Nabarro-Herring Creep	$\dot{\varepsilon} = \text{Const.}\left(D_L/d^2T\right)\sigma$
5. GBS + Dislocation Creep	$\dot{\varepsilon} = \text{Const.}\left(D_L/T\right)\sigma^3(1+0.015d^{-1.32})$
6. GBS + Dislocation Creep (in grain mantles only)	$\dot{\varepsilon} = \text{Const.}\left(D_{GB}/d^2T\right)\sigma^2$
7. GBS + Coble Creep	as for 3.

B, n are constants

D_L is the coefficient of lattice diffusion

D_{GB} is the coefficient of grain boundary diffusion

w is the grain boundary width

d is the grain size

(2, 3, 4 from Nicolas and Poirier, 1976; 5, 6, 7 from Etheridge and Wilkie, 1979).

Table 4.2 Flow laws corresponding to the various mechanisms of ductile deformation.

phases that may enhance diffusion.

4.1.1.4. Recrystallization Mechanisms

Sellars (1978) has described the main mechanisms of recrystallization, which he subdivided as static, dynamic and metadynamic. If a deformed material is retained at, or raised to, a high temperature after the deformation has finished, the structure will undergo further change by the occurrence of static recovery, recrystallization and grain growth. This leads to the sort of textures seen in high grade metamorphic quartz, i.e. large grain size, a lack of a pronounced preferred orientation and optical strain features.

Dynamic recrystallization occurs in a material where the processes of recovery are insufficient to prevent the build-up of stored strain energy. This reduction is carried out by three distinct (although not mutually exclusive) mechanisms, each leading to a distinct mode of recrystallization; nucleation and growth of strain-free nuclei; the bulging out of pre-existing high-angle boundaries into areas of higher stored strain energy, and the incorporation of dislocations into pre-existing sub-grain boundaries.

The first mechanism, sometimes known as classic nucleation, has not been observed in quartz, but the second, known as strain-induced boundary migration (SIBM) or more specifically, grain-boundary migration (GBM) is very commonly observed. White (1976) and Bell and Etheridge (1976) describe the formation of new grains by SIBM, predominantly along deformation band boundaries, and grain boundaries.

The third mechanism, known as sub-grain rotation (SGR) (e.g. Guillopé and Poirier, 1979) or recrystallization in situ (Sellars, 1978) involves the development of separate new grains through the progressive misorientation of sub-grains. The increase in misorientation is caused by the continuous inclusion of dislocation into sub-grain walls; the misorientation across such a boundary is a function of the dislocation density within the wall.

There is, therefore, a continuous variation from a low-angle sub-grain boundary to a high-angle grain boundary with increasing strain. Hobbs (1968) first described this mechanism from experimentally deformed synthetic quartz, and it was recognized in naturally deformed quartz by White (1973(b)).

Metadynamic recrystallization occurs when deformation of a material is stopped where the deformation had involved migratory grain boundaries (Sellars, 1978). The grain boundaries continue to migrate, and nuclei to grow until there is insufficient stored strain energy available. It is difficult to assess the importance of this mechanism in the development of the textures in naturally deformed quartz as the texture produced would be very similar to those from dynamic recrystallization by a SIBM mechanism.

4.1.2 Optical Observations

Quartz has been studied optically, at all stages of mylonitization, in orientated standard thin sections cut perpendicular to the foliation and both parallel, and perpendicular to the lineation in all the samples described. Recrystallization is almost complete by the stage at which a shear strain of $\gamma \sim 2$ is reached (estimated by the rotation of markers) (N.B. this is also the strain at which Carreras et al., 1977, observed a steady state microstructure to have been achieved). Samples from schists, quartz-diorite and microgranites were studied in their least deformed state, at a shear strain of $\gamma \sim 1.5$ and as a thoroughgoing mylonite; the relatively pure quartz samples were studied in only the last two states.

4.1.2.1. Preferred Orientations

No attempt has been made in the present study to look at the preferred orientations developed in quartz in anything more than a superficial way, as these aspects have already been covered in great detail by Carreras and his colleagues. However, by use of a sensitive tint plate it is possible

to determine the presence of a strong preferred orientation, and obtain a rough estimate of the c-axis distribution from the birefringence.

In most cases a strong, but banded, preferred orientation is present (e.g. Plate 4.1(a)) which is thought to represent alternating bands of grain falling in one or other of the main maxima in the typical Cap de Creus pattern (see Fig. 4.1, and Section 4.1.1.2). A similar type of distribution has been figured by Sander (1970, Plate IIb, after Ramsauer (1941)), and also Eisbacher (1970) who suggested that each band was derived from an original grain. Carreras, 1974, has suggested similar origins for the banded preferred orientation of the Cap de Creus mylonites.

Plate 4.1(b) shows a remnant grain from CSE 15(a) (for location of samples from the CSE series, see Map 2(c)), passing laterally into a recrystallized band, all of similar orientation. It is suggested that this band is directly derived from the remnant grain.

4.1.2.2. Recrystallization

In samples unaffected by mylonitization, the quartz grains have well-developed sub-grain networks (Plate 4.1(c)). As the deformation associated with mylonitization becomes more intense a number of 'orders' of sub-grains are formed, with the largest order in general showing the largest mutual misorientations. With increasing strain the different order sub-grains acquire sufficient misorientation to be regarded as separate grains; Plate 4.1(d) shows an intermediate stage in this process. It is clear from this micrograph that SGR recrystallization is not the only mechanism operative; new grains are also being formed by a SIBM mechanism at both grain and sub-grain boundaries (Plate 4.1(e) shows such a boundary at a higher magnification). A similar situation has been described by Bell and Etheridge (1976) for quartz from the granulite facies side of the Woodroffe Thrust.

Plate 4.1 Optical micrographs of quartz microstructures. (all crossed polars)

(a) Bands of differing preferred orientation parallel to foliation in a quartz mylonite. Scale bar = 1mm.

(b) Remnant quartz grain passing laterally into recrystallized band of similar orientation. Scale bar = 250μm.

(c) Well-developed sub-grain network in a quartz grain from an almost undeformed microgranite. Scale bar = 200μm.

(d) Large new grains formed by the misorientation of original sub-grain boundaries. SIBM recrystallization is producing small new grains on the new grain boundaries; note further development of high angle boundaries within the large new grains(arrowed). Scale bar = 200μm.

(e) Grain boundary bulges chacteristic of SIBM recrystallization on high angle grain boundary, also small new grains. Scale bar = 50μm.

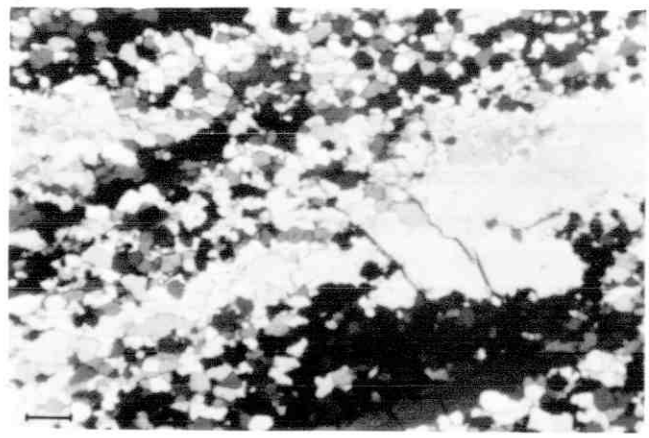
(f) End product of mylonitization, a completely recrystallized quartz mylonite. Scale bar = 100μm.

PLATE 4.1

a



b



c



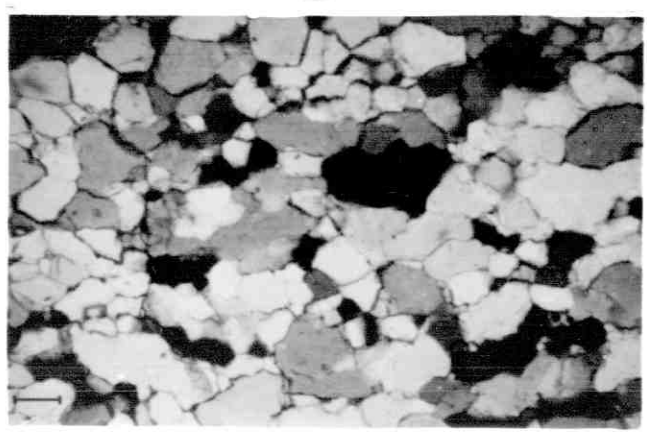
d



e



f



The second mechanism of recrystallization, although only affecting a small part of the grain volume at these strains, becomes increasingly important with increasing mylonitization. It is important to note that the new grain size produced by the SIBM mechanism is smaller than that due to SGR from even the smallest order of sub-grains. At shear strains approaching those at which a steady-state microstructure is achieved the SIBM mechanism has effectively 'consumed' all parts of the parent grain whether previously recrystallized by SGR or not (Plate 4.1(f)).

The significance of this recrystallization sequence as regards the measurement of recrystallized grain size for use in estimation of palaeo-stress will be fully discussed in Chapter 5.

4.1.2.3. Grain Shapes/Boundaries

In the single phase quartz mylonites a range of grain shapes and grain-boundary morphologies are evident. It has proved possible to sub-divide these mylonites into three types: type 1 characterized by moderately elongate grains in sections parallel to the lineation, with extremely irregular shapes and lobate boundaries (e.g. CSE 15 parallel to lineation, Plate 4.2(a)). Type 2 mylonites have approximately equant polygonal grains which may be slightly elongate in the lineation, with grain boundaries that are only slightly irregular (e.g. Plate 4.2(b)). In type 3 mylonites the grains are equant to slightly elongate, rather 'blocky', that is, sub-rectangular, commonly with two of the sides sub-parallel to the foliation in sections parallel to the lineation (Plate 4.2(c)) and, equant polygonal in sections perpendicular to the lineation (Plate 4.2(d)).

Of these types only one type 3 has been observed, CSC04 in quartz mylonite from the constriction zone (see Section 3.3.3.2), four are of type 1 all from relatively low-strain mylonites, and the other twelve mylonites are of type 2. The 'blocky' nature of the grains in CSC04 suggests that a grain boundary sliding mechanism (see Section 4.1.1.3) was operative.

Plate 4.2 Quartz mylonite textures. (all crossed polars)

(a) Type 1 quartz mylonite showing moderately elongate grains with irregular grain shapes and lobate boundaries. (Sample CSE 15(b), parallel to lineation). Scale bar = 100μm.

(b) Type 2 quartz mylonites showing equant to slightly elongate grains with polygonal grain shapes. (Sample CSE 20, parallel to lineation). Scale bar = 100μm.

(c) Type 3 quartz mylonite showing slightly elongate grains with sub-rectangular grain shapes; long sides of grains are sub-parallel to the mylonite foliation (S_m). (Sample CSC 04(b), parallel to lineation). Scale bar = 100μm.

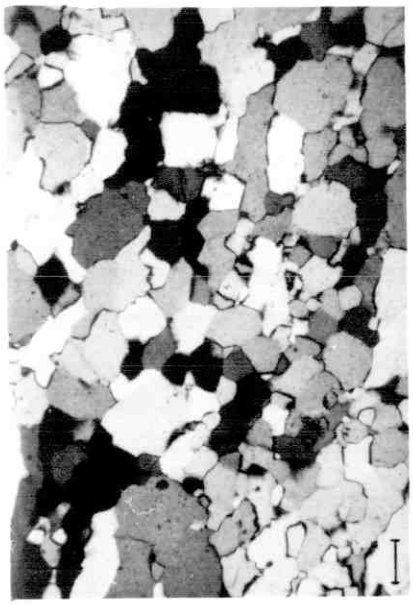
(d) Type 3 quartz mylonite in section perpendicular to lineation to show polygonal grain shapes. (Sample CSC 04(a)). Scale bar = 100μm.

(e) Type 1 quartz mylonite to show detail of lobate grain boundaries (arrowed) consistent with continuing dynamic recrystallization. (Sample CSE 15(b), parallel to lineation). Scale bar = 50μm.

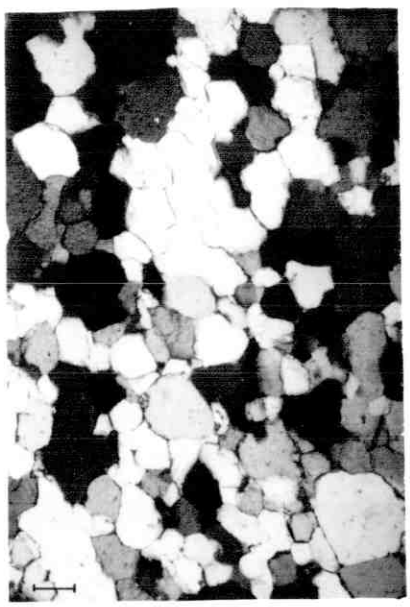
(f) Quartz mylonite showing the effects of fine white micas on grain size (arrowed). Scale bar = 50μm.

PLATE 4.2

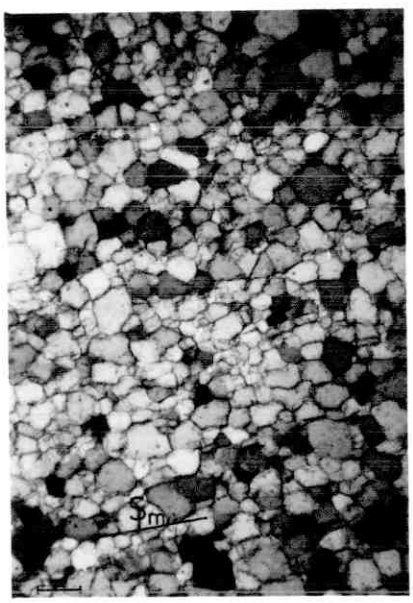
a



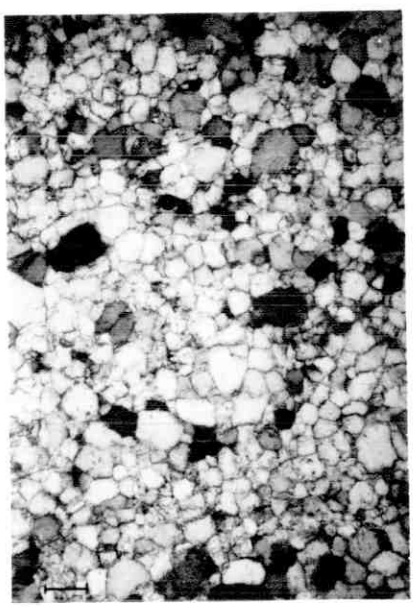
b



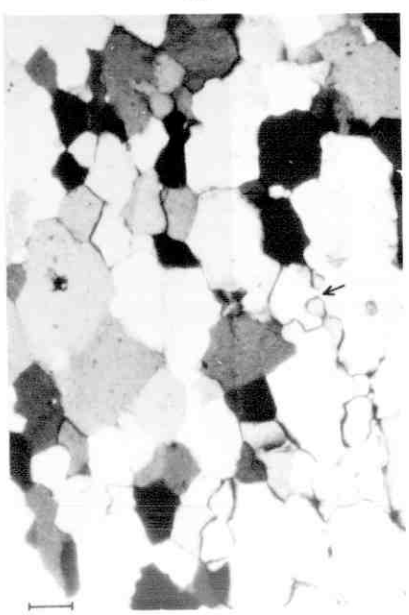
c



d



e



f



TABLE 4.3

MYLONITE TYPE					
3		2		1	
Sample	Grain size (μm)	Sample	Grain size (μm)	Sample	Grain size (μm)
CSC 04(b)	52.3	RDS 04	82.9	PDM 04	155.2
		CSE 27	70.2	PDM 05	135.3
		CSE 04	63.0	CSE 15(a)	144.4
		CSA 10	57.1	CSA 16	357.7
		CSE 25	75.8		
		CSE 23(a)	100.5		
		CSE 20	94.7		
		CSA 18	128.0		
		CSA 17	266.0		
		CSA 15	353.5		
		CSA 21	432.1		
		CSE 08(b)	52.6		

Table 4.3 . Distribution of quartz mylonite samples with respect to textural type showing ranges of grain sizes .

The microstructure typical of the type 1 mylonites is similar to those observed in hot-worked metals that have undergone cyclic SIBM recrystallization; Plate 4.2(e) shows a bulging grain boundary.

Table 4.3 shows the distribution of mylonites within the three types as a function of grain size. All type 1 mylonites have grain sizes greater than 120μm, the only type three mylonite has a grain size less than 60μm. Type 2 mylonites have a larger range but over half of them fall in the range 60-120μm. This grain size variation suggests that the equilibrium recrystallized grain size determines the deformation mechanism.

4.1.2.4. Second Phase Effects

In many of the quartz mylonites a small amount of a second phase such as muscovite or feldspar are present. Often it is these phases which define the macroscopic foliation by causing a reduction in the grain size in the quartz in their immediate vicinity (e.g. Plate 4.2 (f)). In some of the mylonites (generally type 1) the presence of the micas has no apparent effect on the quartz grain size, and are indeed found within grains rather than just in grain boundaries.

4.1.3. T.E.M. Observations

Samples for T.E.M. were prepared from standard petrological thin sections, milled in an ion beam thinning unit to provide areas transparent to electrons, and carbon coated. Observations were carried out using an AEI EM7 microscope operating at 1000 Kv; the range of magnifications available allowing a one to one correspondence to be established between features seen optically and those in T.E.M. The quartz samples were from two series, PDM 01-03 (for location see fig.3.15), CSE 01-03 (for location see Map 2(c)), of samples from microgranites at various stages of mylonitization.

Plate 4.3 TEM micrographs of quartz microstructures.

(a) Area in quartz grain showing curved dislocations with many short segments and loops, and sub-grain boundaries, all features indicative of recovery. Scale bar = 1μm.

(b) Mosaic of quartz/quartz grain boundary showing many small regular voids, with larger irregular voids formed at sub-grain boundary/ grain boundary junctions (arrowed). (Sample CSE 03). Scale bar = 1μm.

(c) Quartz/quartz grain boundary showing voids associated with individual dislocations as well as sub-grain boundaries. Sample CSE 01 . Scale bar = 1μm.

(d) Quartz/oligoclase (O) grain boundary with large void at intersection with sub-grain boundary in the quartz. (Sample CSE 01). Scale bar = 0.5μm.

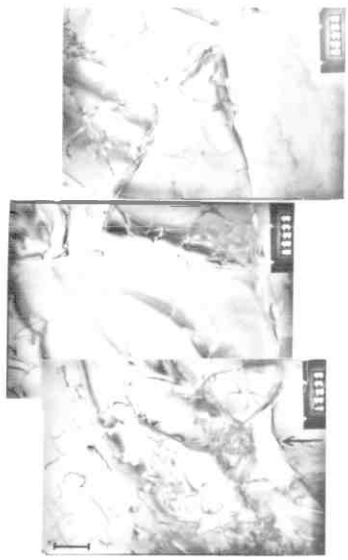
(e) Quartz/quartz grain boundary showing the regular distribution of large voids along the grain boundary surface. One of the voids contains an inclusion (i). (Sample CSE 02). Scale bar = 1μm.

PLATE 4.3

a



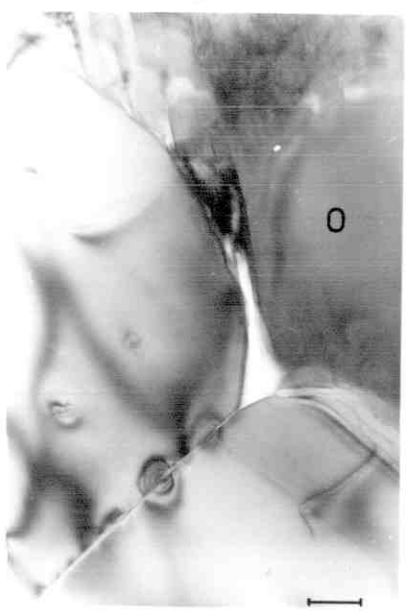
b



c



d



e



4.1.3.1 Dislocation structures

In the least deformed microgranite from Punta del Moli (PDM01) the dislocations are commonly curved, with short segments, loops and well-ordered networks; all features indicative of substantial recovery. The ubiquitously developed sub-grains are sub-equant but commonly prismatic with curviplanar boundaries. Plate 4.3(a) shows a typical area within a quartz grain showing all the features mentioned above.

In the least deformed microgranite from Portixol (CSE 03) the quartz shows similar well-recovered structures to those seen in PDM01 . With further deformation the dislocation microstructures remain essentially unchanged with increasing deformation.

4.1.3.2 Grain-boundary structures

Following the observation of variations in quartz mylonite textures (see 4.1.2.3) particular attention was paid to the structures of grain boundaries in quartz. Recent studies (White and White, 1981) have shown that grain boundaries are rarely simple planar structures and may provide some information as to the operative deformation mechanisms. Voids at grain boundary triple points provide an interconnecting network of while those on grain boundaries themselves serve to shorten the diffusion paths, the combined effect being to enhance diffusive mass transfer processes. The development of voids has been associated with the mechanism of grain-boundary sliding (White, 1979 (b)).

In the PDM 01-03 sample series the recrystallized quartz areas are seen optically to have type 1 textures (see Section 4.1.2.3) and in T.E.M. the grain boundaries are relatively simple curviplanar structures with few voids. In contrast all of the grain boundaries in the series CSE 01-03 (with type 2 textures) have well-developed voids. Even in the least deformed specimen (CSE 03) voids are apparent (Plate 4.3(b)). In this mosaic small voids of regular shape and even distribution may be observed along the

grain boundary with larger voids developed at the intersection on sub-grain boundaries with the grain boundary; still larger voids are commonly developed at grain triple-junctions. Plate 4.3(c) shows a large void developed at the intersection between a sub-grain boundary and a grain boundary with a plagioclase grain. In some boundaries dislocations are seen to be associated with individual voids (Plate 4.3(d)), possibly due to their pinning effect (Knipe and White, 1979). Some of the voids contain inclusions (e.g. arrowed on Plate 4.3(e)) which may be interpreted as impurities from the quartz that have migrated to the grain boundaries and remained there or else as phases crystallized from an original inter-granular fluid in a way analogous to fluid inclusions found wholly within mineral grains.

Samples were prepared from the type 3 quartz mylonite, CSC04 (for locality see Fig. 3.16) for T.E.M. in order that the grain boundary structures could be compared with those described above. The grain boundaries observed were always rather open (as in Plate 4.4(a)) due in part to the effects of specimen preparation. However, such effects were not commonly observed in other quartz mylonite specimens. Also, it was found that when polished sections of CSC 04 were chemically etched in an attempt to reveal the dislocations and sub-grain structure (for details see Section 5) the main effect was to disaggregate the rock. In detail the grain boundaries sometimes appear to have an unusually wide zone of enhanced ion-beam etching; Plate 4.4(b) shows such a boundary.

4.1.3.3 Healed fractures

In CSE 03, the least deformed microgranite planar features with voids have been observed, e.g. Plate 4.4(c). The structures are seen to cut across several sub-grain boundaries, although with no apparent offset. The detailed nature of these features is somewhat variable from irregular with no clear dislocation structure as in Plate 4.4(d) to regular structures

Plate 4.4 TEM micrographs of grain boundaries and healed fractures.

(a) Strongly etched grain boundaries in type 3 quartz mylonite (Sample CSC 04). Scale bar = 5μm.

(b) Grain boundary in type 3 quartz mylonite (Sample CSC 04) showing unusually wide zone of enhanced ion-beam etching (arrowed). Scale bar = 1μm.

(c) Planar feature with voids, cutting sub-grain boundaries without obvious displacement. (Sample CSE 03). Scale bar = 2μm.

(d) Planar feature with voids showing no regular dislocation network. (Sample CSE 03). Scale bar = 1μm.

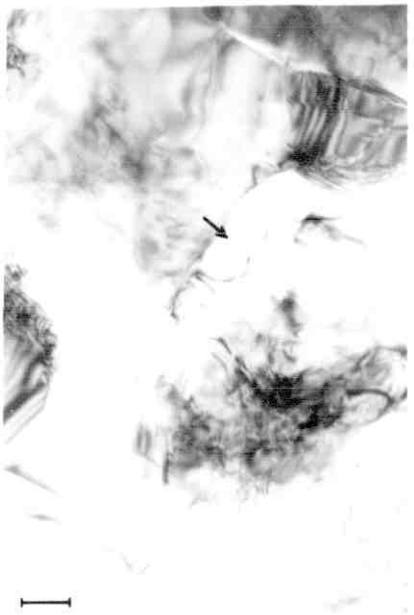
(e) Planar feature with small voids (arrowed), a regular dislocation network, and large voids at intersections with sub-grain boundaries. Note the lack both of displacement and misorientation across this feature. (Sample CSE 03). Scale bar = 1μm.

PLATE 4.4

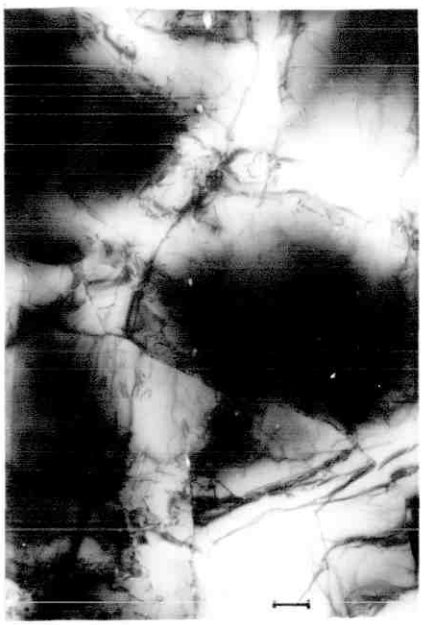
a



b



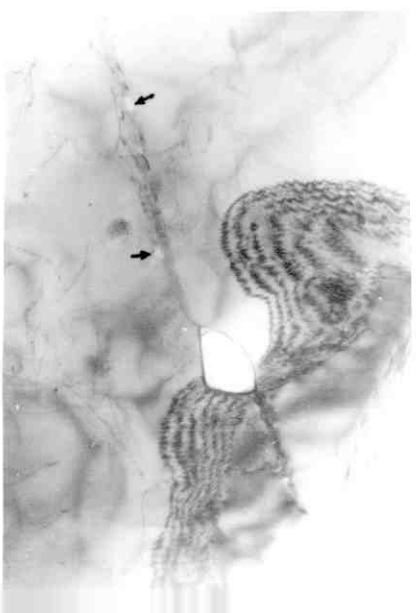
c



d



e



that are similar to sub-grain walls (Plate 4.4(e)); these latter features may be distinguished from sub-grains as they are planar rather than curviplanar, have voids, cut sub-grain boundaries and are not associated with any measurable misorientation. Optical re-examination of the thin section (CSE 03) revealed a few lamellae with inclusions and cutting grain boundaries, features consistent with healed fractures, and it is considered that features observed in T.E.M. have a similar origin. The timing of these fractures is not certain as the evidence of age with respect to sub-grain formation is equivocal.

4.1.4 Discussion

From the optical observation it is suggested that quartz mylonite recrystallizing with an equilibrium grain size under 60μm (i.e. Type 3) deformed by grain-boundary sliding. A strong preferred orientation indicates that dislocation creep was at least partly responsible for the accommodation of the GBS, possibly in combination with Coble Creep. In mylonites of grain size in excess of 120μm (i.e. Type 1) deformation appears to proceed by dislocation creep coupled with cyclic SIBM recrystallization preventing work hardening. Intermediate (Type 2) mylonites show some features common to both the other types which suggests that the strain is taken up by components of dislocation creep, and grain boundary sliding with some recrystallization.

T.E.M. observations of grain boundaries are consistent with grain-boundary sliding being an important contributory mechanism to the deformation of recrystallized quartz grains in type 2, and 3 mylonites. The presence of voids on grain boundaries decreases the diffusion paths and would enhance the Coble creep which is normally in part responsible for the accommodation of GBS. The grain boundaries structures in CSC04 suggest the presence of an unusually wide zone ($\sim$0.5μm) of quartz susceptible to ion-beam thinning (and chemical etching). This may be a zone of distorted

crystal structure or possibly of unusually high OH content (White and White, 1981).

4.2 Feldspars

In the rocks studied two types of feldspar were observed in detail; the feldspar microcline, and the sodic plagioclase feldspars falling in the range albite/oligoclase. In most of the samples studied the feldspars have an igneous origin. The two types of feldspar will be considered separately for although there is a certain gross similarity in their behaviour, the fine scale structures show significant differences.

4.2.1 Microcline

Microcline is present in most of the migrogranites/pegmatites but has only been studied in detail in the series PDM 01-03. In PDM 01 and 02, the least deformed and partially mylonitized specimens respectively, microcline is the dominant feldspar forming c.30% of the rock. In the mylonite sample (PDM 03), however, there is little microcline, and what there is appears to be being replaced by myrmekitic intergrowths. The paucity of microcline in PDM 03, combined with the aforementioned textures may be ascribed to an original variation in mineralogy as the undeformed microgranite contains more mafic inclusions that are as difficult to distinguish in the mylonite. Fortunately the whole microstructural evolution may be observed in samples PDM 01/02.

4.2.1.1 Review of previous work

Since the x-ray data of Laves (1950) microcline has been clearly established as a distinct form of alkali feldspar. Most of the published work (see Smith, 1974, I for review) has concentrated on understanding the formation of microcline, and the development of perthite with which they are commonly associated (see next two sections). In comparison relatively

few detailed studies have been published on the deformation of microcline, or any alkali feldspar.

Williame et al. (1979) have studied experimentally deformed sanidine and reported dislocation glide and microcracking. Sacerdoti et al. (1980) have looked at naturally deformed (2kb, $T<550^{o}C$) orthoclase (still clearly in its monoclinic state without any signs of transformation), and observed evidence for dominant dislocation glide from dislocation tangles and local recovery with sub-grain formation. The only study of plastically deformed microcline is by Vidal et al. (1980) (see also Debat et al., 1978, for general background). They described the deformation structures in microcline from an augen gneiss deformed under the inferred conditions of 2kb confining pressure at a temperature of $550^{o}C$. Both old and new recrystallized grains show the characteristic microcline-twinning caused by the intimate alternation of domains with albite and pericline twins. However from a standard phase diagram (e.g. Smith, 1974, I) such a feldspar (Or_{q4}) would have been monoclinic during deformation with subsequent inversion to microcline.

The old grains contain isolated sub-grains, that increase in number towards the 'recrystallization front." Each new grain is sub-divided into many sub-grains with very variable free dislocation densities; locally dislocation-free zones were observed near grains and sub-grain boundaries. Vidal et al. (1981) suggest that these structures imply grain boundary and sub-grain boundary mobility, and therefore conclude that recrystallization occurred by a SIBM mechanism. There is no significant chemical change accompanying the deformation.

4.2.1.1.1 Ordering phenomena

The origin of the characteristic m-twinning has long been attributed to the transformation from a completely disordered monoclinic structure to a fully ordered triclinic structure. There are two possible ways that

a fully ordered structure may be achieved and these are related by two possible planes of symmetry, the composition planes of twins on the albite or pericline law. There is an equal probability of these two occurring and this leads to the intimate domainal texture.

Not all K-feldspars are able to reach this lowest energy configuration either due to fast rates of cooling, or low temperature crystallization. McConnell (1971) using T.E.M., observed a modulated microstructure in an Adularia (a type of K-feldspar associated with low temperature veins), similar in orientation to the albite and pericline twin composition planes. He has proposed that this microstructure is due to a fine scale ordering that still allows the feldspar to retain its monoclinic symmetry. Putnis and McConnell (1980) figure an orthoclase which appears to have started with the order-modulated structure but that locally is being replaced by M-twinning, and they therefore view the order modulation as being in some cases an intermediate stage in the ordering to m-twinning. This is also backed up by the observations of Akizuki (1972) who showed a variation from order modulation, through a stage in which one modulation becomes locally dominant finally becoming an A or P-twin domain.

4.2.1.1.2 Perthites

The exsolution of Na-feldspar from an initially homogeneous alkali feldspar is extremely well-documented in the literature (see Smith, 1974 for review). Most of the work has been carried out on optically visible perthites (Smith, 1974, II), however many K-feldspars are cryptoperthites (Smith, 1974) that is exsolved on a scale that is not visible optically. McConnell (1969) observed a very fine-scale modulation in a sanidine ($Or_{36}Ab_{64}$) with a wavelength of 10nm, which he ascribed to unmixing into K-rich and Na-rich regions by atomic diffusion controlled by a chemical spinodal . Brown and Williame (1974) figure a lamellar perthite with similar spacing, the lamellae are found to lie near ($\bar{6}01$) which is the

plane of least strain that allows the coexistence of the two feldspars in their monoclinic states.

Williame et al. (1976) have surveyed a number of cryptoperthites and have summarized the microstructural development of alkali feldspar on cooling in Fig. 4.2. Bulk composition of $Or_{\leq 70}$ follow path I in which exsolution occurs by a spinodal decomposition while those of $Or_{\geq 70}$ follow path II in which it occurs by the heterogeneous nucleation and growth of lenticular areas of Na-feldspar.

4.2.1.2. Optical Observations

The deformation behaviour of microcline in PDM 01-03 is very similar to that seen in all the other rocks containing this feldspar, so only these samples will be described. In the last deformed sample PDM 01 microcline occurs as subhedral strain free grains with the characteristic cross-hatched m-twinning generally well-developed, (Plate 4.5(a)). In about half of the grains, irregular veins and blebs of albitic plagioclase occur as a perthitic intergrowth with the microcline; some grains are completely free of the perthite while on others the veining represents up to 40% of the grain (Plate 4.5(b)). Many microcline grains contain sub-spherical inclusions of quartz, locally arranged in concentric zones. The microcline shows little alteration apart from sericitization localized along albite veins. Where the feldspar is adjacent to plagioclase grains myrmekitic intergrowths of albite and quartz are formed. The albite commonly grows in optical continuity with the original plagioclase grain, and the intergrowth apparently replaces the microcline.

In the partially mylonitized material, PDM 02, the microcline commonly shows the development of undulatory extinction with poorly developed subgrains at some grain boundaries. At microcline/microcline grain contacts areas of fine-grained feldspar are developed (Plate 4.5(c)) with a grain size in the range 5-15μm. The new feldspar grains are generally sub-equant

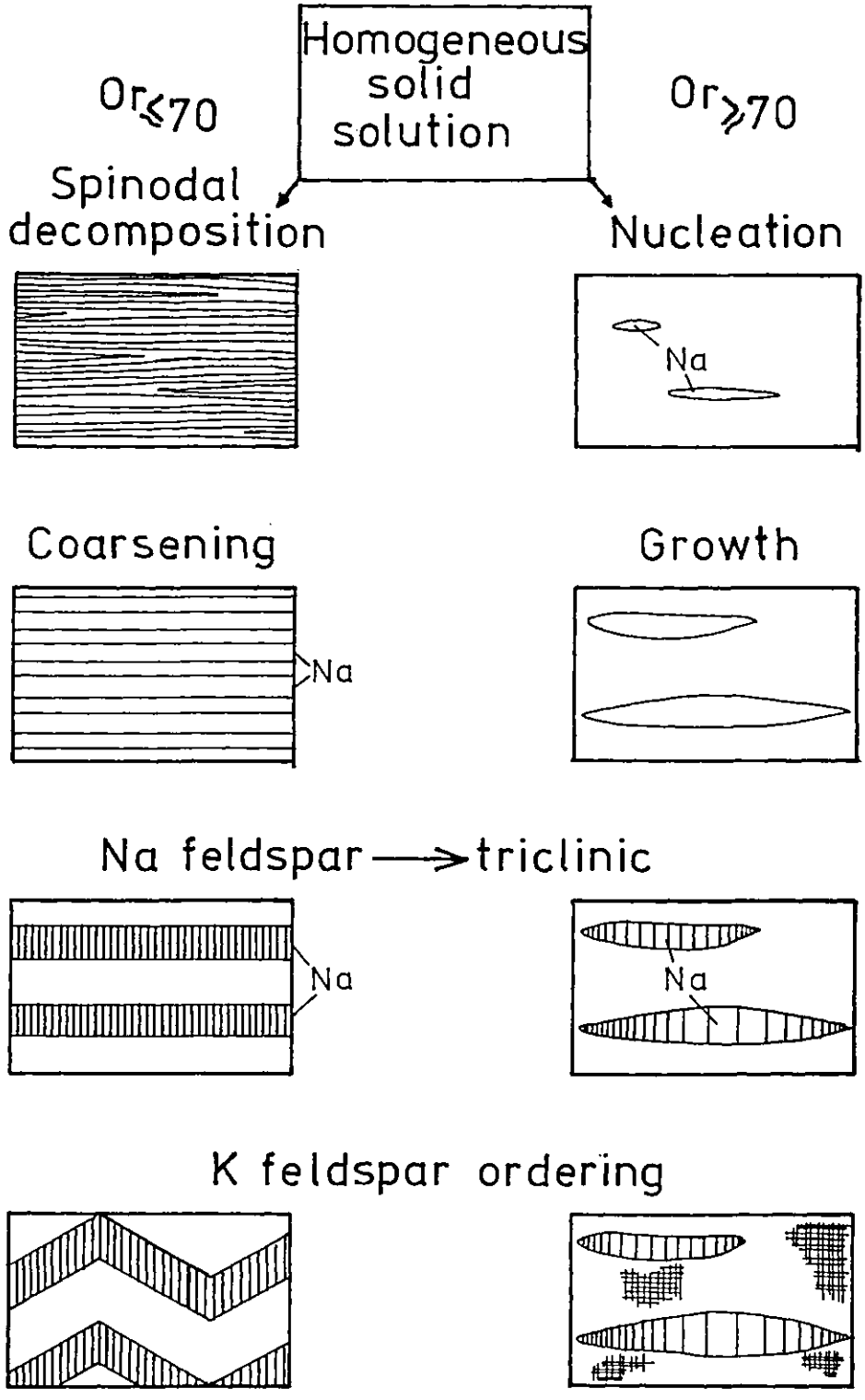


Fig. 4.2 Alternative perthite exsolution paths for alkali feldspars for compositions greater or less than ~Or_{70}. (after Willaime et al.,1976)

Fig. 4.5 Optical micrographs of alkali feldspar. (all crossed polars)

(a) Microcline twinning in K feldspar. Note also the myrmekitic intergrowth into the microcline consisting of an albite (P) and quartz (Q). (Sample PDM 01). Scale bar = 100μm.

(b) K feldspar perthite with lenses of albite. (Sample PDM 01) Scale bar = 100μm.

(c) Recrystallized zones on K feldspar/K feldspar grain boundaries. (Sample PDM 02). Scale bar = 100μm.

(d) Recrystallized zone between two K feldspar perthites with new grains showing a moderate shape fabric; note one new grain showing microcline twinning (arrowed). (Sample PDM 02) Scale bar = 50μm.

PLATE 4.5

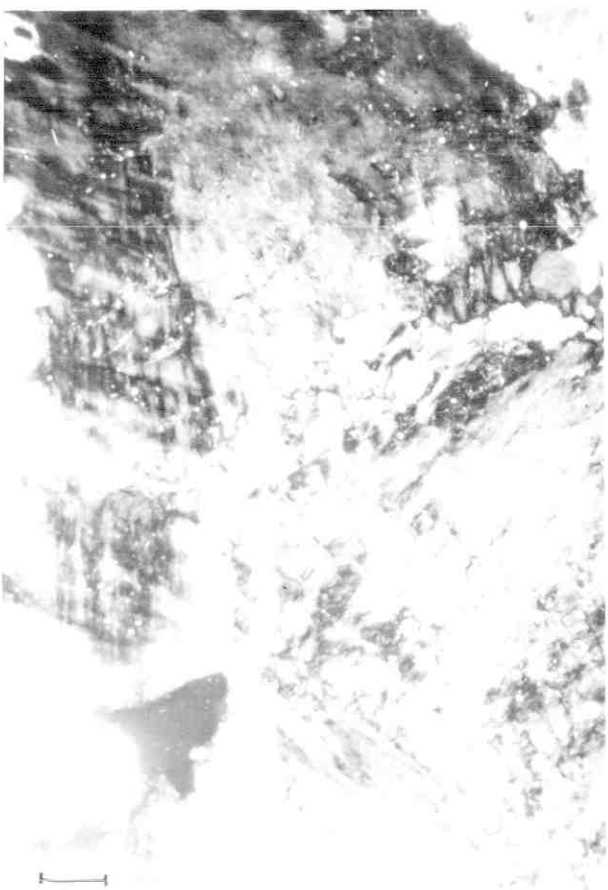
a



b



c



d

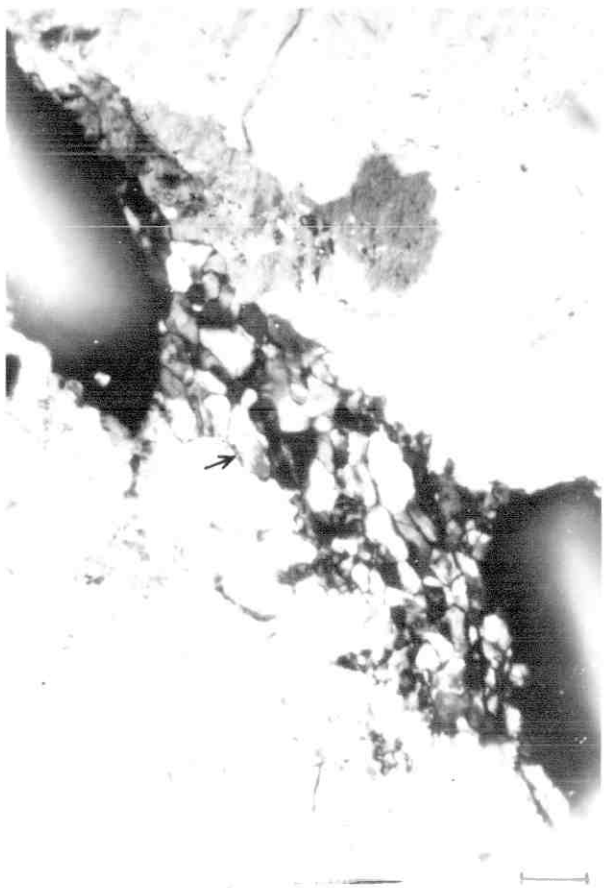


Plate 4.6 TEM micrographs of alkali feldspar.

(a) Microcline twinning developed at a very fine scale. Note the relatively sharp albite twins (A_T) compared to the rather diffuse pericline twins (P_T). (Sample PDM 01). N.B. the diffraction pattern was taken in an adjacent area of the same grain in which twinning was not developed. Scale bar = 1μm.

(b) Cross-hatched modulation in K feldspar. Note diffuse streaking of the spots on the diffraction pattern in the direction of the modulations. Scale bar = 1μm.

(c) Cross-hatched modulation in K feldspar with a regular modulation looking like albite twins in poor contrast in one direction and a rather diffuse irregular modulation orthogonal to it. N.B. This area is adjacent to 4.6(a) and was taken under the same diffracting conditions; there is a rotation of 30° clockwise from (a) to (c). Scale bar = 200nm.

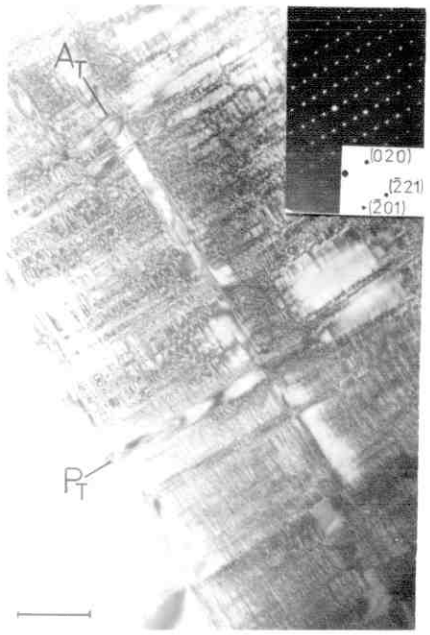
(d) Planar defects in K feldspar (arrowed), the lower of which is seen to terminate at a dislocation. Scale bar = 0.5μm.

(e) Planar features in K feldspar (arrowed). Note that lowest cuts two dislocations. Scale bar = 1μm.

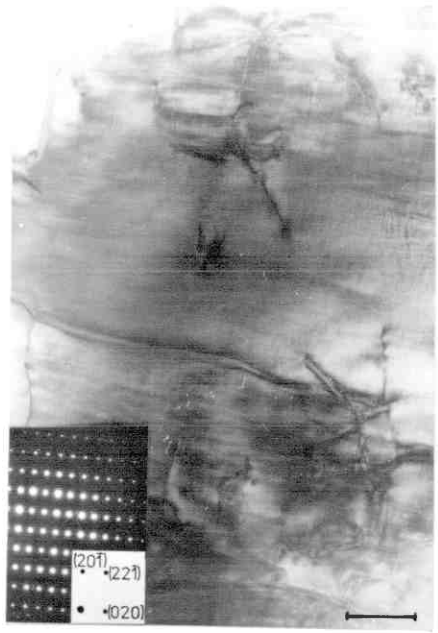
(f) Lamella of Na feldspar in K feldspar with albite twins (A_T) which decrease in spacing as the lamella gets thinner. Note also the very faint lamellae due to the peristerite exsolution (arrowed) in the Na feldspar. Scale bar = 1μm.

PLATE 4.6

a



b



c



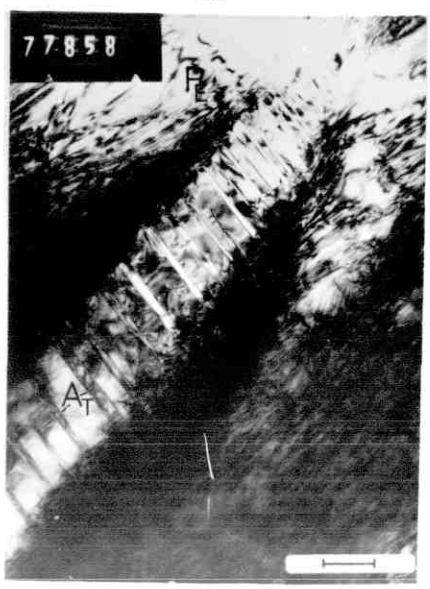
d



e



f



although locally a weak grain-shape fabric is developed in slightly elongate grains (Plate 4.5(d)).

4.2.1.3 TEM Observations

In addition to HVEM a number of observations were made using a JEOL 120CX scanning transmission electron microscope (STEM) operating at 100KV. This instrument has an energy dispersive x-ray analysis which permits the chemical characterisation of areas ∿100nm. The resulting analyses are not as good as those obtained from an electron microprobe but provide a semi-quantitative chemical control.

In PDM 01 two types of microstructure are present, Plate 4.6(a) shows one of these, m-twinning; in this case the alternation of domain of Albite and Pericline twins continues down to a scale of 20nm. The dislocation density measured in such an area is extremely low ($\rho < 10^{11} m^{-2}$). The second type of structure also presents a cross-hatched appearance with traces parallel to the Alpite and Pericline twin traces in the same section (Plate 4.6(b)). In this case, however, the 'tweed' texture is thought to be due to the presence of a modulated structure in two directions similar to those described by McConnell (1971) for adularia , diffraction patterns show only streaking in two directions perpendicular to the traces. Locally (see Plate 4.6(c)) a mixture of the two types is found with a modulation in the direction of the P-twin trace and regular lamellae, looking like Albite-twins in poor contrast, parallel to the (010) trace.

Vidal et al., 1981, describe similar variations in microstructure for their microcline, but attribute the modulation to crypto-perthitic exsolution. As their feldspar has a composition of Or_{94} it seems unlikely that a spinodal type perthite would occur (see Fig. 4.2). Therefore, it is suggested that both the variation in their study and that in the present

study are due to varying degrees of inversion to the triclinic state (see Section 4.2.1.1 ; see also similar structures described by McLaren, 1978).

In the m-twinned areas slightly higher dislocation densities $\rho \sim 10^{11}m^{-2}$ are present; the dislocations are commonly straight and lie parallel to twin traces. Locally planar defects associated with dislocations have been observed (Plate 4.6(d)), similar to those described by et al. 1981 in orthoclase,and interpreted as slip-plane faults (Marshall and McLaren, 1977(a)) i.e. areas of dilatation caused by the passage of dislocations.

Other planar features are common in these areas consisting of highly-strained curriplanar regions (arrowed in Plate 4.6(e)). These structures are not associated with dislocation networks and are thought to be fractures; similar features have been figured by Marshall and McLaren (1977(b)) in experimentally deformed plagioclase feldspars, and Williame et al. (1979) in experimentally deformed sanidine.

In PDM 02 the microcline is clearly much more deformed, dislocation densities of $\rho > 10^{12}m^{-2}$ are quite common. Plate 4.7 shows an incomplete mosaic of the edge of one of the zones of new grains as described in Section 4.2.1.2. The old grain is a perthite containing lenses of Na-feldspar (marked Na) which may be distinguished from the K-feldspar due to the presence of only albite twinning (marked A_T), as compared to m-twinning or an order-modulated structure, with the twin spacing ranging with the thickness of the lens along its length. Note also the curved nature of the dislocations in the albite as compared to the rectalinear nature of those in the microcline (the relatively large degree of recovery common in albite will be discussed in Section 4.2.2.1). The interfaces are clearly incoherent and are formed by closely spaced dislocation walls. Individual lenses appear to have 'grown' into each other.

The relationship between albite twin spacing and lamellae thickness has been derived theoretically byWillaime & Gandais(1972) by a consideration of the strain caused by the structural collapse of the (till then) metastable monocline albite. This analysis predicts that the twin spacing will vary directly with the square of the lamellar width. In the lamellae shown in Plate 4.6(f) measurements were made but these would fit better with a linearlaw (see Table 4.4) It is thought that in this case the twins are not simply twins due to the transformation but also include later deformation twins, indeed some terminate within the grain, a characteristic of deformation twins (see Section 4.2.2.1.1.).

In Plate 4.6(f) it is possible to see (N.B. only clear on the negative) that the lamella of sodium feldspar is itself exsolved to form a peristerite (see Section 4.2.2.1.3.), consisting of regular lamellae of spacing ∿15nm. This exsolution within exsolution has not been previously reported but as alkali feldspars may contain up to a few per cent of the calcic An molecule (Smith, 1974, I) such a structure is not surprising.

At the right-hand end of Plate 4.7 new, strain-free, grains are visible in both components of the perthite. The isolated nature of these grains indicate that a classical nucleation mechanism was responsible for the recrystallization. The new grain at the bottom left of the mosaic shows the development of a lamellar modulation in one direction. The lamellae are twinned about a simple twin (arrowed), giving rise to a herringbone structure. This grain also contains a large number of inclusions , similar to ones in the old grain; inclusions in other grains have been identified as apatite or rarely mica (either by STEM microanalyses or from diffraction patterns).

The composition of the new grain is not known but it is inferred to be a plagioclase feldspar in the peristerite range (i.e. An_{4-16}). The

TABLE 4.4

Lamellar width, t(μm)	Twin spacing, s(μm)	t/s
3.57	0.66	5.4
2.71	0.68	4.0
2.43	0.46	5.3
2.00	0.29	6.9
1.36	0.14	9.7
0.79	0.11	7.2
0.43	0.06	7.2

Table 4.4 Variation of twin spacing with width of Na feldspar lamella (Plate 4.6(f)).

Plate 4.7 Mosaic of K feldspar grain mantle showing the development of Na-feldspar lenses and the formation of strain-free new grains by a classic nucleation mechanism. The Na feldspar is characterised by curved dislocations as opposed to the K feldspar with rectalinear sets of dislocations.

PLATE 4.7

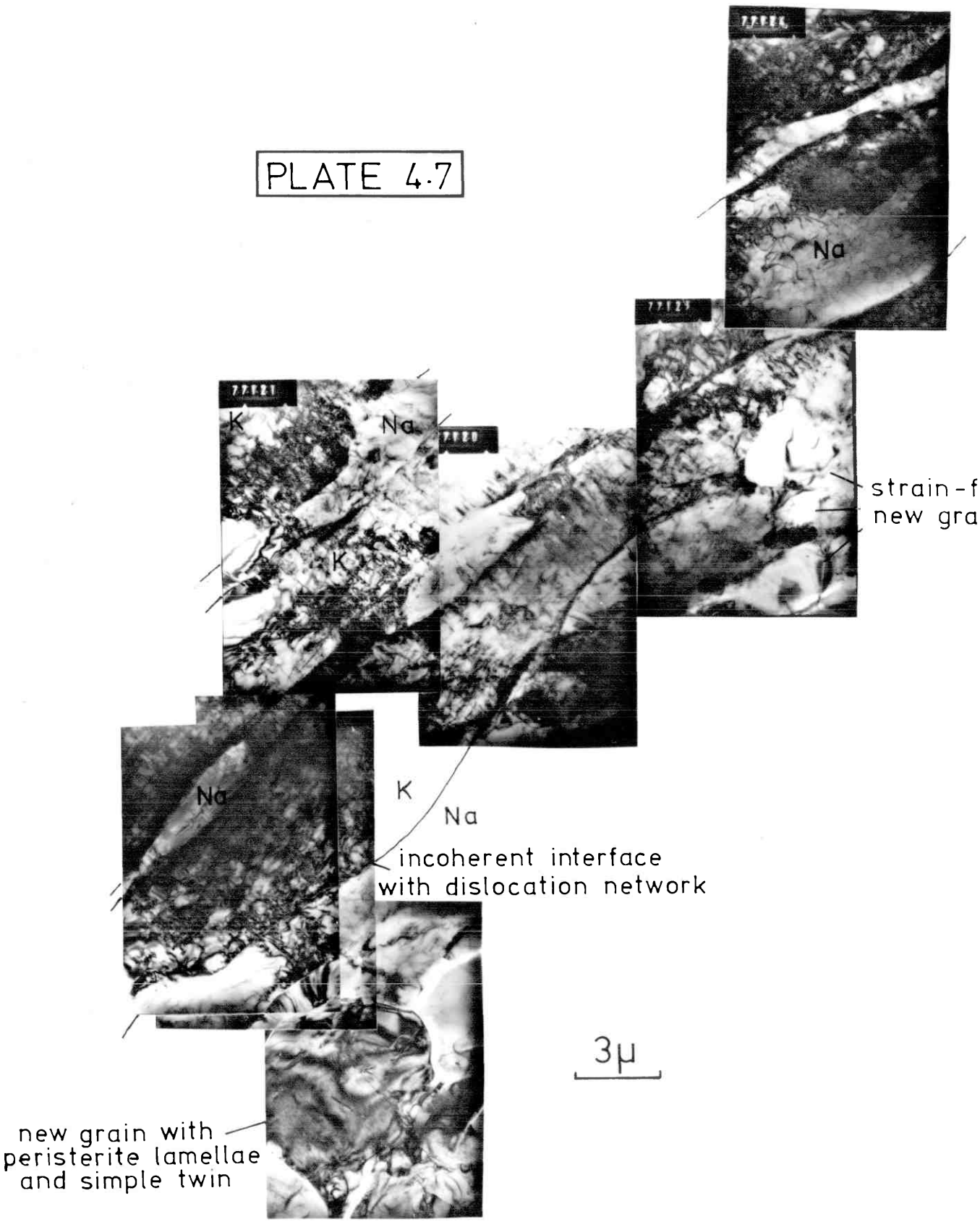
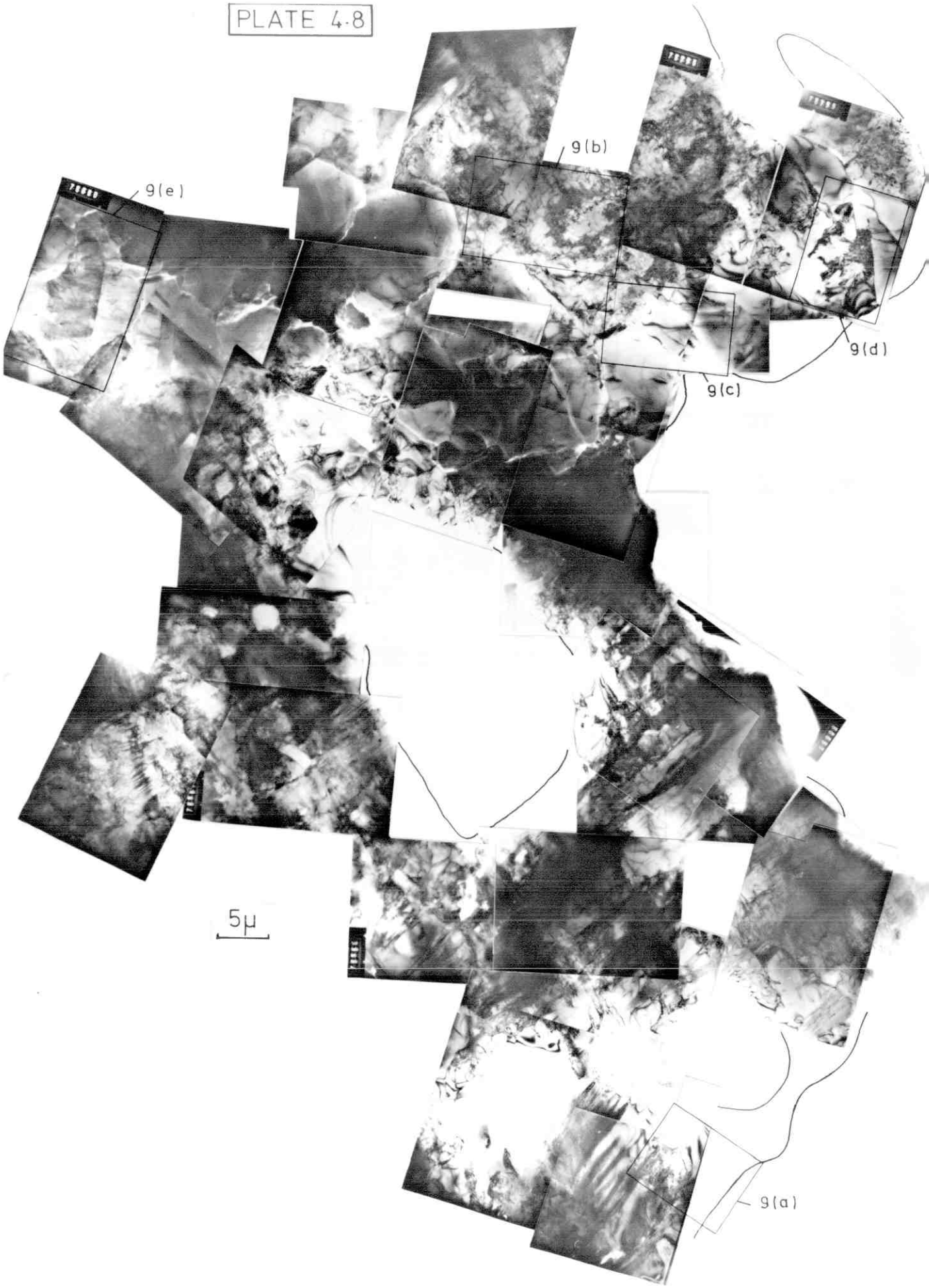

Na
strain-free
new grains
K
Na
K
Na
K
Na
incoherent interface
with dislocation network
3μ
new grain with
peristerite lamellae
and simple twin

Plate 4.8 Mosaic of TEM micrographs of recrystallized zone found between two K feldspar grains. The areas shown in detail in Plate 9 (a-e) are indicated. (see also Fig. 4.3)

PLATE 4·8



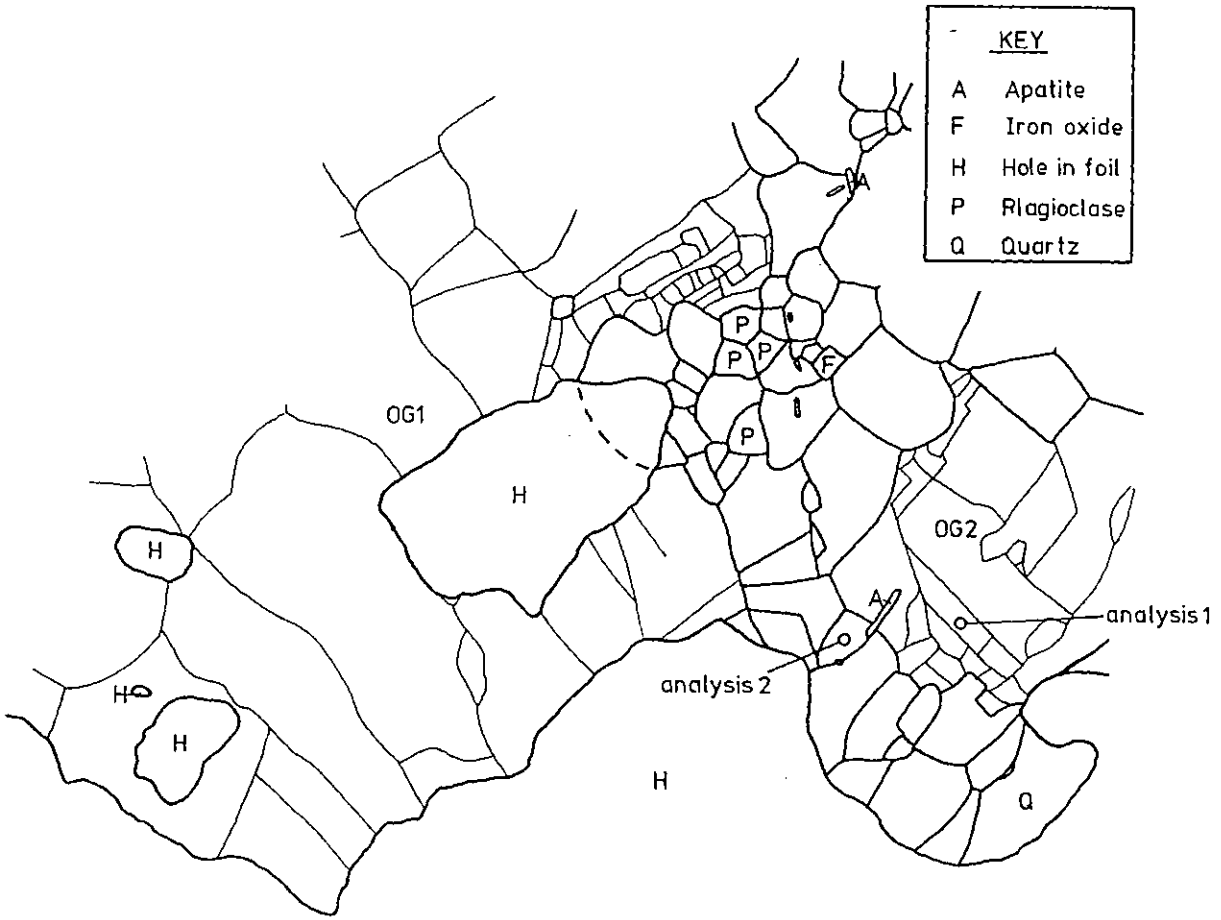


Fig. 4.3 Schematic diagram of mosaic in Plate 4.8, showing areas of STEM analyses

only other type of lamellar intergrowth possible is a perthite which would imply a composition of $Or_{<70}$ whereas the K-feldspar component of the original perthite would be close to Or_{100} following the initial exsolution that gave rise to the albite lenses. The significance of the occurrence of sodic plagioclase in recrystallized alkali feldspars will be discussed later.

A number of recrystallized zones in alkali feldspars were observed, but only one zone was sufficiently well thinned to be studied in detail. Plate 4.8 is a mosaic of an area approx. 100μm x 50μm covering a recrystallized zone between two alkali feldspars, the important details of which are presented in Fig. 4.3. The compositions of the old grains (OG1 and OG2) were determined by STEM microanalysis which gave typical K-feldspar analyses with no detectable Na.

Grain OG1 forms over half of the area covered by the mosaic, and passes from a comparatively undeformed 'core' to the left, through a highly-deformed grain mantle into the recrystallized zone. In the 'core' of the grain the dislocation density is very low ($\rho<10^{11}m^{-2}$) and the sole deformation structures are sub-grain boundaries which appear as somewhat irregular low-angle misorientation dislocation walls, e.g. Plate 4.9 (a). Twins are locally developed, as at the left end of OG1 where a domain of albite twins is part-bonded by a sub-grain boundary. Most of the rest of the 'core' has a strong modulation developed in one direction, trace parallel to the trace of (010), and sometimes in two, the other trace being parallel to the trace of (001). The modulations are often strongly developed in irregular bands approximately parallel to the trace of 010 that terminate at sub-grain boundaries. No modulations are found in areas with twins and vice versa.

Plate 4.9 TEM of areas within Plate 4.8

(a) Area within OG1 showing low dislocation density and a sub-grain boundary (arrowed). The many inclusions are probably apatite. Scale bar = 1μm.

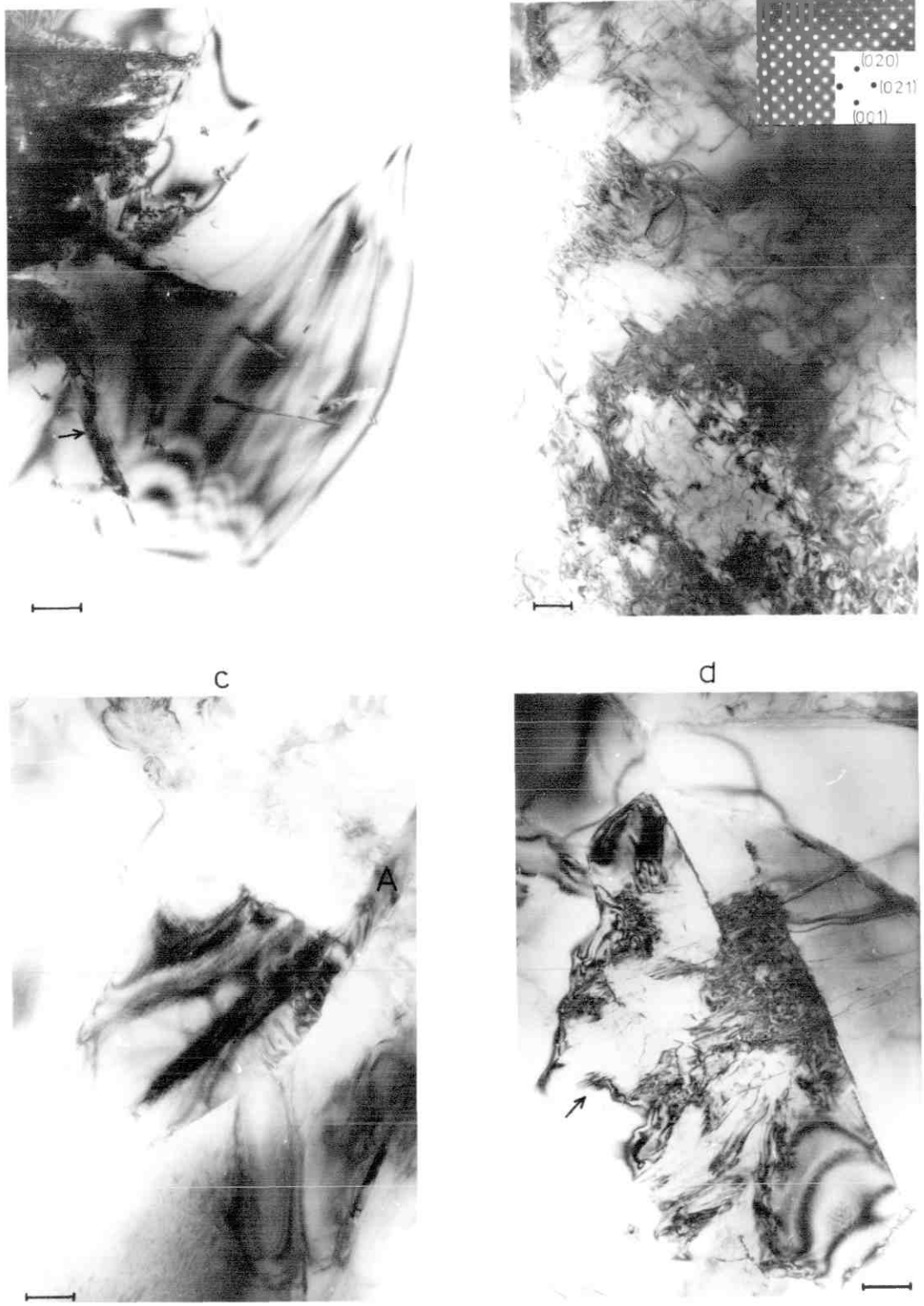
(b) Area within OG2 showing high dislocation density, with dislocations developed in two approximately orthogonal directions. Scale bar = 1μm.

(c) New strain-free K feldspar grain showing cross-hatched modulation . Apatite grain is indicated (A). Scale bar = 1μm.

(d) New, deformed, K feldspar grain showing dislocations, sub-grain boundaries, a modulation in one direction and locally twins (arrowed). Scale bar = 1μm.

(e) New K feldspar grain with many inclusions (presumed apatite), a simple twin (arrowed), and a well-developed modulation. Scale bar = 1μm.

PLATE 4.9



In the mantle of OG1, above the hole, there is an area with many albite twins, upon which is superimposed a cellular structure of sub-areas of slightly differing orientation. The exact nature of these cells is not known, the specimen thickness was too great to image them clearly, their boundaries are however roughly parallel and perpendicular to the twin traces. The other part of the mantle of OG1, below the large hole, is too thick to see any structures except at the very edge of the hole. Here it is possible to see only that the dislocation density is high, and that both domains of albite twins and modulations are present.

The other old grain, OG2, has neither twins nor modulations but has a high dislocation density ($\rho \sim 10^{12}m^{-2}$) throughout (Plate 4.9 (b)). Dislocations are generally straight and in two roughly orthogonal directions and trace analysis has shown one set to be near [010]. A sub-grain structure is quite well-developed, with sub-grain walls lying close to (010) and (001); the spacing of these walls is very variable but an overall decrease in size is apparent as the recrystallized zone is approached.

Both of the old grains contain small, elongate, prismatic inclusions, although they are more numerous in OG1 than OG2, showing no apparent preferred orientation. STEM analysis has shown two of the larger inclusions to be apatite, and it is inferred that most, if not all, of the inclusions are apatite. Similar occurrences of fine apatite inclusions have been described for both alkali and plagioclase feldspars, Smith and Stenstrom (1965), Vernon (1975).

Between the old grains there is a zone of small feldspar grains which are commonly strain free. Certain characteristics; thinning rate, damage rate, inclusions, or style of exsolution or modulation, suggested that two types of feldspar were present in the zone. STEM analysis showed that although the majority of these new grains were K-feldspar with compositions close to those of the old grains (Table 4.5 for analysis), a few grains

TABLE 4.5

Analysis	1	2
	Old Grain (2)	New Grain
Na_2O	0.18 *	0.58 *
MgO	0.62 *	1.12 *
Al_2O_3	20.32	20.58
SiO_2	62.91	61.97
K_2O	15.62	15.07
CaO	0.00 *	0.00 *
TiO_2	0.00 *	0.13 *
MnO_2	0.09 *	0.00 *
FeO	0.26 *	0.55 *
Total	100.00	100.00

N.B. Last element by stoichiometry, total normalized to 100.00

* Concentrations within errors of detection.

Table 4.5 Analysis of alkali feldspars by STEM

had albite compositions. Also included in this zone is a grain of iron oxide (from STEM analysis).

The new grains of K-feldspar typically show a modulated structure in two directions as described for Adularia (McConnell, 1971)(Plate 4.9 (c)), apparently on planes close to (010) and (001). Most of these grains are completely strain free but locally high dislocation densities are attained with development of dislocation networks and Albite or Pericline twin domains at the expense of modulations (Plate 4.9 (d)). Some of the new grains show simple twinning (e.g. Plate 4.9 (e)); in the same grain many apatite inclusions are visible, a feature characteristic of the new K-feldspar grains. Most of the new grains in contact with OG2 have boundaries that bulge into the old grain, suggesting either 'classic' nucleation and growth, or SIBM as described by Vidal et al. (1980). It is impossible in this case to determine the operative mechanism, however, in the grain mantle of OG1 there is a solitary strain free grain some way behind the recrystallization front that indicates nucleation.

In one small area of the recrystallized zone a group of albite grains (marked P on Fig. 4.3) have been identified. Two of these grains were analysed by STEM and gave albite analyses containing no significant K or Ca. Other features that are considered diagnostic include; relatively fast thinning and damage rates (when compared with K-feldspar), a lack of inclusions and a modulated microstructure (considered to be peristerite exsolution lamellae) which is only developed in one direction, and commonly only in patches.

4.2.1.4 Discussion

It is clear from the above observations that one effect of the deformation on these alkali feldspars may be to provide examples from various stages in the ordering and exsolution of the original feldspar.

Particularly, through recrystallization, it allows the observation of these phenomena in feldspars of similar composition but with differing thermal histories. Essentially the deformation may allow transformation to go ahead that would be otherwise kinetically impossible, through the enhancement of diffusion of Al/Si during the passage of dislocation through the feldspar lattice (Yund and Tullis, 1980).

We may now consider the microstructural development of an originally homogeneous alkali feldspar with respect to exsolution, ordering and deformation.

(i) crystallization from melt of a homogeneous monoclinic alkali feldspar.

(ii) nucleation of lenses of albite, initially in the monoclinic state.

(iii) growth of albite lenses, monoclinic state maintained by coherency strains; ordering begins in alkali feldspar.

(iv) structural collapse of albite to triclinic state, with accompanying albite twinning followed by loss of coherency with formation of dislocation wall at interfaces. N.B. For continuing exsolution the coherent solvus no longer applies, leading to compositions correspondingly closer to the end-members (Yund, 1975).

(v) cross-hatched modulation in K-feldspar due to local ordering.

(vi) deformation; K-feldspar by dislocation glide, little recovery, causing local strain enhanced diffusion giving rise eventually to heterogeneous transformation from cross-hatched modulation, through one modulation becoming dominant to development of albite or pericline twin domains.

(vii) continuing deformation: new homogeneous strain-free grains appear by nucleation in highly deformed regions (e.g. grain mantles). Albite grains formed as above or due to neocrystallization.

(viii) new K-feldspar grains start to order, locally this is enhanced as they become deformed, new albite grains and some albite lenses in the perthites start to exsolve, giving rise to peristerite lamellae.

(ix) post-deformation: ordering in K-feldspar continues but increasingly slowly as temperatures fall until effectively it stops; from (v) until this point the old grains continue the transformation as in (vi). In most grains this leads to M-twinning but in some areas where strain enhancement has been important one type becomes dominant. N.B. It should be emphasised that it is not possible to determine the exact relative timing of the deformation and the various stages of this transformation.

Exsolution by nucleation of albite lamellae in the perthite is deduced from the lack of consistent spacing in the observed sodic lenses, which would have been expected from a coarsening spinodal. The terminal growth of these lenses is inferred from observations of lenses apparently growing into one another, as in Plate 4.7, which would also be difficult to explain in terms of a coarsened spinodal.

The effect of strain on the degree of transformation of initially fully disordered K-feldspar to fully ordered microcline is deduced from the observation of localized regions of transformation, particularly in old-grain mantles. Also, deformed new K-feldspar commonly have better developed order-modulation structures than new strain-free grains and rarely twins. The predominance of one law of twinning in a region as opposed to the more normal cross-hatched microcline twinning is also attributed to the effects of strain.

The origin of the new albite grains in the zone in Plate 4.8 is problematical as they cannot have directly recrystallized from a K-feldspar with a negligible Na component. Two possible solutions are:-

(i) The grains represent the recrystallized counterpart of an original albite lens forming a perthitic intergrowth with OG1.

(ii) The grains have simply grown within the recrystallized zone as a new metamorphic mineral.

The evidence is equivocal; no lenses of albite have been observed in either of the old grains, and although some support is given to (ii) by the lack of inclusions this does not explain why all the albite is found at one place in the zone. However, for the peristerite albite in Plate 4.7 the former explanation seems the most likely as albite is clearly present in the old grain, and the new grain contains the same inclusions as the 'parent' feldspar.

A small percentage (~15%) of the new grains, both K-feldspar and albite, show simple twinning. These twins are broad, often found near triple junctions, and do not terminate within the grains. These features are normally considered characteristic of growth twins (see Section 4.2.2.1.1). Further evidence for a growth origin is that new grains must recrystallize in a high (monoclinic) structural state, and there will not be sufficient time for ordering to generate the triclinic state necessary for deformation twinning. It is, therefore, suggested that the observed twins are due to grain growth (as for albite, Marshall and Wilson (1976)).

4.2.2 Albite-Oligoclase

Na-rich plagioclase feldspars form a significant constituent of all the pegmatites, quartz-diorites and microgranites sampled. From optical determinations (using extinction of albite twins in section $\perp x$) the compositions are seen to range from An_{30-40} in some of the quartz-diorite

to An_{5-10} in some of the pegmatites. In addition to primary igneous grains, sodic plagioclase feldspar is found as a component of perthites and myrmekites in association with alkali feldspar.

4.2.2.1 Literature Review, Plagioclase Microstructures

Plagioclase microstructures were studied initially optically, then with x-rays and laterally through electron optical techniques. The microstructures may be divided into those due to deformation and those due to ordering and exsolution.

4.2.2.1.1 Strain Features

In the earlier studies of the plagioclase feldspars, plastic deformation was thought mainly to be restricted to deformation twinning (e.g. Harker, 1895) as most other textures were interpreted as due to brittle processes. However, with the use of electron microscopy many of these 'cataclastic' textures have been re-interpreted as the results of crystal plastic processes.

Undulatory extinction is common in plagioclase feldspars in moderately to strongly deformed rocks; the bulk strain required seems to be much higher than that which produces the same effect in quartz. Deformation lamellae are uncommon in naturally deformed plagioclases except for grains subject to high strain-rate deformation such as meteorite impact (see Smith, 1974, Vol. 1., section 12.5.3).

Sub-grains have not commonly been described in plagioclase feldspars. However, Lorimer et al.(1973) and Marshall and Wilson (1976) report the development of distinct sub-grains in an albite/oligoclase deformed under upper greenschist conditions, White (1974) has observed subgrains in andesines and labradorites deformed under upper amphibolite conditions, and Vernon (1975) describes sub-grains in an andesine (An_{40}) deformed under granulite facies conditions.

In the same study Vernon has described deformation bands developed parallel to (001) with relatively small misorientations and irregular to smooth boundaries. Somewhat different features, also termed deformation bands, have been reported by Seifert (1965) for an albite (An_7)(deformation condition unknown). The morphology of these bands is similar to features termed kink-bands in other minerals, e.g. micas and pyroxenes, but Seifert argues against the use of this as he finds no well-defined axis of internal rotation. White (1975) has described similar deformation bands developed in an oligoclase/andesine (An_{29-32}).

The only known deformation twins occur on the albite and pericline laws, and these have been produced experimentally in all triclinic plagioclase structures except low albite (Borg and Heard, 1969). The nature of the Al-Si ordering in low albite makes mechanical twinning impossible, and this effect may extend up to An_{16-17} in the peristerite sodic oligoclases due to the presence of discrete lamellae of An_{0-2} (Starkey, 1967; Marshall and Wilson, 1976). However if the deformation occurs after the inversion to triclinic but before the inversion to low albite (i.e. in high albite), deformation twins may still be present.

The recognition of deformation twins (as opposed to growth twins) is at best an uncertain process, but certain diagnostic features have been suggested (see also Vance, 1961; Vernon, 1965)

(i) narrow, long, needle-shaped with sharp terminations within grains at dislocation as opposed to broader, less continuous growth with blunt terminations (White, 1975).

(ii) very planar twin boundaries lying exactly along twin planes, as opposed to stepped boundaries in growth twins (Nicolas and Poirier, 1976).

Most of the information on slip planes and burgers vectors have come from experimentally deformed material. Borg and Heard (1969, 1970)

observed slip on (010) from kink-band geometry in single crystals of albite and oligoclase peristerite (An_{13}) deformed under conditions 800°C, $\dot{\varepsilon} = 2.10^{-5}s^{-1}$ and 10kb confining pressure, in an orientation such that twinning was suppressed. From the observation of deformation bands Seifert (1965) inferred (010) slip in naturally deformed albite.

Marshall and McLaren (1977(a),(b)) studied by TEM the experimentally deformed specimens of Borg and Heard plus three samples from an andesine /labradorite (An_{50}) one deformed by Borg and Heard at the conditions mentioned above, and two by Christie and Williame at 800°C, $\dot{\varepsilon} = 10^{-5}s^{-1}$, and 15kb confining pressure. The orientation of slip planes was inferred from the observation of slip plane faults and other planar faults associated with dislocations. Table 4.6 shows a list of slip-planes and suggested burgers vectors from the above study. White (1975) has suggested slip along (010),(100) and (001) from the observation of dislocation loops in an oligoclase/andesine.

4.2.2.1.2 Recrystallization

In many of the early studies of deformed feldspars, relatively fine grains were observed to be developed at grain boundaries and along deformation bands and this 'mortar' texture was put down to cataclasis followed by annealing. However, comparison with textures developed in plastically deformed ceramics and metals led some workers, e.g. Spry (1969), Kehlenbeck (1972) to reinterpret some of these mortar textures as the results of recrystallization, particularly for rocks deformed under granulite facies conditions. TEM studies (White (1975), Marshall and Wilson (1976)) extended the identification of recrystallized feldspars into low amphibolite and upper greenschist conditions, while Allison et al. (1979) describe recrystallized oligoclase (An_{18-25}) from a granite thought to have been deformed under zeolite to phrenite pumpellyite facies conditions (i.e. temperature $\sim$ 2-300°C). This last observation

TABLE 4.6

COMPOSITION	SLIP PLANE	BURGERS VECTOR
An_1	$(10\bar{1})$	$\frac{1}{2}[111]$
An_{38}	$(\bar{1}30) - (\bar{1}20)$	$\frac{1}{2}[001]$
An_{50}	$(10\bar{1})$	$\frac{1}{2}[111]$ $\frac{1}{2}[1\bar{1}\bar{1}]$
An_{77}	$(11\bar{2})$	$\frac{1}{2}[201]$
	$(13\bar{2})$	$\frac{1}{2}[201]$ $\frac{1}{2}[\bar{1}11]$
	(010)	$\frac{1}{2}[201]$ $[100]$
	$(10\bar{1})$	$[101]$ $\frac{1}{2}[111]$ $\frac{1}{2}[1\bar{1}1]$

Table 4.6 Slip planes and burgers vectors observed in experimentally deformed plagioclases (Marshall and McLaren, 1977(a)).

runs counter to that of Voll (1976) who uses a feldspar recrystallization isograd at 450°C below which no feldspar recrystallizes.

The actual mechanisms of recrystallization have only been discussed in a few cases, possibly due to the very fine new grain size commonly found in lower grade rocks which, therefore, require TEM to study them in detail. Table 4.7 shows observed chemical changes with recrystallization from various published and unpublished studies; these changes may be of great importance by providing an additional driving force for recrystallization.

White (1975) identified classic nucleation as the mechanism responsible for the formation of strain-free grains in an oligoclase/andesine A small but consistent change in composition towards a more sodic plagioclase was observed. Vernon (1975) observed a similar change in chemistry for an andesine but suggested an SGR mechanism to account for the spread of new grain orientations away from that of the present grain. Vernon (op. cit.) suggested that recrystallization is helped by the release of chemical free energy, while White (1975) has proposed that deformation helps the chemical change. These two mechanisms are of course not mutually exclusive but will work co-operatively.

In the optical study of Allison et al. (1979) Kerrich et al. (1980) an unusual change in chemistry has been observed. The old oligoclase grains recrystallize to both an oligoclase similar to the 'parent' composition and an albite.

In two related studies Marshall et al. (1976) and Marshall & Wilson (1976) observed recrystallization in experimentally and naturally deformed albites. In the experimentally deformed material, isolated new grains are developed in highly strained regions, and have random orientation, all features characteristic of a classic nucleation mechanism. In the

TABLE 4.7

Old Grain	New Grain	Metamorphic Conditions	Study
An_{29-32}	An_{20-27}	Low amphibolite	White, 1975
An_{40}	$An_{\sim 35}$	Granulite	Vernon, 1975
An_{7-10}	An_{2-10}	Upper greenschist	Marshall and Wilson, 1976
An_{18-25}	An_{5-9} + An_{15-23}	Zeolite - prehnite pumpellyite	Allison et al., 1979
An_{51-63}	An_{70-80}	Amphibolite	Brodie, 1981
$An_{<54}$ $An_{>54}$	An_{46} An_{63}	Amphibolite	Leach et al., 1982.
An_{17-23}	An_{17-21}	Mid-greenschist	This study

Table 4.7 Chemical changes with recrystallization of plagioclase feldspar.

naturally deformed albite recrystallization occurs by an SGR mechanism, as shown by the preferred orientation of the new grains; no significant change in chemistry is reported.

Kehlenbeck (1972) shows micrographs of 'protoclastic' anorthosite with strongly serrated grain boundaries passing gradually into anorthosite with mortar textures. However, in the light of more recent studies, these textures are more consistent with an SIBM mode of recrystallization.

4.2.2.1.3 Peristerites

Plagioclase feldspars in the compositional An_2-An_{16} (Smith, 1974 II) commonly have a substructure consisting of alternating lamellae of two distinct plagioclases with compositions roughly corresponding to An_0 and An_{25}. This peristerite structure is responsible for the Schiller iridescence observed for some of these feldspars in reflected light.

Many optical studies, e.g. Bøggild (1924), Brown (1960), Fleet and Ribbe (1965) have shown the plane of irridescence to be close to $(0\bar{4}1)$[1] although $(12\bar{1}4)$was also found. TEM studies have confirmed that lamellae lie between $02\bar{1}$ and $04\bar{1}$ with the variation towards $(12\bar{1}4)$ caused by a relatively high Or component, Olsen (1974). Olsen op.cit. has also observed a second set of lamellae near $\bar{7}14$. These orientations are all in good agreement with considerations of strain energy associated with interfaces by Williame and Brown (1972) who predicted two strain energy minima near $04\bar{1}$ and $3\bar{1}2$.

Korekawa et al. (1970) found a microstructure modulated in two directions in a peristerite from Sultan Hamid and Putnis and McConnell (1980) consider this to represent the early stages of exsolution prior

[1] Indexed using a 1.4nm cell in accordance with modern convention

to significant coarsening. With time either the $(04\bar{1})$ modulation is the only one to coarsen, Olsen (1974), or on coarsening $(04\bar{1})$ is the more stable orientation (Putnis and McConnell, 1980). Either way the $(04\bar{1})$ modulation coarsens, forming lamellae, possibly leading eventually to loss of coherency.

Only one study (Marshall and Wilson, 1976) has linked the formation of peristerite to deformation processes. In the albite studied no peristerites are present in the old grain, and only in the larger new grains are they well developed, the smaller grains having only patches of lamellae. The lamellae are very regular and range in spacing from 30 to 40nm. The peristerite intergrowth is only found in new grains with no dislocation and Marshall and Wilson (op.cit.) suggest that the lamellae form during the migration of high-angle boundaries due to the enhancement of diffusion along the interface.

4.2.2.2 Optical Microscopy

Optical deformation features appear to depend on the original form of the feldspar as well as its composition. Four sets of thin sections were studied in detail, two of which, both microgranites (PDM 01-03, CSE 01-03) were then looked at by TEM. The essential features of the other two sets, both from tourmaline-bearing pegmatite (RDS01-03, CSC 01-03) are very similar and they will be considered together. Sodic plagioclases were observed in other thin sections but were found to be very similar to one of the three types described below.

The samples will be considered in order of increasing shear strain. Each set consists of three samples, least deformed, partly deformed (at a shear strain of $\gamma \sim 1.5$) and mylonite (for localities see Chapter 3).

A range of grains in each sample were analysed by electron microprobe from polished thin sections taken adjacent to those used for the optical and TEM work. The analyses were taken as accurate to $\pm An_2$ as

Plate 4.10 Optical micrographs of plagioclase feldspar sample series (PDM 01-03, CSE 01-03), all crossed polars.

(a) Typical albite twinned oligoclase in the least deformed microgranite (PDM 01). Scale bar = 100μm.

(b) Rather altered grain mantle in oligoclase, with some recrystallization ; a new twinned grain is arrowed. (Sample PDM 03) Scale bar = 100μm.

(c) Sub-grain network developed in an oliglclase (outlined) from the partly deformed microgranite, CSE 01. Scale bar = 50μm.

(d) Area of oligoclase grains all with small misorientations relative to one another consistent with having recrystallized by the progressive misorientation of sub-grain boundaries. (sample CSE 01). Scale bar = 100μm.

(e) Recrystallization of oligoclase at grain boundaries. (Sample CSE 02). Scale bar = 100μm.

(f) Microgranite mylonite (Sample CSE 02) with ribbons of recrystallized quartz , and bands of fine-grained mica, and recrystallized feldspar, with a few mica and feldspar porphyroclasts. Scale bar = 100μm.

PLATE 4·10

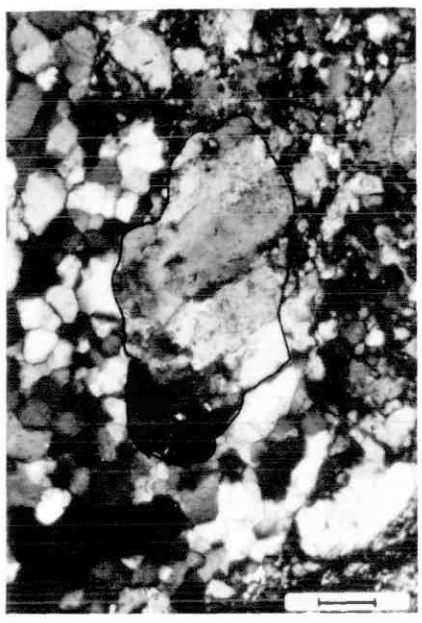
a



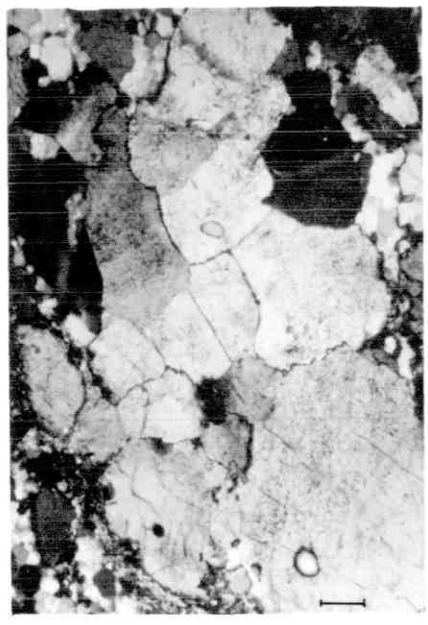
b



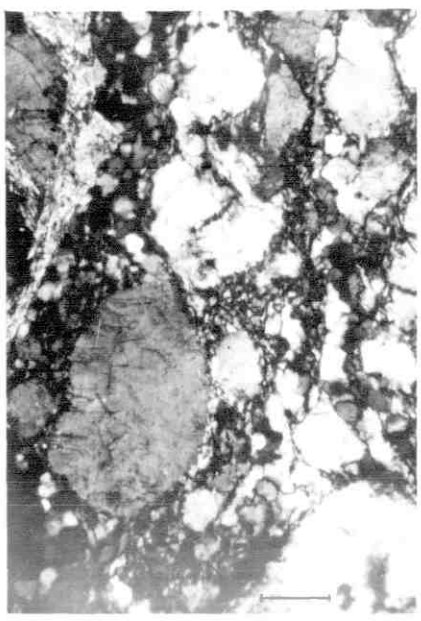
c



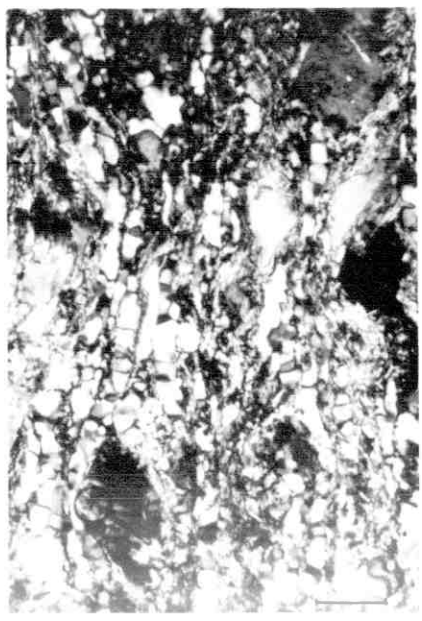
d



e



f



totals and stoichiometry were quite good (see Table 4.8 for examples of analyses). The plagioclase old grains in the series PDM 01-03 fall within the range An_{13-19}, no new grain analyses were possible due to alteration in recrystallized areas. All old and new grains in the series CSE 01-03 fall within the range An_{18-23}.

4.2.2.2.1 Sample series PDM 01-03

In the least deformed microgranite, sample PDM 01, the oligoclase feldspars show no strain features other than slight undulatory extinction. The grains are commonly twinned on the albite law (Plate 4.10(a)), but completely untwinned grains have been observed. The association of plagioclase with alkali feldspar has already been mentioned (section 4.2.1.2) and will not be discussed here. Alteration in these feldspars is variable, but is commonly confined to minor sericitization.

In the protomylonite (PDM 02) the only strain features visible are undulatory extinction with poorly-developed sub-grains in some grain mantles. In the mylonite (PDM 03) many grains appear to be no more deformed than in earlier stages although twinning is often more intense. However, a few grains show recrystallization at grain boundaries (Plate 4.10(b)) and rarely along 'deformation bands', planar zones of high strain. The new grains are too small (10μm) to be measured accurately in standard optical thin sections, some of these new grains are seen to be twinned, possibly as result of secondary grain growth. The volume of recrystallized feldspar in the mylonite is no greater than 5-10%.

TABLE 4.8

Sample	PDM01	PDM02	PDM03	CSE03	CSE01 (old grain)	CSE01 (new grain)	CSE02 (old grain) centre	CSE02 (old grai edge
Na_2O	9.74	9.26	9.66	9.10	8.78	8.95	8.80	9.21
MgO	0.02	0.16	0.15	0.14	0.03	0.00	-	-
Al_2O_3	21.93	22.34	21.65	22.70	23.08	22.80	22.96	22.97
SiO_2	63.98	63.52	63.85	63.08	62.66	62.75	62.94	64.46
K_2O	0.12	0.11	0.00	0.18	0.18	0.15	0.21	0.11
CaO	3.31	3.80	3.25	4.37	4.73	4.60	4.47	4.17
TiO_2	0.00	0.00	0.02	0.00	0.00	0.03	-	-
Cr_2O_3	0.00	0.04	0.00	0.02	0.08	0.00	-	-
MnO_2	0.00	0.00	0.00	0.85	0.00	0.08	-	-
FeO	0.00	0.02	0.17	0.00	0.02	0.00	0.20	0.01
NiO	0.09	0.00	0.00	0.06	0.00	0.00	-	-
Total	99.17	99.23	98.75	99.73	99.55	99.35	99.57	100.92
Ab	83.6	81.0	84.4	78.2	76.3	77.1	76.6	79.5
An	15.7	18.4	15.6	20.8	22.7	22.1	22.1	19.9
Or	0.7	0.6	0.0	1.0	1.0	0.8	1.3	0.6

Table 4.8 Electron microprobe analyses of plagioclase feldspars

Plate 4.11 Optical micrographs of plagioclase feldspar from the sample series (CSE 01-03, RDS 01-03, CSC 01-03). (all crossed polars)

(a) Crack with alteration (arrowed) in oligoclase. (Sample CSE 01) Scale bar = 100μm.

(b) Sericitization in an oligoclase from the CSE 01-03 series. The alteration is particularly intense along fractures and in the grain mantle. SCale bar = 100μm.

(c) Deformation by kinking in a strongly twinned plagiocase grain from RDS 02, a partly deformed tourmaline bearing pegmatite. SCale bar = 100μm.

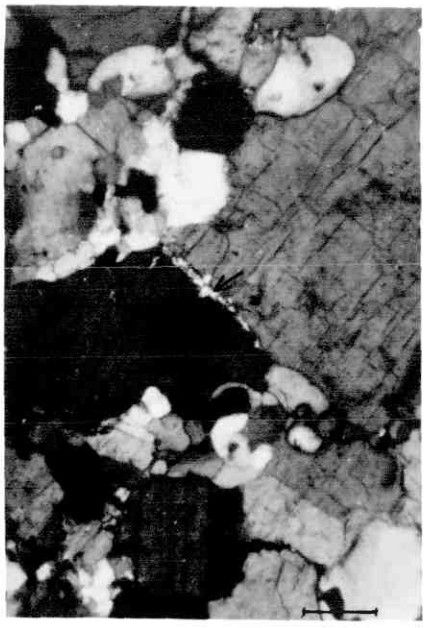
(d) New grain (arrowed) developed from kink-band in an albite from RDS 02. SCale bar = 50μm.

(e) Deformation twins formed in a plagioclase grain mantle. (Sample csc 03, pegmatite mylonite). Scale bar = 25μm.

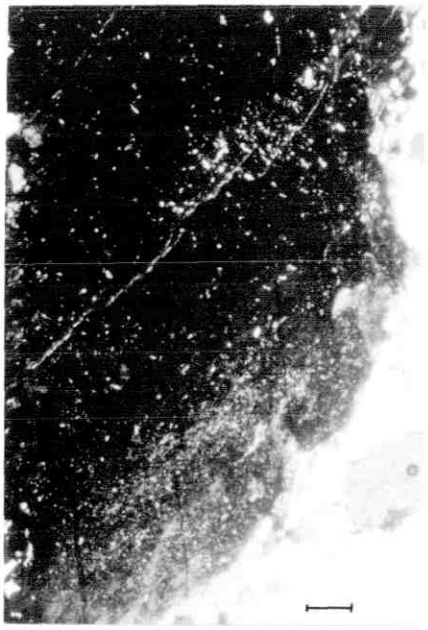
(f) Strongly sericitized plagioclase in CSC 03. Scale bar = 100μm.

PLATE 4.11

a



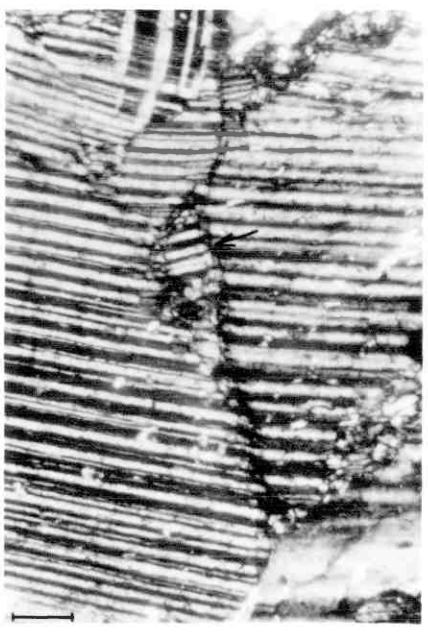
b



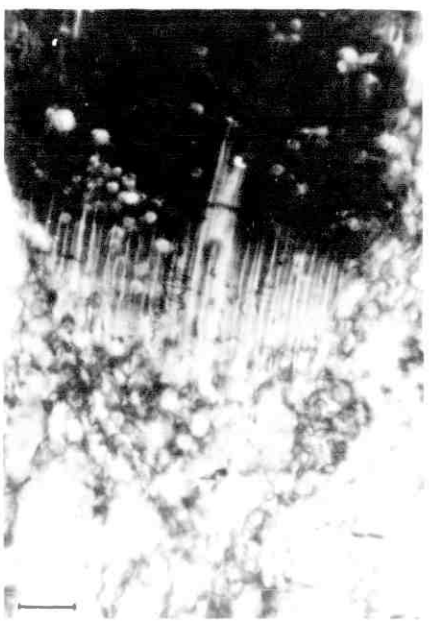
c



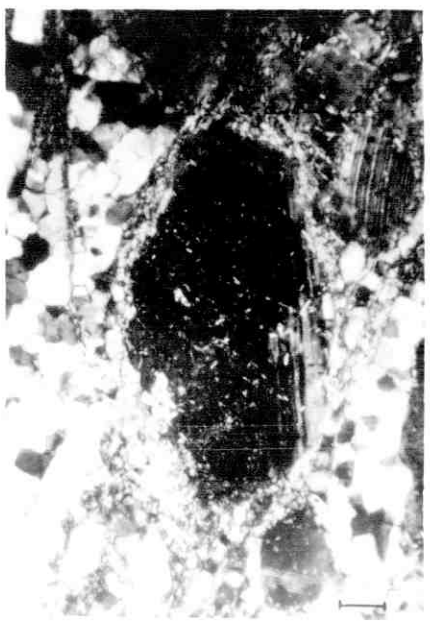
d



e



f



4.2.2.2.2 Sample series CSE 01-03

The oligoclases in this microgranite start with no deformation features at all and are commonly twinned. In the protomylonite the feldspar shows undulatory extinction with the development of sub-grains often throughout the whole grain (Plate 4.10(c)). With slightly increased strain these sub-grains become misorientated sufficiently to give rise to aggregates of smaller grain (Plate 4.10(d)) ($d_{RG} \sim 250\mu m$) by an SGR recrystallization mechanism. Minor recrystallization at grain boundaries producing fine new grain ($d_{RG} \sim 5\mu m$) is already evident at this stage.

With increasing deformation the newly formed grains start to recrystallize at their grain boundaries (Plate 4.10(e)), they are also affected by further SGR recrystallization. In the mylonite the end product of these two types of recrystallization is small remnants ($\sim 50\mu m$) of the by now highly-strained parent grains set in a matrix of very fine new grains drawn out into the foliation. (Plate 4.10(f)). The feldspar at this stage is approximately 50% recrystallized to the fine grains. Even at the highest strains the feldspar commonly remains untwinned although locally both albite and pericline twins are present.

Along with the ductile deformation there is a minor amount of brittle fracturing (Plate 4.11(a)). Displacements on these fractures are small, and only rarely are they open, with quartz infilling. Sericitization of these feldspars is moderate, but locally becomes intense (Plate 4.11(b)).

4.2.2.2.3 Sample Series RDS 01-03/CSC 01-03

In these pegmatites the only feldspars found are albite /oligoclases commonly showing very well developed albite twinning with subsidiary pericline twinning, although some grains are completely untwinned (90% of grain in RDS are twinned, 40% in CSC). In both sets of samples the least deformed material shows well developed strain features. The untwinned grains are deformed in a similar way to the oligoclases in the CSE series, that is with initial grain size reduction by SGR recrystallization. The twinned grains are strongly kinked, commonly with high angle grain boundaries, or possibly in some cases fractures formed along the kink band boundaries (KBBs) (Plate 4.11(c)), giving rise locally to new grains. The new grains formed by progressive misorientation are commonly prismatic in the twinned grains, and polygonal in the untwinned grains.

Even at this early stage of the deformation minor recrystallization is occurring along original grain boundaries, newly developed grain boundaries (through SGR), and KBBs giving rise to fine-grained (<10μm) feldspar. In some cases the recrystallization mechanism is clear. In Plate 4.11(d) a KBB has developed into a recrystallized zone, in which slightly misorientated sub-grains at the edge of the zone become highly misorientated new grains at the centre, indicating that an SGR mechanism was responsible, although on a much smaller scale than previously described. In most cases, however, the mechanism could not be identified optically.

In the mylonites at least 60% of the original feldspar grains have been recrystallized to an aggregate of fine new grains.

Locally grains that are otherwise untwinned are seen to develop deformation twins (Plate 4.11(e)) which would indicate that the albites

were not in their lowest structural state. Evidence for a deformation origin is that the twins are sharp, terminate within the grain, and only occur in the most strained part of the grain. At the very edge of the grain, sub-grains are formed and the twins become indistinct. Observations using a sensitive tint plate suggest that the new grains directly adjacent to the old grains have similar orientation to it, but that this misorientation increases with distance into the recrystallized zone; again this suggests an SGR mechanism.

Brittle fractures are again common but are not responsible for the grain size reduction, except in those cases where KBB appear to have developed into fractures and movement on these has given rise to the observed misorientation. The feldspars are all moderately sericitized, but locally this effect becomes intense, as shown in Plate 4.11(f). In this band in the mylonite, originally containing a single large muscovite grain, and now a mass of fine white mica, all the feldspars show intense sericitization, especially along KBBs and fractures.

4.2.2.3 TEM Observations

The paucity of plagioclase feldspar in PDM 01, 02 means that only a rather incomplete picture of the deformation is possible from these samples. They will, however, be described separately as there are important differences between these feldspars and those observed in samples CSE 01-03.

4.2.2.3.1 Deformation features, Sample Series PDM 01-03

In the least deformed microgranite (PDM 01), plagioclase feldspars commonly have low dislocation densities ($\rho \sim 10^{11} m^{-2}$)(Plate 4.12(a)). The dislocations are often straight and occur in parallel sets (Plate 4.12(b)). A few trace analyses were done using standard techniques (e.g. Fig. 4. 4) and these gave directions close to [001] and others close tc [100] In

Plate 4.12 TEM micrographs of deformation microstructures in the sample series PDM 01-03.

(a) Oligoclase from the least deformed microgranite PDM 01 showing low dislocation density, a few twins and a number of cracks (arrowed). Scale bar = 1μm.

(b) Very regular set of dislocations showing oscillatory contrast, with a second set approximately orthogonal. (Sample PDM 01). Scale bar = 1μm.

(c) Oligoclase from PDM 01 showing deformation twins on both albite (A_T) and pericline (P_T) laws. Note also cracks with alteration and corrosion of the feldspar. Scale bar = 1μm.

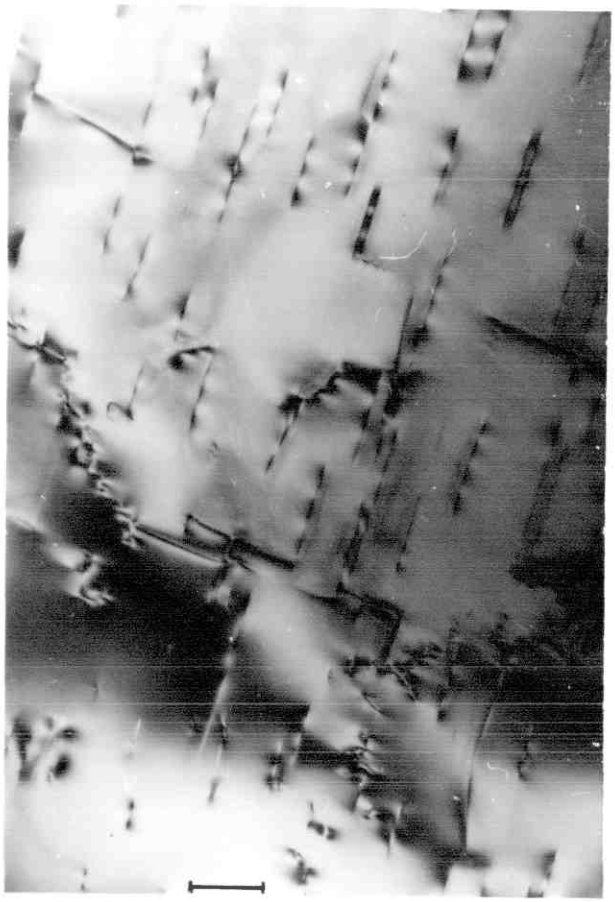
(d) Strain-free new grains formed by classic nucleation, and growth in an oligoclase grain mantle in PDM 02, the partly mylonitized microgranite. Scale bar = 1μm.

PLATE 4·12

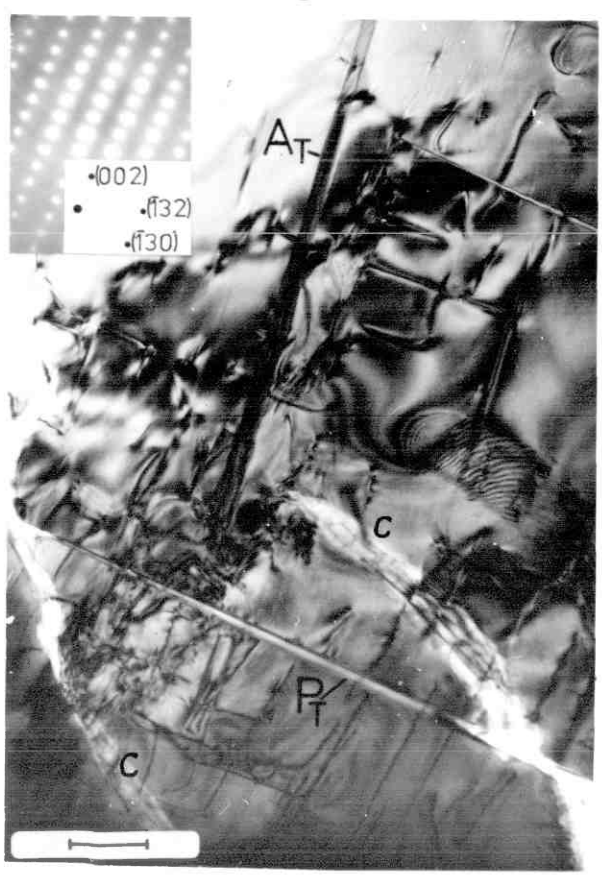
a



b



c



d

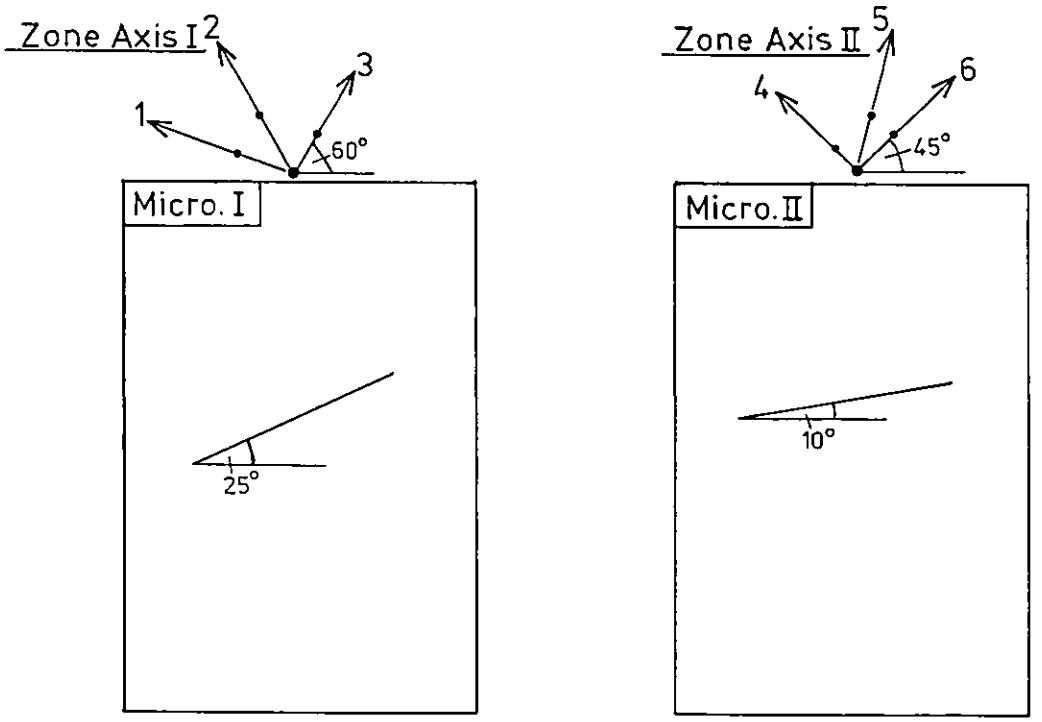


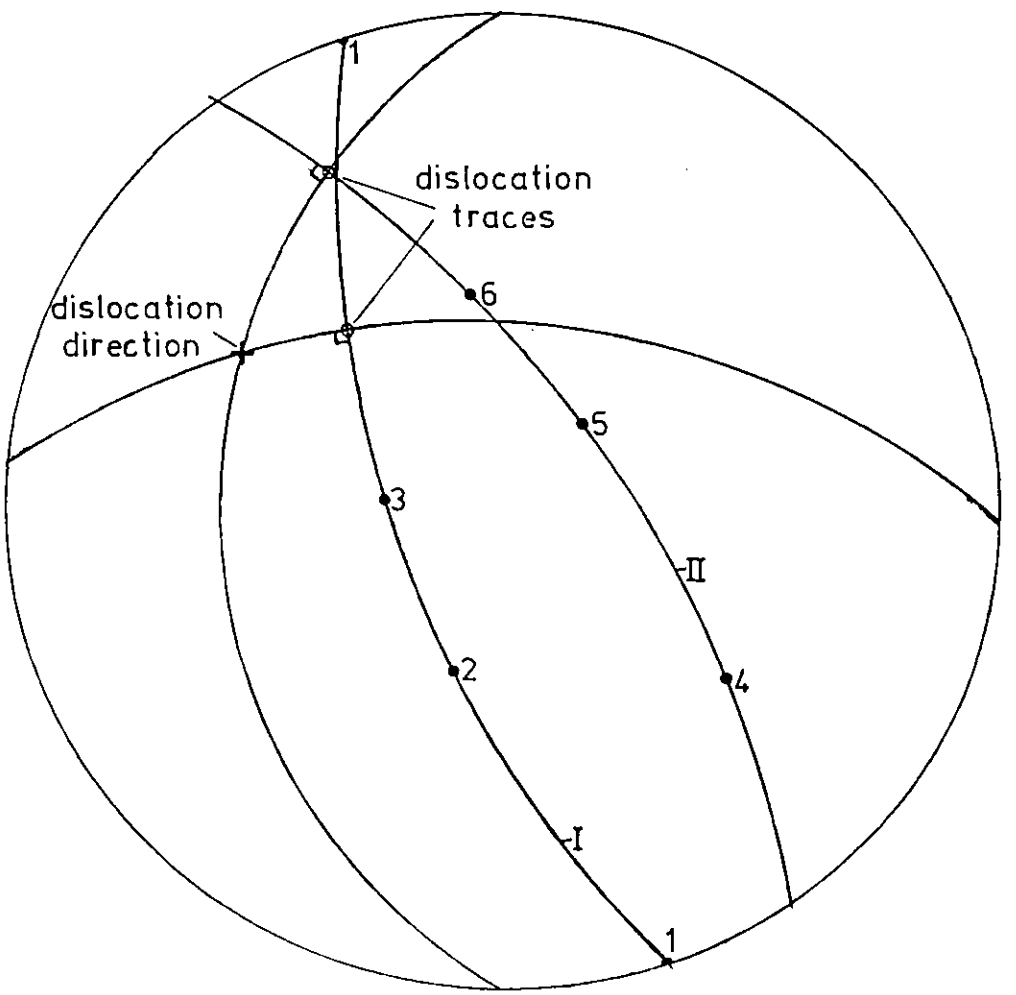
Fig. 4.4 Example of trace analysis for obtaining the direction of dislocation lines using a stereographic projection.

Two micrographs (Micro.1,Micro.2) are obtained of the dislocation at different orientations with accompanying diffraction patterns. The indexed diffraction patterns are orientated correctly with respect to the micrographs. The plane perpendicular to the zone axis is plotted in each case. (that is the plane containing the plane normals to the diffracting planes represented by the spots on the diffraction pattern). The dislocation traces are marked on their respective great circles with respect to the directions of the plane normals.

Great circles are then drawn through the dislocation traces and perpendicular to their respective zone axis great circles. The point of intersection of these great circles is the direction of the dislocation line.

FIG. 4.4


Zone Axis I
2
3
1
60°
Micro. I
25°
Zone Axis II
5
4
6
45°
Micro. II
10°


1
dislocation
traces
dislocation
direction
6
5
3
II
2
4
I
1

some grains a few deformation twins are present (Plate 4.12(c)), identified as such by their sharp terminations, developed on both albite (A_T) and pericline (P_T) laws . In the same micrograph fractures are developed (marked c); one of these fractures appears to have been healed (arrowed).

In PDM 02 (at $\gamma \sim 1.5$) the oligoclases are more strongly deformed. Plate 4.12(d) shows new strain-free grains in an old grain with a moderate dislocation density ($\rho \sim 10^{12} m^{-2}$), the dislocations are tangled, and there is little evidence for recovery; recrystallization is clearly by nucleation.

In the mylonite (PDM 03) the comparative abundance of oligoclase has provided a more complete picture of the deformation process. In this sample almost undeformed grain cores are present with very low dislocation densities (e.g. Plate 4.13(a)). In such areas of low dislocation density it is possible to observe the slip-plane faults associated with individual dislocations (arrowed in Plate 4.13(a));for a possible explanation of their formation in terms of either dilatation or compression due to the passage of a dislocation see Marshall and McLaren (1977(a)).In the more deformed parts of the grains deformation twins and very heterogeneously developed areas of high dislocation density are observed (Plate 4.13(b)), as are cleavage controlled fractures.

In one particular foil taken from the microgranite mylonite, grains suspected of having a more sodic composition were found. The different nature of these grains as compared to the oligoclases is clearly visible in Plate 4.13(c); there are no twins, dislocations are homogeneously distributed, a well-developed sub-grain network is present, and no fractures are observed. These grains are thought to form part of a myrmekitic intergrowth on one of the few K-feldspar grains present in PDM 03.

Plate 4.13(d) shows an area from within Plate 4.13(c) at higher magnification to show the development of very small equant sub-grains bounded by low-angle tilt dislocation walls. The larger sub-grains are

Plate 4.13 TEM micrographs of plagioclase microstructures sample PDM 03

(a) Core of oligoclase grain showing low dislocation density. A number of planar defects associated with dislocations are indicated (arrowed). Scale bar = 2μm.

(b) Oligoclase grain showing very heterogeneously developed areas of high dislocation density and deformation twins. Note also the cleavage controlled fractures and the ubiquitous lamellar peristerite exsolution.Scale bar = 1μm.

(c) Area of albite showing complete lack of twins,and cracks, and the the development of sub-grains. The sub-area marked is shown in more detail in 4.13(d). Scale bar = 1μm.

(d) Small area within grain in 4.13(c) showing small cells (C) bound by dislocation walls. Scale bar = 0.5μm.

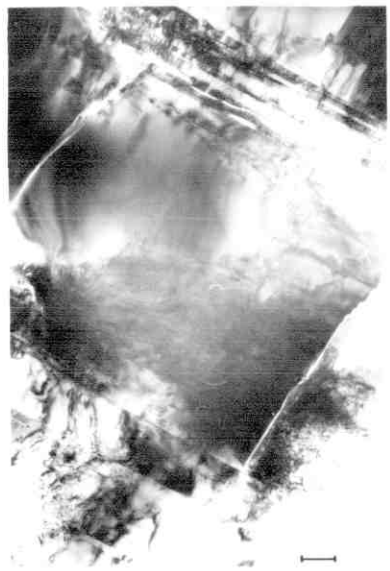
(e) Recrystallized oligoclase grain with dislocations, growth twins and patchy peristerite exsolution. Scale bar = 2.5μm.

PLATE 4.13

a



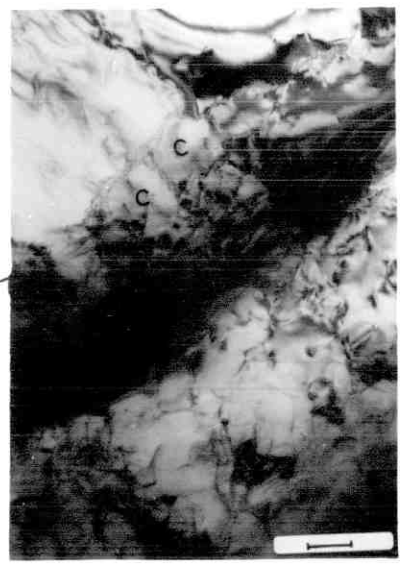
b



c



d



e



elongate and sub-rectangular with walls lying near $(0\bar{1}1)$, $(\bar{1}01)$ and locally $(\bar{1}22)$. The free dislocations are generally curved, but with straight segments common parallel to two directions, one near [100], the other near [010].

Recrystallized plagioclase feldspar grains from this series (grain size $d_{RG} \sim 6\mu m$), vary from completely strain-free, with no twins or dislocations (as in Plate 4.12(d)), to grains showing moderate dislocation densities with multiple twinning (Plate 4.13(e)). The twins in the new grains commonly occur near triple junctions, and are interpreted as being due to grain growth.

4.2.2.3.2 Deformation features, sample series CSE 01-03

In CSE 03, the least deformed microgranite, the microstructures developed in the plagioclase feldspars are rather varied and moderate dislocation densities are common (e.g. Plate 4.15(a)). The dislocations are commonly found on two or more sets; some dislocation lines parallel to [010] have been deduced.

In the partly mylonitized material (CSE 01) very strong 'core and mantle' structures are developed in the old grains. Plate 4.14 shows a good example of this type of structure. The least deformed internal parts of the grain are characterized by a low dislocation density, broad pericline twins (presumed to be growth twins), with just a few deformation twins on the same law , and occasional fractures. As the grain mantle is approached the dislocation density increases dramatically although large local variations are common. In areas of high dislocation density a roughly cellular structure is developed, and the number of deformation twins increases. In the mantle itself it can be seen that dislocation networks have started to form, the unbound dislocations are more irregular,

Plate 4.14 Mosaic of TEM micrographs showing the development of a strong core and mantle structure in old oligoclase feldspars with heterogeneous dislocation density, cracks and deformation twins. At the top of the mosaic a recrystallized zone is formed between the main grain (1) and an adjacent oligoclase grain.

PLATE 4.14

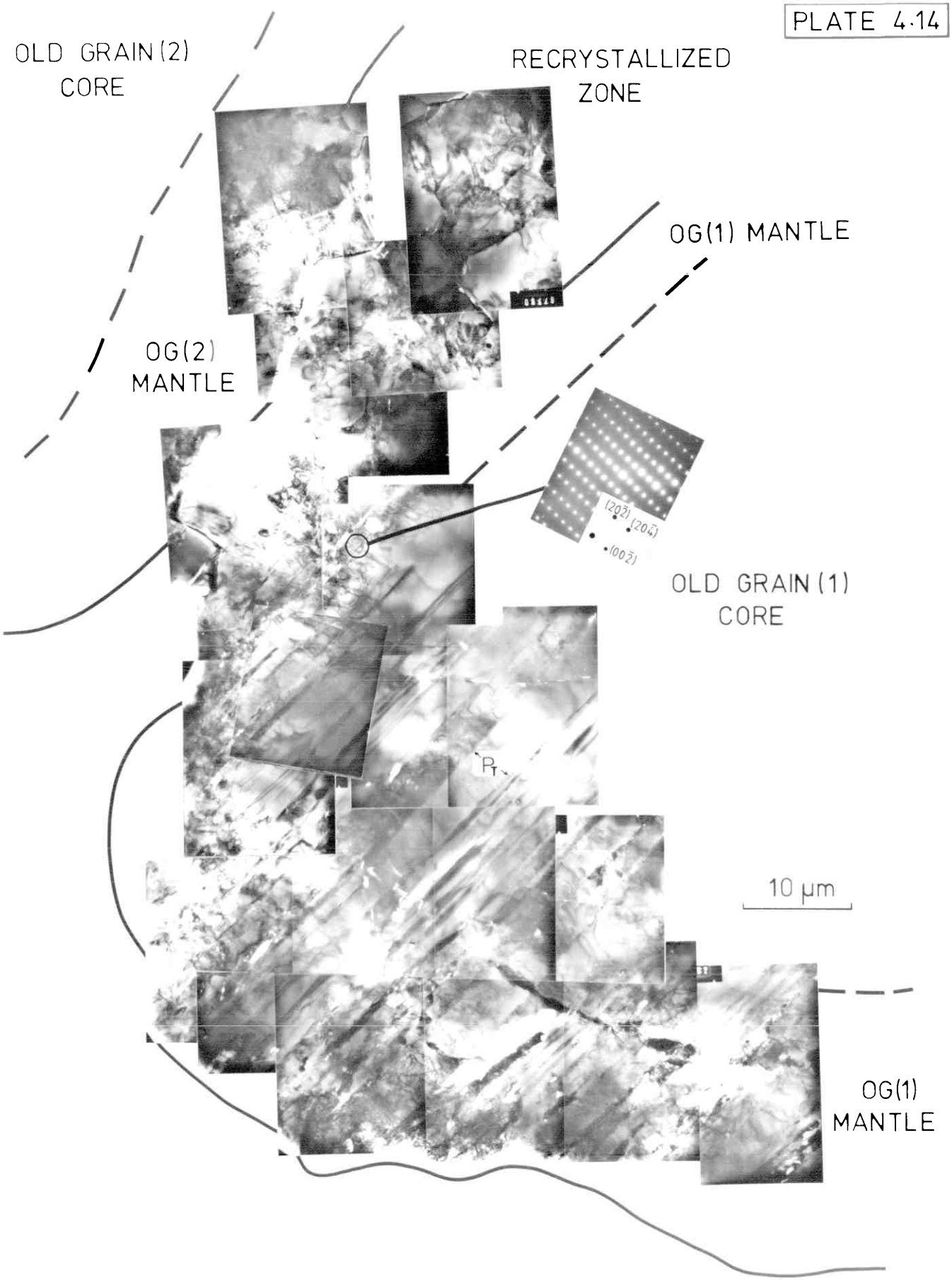

OLD GRAIN (2)
CORE
RECRYSTALLIZED
ZONE
OG(1) MANTLE
OG(2)
MANTLE
(20$\bar{2}$) (20$\bar{4}$)
(00$\bar{2}$)
OLD GRAIN (1)
CORE
Pt
10 µm
OG(1)
MANTLE

Plate 4.15 TEM micrographs of deformation microstructures in oligoclase from sample series CSE 01-03.

(a) Area within oligoclase from CSE 03, least deformed microgranite showing moderate dislocation density and albite twins(A_T). Note also the peristerite exsolution lamellae sub-parallel to the twins. Scale bar = 1μm.

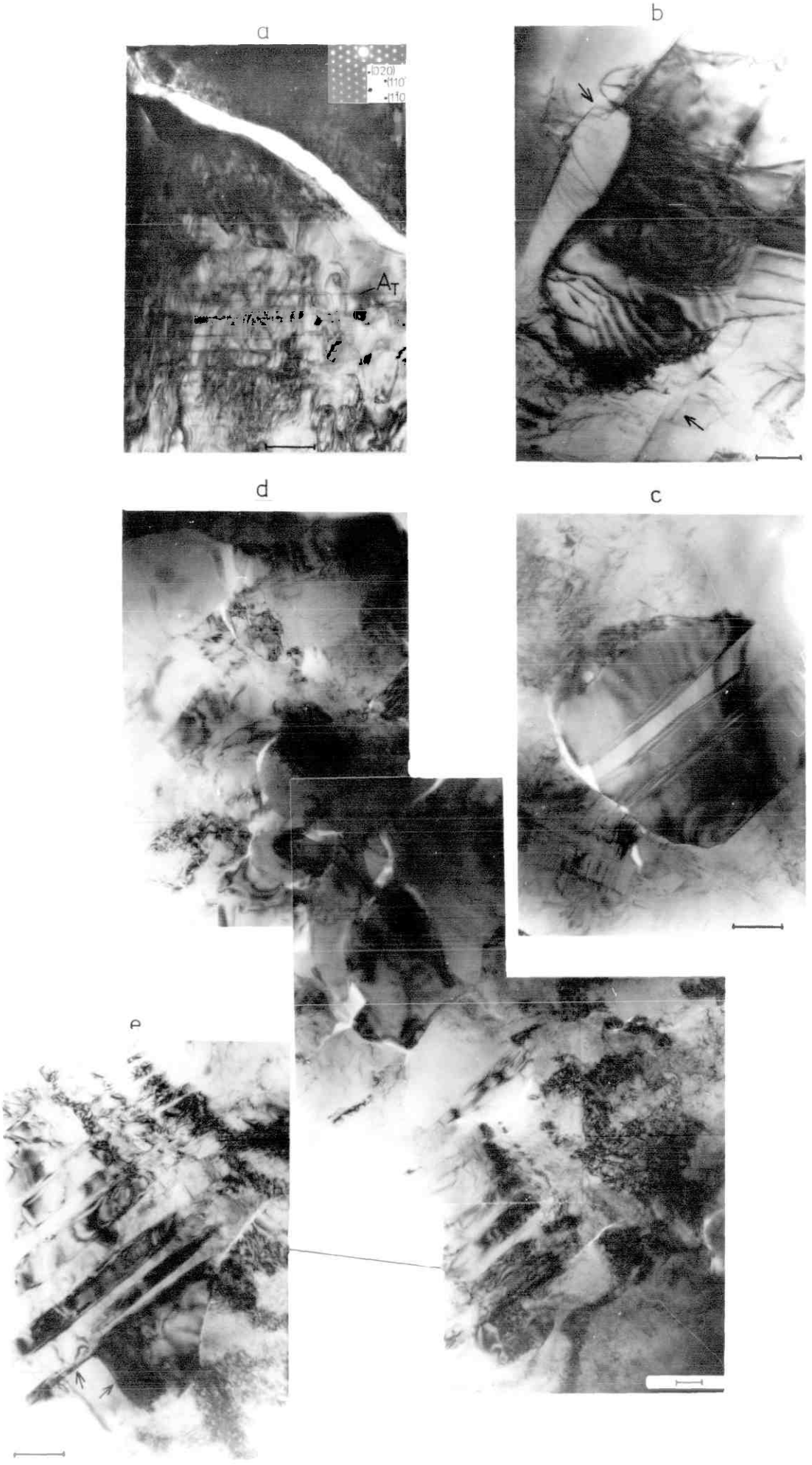
(b) Area within the oligoclase grain mantle depicted in Plate 4.14 showing the development of dislocation networks and the local modification of pericline twin boundaries (arrowed). Scale bar = 0.5μm.

(c) New grain nucleated within highly deformed old oligoclase grain mantle. Scale bar = 1μm.

(d) Mosaic of recrystallized grains in oligoclase grain mantle with new grains varying from strain-free to twinned with moderate dislocation density. Scale bar = 1μm.

(e) Detail of new grain at lower end of 14(d) showing sub-grain boundaries (arrowed). Scale bar = 1μm.

PLATE 4.15



and twin boundaries are apparently modified (Plate 4.15(b)).

In the top left of the mosaic it can be seen that the mantle passes into an area of small, relatively strain-free, grains separating the old grain forming most of the mosaic, from another old oligoclase grain showing very similar deformation features to those already described. The mechanism of recrystallization in this case is not clear.

Plate 4.15(c) shows an area where the mechanism can be identified, in this example nucleation followed by grain growth is clearly indicated. A good example of a recrystallized zone is shown in Plate 4.15(d) from an area close to Plate 4.15(c). These new grains show varying degrees of deformation with in some cases moderate dislocation densities, sub-grains and multiple twinning developed (Plate 4.15(e) shows a higher magnification of one of these grains).

In CSE 02, the mylonite, all the remnants of the original plagioclase grains are strongly deformed with moderate to high dislocation densities ($\rho \sim 10^{12} - 10^{13} m^{-2}$), and show varying degrees of recovery. In some grains dislocation densities are very heterogeneous and the dislocations form tangles. One of these grains is shown in Plate 4.16(a) in which a single dislocation (arrowed) lying in the plane of the foil in the direction [111] has interacted (marked i) with a series of dislocation gliding on approximately parallel slip planes. In other grains more recovered microstructures are present with homogeneous dislocation densities and formation of sub-grain boundaries. Plate 4.16(b) and 4.16(c) come from different parts of a grain showing the above features. Dislocations are found in the form of "rectangular" loops lying near (010) with segments parallel to [001] and [100]. Exsolution lamellae (arrowed) are well-developed in part of the grain shown in Plate 4.16(c) (see next Section).

As observed optically, over half the feldspar in the mylonite is in

Plate 4.16 Deformation microstructures in oligoclase from CSE 02, microgranite mylonite.

(a) Old oligoclase grain core showing heterogeneous dislocation density. One dislocation lying in the plane of the foil is seen to interact with (i) a series of dislocations each with an associated planar defect. The planar feature with voids running top left to middle right is thought to be a fracture. Scale bar = 1μm.

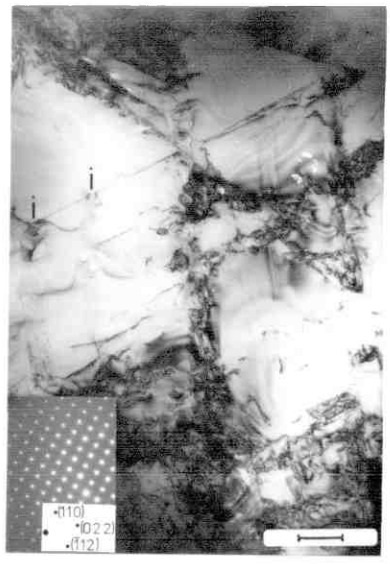
(b) Area within old oligoclase grain core showing broad pericline growth twins (P_T), narrow albite deformation twins (A_T), dislocation loops sub-parallel to (010), and lamellar peristerite exsolution (P_E). N.B. The diffraction pattern was taken with the foil several degrees from the orientation in which the micrograph was taken and the albite twins are not therefore vertical. Scale bar = 1μm.

(c) Area within mantle of oligoclase grain shown in 4.16(b) showing the the more recovered microstructure with the development of dislocation walls (arrowed) and ubiquitous peristerite exsolution lamellae. Scale bar = 0.5μm.

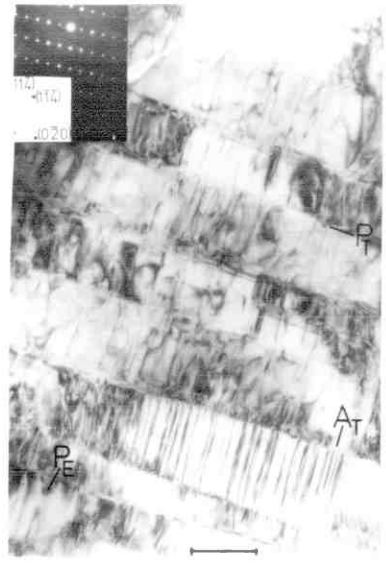
(d) Mosaic of oligoclase old grain mantle with adjacent recrystallized zone. The accompanying line diagram (Fig. 4.5) shows the orientation of traces of peristerite exsolution lamellae in each new grain and in sub-areas within the old grain; dotted lines indicate sub-grain boundaries, M denotes muscovite grain. Scale bar = 2μm.

PLATE 4.16

a



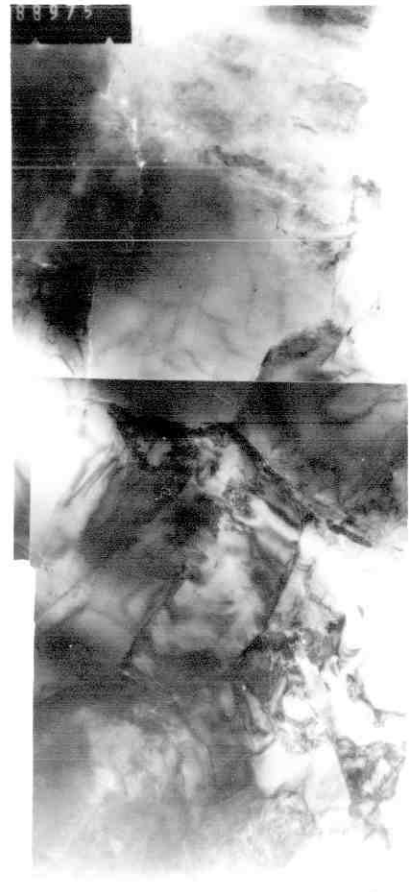
b

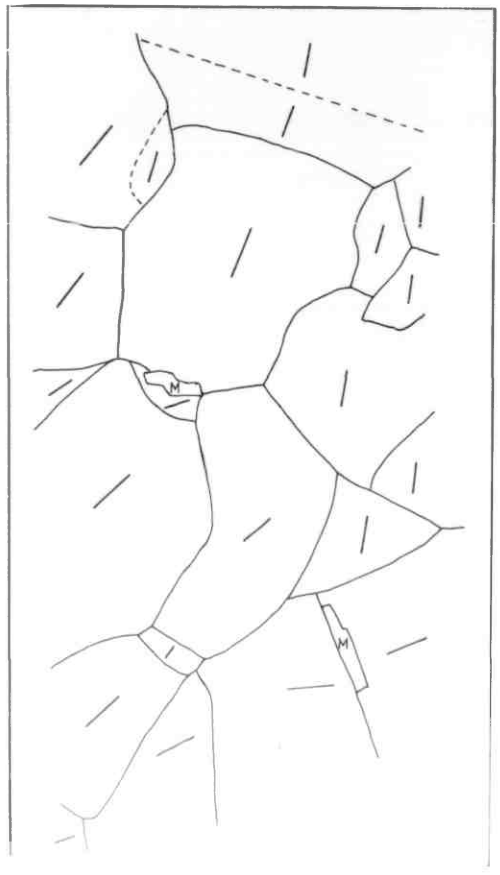


c



d





the form of small ($\sim$ 4μm) recrystallized grains. The mechanism of recrystallization is unclear in most cases, but good evidence for a form of SGR mechanism has been found in one area. Plate 4.16(d) shows the edge of the recrystallized zone from old grain mantle well into the recrystallized area. The new grains have a lower dislocation density than the parent grain, although they are not strain-free, and micas occur on some of the grain boundaries. In Fig. 4.5 the traces of exsolution lamellae (in poor contrast in the micrograph but visible on the negatives, in all the grains) are marked on all parts of the old grain, and on all the new grains. The traces show relatively small (1-30^{o}) misorientation (when compared with the random orientations anticipated from nucleation) from grain to grain but an overall smooth variation from the old grain to those new grains farthest from the parent grain giving a total misorientation of 70^{o}-80^{o}. This microstructure is not consistent with either nucleation or boundary migration mechanism, but fits well with a form of sub-grain rotation (sub-grain boundaries in the old-grain are shown as dashed lines in Fig. 4.5).

4.2.2.3.3 Exsolution phenomena

Peristerite exsolution was studied with regard to; orientation, spacing (or wavelength if a modulation rather than lamellae), sharpness and distribution. Orientations were obtained by trace analysis which yielded one trace per grain (the intersection direction of foil and exsolution) lying within the plane of exsolution (see Fig. 4.6). In some cases two directions of exsolution were observed, but one set was normally rather diffuse and the orientations obtained are likely to be inaccurate.

Fig. 4.7 is a stereographic projection for all exsolution traces in plagioclase feldspar. One set (the stronger if two are developed) gives a fairly well defined great circle which corresponds to a plane between

FIG. 4.6

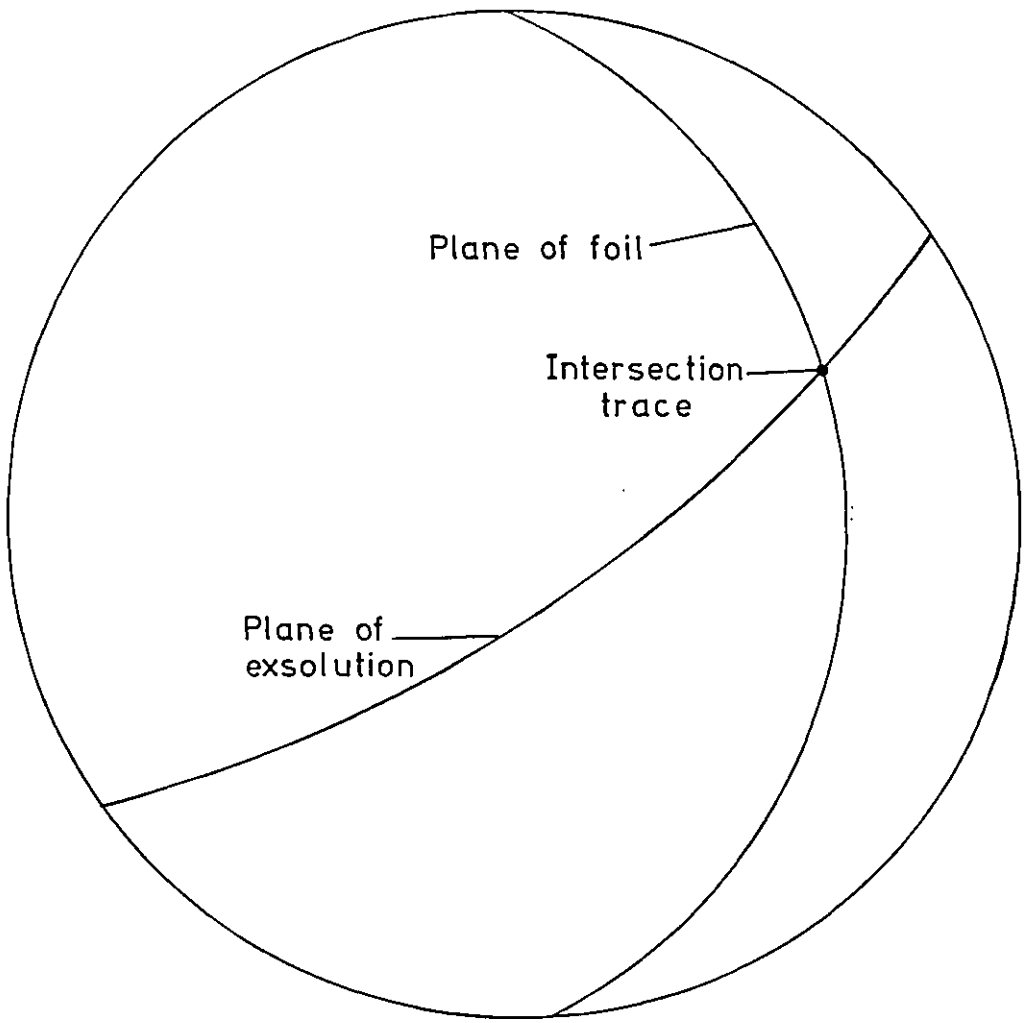
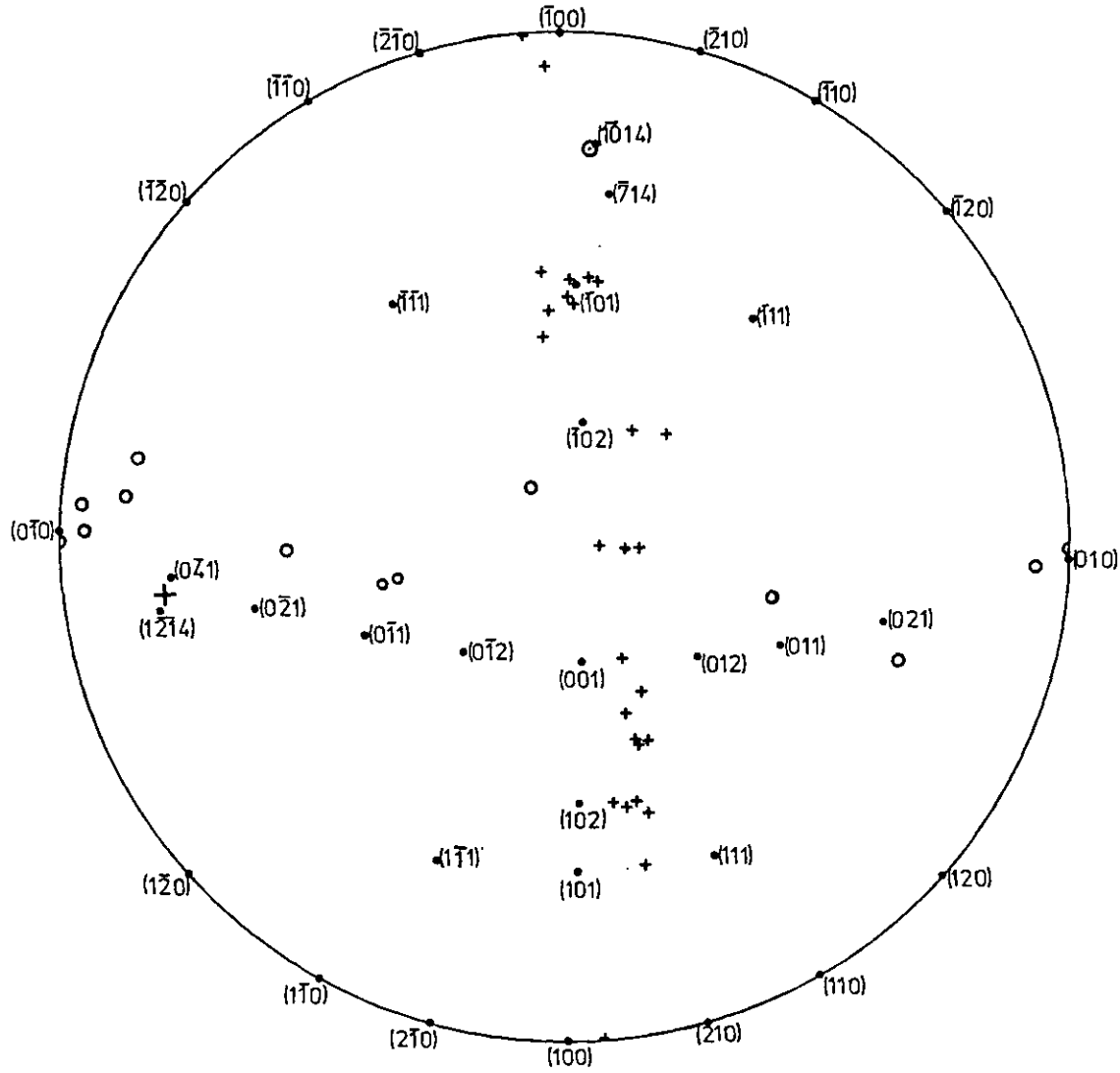


Fig. 4.6 Stereo graphic projection showing the intersection between an exsolution plane and the plane of the foil. It is the trace of this line of intersection that has been measured in order to find the orientation of peristerite exsolution lamellae. The plane of the foil is found by obtaining a diffraction pattern at near zero tilt.

FIG. 4.7



KEY

Traces exsolution lamellae

\+ Main set

O Diffuse second set (if present)

+, O Poles to respective best-fit great circles

Fig. 4.7 Stereographic projection of sodic plagioclase showing peristerite exsolution traces. If only one orientation of exsolution was present these were plotted as part of the main set ; if two orientations were developed the more diffuse was plotted as the secondary set, and the stronger as the main set. Poles to the best-fit great circles to the two sets of traces are indicated as are plane normals close to them.

$(04\bar{1})$ and $(\bar{1}\ 21\ 4)$. These are the two orientations found for peristerites by Olsen, 1974, with K-feldspar components of Or_{1-2} and Or_{4-7} respectively. In the same study Olsen reported a second orientation close to $(\bar{7}14)$ which is similar to that obtained in this study $(10\bar{1}4)$ considering the likely errors.

Measurements of lamellar spacings were obtained by averaging the spacings of 10-20 lamellae from each grain (only those lamellae near $(04\bar{1})$ were measured as the $(10\bar{1}4)$ were too diffuse). Care was taken to ensure that spacings were measured on micrographs in which the beam direction was parallel to the lamellae. This was done either by looking for changes in thickness with changes in foil thickness, or from the diffraction pattern (assuming the lamellae to be exactly on $(04\bar{1})$).

Fig. 4.8(a) shows the variation in spacing for sample series PDM 01-03 subdivided by sample, and old or new grains in the same sample. A clear trend is visible, spacings increase both from old to new grains in the same sample and from less-deformed samples to more deformed. For the sample series CSE 01-03 an opposing trend is apparent (Fig. 4.8(b)), with finer lamellae developed in the more deformed samples, and in new grains with respect to co-existing old grains. In CSE 03, the least deformed sample in this series, there is a large variation in observed spacings, while the other two samples are well-grouped.

Table 4.9 shows the variation in development of exsolution in both old and new grains. U stands for ubiquitous indicating that the lamellae are developed throughout the grains, whereas P stands for patchy indicating only local development. A similar trend is apparent in both sets of samples viz. those few undeformed grains that do show exsolution have it developed throughout, at higher strains a large proportion of both old and new grains show patchy

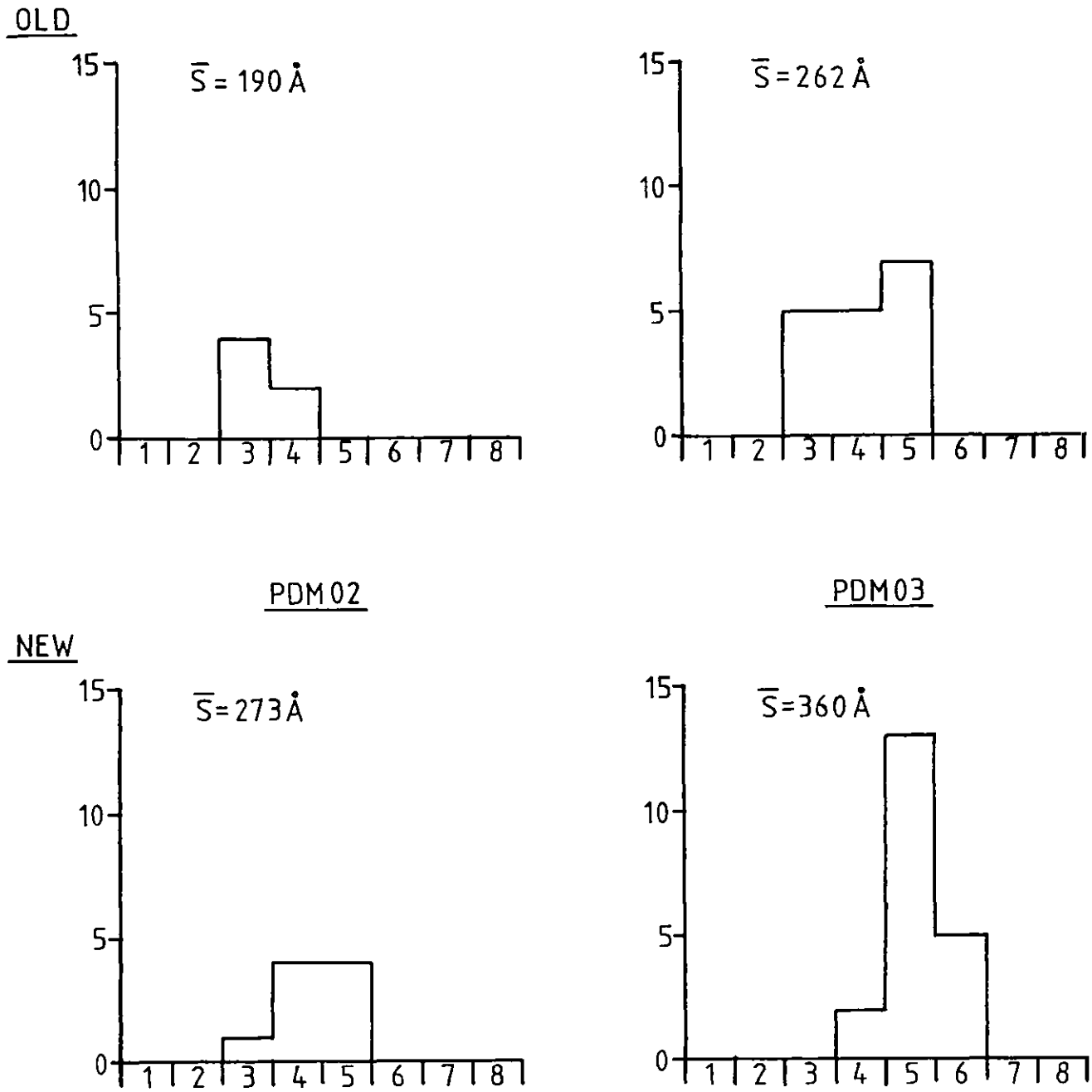
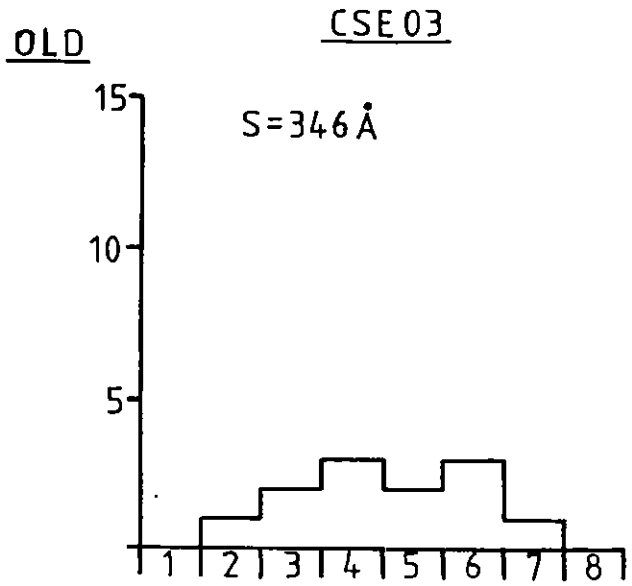
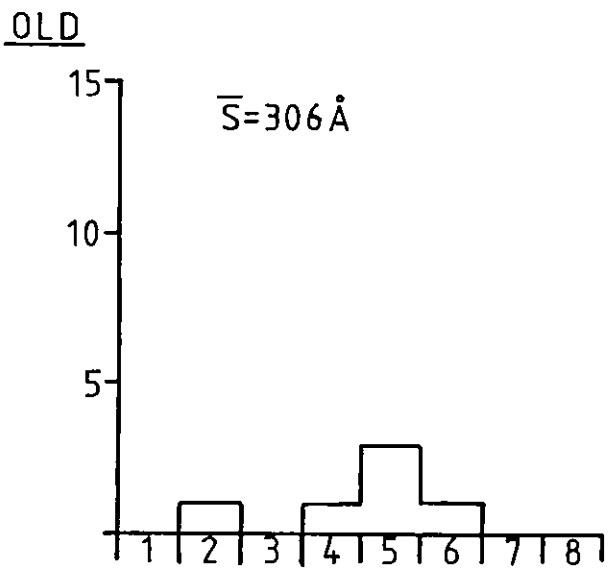


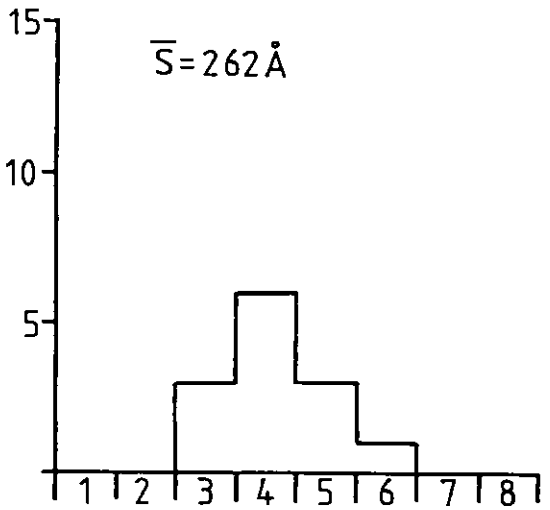
Fig. 4.8 Variation in lamellar spacing with bulk strain and from old to new grains , from the two sample series, in order of increasing strain

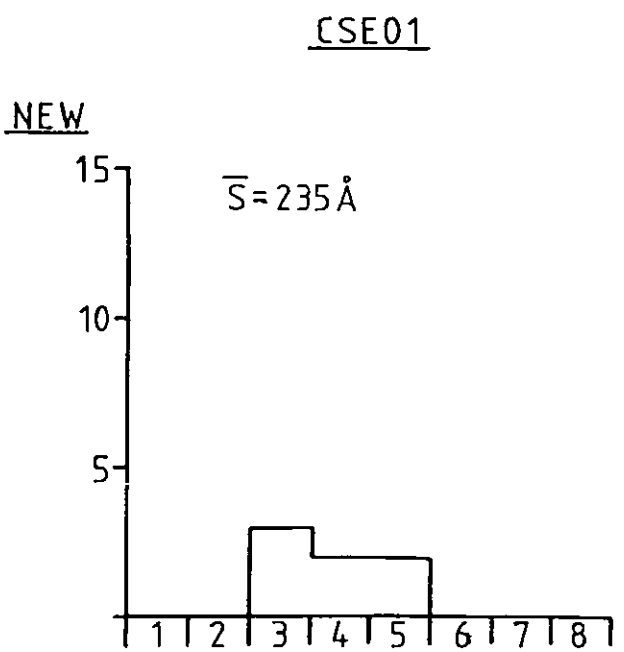
(a) PDM 02, 03

(b) CSE 03, 01, 02


OLD
CSE03
S=346Å
15
10
5
1 2 3 4 5 6 7 8


OLD
S=306Å
15
10
5
1 2 3 4 5 6 7 8


S=262Å
15
10
5
1 2 3 4 5 6 7 8


CSE01
NEW
S=235Å
15
10
5
1 2 3 4 5 6 7 8

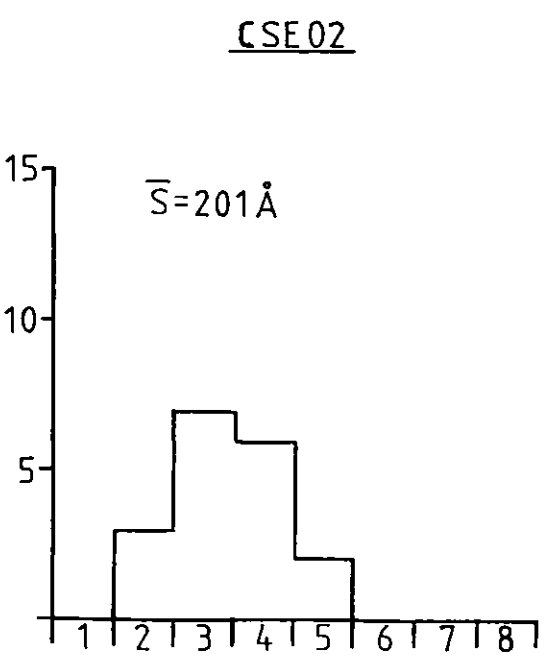

CSE02
S=201Å
15
10
5
1 2 3 4 5 6 7 8

TABLE 4.9

increasing strain ↓

SAMPLE	OLD GRAINS		NEW GRAINS	
	P	U	P	U
CSE O3	-	12	-	-
CSE O1	5	1	4	3
CSE O2	-	15	1	16
PDM O1	1	-	-	-
PDM O2	2	4	7	3
PDM O3	7	9	1	18

Table 4.9 . Numbers of plagioclase grains showing patchy (P) or ubiquitous (U) lamellar exsolution .

development, while in the mylonites most grains have lamellae throughout.

Although, as indicated above, the least deformed grains are normally either unexsolved or show ubiquitous development one grain in a foil from the least deformed microgranite CSE 03 showed a very heterogeneous exsolution structure. Plate 4.17 is a mosaic of part of this old grain. Three different bands may be distinguished running roughly parallel to the grain boundary.

The band nearest to the grain boundary has relatively coarse (∿50nm) lamellae throughout, no dislocations, but a few albite twins. This passes into the next band over a sharp boundary across which the twin and exsolution traces are visibly misorientated by ca. 5^{o}. This next band contains much finer lamellae (∿ 15nm), locally with a rather diffuse second set developed (only seen clearly on the negative), no dislocations, and is also affected by a few albite twins. The innermost band, which has a gradational boundary with the previous band, has no exsolution lamellae, except in patches at edges of the band, no twins, but moderate density of dislocations. This type of structure could be consistent with compositional zoning but the foils did not survive transfer to the STEM for microanalysis. However, Carter et al. (1980) observed a progressive decrease in lamellar spacing (or modulation wavelength) for peristerite exsolution in a zoned oligoclase over the range An_{13} - An_{22}, and a concomitant change from one sharp set of lamellae, to two diffuse modulations.

In many grains that contain no lamellae there is a diffuse streaking, commonly in two directions. In Plate 4.18(a) an old deformed grain shows

Plate 4.17 Mosaic of TEM micrographs of oligoclase grain from the least deformed microgranite CSE 03. Three bands of different microstructure are developed roughly parallel to the grain boundary. In band (1), relatively coarse peristerite exsolution lamellae are found with a few albite twins and no dislocations. Band (2) has a rather diffuse cross-hatched modulation with a few albite twins and no dislocations In the innermost band (3) there is no exsolution structure at all but a moderate dislocation density is developed.

PLATE 4·17

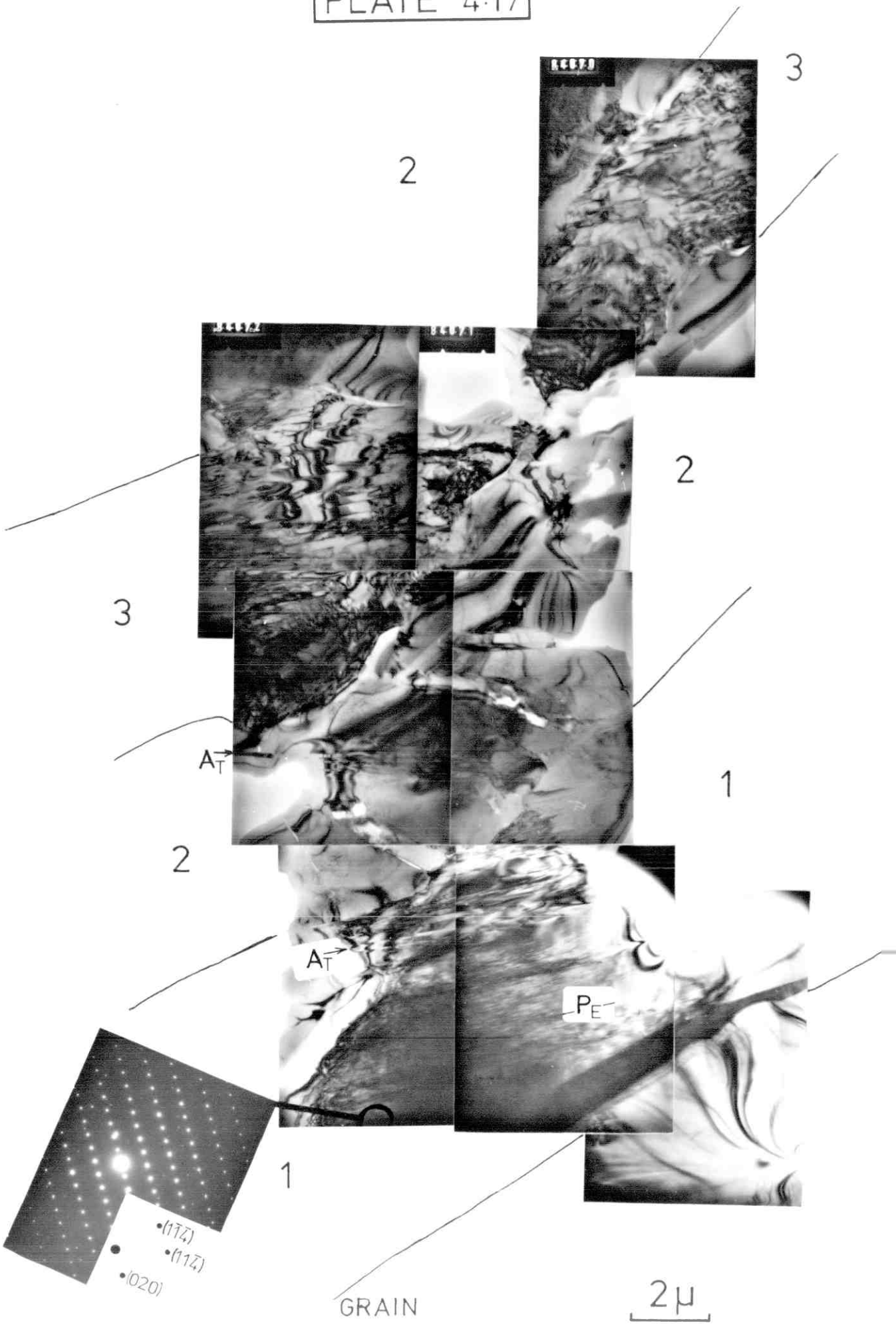


Plate 4.18 Exsolution microstructures in CSE01-03 series oligoclases.

(a) Old oligoclase grain showing local coarsening (arrowed) of one of the two modulations which otherwise form a diffuse cross-hatching. Scale bar = 0.5μm.

(b) New ologoclase grain showing local coarsening (arrowed) of one component of a diffuse cross-hatched modulation. Scale bar = 250nm.

(c) Area within deformed new oligoclase grain with lamellar peristerite exsolution giving rise to the diffraction pattern shown in 4.18(d). Scale bar = 0.5μm.

(d) Diffraction pattern of area within 4.18(c) showing the development of side-bands (satellite reflections) on each spot due to the very regular fine-scale peristerite exsolution lamellae.

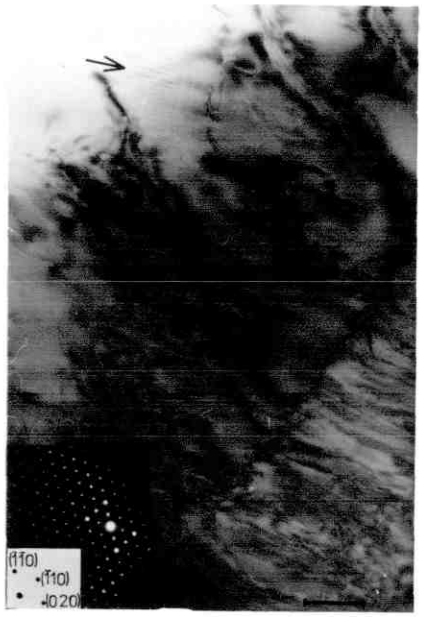
(e) Area within deformed new oligoclase grain with lamellar peristerite exsolution giving rise to teh diffraction pattern shown in 4.18(f). Scale bar = 0.5μm.

(f) Diffraction pattern of area within 4.18(e) showing divergence of the reciprocal lattice for the albite and the more calcic components of the peristerite by $\sim 1.5^{\circ}$ along the normal to $(\bar{2}02)$; the reciprocal lattices co-incide along the normal to (020).

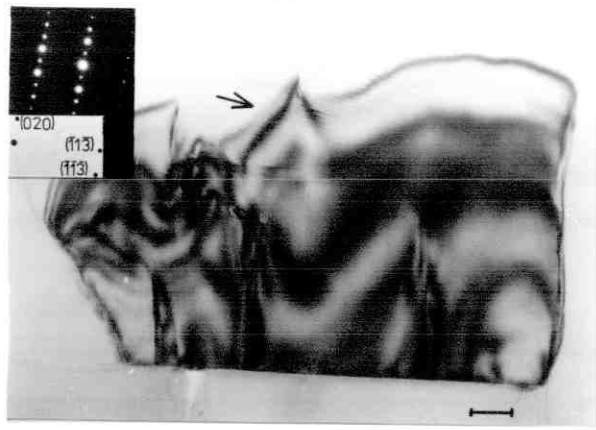
N.B. For both 4.18(c) and 4.18(e) there is a 20° clockwise rotation frem the diffraction pattern to the micrograph.

PLATE 4·18

a



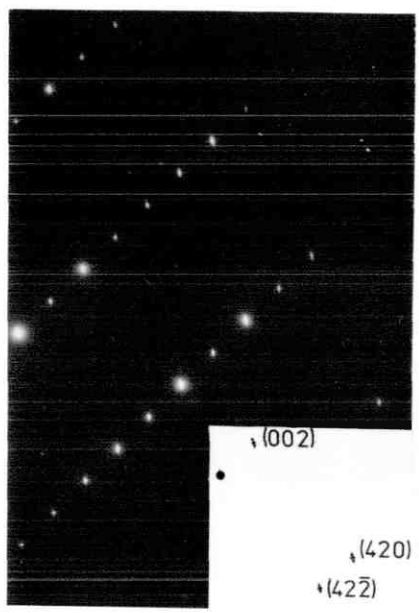
b



c



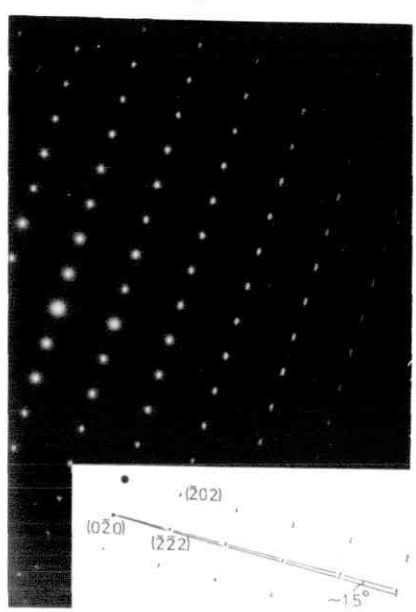
d



e



f



this diffuse cross-hatching, but locally this is being replaced by coarser and better defined structures (arrowed) which could be termed lamellae. Plate 4.18(b) shows a similar structure developed on a partly deformed new grain, with a very fine cross-hatched modulation (wavelength $\sim$ 10nm) locally coarsening in one direction at the expense of the other to give distinct lamellae (spacing $\sim$ 25nm). This local variation is found only in deformed grains; in strain free grains, both old and new, any modulated microstructure is evenly developed throughout.

Peristerite lamellae with wavelengths in the range 10-25nm give rise to particular diffraction effects examples of which are described below. Plate 4.18(c) is a micrograph of a new grain from the microgranite mylonite CSE 02, showing regular lamellae; Plate 4.18(d) is the associated diffraction pattern. Each main spot of the pattern has two 'side-bands', and in addition both main spot and side-bands are diffusively streaked in a direction normal to the side-bands. Distinct side-bands are the direct result of any very regular periodic structure with wavelengths less than a few tens of nanometres; the separation of the side-bands from the principal reflections is inversely proportional to the wavelength of the periodic structure (Hirsch et al., 1967).

In certain favoured orientations it is possible to observe the mismatch between the reciprocal lattices of the albite and oligoclase components in the peristerite. Plate 4.18(e), (f) shows an area of lamellae and associated diffraction pattern. The reflections in the direction normal to (020) coincide, whilst those along the normal to $(\bar{2}01)$ diverge by an angle $\sim 1.5^{o}$. This angle of mismatch is consistent with components of An_{0-2} and $An_{25\pm5}$ as described by Olsen (1974) and Ribbe (1975).

4.2.2.4. Discussion

The deformation of the sodic plagioclases has been observed to depend both on the original composition and initial growth features. The principal effect of compositional variation is the difference in degree of recovery as shown by the albites and oligoclases in the microgranite mylonite PDM 03. These may be summarized as; homogeneous dislocation densities, and sub-grain formation in albite, with no deformation twins, compared to heterogeneous dislocation densities, irregular cell formation, deformation twins and fracturing in the oligoclases. This variation in behaviour has been linked (e.g. Borges, 1978) to the development of a super lattice, which is present in the intermediate plagioclases, but not in albite. Dislocations move through a super lattice in pairs separated by stacking faults and are known as superdislocations; such dislocations are relatively immobile in climb which is the main mechanism of recovery.

The presence or otherwise of regular albite growth twinning has been found to have a considerable effect on the progressive deformation of albites in two sample series from tourmaline pegmatites RDS01-03, and CSC 01-03. In the untwinned grains the initial effect of deformation is to form a network of sub-equant sub-grains, which show increasing mutual misorientation with strain. In the twinned grains kinking is initially the dominant mechanism locally associated with fracturing along the kink axial planes. With further strain both sub-grains in one case and kink-bands in the other continue to misorientate leading to the development of high angle boundaries. Kinking in the twinned grains is thought to be due to pseudo-single slip system behaviour as a result of twin interfaces impeding slip on all planes except (010).

Grain size reduction in these feldspars is carried out by three distinct mechanisms.

(i) Fracturing; generally unimportant but may be locally significant.

(ii) Sub-grain rotation recrystallization; responsible for the initial grain size reduction, giving grains in the range 50-250μm. SGR is also responsible in part for the formation of small grains ∿ 5μm at grain boundaries.

(iii) Nucleation; produces small strain-free grains ∿ 5μm in the most deformed part of the grain, generally the grain mantle.

Both of the recrystallization mechanisms have been identified before in naturally deformed plagioclase feldspars but not operating simultaneously in the same specimen. The simultaneous operation of more than one recrystallization mechanism is discussed in Section 5.3 In the feldspars in the present study the dominant mechanism is thought to be controlled by the degree of recovery.

Dislocation lines were observed to be close to major crystallographic direction [001], [100], [010] and [111]. In only one foil were loops observed indicating the slip plane, and this was found to be near (010). These observations are consistent with previously published slip planes (see Table 4.6) for the more sodic plagioclases.

The progressive development of exsolution structures in these feldspars has been found to be complex, but the main observations are summarized below.

(i) Relatively undeformed grains only rarely show lamellar exsolution, normally throughout the grain if developed, and rather more show a very diffuse fine cross-hatched streaking.

(ii) With increasing strain, a greater proportion of the old grains show lamellar exsolution. In many cases this is patchily developed and replaces the diffuse cross-hatching apparently by coarsening one of the modulations $(0\bar{4}1)$ at the expense of the other $(\bar{1}014)$. New grains

at the same bulk strain commonly show ubiquitous modulations, often with a fainter second set; rarely this is patchily developed.

(iii) In the mylonites most old and new grains show ubiquitous lamellar exsolution on $(04\bar{1})$.

(iv) The two suites of samples show clear but contradictory trends for lamellar spacing with bulk strain, and from old to new grains at the same bulk strain; lamellae in PDM 01-03 become coarser, while those in CSE 01-03 become finer. In the latter set of samples the more deformed grains show a smaller spread of spacings than that observed in the least deformed.

Before attempting to explain the above observations it is necessary to examine the possible effect on spacing of; exsolution mechanism, degree of undercooling, thermal history, chemistry and strain.

The three main possible mechanisms of exsolution are homogeneous nucleation, heterogeneous nucleation, and spinodal decomposition (Putnis and McConnell, 1980). Homogeneous nucleation can take place within regions of perfect crystal structure and is independent of crystal defects such as vacancies, dislocations and twin boundaries. Small nuclei of a lower energy phase form as a result of random thermal fluctuations, and, over a certain critical size, these will be stable and grow. The size of the critical nucleus will depend on the activation energy and, if this is relatively high, random thermal fluctuations of sufficient size are unlikely to occur. In such a case the additional energy which is required to overcome this barrier may come from the energy associated with a crystal defect (e.g. the stored elastic strain energy associated with a dislocation), and the process is then termed heterogeneous nucleation.

In contrast to these discontinuous (i.e. first order) transformation

processes, spinodal decomposition provides a mechanism by which a homogeneous solid solution may decompose continuously into regions of differing composition (Cahn, 1968). Sinusoidal composition waves form simultaneously throughout the whole structure. Such compositional modulations may grow in both amplitude and wavelength until two discrete phases are formed. All the mechanisms mentioned above will lead to lamellar exsolution in materials in which there is a significant degree of elastic anisotropy. The orientation of the lamellae are governed by the minimization of strain energy (e.g. Brown and Williame, 1974).

In addition to these three mechanisms metastable phases unable to exsolve in any of the ways already mentioned may develop transitional phases (Putnis and McConnell, 1980), the commonest of which are known as G-P zones (after Guinier and Preston who first detected them), but these occur in the form of platelets rather than lamellae.

It is not always possible to ascertain the mechanism by which lamellar exsolution has been formed except in the very early stages of the process. However, Owen and McConnell (1974), and Champness and Lorimer (1976) have both figured microstructures that they regard as being 'consistent with a mechanism of spinodal decomposition'. Many of the more diffuse, modulated structures observed in the feldspars in this study are very similar to those that they describe.

Some degree of undercooling (ΔT) is necessary for almost all transformations to take place. In some cases ΔT may be only a fraction of a degree but for certain transformations several hundred degrees of undercooling may be required. The reason that a particular transformation takes place at a temperature considerably lower than that indicated by the thermodynamics is due to the inability of atomic diffusion to keep pace with thermodynamic requirements. In such a case the temperature of trans-

formation will be controlled by the kinetics of atomic mobility. The degree of undercooling required for the transformation depends, therefore, on the rate of cooling.

If an old grain has started to exsolve prior to deformation at a temperature T, and then recrystallizes by nucleation to a new grain of similar composition, at a lower temperature T_2, the resultant new grain will start to exsolve with a greater degree of undercooling ($T_1 - T_2$). The degree of undercooling directly affects the initial wavelength of modulation due to spinodal decomposition (Cahn, 1968); the greater ΔT, the smaller the resultant wavelength.

One of the possible effects of differences in composition is that the more calcic plagioclases in the albite-oligoclase field are thought to start exsolving at lower temperatures. This follows from both of the schemes proposed to explain peristerite exsolution, the binary loop (Tuttle and Bowen, 1950; Smith, 1974) or the asymmetric solvus (Laves, 1960; Ribbe, 1962) (Fig. 4.9). At lower temperatures the kinetics of atomic mobility become very sluggish, and even if an initial modulation is formedit is very unlikely to coarsen; this is supported by the observations of Carter et al. (1980) on variation in wavelength with compositional zoning.

Compositional modulations, once formed, tend to increase in wavelength. This is due to the decrease in free energy possible from a reduction in the energy associated with the interfaces (coherency strain energy, surface energy). Such coarsening is well documented in both the metallurgical literature (e.g. Cahn, 1968) and the mineralogical literature (e.g. Yund et al,1974; Owen and McConnell, 1974). The final amount of coarsening will depend partly on the diffusion distance (the distance above which

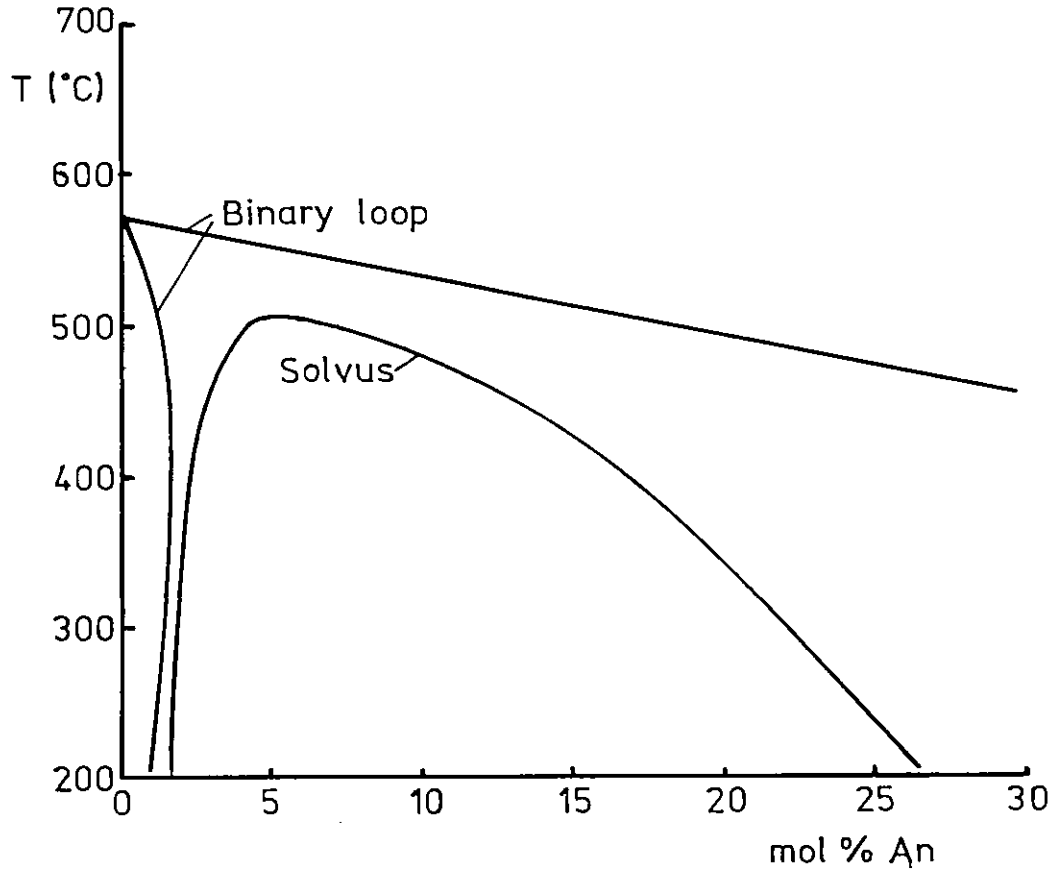


Fig. 4.9 Models for the peristerite miscibility gap in terms of a binary loop, and an assymetric solvus. (after Carpenter,1981)

diffusion is negligibly slow for a given temperature), and partly on the ease with which the interfaces may move through the crystal. Lorimer and Champness (1976) have pointed out that this movement will be inhibited if different types of ordering are found in the two components, and this will be so in peristerites if the metastable ordered '$_e$'-structure is formed in the calcic component, the sodic component is thought to form initially as fully ordered low-albite (Carpenter, 1981).

Carpenter (op.cit.) has proposed that peristerite exsolution is controlled by a conditional spinodal. This type of spinodal decomposition is conditional on one of the exsolved phases being fully ordered while the other component remains disordered. Fig. 4.10 shows a series of free-energy v. composition curves proposed by Carpenter for the sodic plagioclases at various temperatures below the onset of the intermediate-low albite transition.

The preferred composition for the calcic component is shown to vary from An_{20} to An_{30} as the temperature decreases. Therefore, assuming that the more calcic plagioclases in the peristerite field start to exsolve at low temperatures than the more sodic ones, the oligoclase component in such feldspars will initially be more calcic, and consequently more liable to develop the 'e' structure prior to significant coarsening (McConnell, 1974).

The last factor to be considered is the effects of strain. The movement of dislocation through the lattice allows fast diffusion in the region of the slip plane (Yund and Tullis, 1980) while immobile dislocations may act as channelways for migrating species, a phenomenon known as 'pipe diffusion' (Cohen, 1970). Therefore effective diffusion rates may be related to strain-rates (thereby altering the wavelength of any modulation), and the completeness of the process, i.e. just how close the system approaches equilibrium, may be related to total strain. It is significant

Fig. 4.10 (a-c) Free energy (G) - composition (X) curves for ordered albite (ord) and disordered plagioclase solid solution (dis).

(a) At temperature T_1, the curves have the configuration of a typical non-first order transformation with $\delta G/ \delta X$ continuous.

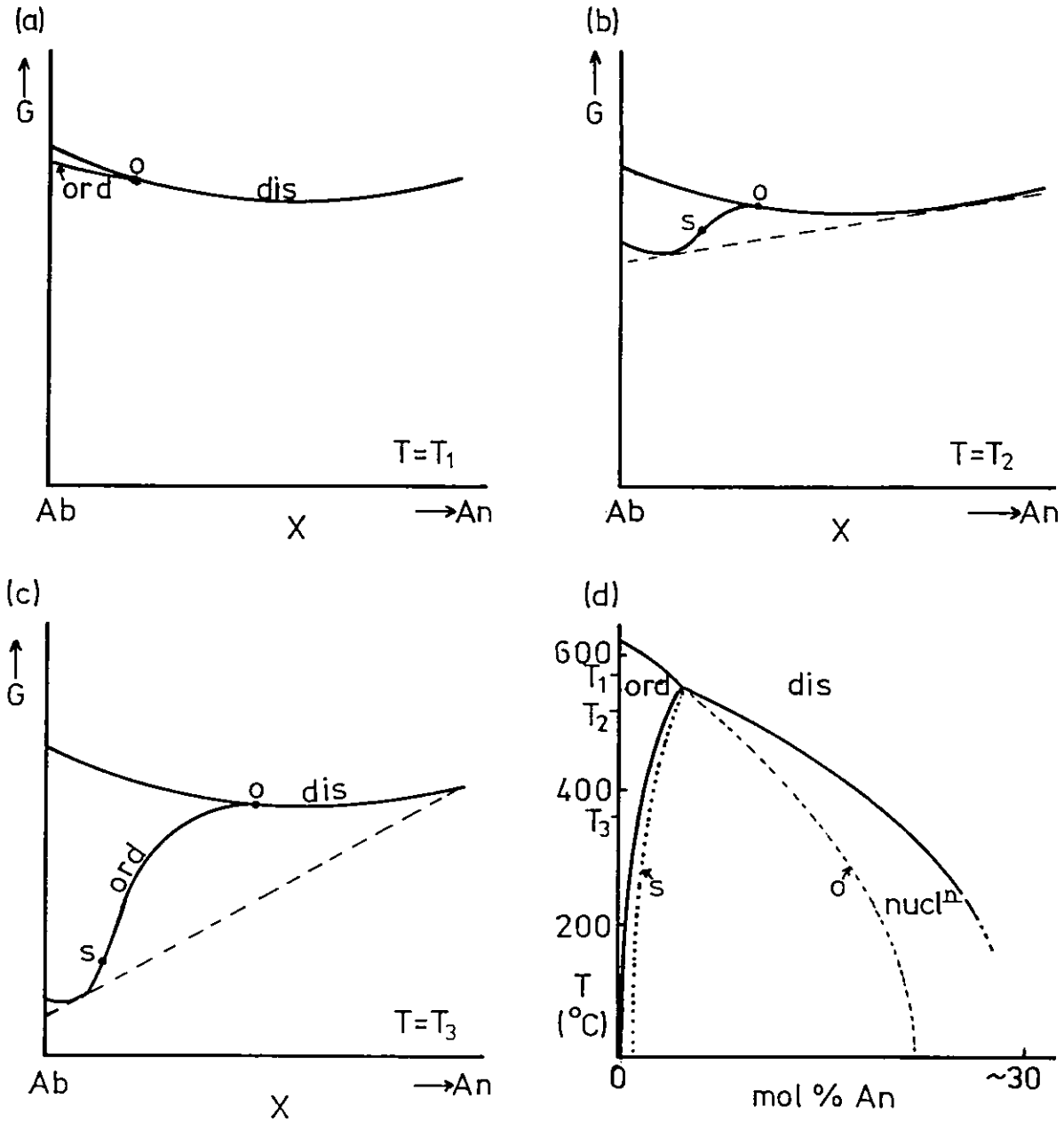
(b) At temperature T_2 the substitution of excess Al in ordered albite has become so unfavourable that a two phase field, given by the common tangent, (broken line), haa developed. Spinodal decomposition is possible in phases lying on the curve between the points o and s .

(c) At lower temperatures the two phase field widens.

(d) Temperature-composition diagram illustrating fields where spinodal decomposition is possible (between the broken lines s and o), and in which nucleation ($nucl^n$) is the only possible mechanism.

(After Carpenter,1981)

FIG. 4·10


(a)
G
ord
o
dis
T=T1
Ab
X
→An
(b)
G
o
s
T=T2
Ab
X
→An
(c)
G
o
dis
ord
s
T=T3
Ab
X
→An
(d)
600
T1
ord
dis
T2
400
T3
s
o
nucln
200
T
(°C)
0
~30
mol % An

that local coarsening only occurs in strained areas, indicating that one of the above effects allows otherwise kinetically slow, or impossible transformations to proceed.

We may now return to the observations summarized at the beginning of this section. The relative degree of development of lamellar exsolution with strain, viz. initially ubiquitous where present, then patchy, and finally ubiquitous again, may be viewed as a result of the following sequence. Before deformation only a few grains have exsolved, forming lamellae throughout (probably the more sodic, Carter et al. 1980). Deformation brings with it increased diffusion and previously unexsolved grains begin to unmix, and just as the strain is heterogeneous, so is the development of the lamellae. Finally, at the much higher strains found in the mylonites, almost all the grains become exsolved throughout.

The establishment of distinct but opposing trends of fining and coarsening in lamellar spacings from the two sets of samples allows no such simple explanation. However, the difference in compositional ranges between the two series (PDM 01-03, An_{13-19}, CSE 01-03, An_{17-23}) is significant, particularly as lamellar peristerite exsolution has not been reported before in plagioclase more calcic than $\sim An_{16}$ (Carpenter, 1981).

The trend evident in the PDM 01-03 series is consistent with the enhancement of coarsening due to increasing strain and strain-rate on initially exsolved grains. The trend for the CSE 01-03 series may similarly reflect the enhancement of diffusion due to increasing strain and strain-rate but in this case by allowing lamellar exsolution in grains in which it would not otherwise occur. Thus in the least deformed feldspars only those at the most sodic end of the compositional range would have developed exsolution lamellae. With increasing deformation progressively more calcic

grains would exsolve until in the mylonite most of the oligoclase would be exsolved. The trend in mean lamellar spacing may simply reflect the fact that progressively more calcic grains are included in the distribution of exsolved grains. The most calcic grains are expected to be characterized by the finest lamellar spacings, in accordance with the observations of Carter et al. (1980).

The observations on the relative development and spacing of exsolution lamellae presented here strongly suggest that the process of exsolution is significantly enhanced by deformation.

4.3 Micas

A limited number of observations have been made on the microstructure developed in micas. The lack of detail in this study was due to an early appreciation that micas in the rocks studied would be of no use in palaeostress estimation due to the presence of populations of new grains from several sources.

4.3.1 Review of previous work

The deformation behaviour of the micas is controlled by the lack of any other slip system to combine with basal slip allowing anything approaching homogeneous deformation. Microstructures typical of mica are, therefore, those characteristic of any material with a single dominant slip system; grains fold and kink, commonly with the development of cracks along the basal plane (Nicolas and Poirier, 1976; Bell, 1979; Wilson, 1979). Recrystallization by a form of SGR mechanism has been noted by Bell (1978) and Wilson (1979), with new grains developing from highly misorientated areas associated with kink bands.

4.3.2 Optical strain features

Similar observations were made in all the samples looked at in this study, and they will be considered together. Optically it is possible to delimit seven populations of mica grains; old igneous biotites, old igneous muscovites, muscovites replacing biotite with exsolution of iron oxide, new fine-grained white micas from breakdown of old biotites, new fine-grained white micas from breakdown of old muscovites, new fine-grained white micas from the alteration of feldspars, and new fine-grained white micas growing in the foliation. (Plate 4.19(a), (b), (c) show examples of the last three types.)

Most of the old micas have undulatory extinction, and, with increasing strain kink-bands may form (Plate 4.19(d)) or alternatively rather more rounded folds (Plate 4.19(e)). In a few grains recrystallization by an SGR mechanism (Bell, 1979(b)) was suspected (Plate 4.19(d)), with new grains forming on kink-band boundaries.

The combination of a fine grain size and high birefringence in the new white micas renders the observation of strain features difficult. It does appear, however, that many of the micas of alteration and recrystallization origin are relatively strain free, with just the local development of undulatory extinction.

4.3.3 TEM of Micas

Micas from both the PDM 01-03 and CSE 01-03 series were studied but only a few deformation microstructures have been observed by TEM, partly due to the beam damage, but also simply due to the presence of many relatively unstrained grains. Old micas commonly show the best-developed deformation microstructures. Plate 4.20(a) shows an old biotite grain with stacking faults (arrowed) terminating at dislocations, in the

Plate 4.19 Optical micrographs of white micas. (allcrossed polars)

(a) White micas forming by the alteration of oligoclase porphyroclasts at their grain boundaries. Scale bar = 100μm.

(b) White micas forming by the alteration of a muscovite porphyroclast at its grain boundary. Scale bar = 100μm.

(c) Isolated fine white micas (arrowed) found on recrystallized quartz grain boundaries. Scale bar = 100μm.

(d) Kink-band (arrowed) developed in a muscovite porphyroclast. Scale bar = 100μm.

(e) Rounded fold in muscovite porphyroclast. Scale bar = 100μm.

(f) Recrystallization along kink-band boundaries (arrowed) in a muscovite porphyroclast. Scale bar = 25μm.

PLATE 4·19

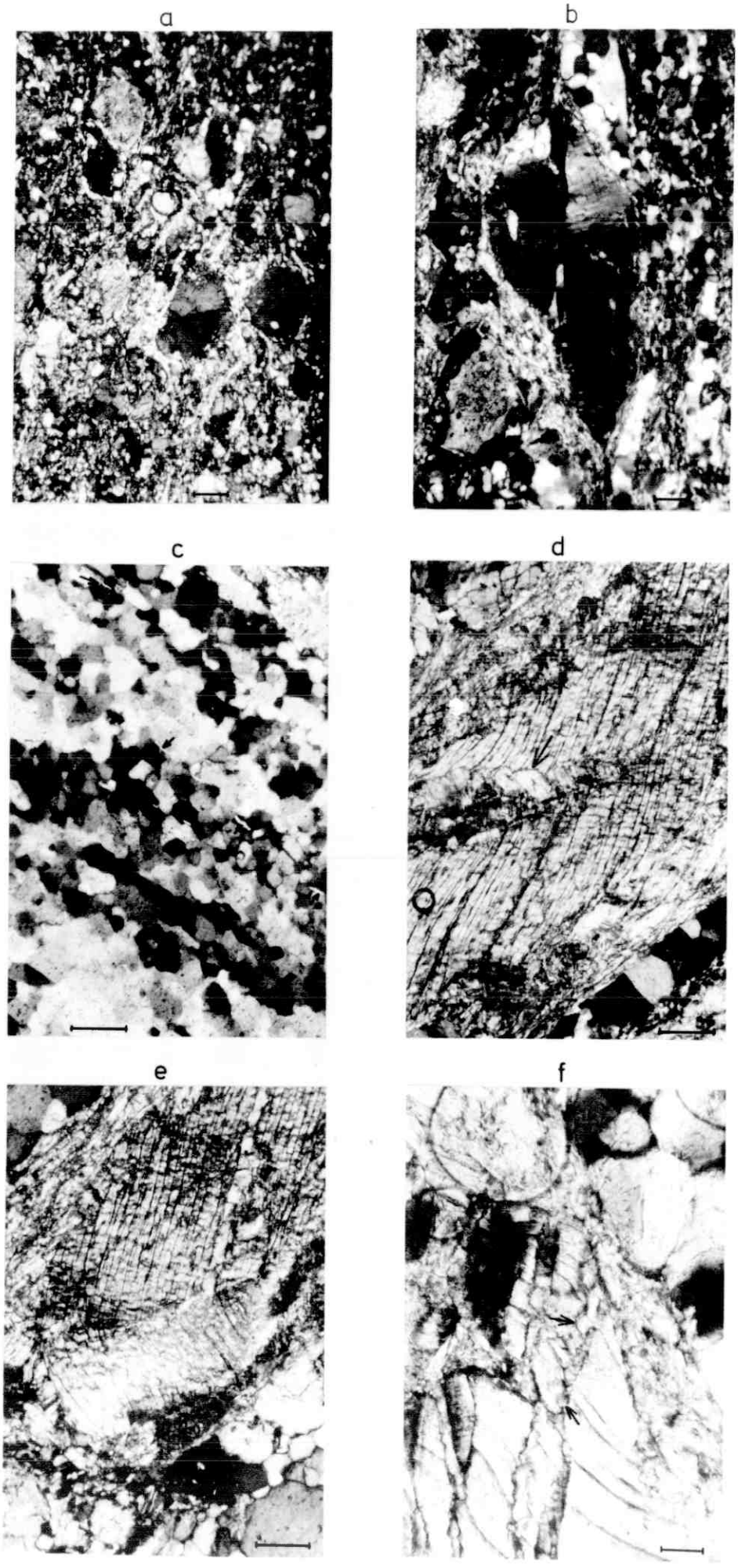


Plate 4.20 TEM micrographs of micas.

(a) Area in biotite porphyroclast showing stacking faults (arrowed) in the basal plane. Scale bar = 1μm.

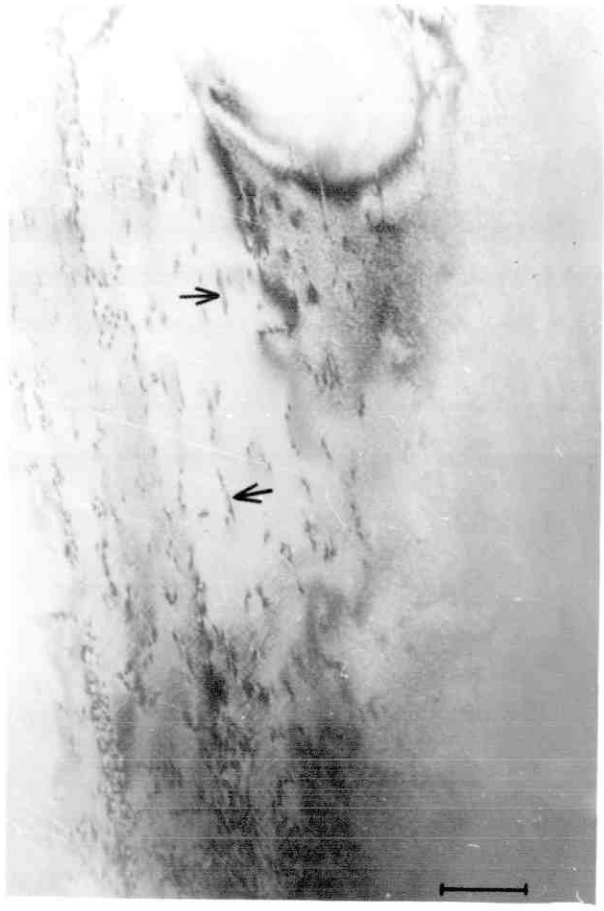
(b) Kink-band developed in strongly deformed muscovite porphyroclast; note the formation of voids within the hinge zone. Scale bar = 1μm.

(c) Band of fine white micas. Individual grains are relatively undeformed, note particularly the unstrained nature of those micas lying perpendicular to the foliation (arrowed). Scale bar = 5μm.

(d) New grains formed along a kink-band boundary in a muscovite porphyroclast. The highly strained nature of some of the new grains (arrowed) indicates that recrystallization was not by nucleation and growth. Scale bar = 2.5μm.

PLATE 4·20

a



b



c



d



basal plane. Some old muscovite grains show well-developed kink-bands, similar to, but on a much smaller scale than those observed optically (Plate 4.20(b)). In this micrograph the kinking is seen to be associated with fractures along basal planes, especially along the hinge zones of kink bands.

The zones of fine-grained micas that result from the alteration of old micas and feldspars show little evidence of large strain deformation. The lack of marked internal strain features in most of these grains might be due to deformation by diffusive mass transfer accommodated grain boundary sliding. However, in many areas (e.g. Plate 4.20(c)) a proportion of grains are found lying at high angles to the foliation which suggests that such zones have not been the sites of large strain deformation. Alternatively, such features could be interpreted as due to post-tectonic grain growth.

Recrystallization on kink-band boundaries has not been commonly observed. However, Plate 4.20(d) shows an area in which it is strongly suggested. A kink band boundary in an old muscovite contains several small grains, one of which (arrowed) has a moderate dislocation density suggesting that it may have formed by progressive misorientation of part of the kink-band boundary, in a similar way to that described by Bell (1978).

4.4 Assessment of use of feldspars and micas in palaeostress estimation

The microstructures most commonly used in the estimation of palaeostresses are; dislocation density, sub-grain size and recrystallized grain size (see also Chapter 5). Dislocation densities in the feldspars are extremely heterogeneous and appear to vary with composition and are

therefore discounted. The formation of sub-grains is also heterogeneous, often only in grain mantles, with irregular cells due to tangled dislocations in grain cores. Only in albite do regular sub-grain networks form throughout grains and it may be possible to use sub-grain size in this mineral. Recrystallized grains in feldspars are formed by two distinct mechanisms, 'classical nucleation' which gives rise to new grains in the range 2-10 μm, and SGR which occurs at all scales giving grain sizes varying from 2 - 250 μm, depending on the strain. In addition a small amount of neocrystallization of feldspars is suspected.

Attempts were made to measure feldspar grain size optically but it was found difficult to resolve the smaller grains in standard (30μm) thin sections. It may be possible to use ultra thin (5-10μm) sections although the smallest grains will still be at the very limits of resolution of the optical microscope. Grain sizes were measured using TEM but no significant variation was found with strain, all mean grain sizes lying in the range (4-8μm). Etheridge and Wilkie (1979) have reported that feldspar recrystallized grain sizes are from one third to one fifth of quartz recrystallized grain size in the same sample. The factor of difference found in this study is ∿20.

As already mentioned in Section 4.3, the degree of recrystallization of white micas combined with the number of separate sources precludes the use of grain size in white micas for the estimation of stresses. However, in rocks in which alteration is limited and recrystallization is common (e.g. Bell (1979)) mica grain size may still provide some useful information. Dislocation densities in micas are heterogeneous, and regular sub-grain networks are not formed.

CHAPTER 5 THE ESTIMATION OF PALAEOSTRESSES

In this chapter the present 'state of the art' in palaeostress estimation is reviewed. Use is made of the internal consistency of the stresses estimated from different parameters for the same sample, with available experimental data, to obtain empirical relationships with stress for dislocation density, sub-grain size, and recrystallized grain size, for both quartz and olivine. The practical use of these equations is outlined, with examples taken from the literature. Finally observations made on samples from the Cap de Creus area are described, and the implied stress levels are discussed.

5.1 Palaeostress estimation, a review

During the past decade attempts have been made to estimate the flow stresses obtaining during deformation using microstructural features of the rocks themselves. Sub-grain size was the first parameter to be considered (Raleigh & Kirby, 1970) followed by recrystallized grain size (Post, 1973) and dislocation density (Goetze & Kohlstedt, 1973). Deformation twinning has also been used (Jamison and Spang,1976), but is only of use in calcite, dolomite and orthopyroxene (Tullis, 1980) and is not considered further here.

Each of the parameters will be reviewed in turn, both in terms of theoretical relationships, and empirical relationships derived from experimentally and naturally deformed material. Problems associated with the measurement of these parameters, and their stability during subsequent deformation and thermal events will also be discussed.

5.1.1 Dislocation density

Kohlstedt (1980) has reviewed the present theoretical relationships linking the differential stress (σ_1-σ_3) to the free dislocation density (ρ_f) (that is the density of dislocations not part of organized networks). He

has identified two types of theoretical approach. The first looks at the interaction between the stress fields of dislocations and determines the density of dislocations for which adjacent dislocations will be just unable to pass each other under the applied differential stress. The alternative model takes a well-annealed grain (i.e. containing a negligible number of dislocations) and applies a certain level of differential stress. Under this stress, dislocations multiply from 'Frank-Read' type sources, and continue until the back stress has reduced the effective stress to a level below the critical stress required to operate such a source.

Both these approaches give the relationship,

$$\sigma_1 - \sigma_3 = \alpha\mu\underline{b}\rho_f^{0.5} \qquad (1)$$

where μ is the shear modulus, $\underline{b}$ the burgers vector, and α is a dimensionless constant generally within the range $0.5<\alpha<5.0$ (Takeuchi & Argon, 1976); the variation being considered to be due to the types of dislocation arrays found on different lattices, and the exact relationship of differential stress with internal stress.

Experimental data from metals (Takeuchi & Argon, op.cit.) show that the exponent of the dislocation density varies significantly from 0.5. A more general form of equation (1) is, therefore,

$$\sigma_1 - \sigma_3 = k_1\mu\underline{b}\rho_f^{u} \qquad (2)$$

where k_1 replaces α as a constant that is only dimensionless for $u = 0.5$. It is important, therefore, when using empirically derived relationships to take account of the units in use. All the relationships quoted in this chapter have been recalculated in terms of stress in Pa, dislocation density in intersections m^{-2}, and grain and sub-grain sizes in m, unless otherwise stated.

Takeuchi & Argon (op.cit.) report values of u for pure metals, and

alloys, and, although these fall in the range $0.45<u<3.00$, most (c.70%) fall in the more restricted range $0.50 \leqslant u \leqslant 0.70$.

Quartz and olivine are the only geological materials for which there are reliable experimental data. For quartz, one experimental relationship has been reported (McCormick, 1977) for a suite of deformed synthetic quartzes,

$$\sigma_1 - \sigma_3 = 0.37\rho_f^{0.66}$$

which is very different to the equation used by Cooper et al. (1978)

$$\sigma_1 - \sigma_3 = 66\rho_f^{0.5}$$

obtained by putting 'likely' values of α, μ & $\underline{b}$ into equation (1).

More experimental data are available for olivine:-

Goetze (1975) for experimentally deformed olivine, found the relationship,

$$\sigma_1 - \sigma_3 = 100\rho_f^{0.5}$$

while Durham et al. (1977) found

$$\sigma_1 - \sigma_3 = A\rho_f^{0.62}$$

All the available experimental data for quartz and olivine have been plotted together on normalized axes of $\sigma_1-\sigma_3/\mu$ v. $\rho\underline{b}^2$ by Kohlstedt (1980) (Fig.5.1) which include the data from McCormick (1977), Goetze (1975) and Durham et al. (1977) already mentioned plus that of Zeuch and Green (1979).

The data for olivine and quartz fall on roughly the same line and the following relationships may, therefore, be derived

For quartz $\sigma_1 - \sigma_3 = 0.77\rho_f^{0.66}$ (3)

For olivine $\sigma_1 - \sigma_3 = 2.23\rho_f^{0.66}$ (4)

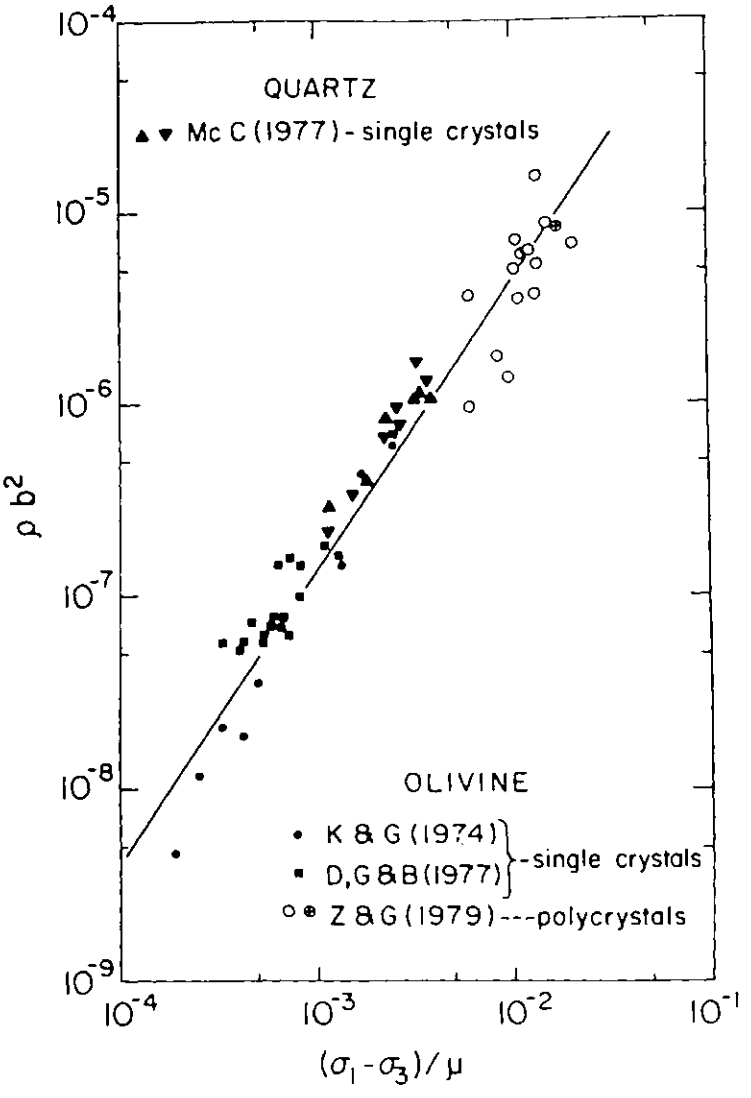


Fig. 5.1 Plot of dislocation density, normalized by the square of the burgers' vector, against differential stress, normalized by the rigidity modulus, for experimentally deformed quartz (McCormick,1977) and olivine (Kohlstedt & Goetze,1974; Durham et al., 1977; Zeuch & Green,1979). (from Kohlstedt,1980)

The value of u determined above falls in the range $0.50 \leqslant u \leqslant 0.70$ commonly found for metals, as previously described.

Methods used for the measurement of dislocation density may be divided into: decoration, etching and T.E.M., each with various restrictions affecting their use. Although a decoration technique has been described for quartz (White, 1970) no observations of dislocation structures have since been made using this method. In contrast the decoration technique for olivine has been much used since it was first described by Kohlstedt et al. (1976). (N.B. for a critical re-assessment of the use of this technique see Brodie & White, 1982).

Etchants capable of producing etchpits at the site of individual dislocations on polished or cleaved surfaces have been described both for quartz (Ball & White, 1977, Christie and Ord, 1980) and olivine (Wegner and Christie, 1974). The resultant etchpits are then observed by reflected light or S.E.M. The direct observation of dislocations in minerals using T.E.M. has been used in a large number of studies during the last decade e.g. White (1971) and Boland et al. (1971).

The actual measurement of dislocation density is similar for decorated thin sections studied optically, and for thin foils studied by T.E.M., and is subject to the same drawbacks. The standard method is to measure the number of intersections of dislocation with the foil or section surface, for a known area; the relationship of this to the true dislocation density depends strictly on the randomness of dislocation orientation (McCormick, 1977). The technique becomes difficult to apply at high dislocation densities $\geqslant 10^{12}\ m^{-2}$ for a thin section studied optically, and $\geqslant 10^{13} m^{-2}$ for T.E.M.

Dislocation densities are often markedly heterogeneous across single grains, and large areas generally need to be looked at to obtain a statistically valid result. This is particularly important in the case of T.E.M.

studies of grains containing high dislocation densities. In order to allow measurement, such high magnifications may be required that areas of only a few μm^2 are measured on each micrograph and as many as a hundred such micrographs may be needed for each grain.

On etched, cleaved or polished, surfaces dislocation densities may be measured simply from the number of dislocation etch-pits, not part of sub-grain walls, per area. The principle constraint on such measurements is the size of etch-pit produced; accurate determinations may only be made as long as individual etch-pits are resolved. Ball & White (1977) figure etch-pits $\sim$1.0 x 0.5 μm allowing densities of $\rho_f \sim 10^{13} m^{-2}$ to be measured, whereas Christie and Ord (1980) figure larger etch-pits which they say are only usable up to $\rho_f \sim 10^{11} m^{-2}$. For olivine, the pits figured by Wegner and Christie (1974) are $\sim 2\mu m$, and would, therefore, be suitable only up to a density of $\rho_f \sim 5 \times 10^{11} m^{-2}$.

5.12 Sub-grain size

Theoretical relationships for the variation of sub-grain size (d_{SG}) with the applied differential stress have been given by Holt (1970), and Twiss (1977). Holt (1970) derived a relationship between the free dislocation density and the spacing of dislocation networks in an analysis analogous to that used to describe the spinodal decomposition of an initially homogeneous solid solution. He considered, in this case, an initially homogeneous distribution of dislocation of alternating positive and negative sign, and looked at how the total strain energy might be minimized by incorporating dislocations into networks. As in the case of a spinodal decomposition, the analysis gives rise to a dominant wavelength λm, which he equates with an equilibrium sub-grain size, that is a function of the remaining face dislocation density,

$$d_{SG} = C\rho_f^{-0.5} \qquad (5)$$

where C is a dimensionless constant.

The differential stress is introduced by combining this with equation (1) to give

$$\sigma_1 - \sigma_3 = \beta\mu\underline{b}d_{SG}^{-1.0} \qquad (6)$$

where β is another dimensionless constant.

Twiss (1977) used a different approach (described in the next section as applied to recrystallized grain size), but obtained the same expression.

Experimental observations (Takeuchi & Argon, 1976) have shown that the exponent of the sub-grain size varies from -1, and the more general version of equation (1) is

$$\sigma_1 - \sigma_3 = K_2\mu\underline{b}d_{SG}^{v} \qquad (7)$$

where K_2 replaces β as the constant.

Observed values of v in metals vary for the range $0.5 \leqslant v \leqslant 4.0$, but most ($\sim$80%) fall in the range $1.0 \leqslant v \leqslant 1.42$. Two recent studies have determined this relationship for olivine; Ross et al. (1980) found the following

$$\sigma_1 - \sigma_3 = 4.7d_{SG}^{-1.61} \quad \text{('dry')}$$

$$= 10.2d_{SG}^{-1.45} \quad \text{('wet')}$$

N.B. The dry tests of Ross et al. (op.cit.) are better described as 'damp' due to water escaping into the sample from dehydration of the confining medium.

whereas Karato et al. (1980) obtained

$$\sigma_1 - \sigma_3 = 4.7d_{SG}^{-1.50}$$

which all differ considerably from equation (6). However, if account is taken of the observed values of u in equation (2), and if this is then substituted in equation (5) we obtain

$$\sigma_1 - \sigma_3 = k_2 \mu \underline{b}\, d_{SG}^{-1.33}$$

There are no such experimentally determined relationships between stress and sub-grain size in quartz.

In the first study that looked at the variation of sub-grain size with flow stress, Raleigh & Kirby (1970) measured the sub-grain size optically. Green and Radcliffe (1972(a), 1972(b)) reexamined the same samples using T.E.M. and found much smaller sub-grains. Mercier et al. (1977) measured them again using a decoration technique and obtained values between those of the other two studies. Mercier et al. (op.cit.) suggested that the T.E.M. study was biased towards areas with the smallest sub-grains, whilst normal optical microscopy simply failed to pick up the low misorientation boundaries visible by T.E.M. White (1973(a)) had already noted the existence of what he called sub-grain in sub-grain structures, and concluded that only the larger order of sub-grains with misorientation > 1^{o} would be visible optically.

In measuring sub-grain size, therefore, it is necessary to use one of the three techniques already described for measuring dislocation density. Of these, T.E.M. and decoration have been used on olivine, the former being more suited to the smallest sub-grain size and the latter being essential for the measurement of large spacings (sub-grain size of up to 1mm have been reported).

In quartz most observations of sub-grain size have been carried out using T.E.M. This is valid for small sub-grain sizes, especially if H.V.E.M. is used, allowing large continuous, areas of sub-grains to be measured. However, as has been pointed out by Christie and Ord (1980), for sub-grain sizes of $d_{SG} > 20\mu m$, most T.E.M. studies will fail to observe the upper end of the size distribution. They therefore advocate the use of etching, a technique already used successfully to observe sub-grains of $d_{SG} \sim 50\mu m$ (Ball

and White, 1977), and it is this latter method that has been used throughout this study.

5.1.3 Recrystallized grain size

Theoretical relationships between the size of recrystallized grains and the flow stress have been developed by Mercier (1976), and Twiss (1977, 1980). Both analyses relate to the formation of strain-free nuclei followed by grain boundary migration that can be related to GBM recrystallization mechanisms (Section 4.1.1.4)

Mercier (1976) based his analysis on a 'classical nucleation' occurring preferentially at the intersections of sub-grain, and grain boundaries. Fig. 5.2 (after Mercier et al. 1977) illustrates the formation of a strain-free nucleus, with the main driving force for growth coming from the sub-grain boundaries. This analysis gave the following equation:

$$\sigma_1 - \sigma_3 = \gamma d_{PG}^{-0.71} \exp.(-13500/RT) \qquad (8)$$

where R is the Gas Constant and T is the Absolute Temperature.

Twiss (1977) presented a general analysis of the relationship of grain, and sub-grain size to stress. This rests on the basic assumption that the formation of sub-grains and recrystallized grains must be energetically favourable processes, which leads to an equality between the energy due to the boundary and the total energy associated with dislocation in the enclosed volume.

For recrystallized grain size this gives the expression

$$\sigma_1 - \sigma_3 = k_3 d_{RG}^{w} \qquad (9)$$

where w lies in the range $0.67 < w \leqslant 0.78$. This relationship is derived using the expression $\sigma \alpha \rho_f^{0.5}$; if a value of u = 0.66 is used in equation (2) the range becomes $0.86 \leqslant w \leqslant 0.98$.

Empirical relationships for experimentally deformed olivine have been

reported by; Post (1973), Mercier et al. (1977), Ross et al. (1980), and Karato et al (1980).

$$\sigma_1 - \sigma_3 = 1.8 \times 10^5 d_{RG}^{-0.67} \quad \text{('dry')} \quad \text{Post}$$

$$= 5.5 \times 10^4 d_{RG}^{-0.81} \quad \text{('dry' \& 'damp')} \quad \text{Mercier et al.}$$

$$= 8.9 \times 10^4 d_{RG}^{-0.79} \quad \text{('damp')} \quad \text{Ross et al.}$$

$$= 1.7 \times 10^4 d_{RG}^{-0.85} \quad \text{('dry')} \quad \text{Karato et al.}$$

$$= 8.9 \times 10^4 d_{RG}^{-1.22} \exp(14.2 \times 10^3/RT) \quad \text{('wet')} \quad \text{Ross et al.}$$

The temperature dependence observed in this last series of tests is small, but over the range of possible temperatures under which olivine can deform ductilely, it may be significant (see also next section).

For quartz only two studies have been published that link grain size to flow stress; Mercier et al. (1977) and Christie et al. (1981).

$$\sigma_1 - \sigma_3 = 2.1 \times 10^4 d_{RG}^{-0.71} \quad \text{('wet')} \quad \text{Mercier et al.}$$

$$= 900\, d_{RG}^{-1.11} \quad \text{('wet')} \quad \text{Christie et al.}$$

Naturally deformed quartz and olivine have both been observed to recrystallize by SGR (see section 4.1.1.4) mechanism. (White, 1973(b), Poirier & Nicolas, 1975). It is normally assumed (e.g. Mercier 1980) that size of new grains formed by this mechanism will be directly proportional to the equilibrium sub-grain size, i.e.

$$\sigma_1 - \sigma_3 = k_4 d_{RG}^{v} \qquad (11)$$

No experimental relationships have been determined for quartz or olivine for this mechanism, but work on halite (Guillopé and Poirier, 1979) suggests that the exponent of grain size is not necessarily the same as that of sub-grain size.

Grain sizes are commonly measured optically, either by transmitted or reflected light. However, a few mylonites have been observed with a re-

crystallized grain size of $d_{RG} < 5\mu m$ (e.g. White, 1979(b)), and the smaller end of the distribution will be difficult to resolve optically. This may be overcome by looking at etched surfaces on S.E.M., or thin foils by T.E.M.

It has been emphasised by many workers, (e.g. Twiss, 1977; White, 1979(a); Etheridge and Wilkie, 1979) that only relatively 'pure' (i.e. monominerallic) rocks can be used for the estimation of stress from recrystallized grain sizes. It is commonly observed (e.g. Spry, 1976; Hobbs et al. 1976) that the effect of a second phase, such as fine micas, is to reduce the grain size when compared with adjacent bands, free of the other phase. The second phase is thought to prevent the grain size increasing to reach an equilibrium size by pinning the grain boundaries. It is more difficult, however, to determine how an initially coarse-grained, but impure rock is prevented from attaining its equilibrium size, as the second phase must be present in a high percentage of grain boundaries to prevent secondary grain growth after the new grains have been formed. Also, new grains formed by an SGR mechanism should be completely unaffected by the presence of a second phase.

5.1.4 The effect of intrinsic and extrinsic variables

The only intrinsic variable that has been considered as likely to affect the proposed relationships is the initial water content (White, 1979(a)), but no experimental study has as yet been made to look for such an effect. It has been suggested, for the extrinsic variables, that temperature, strain-rate and P_{H_2O} may all alter the relationships; it should be remembered that these are not independent variables.

Mercier (1976) included a small temperature dependence in his equation for grain size (Equation 10), that predicts a smaller equilibrium grain size at a lower temperature for the same stress. Ross

et al. (1980) have observed a temperature dependence of similar magnitude on their 'wet' tests, but could find no significant variation in their 'damp' tests. No temperature dependence has been observed for dislocation density or sub-grain size in experimentally deformed geological materials. In the metallurgical and material science literature, however, several studies (e.g. Streb and Reppich (1973) LiF, Belkin et al. (1973) Al) have reported temperature effects, with lower dislocation densities and larger sub-grains developed at higher temperatures under the same stress. White (1979(a)) has pointed out that considerable errors will result, even for small temperature dependencies, from extrapolation from the conditions available in the laboratory, to those obtaining in the lithosphere.

Any effects due to a variation in strain-rate cannot be divorced from those due to temperature as they are linked by the flow law of the material. Thus when Roberts and Ahblom (1978) report that for fixed stress a smaller

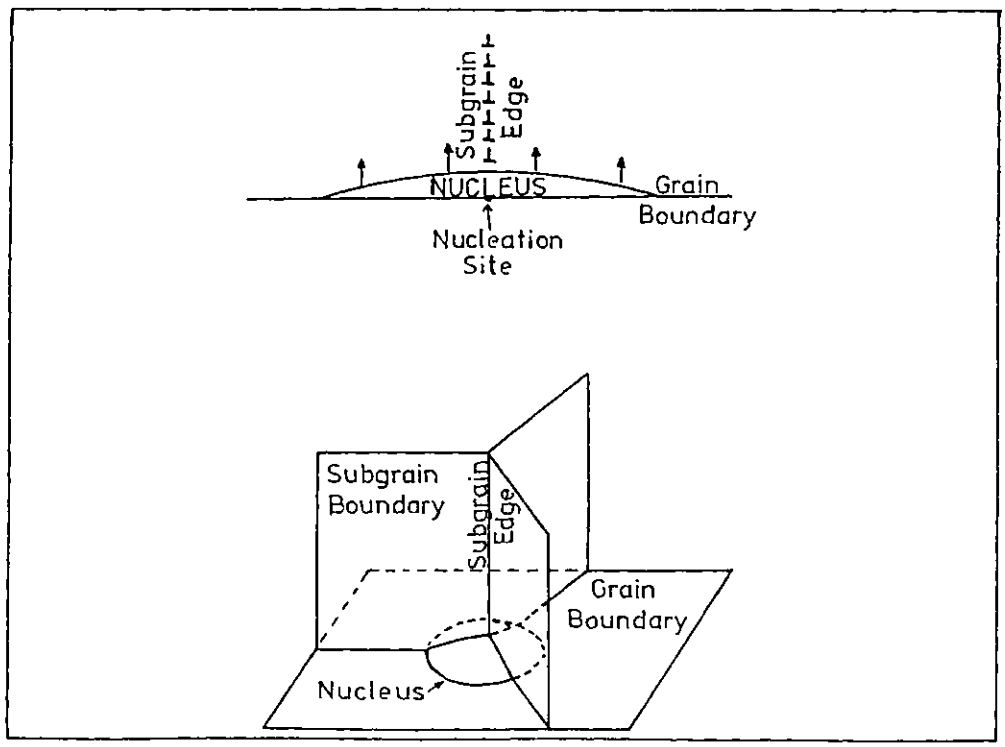


Fig. 5.2 Formation of a nucleus at a sub-grain-grain intersection. The formation of a flattened nucleus increases the surface energy only slightly, the main driving force for growth being normal to the grain boundary. Below three-dimensional view of growing nucleus.

grain size is generated as the strain-rate is lowered, the temperature must also have been lowered.

Ross et al. (1980) have observed a considerable change in the equation relating grain size to stress from olivine deformed 'damp' to those samples deformed 'wet'. No similar observations have been made for quartz as the only published work is on hydrous assemblies. It is not clear why there should be a variation of the exponent with P_{H_2O}. Ross et al. (op.cit.) do not find any similar effect on the relationship between sub-grain size and stress.

From the available experimental data it is, as yet, impossible to confirm or deny that extrinsic variables may alter the derived expressions for one or all of the parameters in geological materials. In the absence of firm evidence it is considered advisable to neglect the possible effects for the purpose of this study, rather than include arbitrary factors in the equations.

5.2 Internal consistency of stress estimates

In many recent studies (e.g. Christie and Ord, 1980, Kohlstedt et al. 1979) there has been a tendency to calculate stresses for each of the measured parameters using published equations, sometimes as many as three separate ones for each parameter. The results are, therefore, extremely difficult to interpret. For example, if the stress from the recrystallized grain size in a quartzite sample is estimated using both the theoretical equation of Twiss (1977) and the empirical expression of Mercier et al. (1977) and the stress from the sub-grain size is estimated using the equation of Twiss (1977), one might get values of 50MPa and 30MPa respectively for grain and 30MPa for the sub-grain size.

If the higher of the two estimates for the grain size is accepted, this implies that either the two microstructures reflect different stresses, or that annealing has taken place. If, however, we accept the smaller estimate

from the grain size the two stress values are consistent. It is important to be able to determine whether or not measured parameters were set in equilibrium with the same flow stress and a method for doing this will now be outlined.

The approach used is one taken by Toriumi (1979) and Matsui et al. (1980) for comparing sub-grain size and dislocation densities in olivine. One parameter is plotted against another for each of a series of samples in an attempt to define an equilibrium line.

Starting with the two parameters compared in the above studies; by combining equations (2) and (7) we obtain

$$k_1 \rho_f^{\,u} = k_2 d_{SG}^{\,v} \qquad (12)$$

which becomes, on taking logs and rearranging

$$\log_{10}\rho_f = {}^{v}/_{u} \log_{10} d_{SG} + {}^{1}/_{u} \log_{10} {}^{k_2}/_{k_1} \qquad (13)$$

which is the equation of a straight line whose slope is the ratio of the two exponents and whose intercept is related to the two constants.

Fig. 5.3 is a plot of $\log_{10}\rho_f$ against $\log_{10} d_{SG}$ for all the available data on naturally deformed olivine. Although no observations were made in this study on olivine, the data available were much better than those for quartz and are better suited to testing the internal consistency of stress estimates. Four different types of deformed olivine bearing rocks are distinguished; alpine-type peridotite, peridotite xenoliths from basalts, peridotite xenoliths from kimberlites and Pallasite meteorites.

The data cover three orders of magnitude of sub-grain size, five orders of magnitude of dislocation density and show a consistent trend. Within this overall trend it can be seen that the points fall into two separate fields; one being defined mainly by alpine-type peridotites and xenoliths from basalts, the other mainly by xenoliths from kimberlites and Pallasite meteorites. Gueguen (1977) has noted consistent differences in dislocation

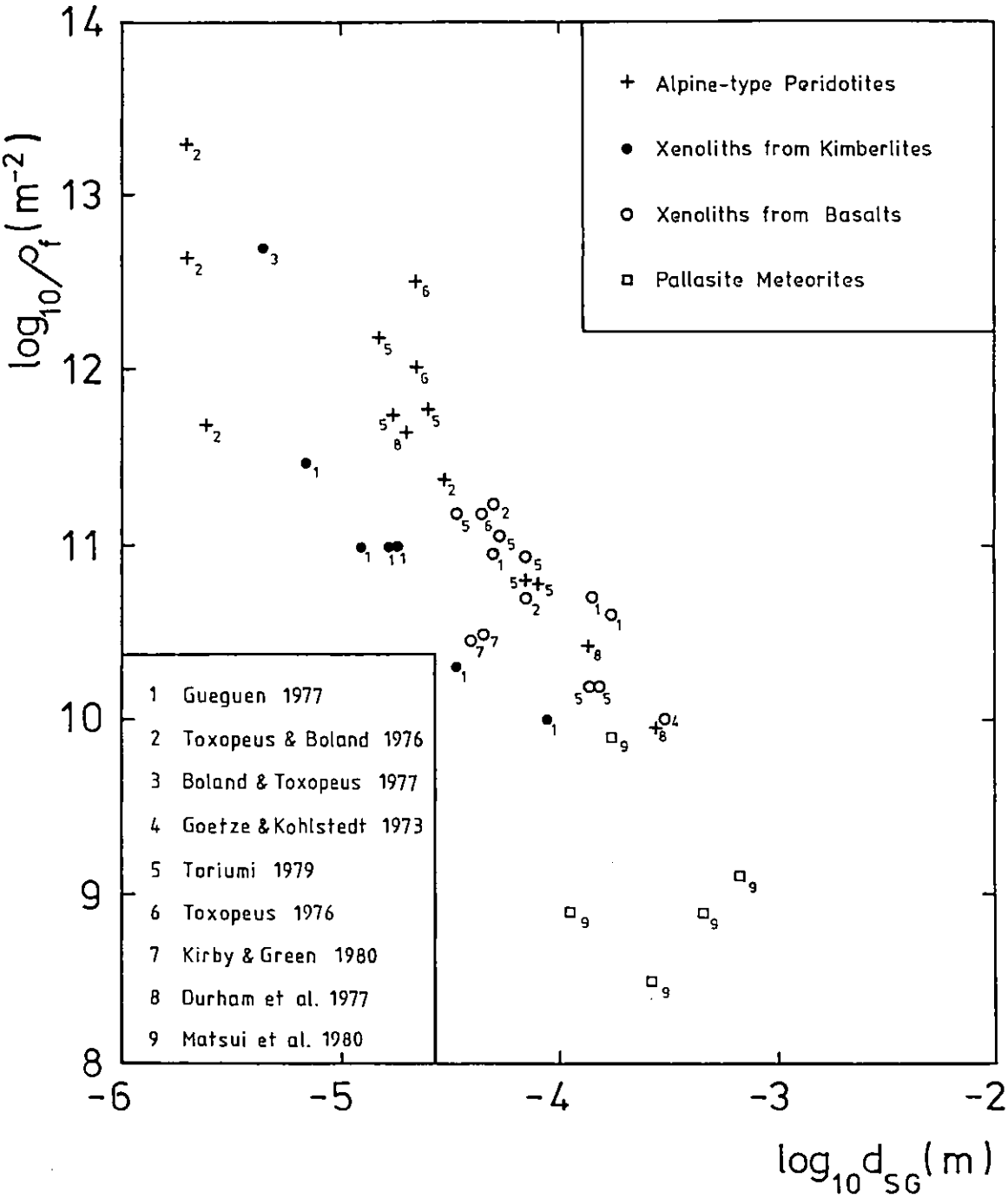


Fig. 5.3 Log-log plot of dislocation density (ρ) v. sub-grain size (d_{SG}) for all the published data on naturally deformed olivines from ; alpine-type peridotites, xenoliths from basalts, and kimberlites; and Pallasite meteorites.

microstructures developed within nodules from basalts and kimberlites, with the latter being more recovered. Matsui et al. (1980) have shown that data from Pallasite meteorites fall away from the line as defined by the data of Toriumi (1979) for alpine-type peridotites and basalt xenoliths and have ascribed this difference to annealing.

Taking all the data together it is suggested that most of the kimberlite nodules and Pallasite meteorites have suffered extensive annealing, and that the line as defined by basalt xenoliths and alpine-type peridotites represents data from samples whose sub-grain sizes and dislocation densities are in equilibrium with the same stresses. Fig. 5.4 shows a log-log plot with the equilibrium line marked, plus some experimental data from Matsui et al. (1980). The two unannealed data points fit well onto the empirical line for equilibrium, while the annealed samples fall within the same field as the kimberlite nodules.

The equation of the equilibrium line is

$$\log_{10}\rho_f = -1.68 \log_{10} d_{SG} + 3.88$$

where $-1.68 = {}^{v}/_{u}$ and $3.88 = {}^{1}/_{u} \log_{10} {}^{k_2}/_{k_1}$

from equation (3), $u = 0.66$ and $k_1 = 4.09 \times 10^{-2}$ (for $\mu = 7.8\times10^{10}$Pa, $\underline{b} = 6.98\times10^{-10}$m from Twiss (1977))

this gives $v = -1.11$ and $k_2 = 14.9$

$$\therefore \quad \sigma_1 - \sigma_3 = 809 d_{SG}^{-1.11} \qquad (14)$$

Fig. 5.5 is a synoptic diagram showing the experimentally determined relationships between stress and sub-grain size of Mercier et al. (1977), Durham et al. (1977), Karato et al. (1980), Ross et al. (1980) and the empirical relationship given by equation (14) from this study. The experi-

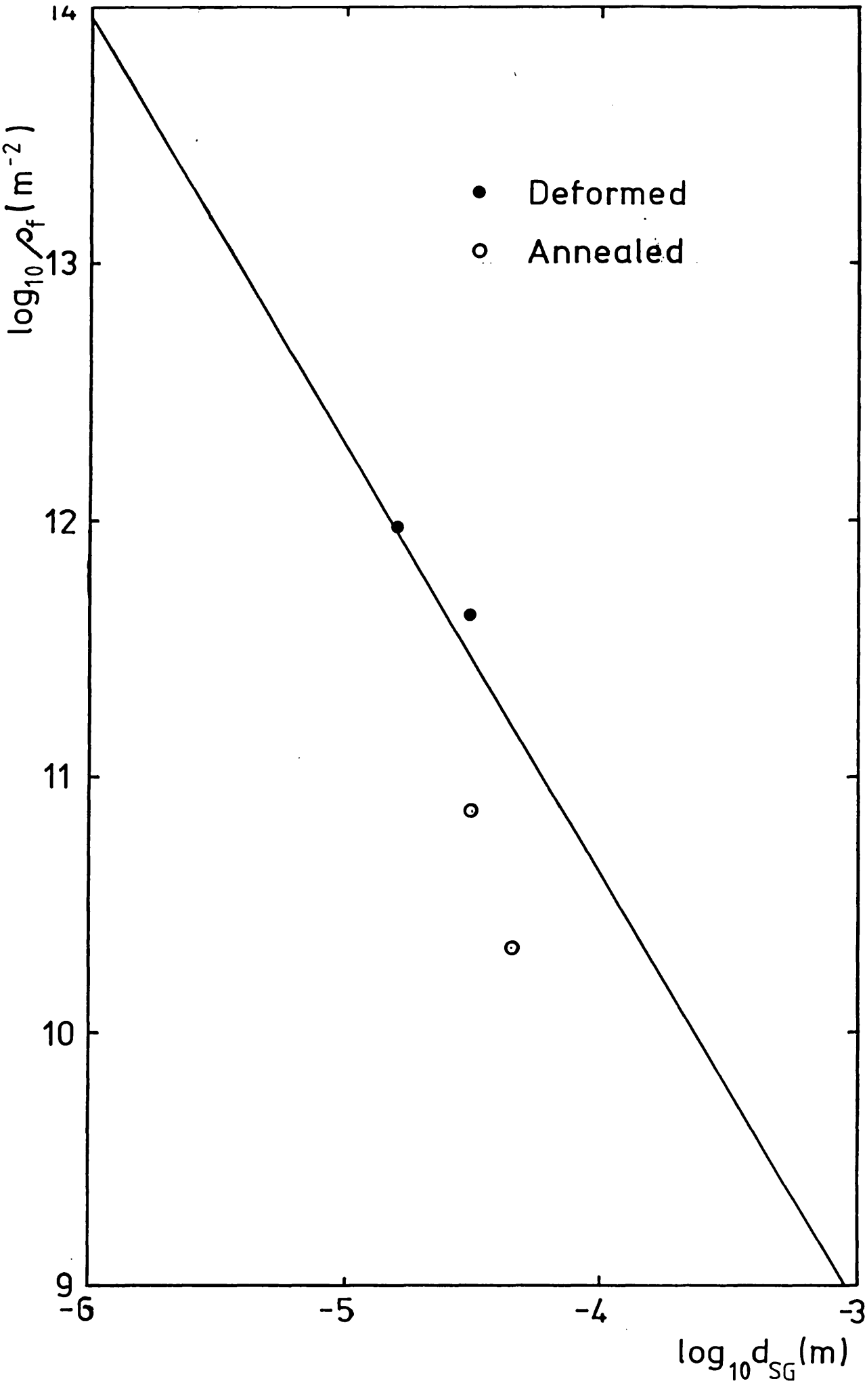


Fig. 5.4 Log-log plot if dislocation density (ρ) v. sub-grain size (d_{SG}) showing equilibrium line from Fig. 5.3 and data points from experimentally deformed olivine, from Matsui et al., 1980, two of which are annealed.

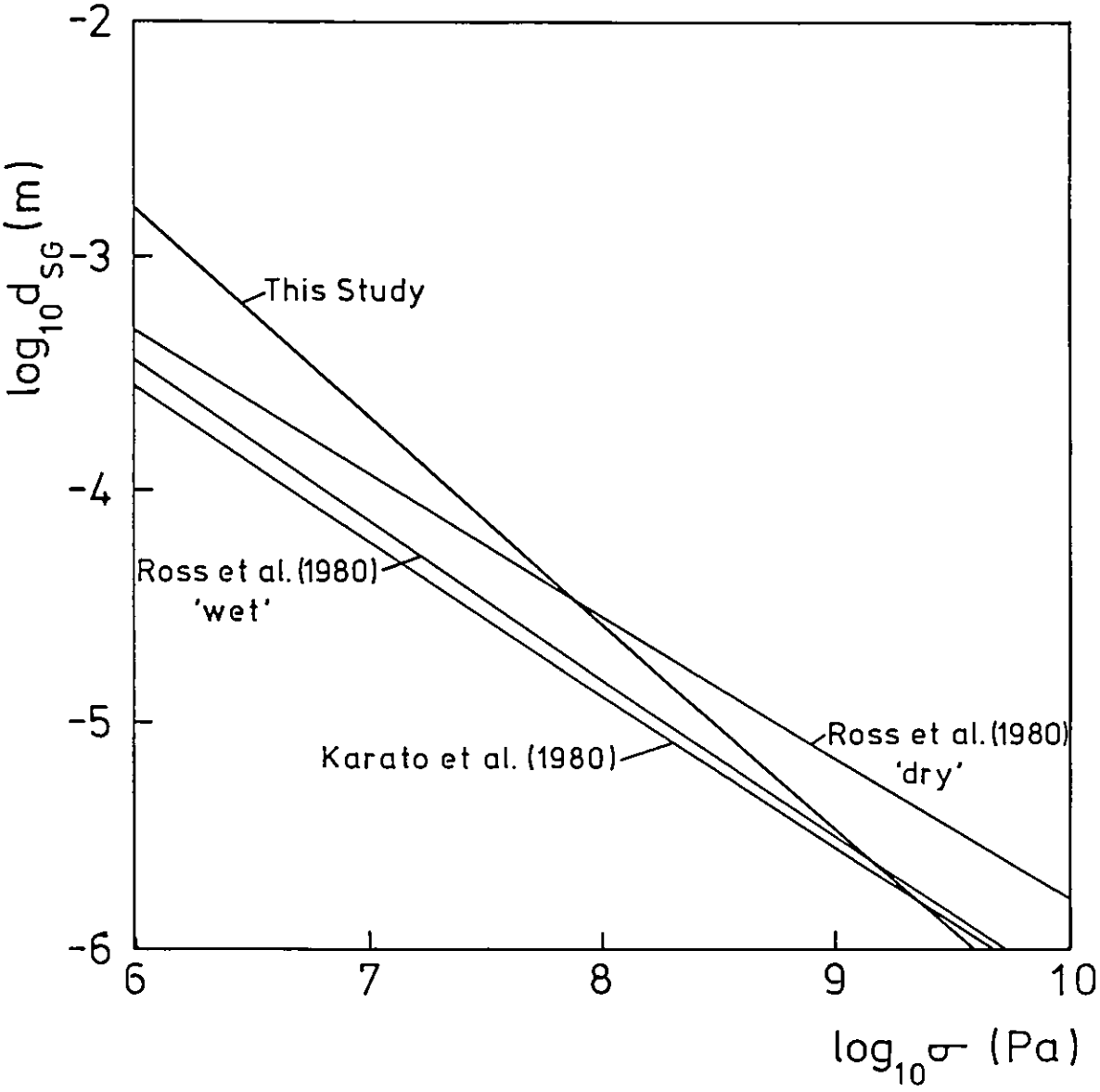


Fig. 5.5 Synoptic diagram of relationships between stress and sub-grain size for experimentally deformed olivine, with line derived from Fig. 5.3.

mental relationships give lines of similar slope but that are shifted from each other possibly due to the combined effects of variations in extrinsic variables, e.g. between Ross et al. (1980), 1000°C - 1300°C temperature range, 10^3MPa confining pressure, and Karato et al. (1980), 1650°C unconfined.

The empirical relationship represented by equation (14) falls within the range of the experimentally determined relationships. There is, therefore, good evidence that the experimental stress dependencies, and the observed microstructural variations in naturally deformed olivine are internally consistent.

The dislocation density and sub-grain size data for quartz are not as good as those for olivine, but they are all plotted on Fig. 5.6 combined with the data obtained from this study (for full details see section 5.5). The data are quite badly scattered, but are interpreted as representing an equilibrium line, with a spread away from it caused by the resetting of dislocation densities during later events (e.g. uplift).

The best-fit line has the equation

$$\log_{10}\rho_f = -1.51 \log_{10} d_{SG} + 4.39$$

which, when combined with equation (4), gives

$$\sigma_1 - \sigma_3 = 618 d_{SG}^{-1.00} \qquad (15)$$

Fig 5.7 shows how this compares with the theoretical expression due to Twiss (1977), and that proposed by White (1979(a)) using the experimental observation of Ardell *et al.* (1973). The relationship represented by equation (15) is in close agreement with the latter.

A relationship between sub-grain size and recrystallized grain size may be obtained from equations (7) and (9)

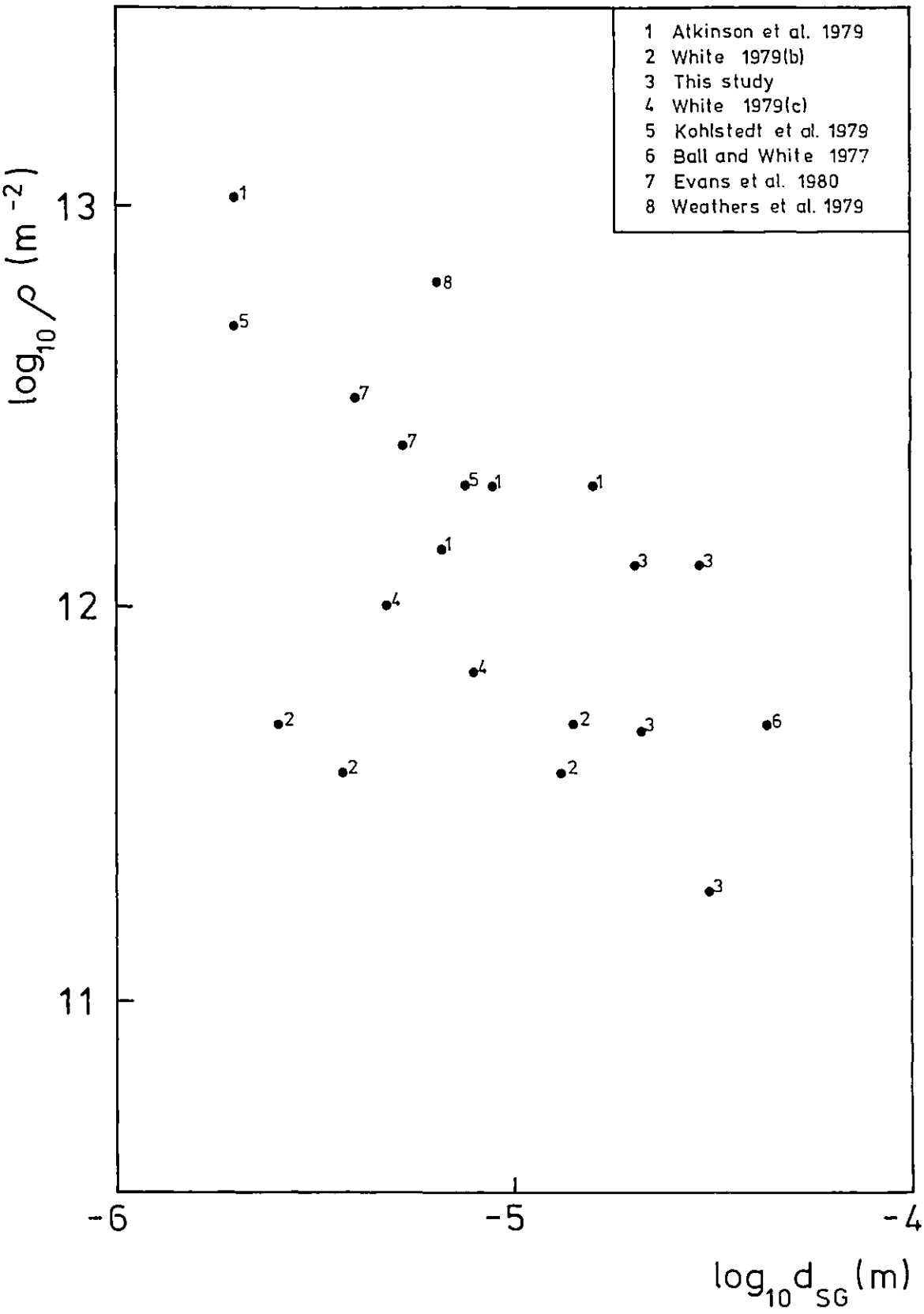


Fig. 5.6 Log-log plot of dislocation density (ρ) v. sub-grain size (d_{SG}) for all the published data on naturally deformed quartz, with data from this study.

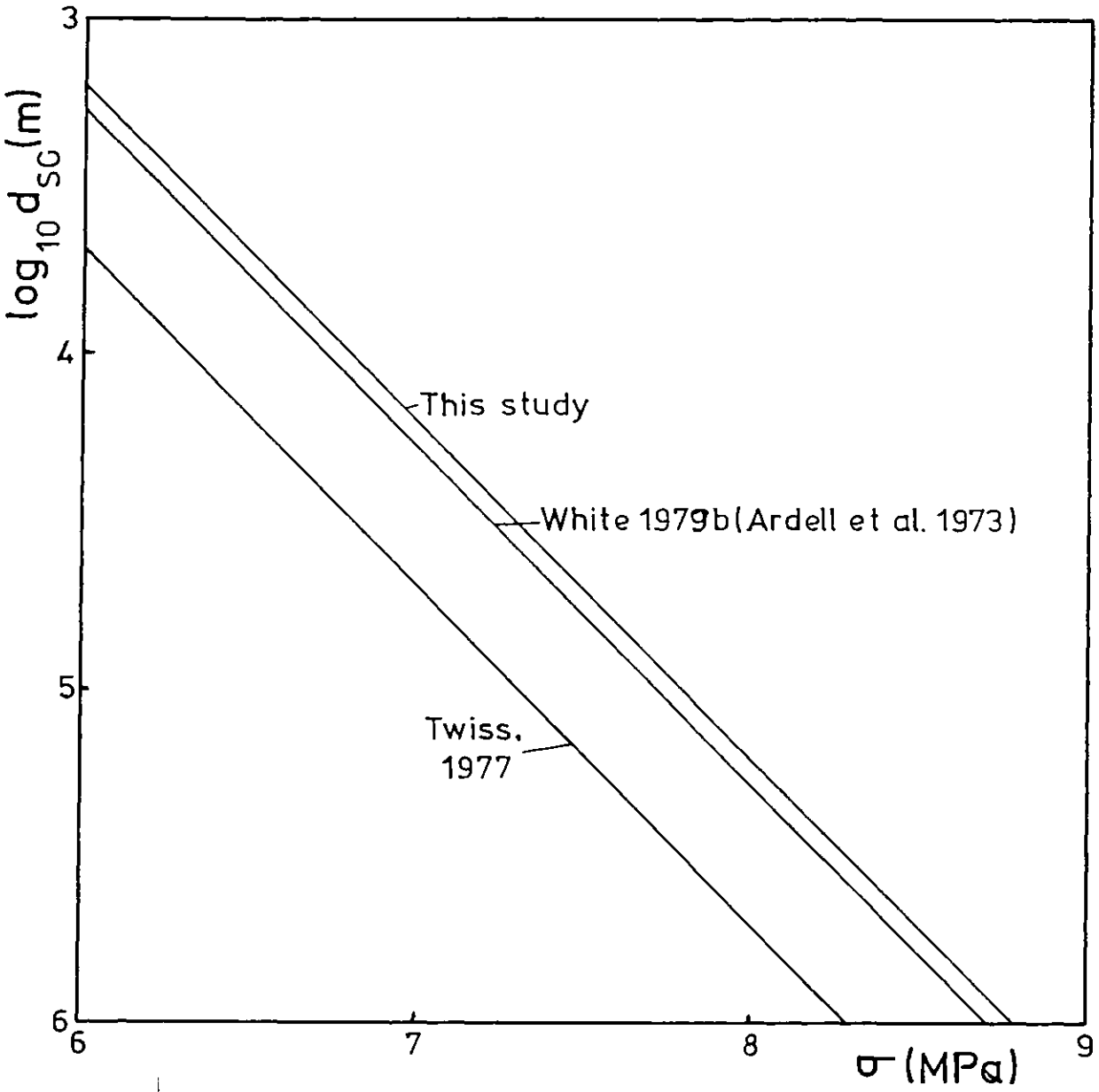


Fig. 5.7

Synoptic diagram of experimental (White, 1979(a) using the data of Ardell et al., 1973) and theoretical (Twiss, 1977) relationships between stress and sub-grain size for quartz, plus line from Fig. 5.6.

$$k_3 d_{RG}^{w} = k_2 \mu b d_{SG}^{v} \qquad (16)$$

taking logs as before

$$\log_{10} d_{RG} = {}^{v}/_{w} \log d_{SG} + {}^{1}/_{w} \log (k_2 \mu b / k_3) \qquad (17)$$

Fig. 5.8 shows all the available data for olivine of coexisting grain and sub-grain size. Two types of grain are distinguished, here designated 'old' and 'new'. The 'old' grains include data from samples that have textures described as protogranular (Gueguen, 1977) or palaeoblasts in partially recrystallized material. The 'new' grains are either the neoblasts in partially recrystallized material or from samples that have textures thought to be due to total dynamic recrystallization.

Clearly most of the 'new' grains are in equilibrium with sub-grain size, whilst only those old grains with very large sub-grain sizes fall near the equilibrium line. It has been suggested by many workers on peridotite nodules that protogranular textures represent flow in the mantle (for a recent review see Gueguen & Nicolas (1980)) and it is, therefore, presumed that these latter grains have been subject to insufficient deformation to alter their original sub-grain structure.

Two 'new' grain data points fall well away from the equilibrium line, both from the Kittefjall peridotite (Toxopeus and Boland (1976)). In this rock, however, two periods of dynamic recrystallization have been recognized (Toxopeus and Boland, op. cit.) with differing recrystallized grain sizes. It is the finer of these that appears to be in equilibrium with the sub-grain size, which is in accord with the observation (Pontikis and Poirier (1975), Ross et al. (1980)) that the sub-grain size reflects the highest stress that has affected the material.

The equilibrium line as marked gives the equation

$$\log_{10} d_{RG} = 1.22 \log_{10} d_{SG} + 1.72$$

which, when combined with equation (12) gives,

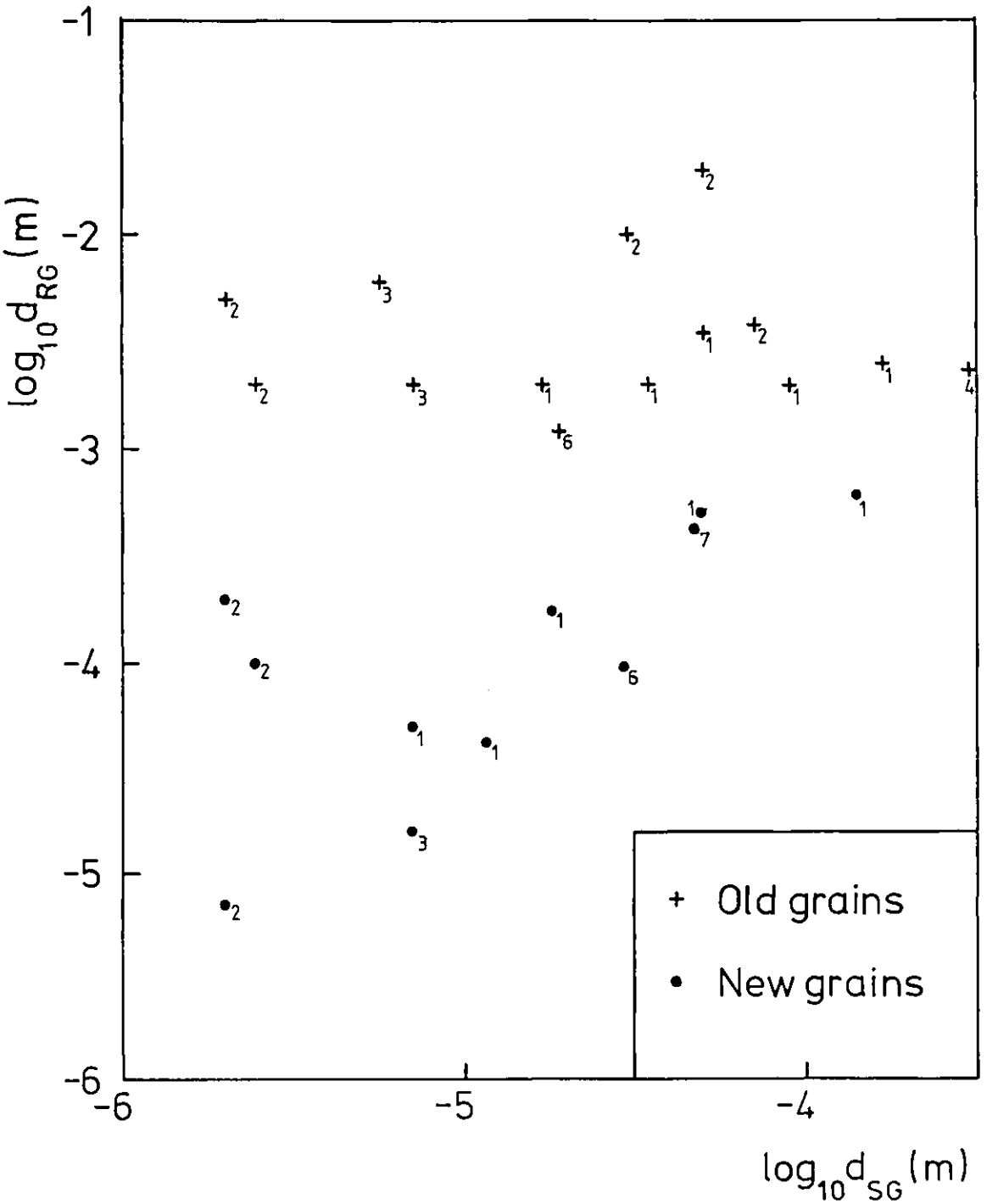


Fig. 5.8 Log-log plot of recrystallized grain size (d_{RG}) v. sub-grain size (d_{SG}) for all the published data on naturally deformed olivine, distinguishing between old (protogranular) grains and new recrystallized grains.

$$\sigma_1 - \sigma_3 = 3 \times 10^4 d_{RG}^{-0.91} \quad (18)$$

Fig. 5.9 is a synoptic diagram of all the observed experimental relationships for olivine, with equation (18). There is fair agreement between the empirical relationship and those determined experimentally for dry/'damp' olivine.

The corresponding data for quartz (Fig. 5.10) are again more scattered but the trend is well-defined. The best-fit line gives the equation

$$\log_{10} d_{RG} = 1.19 \log_{10} d_{SG} + 1.69$$

which combines with (15) to give

$$\sigma_1 - \sigma_3 = 1.6 \times 10^4 d_{RG}^{-0.84} \quad (19)$$

Fig. 5.11 shows the theoretical relationship of Twiss (1977), the experimentally determined ones of Mercier et al. (1977), Christie et al. (1981), and White (1979a) (using data from Ardell et al. (1973)), and the empirical relationship described by equation (19).

The empirical line fits very well with the relationships of Twiss (1977) and White (1979a), less well with that of Mercier et al. (1977) and is very different to that found by Christie et al. (1981). Considering the small amount of experimental data available for quartz, the empirical relationships derived for sub-grain, and grain size with stress fit them quite well and indicate that the three parameters are internally consistent in their variations with stress.

Returning to Fig. 5.10, one datum point falls well clear of the other data and is denoted by a different symbol. The difference is one of recrystallization mechanism, with SGR (see Section 5.1.3) in this case (Weathers et al. (1979)), as opposed to GBM in all the others. It is not certain that this discrepancy is due to the difference in mechanism, or due to a later high stress event that reset the sub-grain size but with insufficient

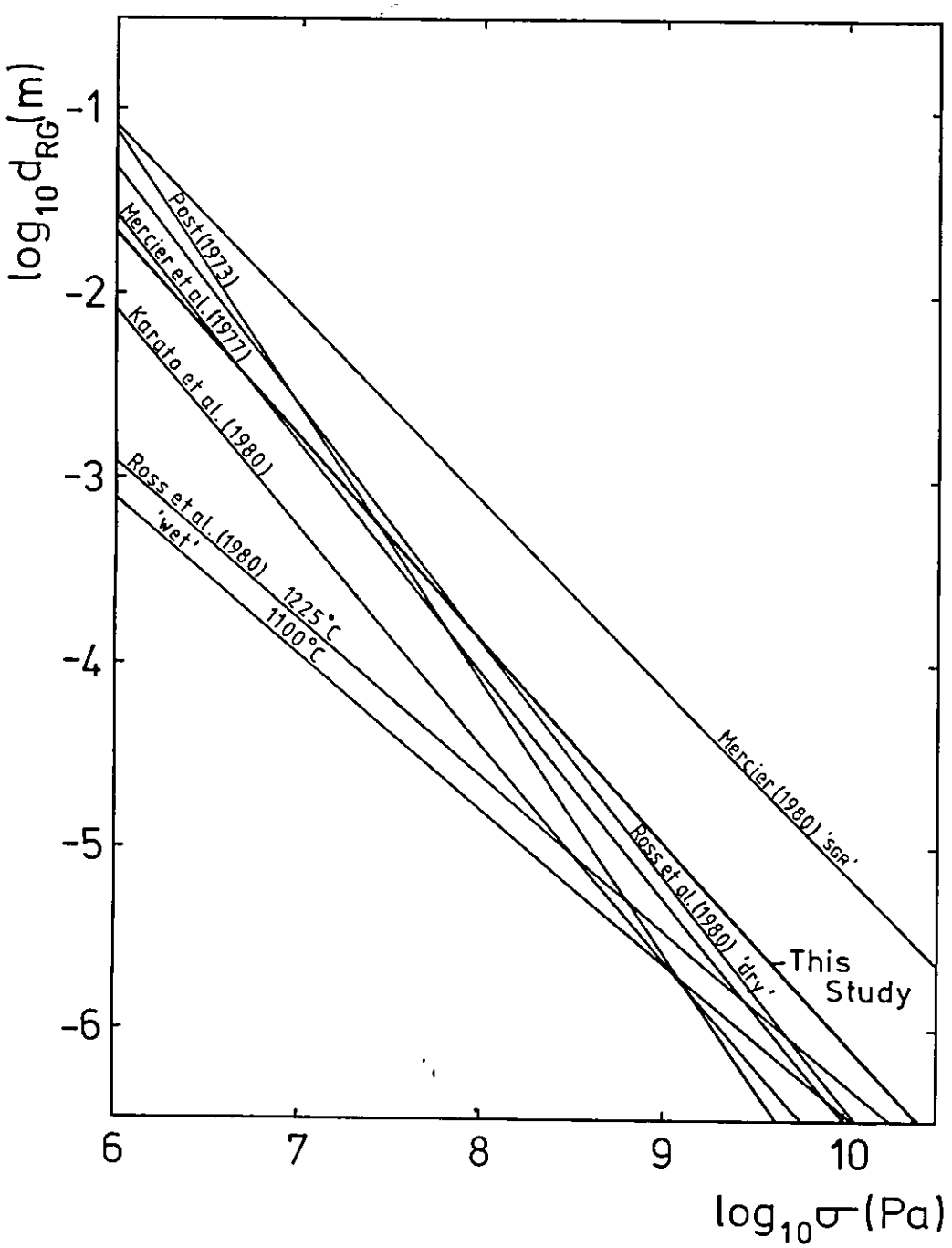


Fig. 5.9 Synoptic diagram of relationships between stress and recrystallized grain size in experimentally deformed olivine, plus line from Fig. 5.8.

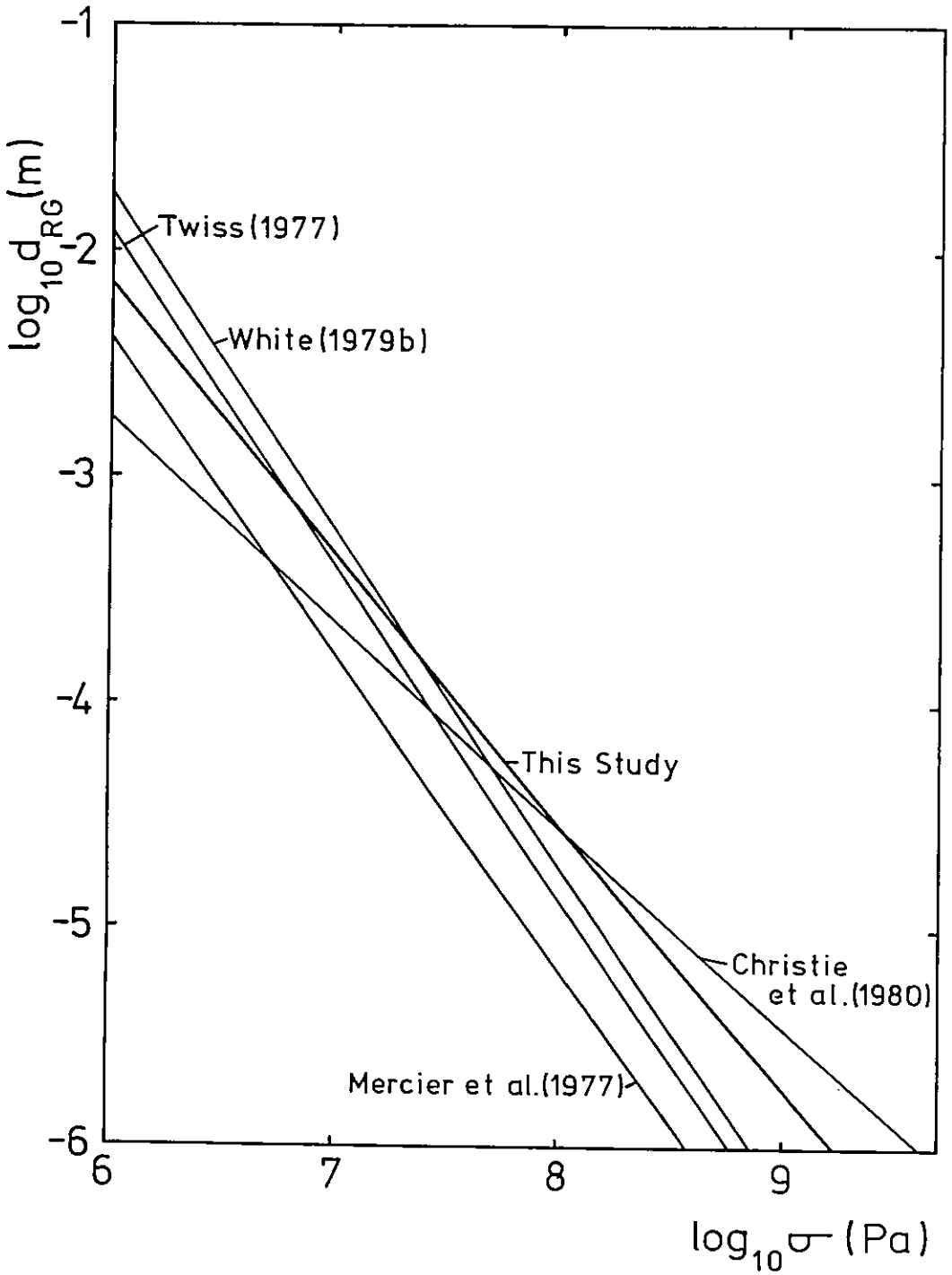


Fig. 5.11 Synoptic diagram of experimentally and theoretically derived relationships between stress and recrystallized grain size, including the line from Fig. 5.10.

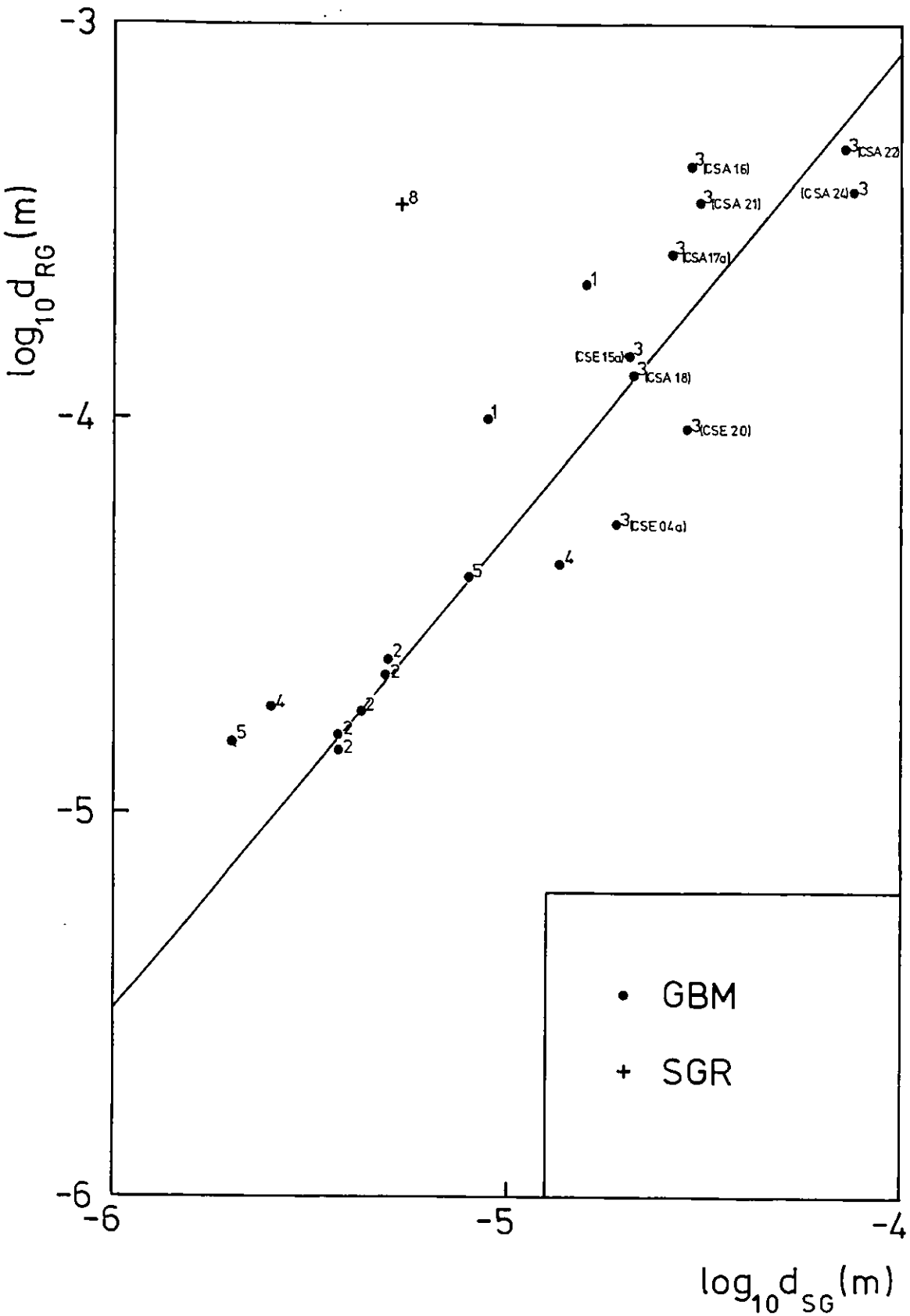


Fig. 5.10 Log-log plot of recrystallized grain size (d_{RG}) v. sub-grain size (d_{SG}) for all the published data on naturally deformed quartz, with data from this study (sample nos. indicated). The best-fit line is marked.

strain to cause recrystallization. However, such a change in the relationship between stress and recrystallized grain size has been suggested for olivine (Mercier (1980)) and, as the SGR mechanism has been observed to be the sole grain size reduction mechanism in some quartz tectonites (e.g. the amphibolite side of the Woodroffe Thrust, Bell and Etheridge (1976)), it is important to consider what effect this will have.

5.3 Effect of a change in recrystallization mechanism

Recent experimental studies (Guillopé and Poirier (1979), Schmid et al. (1980)) have shown that a change in recrystallization mechanism leads to a change in the grain size in equilibrium with the applied stress. The two mechanisms (already discussed in section 4.1.1) SGR, and GBM, have been shown in the aforementioned studies to characterise certain parts of stress temperature space, as shown in Fig. 5.12, using stress (normalized by the rigidity modulus)versus the homologous temperature (i.e. T/Tm, the ratio of the temperature to the melting point of a material in degrees kelvin).

Guillopé and Poirier (1979) have suggested that the boundary between the two curves represents critical values of grain boundary mobility, with part of the curve representing a critical stress with a slight temperature dependence, and the other a critical temperature with a slight stress dependence. This follows from a consideration of the effect of the impurity cloud found in the grain boundaries of all but the purest of materials, on the boundary mobility. Using the model of Lücke and Stüwe (1971) they show that grain boundary velocity variation with driving force is discontinuous and at a certain critical temperature and stress the grain boundary breaks away from the impurity cloud and becomes highly mobile. The exact position of the critical curve depends on the impurity content, the higher the content, the higher the temperature required for the boundary to break free.

Below the critical curve SGR recrystallization is the sole operative mechanism, while above the curve a combination of the two mechanisms operates.

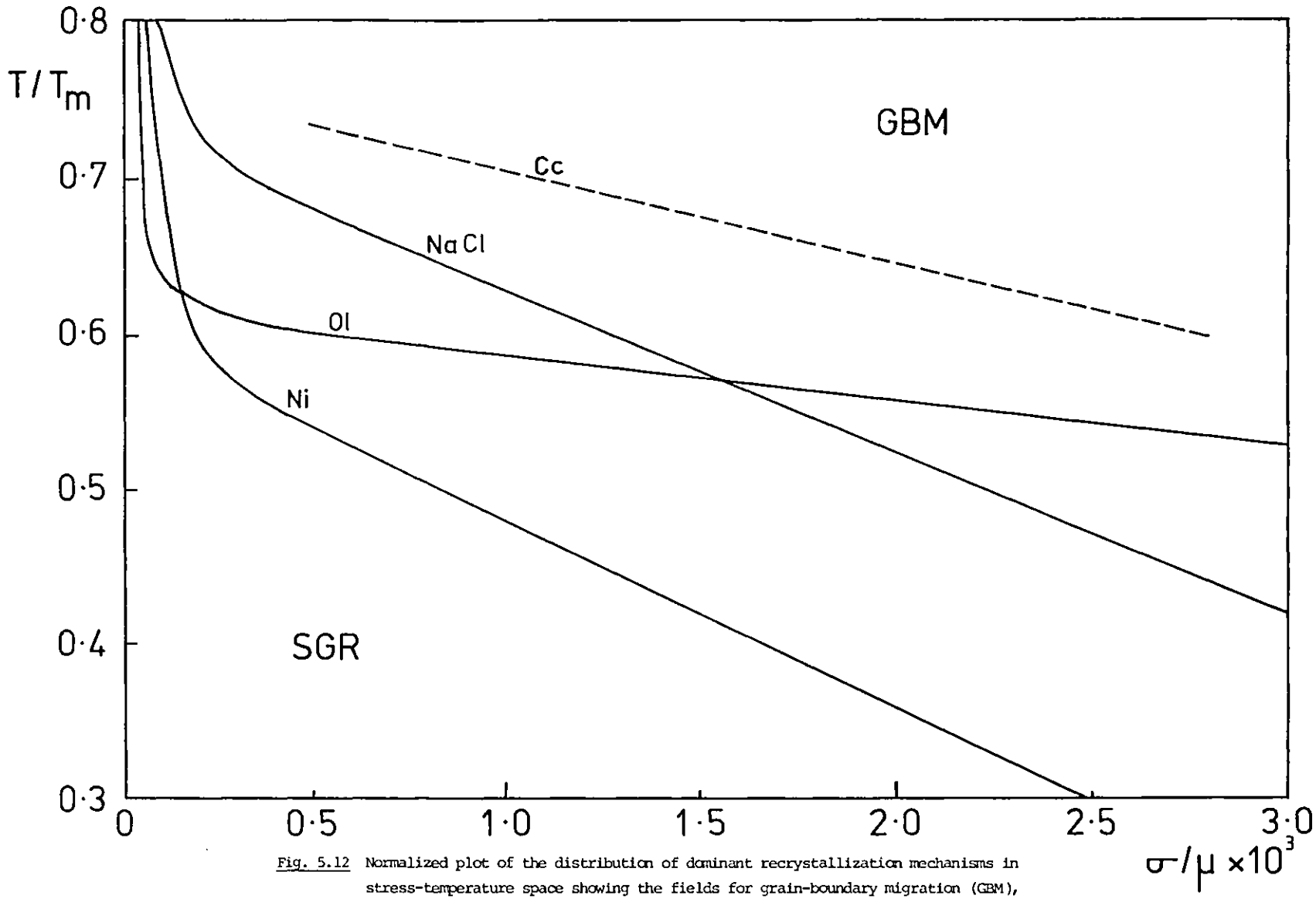


Fig. 5.12 Normalized plot of the distribution of dominant recrystallization mechanisms in stress-temperature space showing the fields for grain-boundary migration (GBM), and sub-grain rotation (SGR), for olivine (Mercier,1980), halite (Guillopé and Poirier ,1979) and nickel (Sellars,1978); the dotted line is for calcite estimated from the data of Schmid et al.1980.

The simultaneous operation of two mechanisms has also been observed in naturally deformed materials; in the present study and in the granulite side of the Woodroffe Thrust (Bell and Etheridge (1976)), both in quartz. However, there is a major difference between the grain sizes due to each mechanism in the experimentally deformed material compared with that found naturally.

The grain size due to GBM in the experimental studies is two to three orders of magnitude larger than that produced by SGR at the same stress. This leads to a cyclic type of deformation with initial SGR producing small new grains of increasing misorientation until one of the newly formed grain boundaries becomes sufficiently high angle to be highly mobile and sweeps across the other new grains, consuming them, until an equilibrium size is reached. This newly formed grain then undergoes sub-grain formation leading to further SGR recrystallization, and so on.

In minerals deformed under geological conditions it appears that the new grains formed by a GBM mechanism are of the same order as, and in some cases smaller than, those formed by SGR (see for olivine, Mercier (1980) and quartz, Bell and Etheridge, 1976). Because SGR is only a grain-size reduction mechanism, if a mineral has recrystallized by GBM to a size smaller than the SGR equilibrium size, no further recrystallization by a SGR mechanism can take place.

In geological materials there is little evidence for grain boundaries of high mobility except under high grade metamorphic conditions. Guillopé and Poirier (1979) have suggested that such materials may never undergo GBM recrystallization due to their relatively high impurity content. However, Schmid et al. (1980) have observed GBM recrystallization during the experimental deformation of a marble. It is possible from their observations to

construct a rough critical curve in stress/temperature space and this is shown in Fig. 5.12. In comparison with the other materials the critical curve for the marble is displaced to considerably higher temperatures, probably due to a small but significant impurity content.

If boundary migration of the type observed in halite and calcite is impossible in geological materials under low to medium- grade metamorphic conditions this suggests that the boundary migration that is observed must occur within the low-velocity regime of Lucke and Stüwe (1971) i.e. when the impurity cloud moves with the boundary. For the much slower rates of grain growth an analysis such as that due to Twiss (1977) would predict a much smaller equilibrium grain size. Tungatt (pers.comm.) has found just such an effect in sodium nitrate. The addition of calcium as an impurity anion completely suppresses the highly mobile GBM that is observed in the pure material. Some migration does still occur giving rise to an equilibrium grain size some two to three orders of magnitude smaller than that otherwise formed at the same stress and temperature.

It seems, therefore, that two distinct types of migration recrystallization mechanism may be developed; high-mobility grain boundary migration (HMGBM) in which the boundary escapes its impurity cloud, low-mobility grain boundary migration (LMGBM) in which the migration is controlled by impurities within the boundary. The latter mechanism will also be thermally activated, that is there will be a temperature below which the boundary velocity will be negligibly slow. Fig. 5.13 shows the suggested boundaries between the mechanisms in stress/temperature space. Not all impurities will necessarily act to suppress boundary mobility, particularly the presence of water may enhance the migration in silicates. The principal effect on the curves shown in Fig. 5.13 for a silicate such as quartz is likely to be to move the boundaries towards lower temperatures.

In any area in which there are sufficient variations in temperature

Fig. 5.13 Schematic diagram of boundaries between recrystallization mechanisms in stress-temperature space showing the expected fields for SGR, LMGBM (low-mobility GBM), and HMGBM (high-mobility GBM), indicating the effect of impurity content on the boundary for HMBGM.

Fig. 5.14 Schematic log-log plot of stress v, recrystallized grain size, showing the effect on equilibrium grain size at constant stress of an increase in temperature that leads to progressive changes in recrystallization mechanisms.

FIG. 5.13

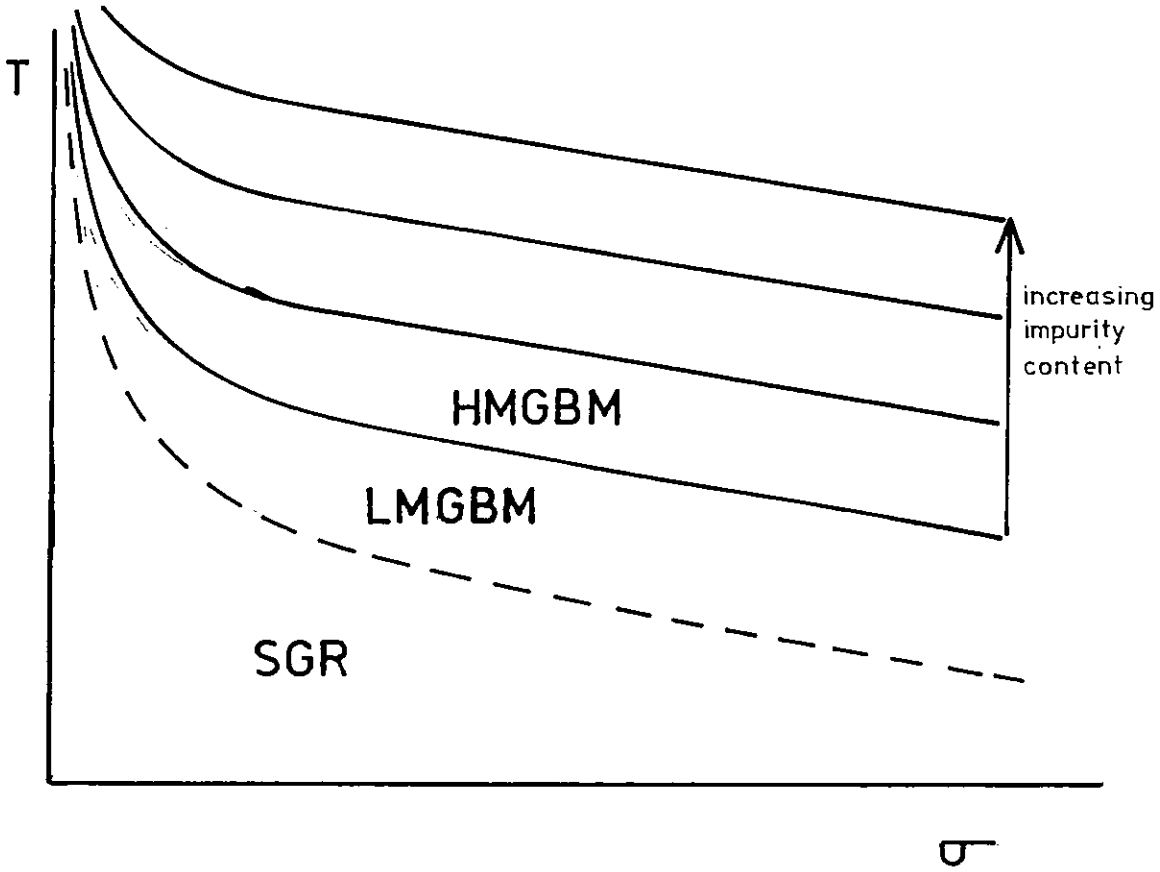
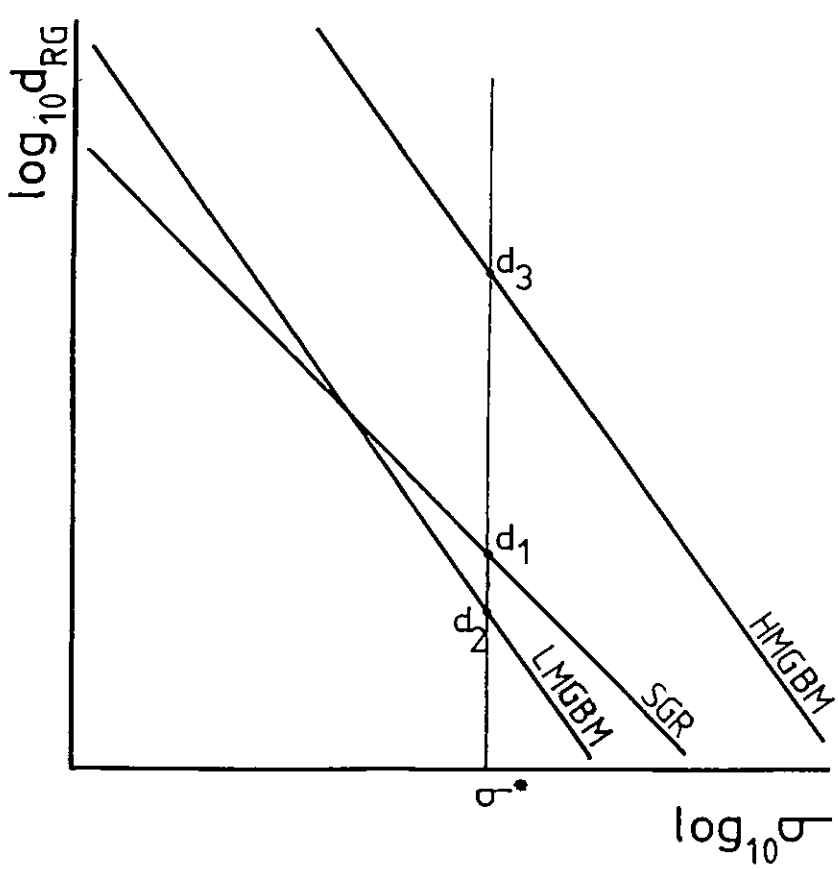


FIG. 5.14



and stress, there will be a changeover in the recrystallization mechanism responsible for the observed grain size. If no account is taken of this, any attempt to use recrystallized grain sizes to study the variation of flow stresses in such an area will lead to considerable errors. In partially recrystallized material it should be possible to identify the operative mechanism, but in mylonites, which are commonly 90-100% recrystallized, this will not always be so.

Fig. 5.14 shows the sort of stress - grain-size relationships expected for each of the three mechanisms described above. The effect of increasing temperature is illustrated in this diagram for a constant stress σ^*. The equilibrium grain at low temperature from SGR is d_1, with increasing temperature LMGBM becomes the dominant mechanism causing a small reduction in the grain-size to d_2, finally, at higher temperatures still, the grain size dramatically increases to d_3 as HMGBM becomes possible. Changes in mechanisms are, therefore, likely to be correlated with discontinuities in recrystallized grain sizes.

Discontinuities have been observed by Mercier (1980) in stress/depth profiles calculated from recrystallized grain size for olivine, and single pyroxene geothermometry/geobarometry, for nodules from basalts and kimberlites. These discontinuities are seen to be correlated with a change in recrystallization mechanism from SGR to GBM.

5.4 The practical use of microstructures in the estimation of palaeostresses

If we wish to use microstructures to estimate the palaeostresses associated with the deformation of a series of samples we must answer the following questions:-

(1) Which parameters should be measured?

(2) How should these parameters be measured?

(3) Which equations should be used?

(4) How should the stresses obtained be interpreted?

To obtain the fullest possible picture of the deformation history of a rock it is necessary to make use of all the information contained in the microstructure, i.e. all the parameters available should be used.

The methods of measurement to be used will depend on the mineral in question and the range of values to be observed. For quartz the study of etched, polished, sections by reflected light and SEM will be effective for the entire range of possible grain and sub-grain sizes and all but the highest dislocation densities ($\rho_f > 10^{13} m^{-2}$). for olivine, decorated thin sections can similarly be used for all grain and sub-grain sizes but not for dislocation densities in excess of $\rho_f \sim 10^{12} m^{-2}$ (Brodie and White, 1982). T.E.M. is, therefore, only necessary for the measurement of high to very high dislocation densities.

As has been indicated earlier, there are a host of theoretical and empirical equations relating the various parameters to the differential stress. There are consistent data available from the experimental calibration of dislocation density (Kohlstedt, 1980). For grain and sub-grain size, however, this is not so. The results from the several studies on olivine cannot be successfully combined, while for quartz there is very little reliable experimental data at all. There is also no experimental calibration available for either mineral for the equilibrium size produced by a SGR mechanism. It is, therefore, considered preferable to make use of data from naturally deformed samples as outlined in the previous section. The equilibrium lines obtained in this way will obviously become better defined as more observations are made.

When interpreting the various stress estimates obtained for a single sample, account must be taken of the stability of each parameter during changing conditions of deformation, and later annealing or uplift.

Dislocation densities require only very small strains (White, 1979(a))

to be completely reset and, therefore, tend to reflect the most recent mechanical or thermal event. Dislocation densities will alter even when there is no recovery, i.e. when neither sub-grain formation nor recrystallization is possible, and will tend to be affected by the stresses set up during uplift. They are also susceptible to subsequent annealing as shown both in recent experiments (Ricoult, 1980; Matsui et al. 1980) and from the interpretation of Fig. 5.3, but the rates of annealing are only significant at high homologous temperatures for initially high dislocation densities, unless it is maintained for a very long period in geological terms.

Sub-grain sizes re-equilibrate quickly in response to increasing stress, but respond very sluggishly indeed to a decrease in stress (Pontikis and Poirier, 1975; Ross et al., 1980). In general, therefore, the sub-grain size of a sample will relate to the highest stress to which it has been subjected, assuming that sufficient strain was available to reset it. Only prolonged annealing, or <u>total</u> recrystallization by a mechanism involving grain boundary migration will obliterate a high stress event recorded in this way.

In contrast to the other two parameters the grain size requires considerable strain to be completely reworked; even in high strain mylonites there are commonly relict grains. It is common, therefore, to have two or more events recorded in a sample recorded by populations of recrystallized grains (e.g. White, 1981b and Ross et al. 1980, Fig. 5(D)), for each of which a stress may be estimated. Grain sizes are not expected to be affected by uplift, and only by prolonged annealing at high homologous temperatures. However, a major drawback is that reliable results can only be obtained from relatively pure single phase aggregates due to the effects on grain size of secondary phases (see Section 5.13.).

As yet it is not possible to determine whether relatively small ($\sim\pm$20%) differences on stress estimates from different parameters are significant,

or their accuracy as absolute values, due to the uncertainties in the relevant equilibrium relationships. However, systematic variations within suites of samples may be used in a semi-quantitative way to determine stress variations in space and time.

5.4.1 Examples of use

(i) 'Pipe-rock' mylonite zone, Moine Thrust Zone

In this example, White (1979b) looked at variations in dislocation density and grain and sub-grain size across the boundary of a shear zone developed within the 'pipe-rock' quartzite from the Moine Thrust Zone. Table 5.1(a) summarizes the observations using optical measurements for grain size (except for PRM5 which is from T.E.M.), and T.E.M. for sub-grain size and dislocation density. Table 5.1(b) gives the stress estimated using equations (3), (15) and (19).

Estimates from sub-grain and grain size vary systematically (N.B. The similarity in values is at least in part due to the observations forming part of Fig. 5.10 from which equation (19) was obtained) except for the grain cores in sample PR which have a sub-grain size that indicates a much lower stress. It is significant that both parameters record the same increase in stress into the shear zone which is thought to represent the stress profile during the shear zone initiation (White, op.cit., see also Section 6.1) That this gradient should be preserved in both parameters indicates that further deformation was not by cyclic dynamic recrystallization, lending further weight to the grain-boundary sliding dominant deformation proposed by White (op.cit.).

The large sub-grain size in the grain cores from sample PR may well relate to the 'background' stress level prior to the shear zone formation with insufficient strain resulting from the initiation event to reset the sub-grain structure; it is interesting that the dislocation density

TABLE 5.1(a) Microstructural Parameters from White (1979(b))

	Grain Size (μm)	Sub-grain size (μm)	Dislocation density (m^{-2})
PR	24.6	13.3^{c} 5.0^{m}	
PRM 1	22.2	6.2^{c} 4.9^{m}	
PRM 2	18.0	4.0	$4\text{-}5.5\times10^{11}$
PRM 3	16.0	3.7	
PRM 4	14.6	3.7	
PRM 5	2.8	-	

Increasing strain ↓

c = grain core

m = grain mantle

(b) Estimated Stresses (MPa)

	Grain Size	Sub-grain Size	Dislocation density
PR	119	46.5^{c} 124^{m}	
PRM 1	130	100^{c} 126^{m}	
PRM 2	155	155	39
PRM 3	171	167	
PRM 4	185	167	
PRM 5	739	-	

characteristic of all the samples indicates a very similar stress level, suggesting that the whole area returned to this 'background' level (White, op. cit.).

The very small grains in PRM5 suggest a very high stress (~700MPa), but White (op.cit.) has proposed that chlorite or mica grains have inhibited grain growth and that this value is a considerable overestimate. However it is difficult to see how phyllosilicates grains (unless as inclusions in the original quartz clasts) could prevent the equilibrium size from being achieved.

Bell and Etheridge (1976) reported a comprehensive series of recrystallized grain sizes in quartz-bearing mylonites from the Woodroffe Thrust Zone. The samples were collected in a traverse from granulite facies gneisses on one side to amphibolite facies gneisses at the other. Fig. 5.15(a) shows the position of the traverse (A-A) in the Woodroffe Thrust Zone. A strain profile along this traverse is shown in Fig. 5.15(b), estimated from the degree of elongation of remnant grains in the mylonites; the sampling points are also indicated (N.B. The eastern end of the strain profile has been modified to be consistent with the map (Fig. 5.15(a). This shows that the traverse passes back into mylonite at its eastern end; this is also consistent with the variations in Rb/Sr ratio and H_2O content shown in Bell and Etheridge (op.cit. Fig. 2.).

Fig. 5.16 shows the variation in quartz recrystallized grain size across the traverse; note the apparent discontinuity between stages G3(c) and G4. A stress profile was constructed using equation (19), Fig. 5.17 and this shows a similar effect. However, the recrystallization mechanism on the partly recrystallized quartz on the amphibolite side is one of SGR and equation (19) is, therefore, inappropriate. Fortunately Bell and Etheridge (op.cit.) figure recrystallized grains developed by both mechanisms (GBM and SGR) at the same stage (G3(a)) on the granulite side. Using

FIG. 5.15

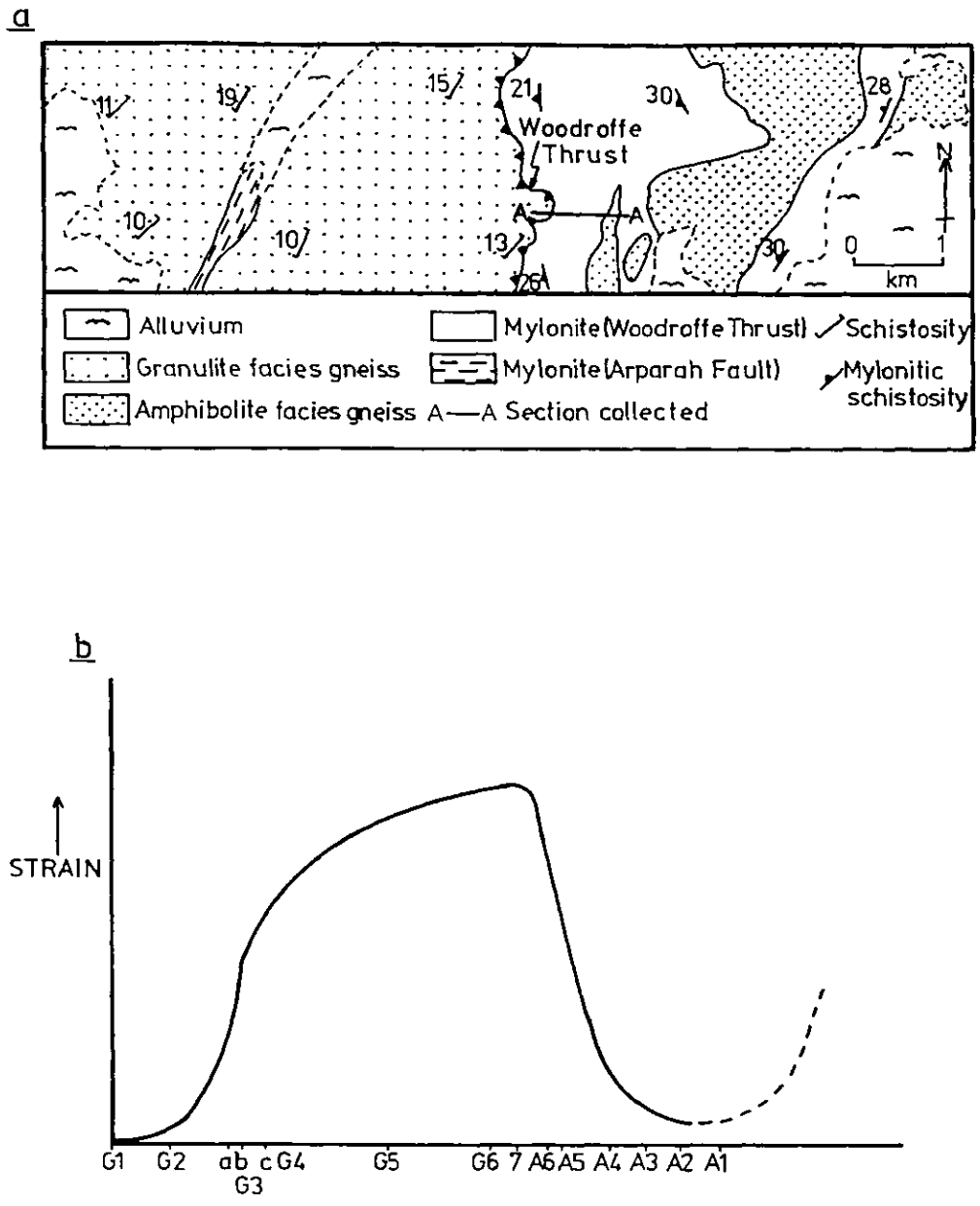


Fig. 5.15 (a) Geological map of part of the Woodroffe thrust, showing traverse (A–A) along which samples were collected.

(b) Approximate strain profile across the Woodroffe thrust estimated from remnant grain elongations. The eastern part has been altered to fit with the map (5.15a) which shows the traverse passing back into mylonite.

(after Bell and Etheridge, 1976)

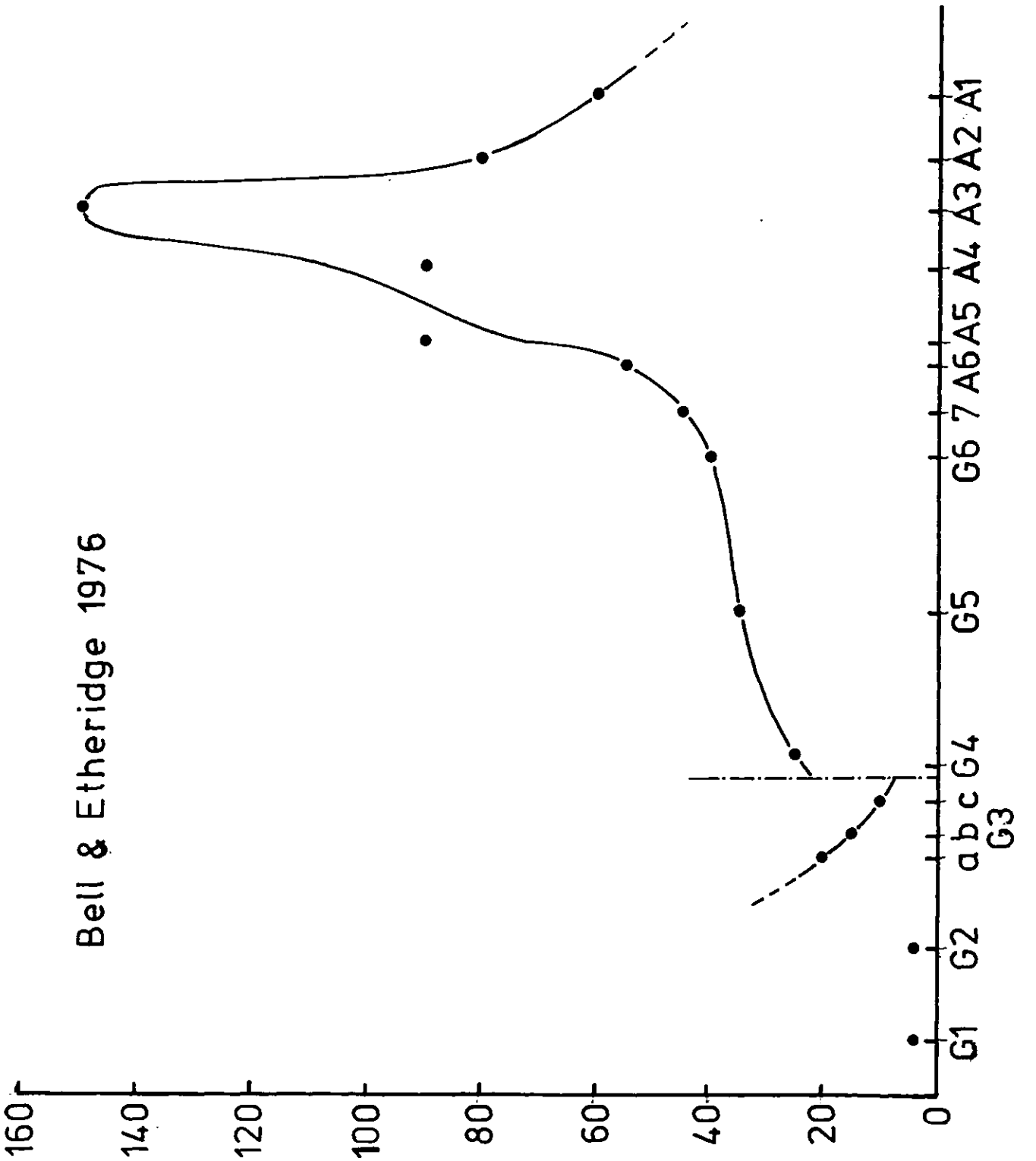


Fig. 5.16

Variation of quartz recrystallized grain size across the traverse shown in Fig.5.15a, (data from Bell and Etheridge, 1976); note the apparent discontinuity between stages G3(c) and G4.

FIG. 5.18

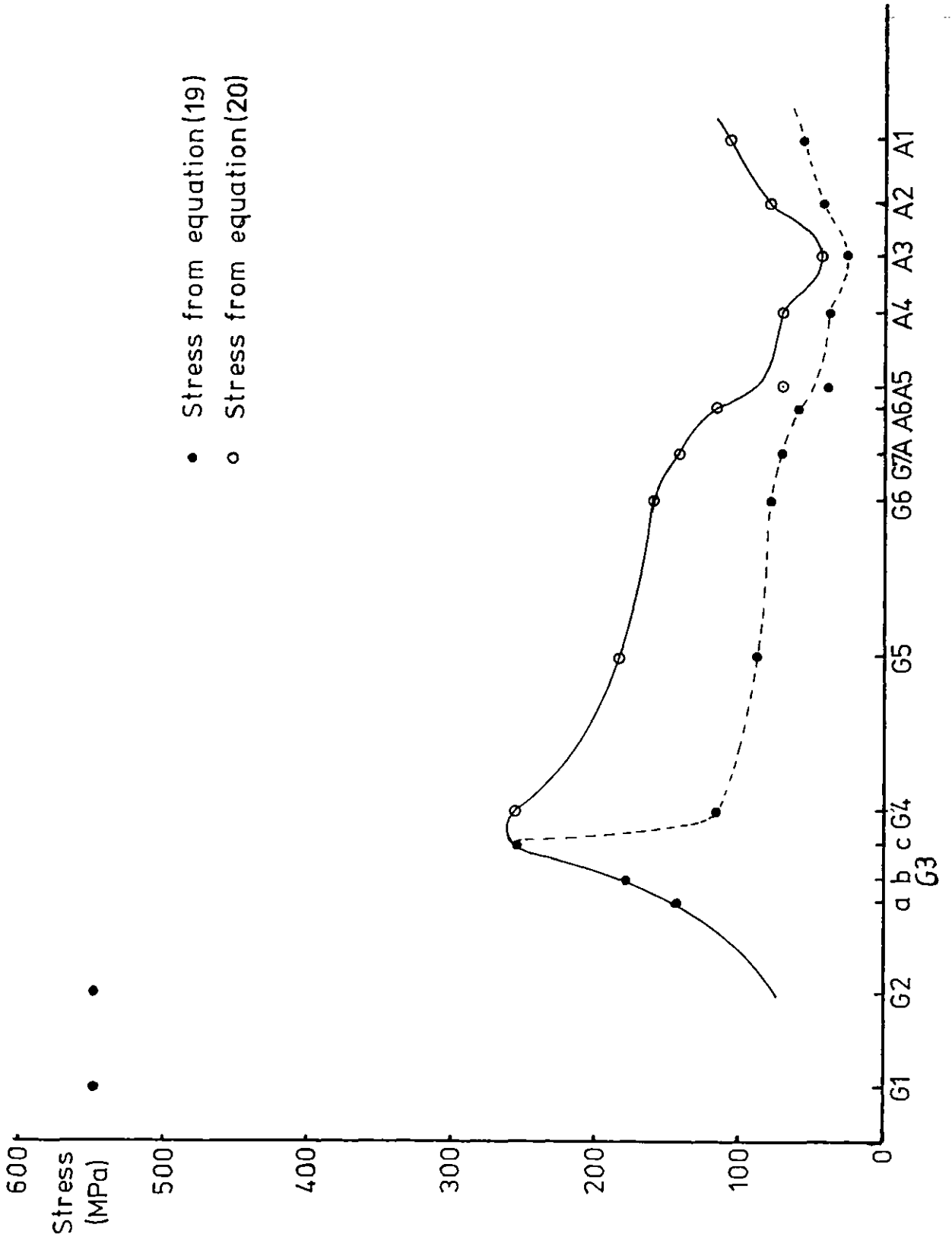


Fig. 5.17 Stress profile across the Woodroffe thrust estimated using equation (19) , note the discontinuity between stages G3(c) and G4.

Fig. 5.18 Stress profile across the Woodroffe thrust estimated using equation (20) for those samples east of G3(c) to take account of the change in dominant recrystallization mechanism to SGR.

values of D_{RG} from GBM ~20μm, and D_{RG} from SGR ~45μm it is possible to obtain an approximate value for K_3 in equation (9).

$$\sigma_1 - \sigma_3 \simeq 7.5 \times 10^3 d_{RG}^{-1.0} \qquad (20)$$

As it is impossible to tell where the change in mechanism occurs along the traverse in the totally recrystallized samples, equation (10) has been used to estimate stresses for all samples east of G3(a), Fig. 5.18. Thus a smooth profile results from the assumption that the grain size discontinuity coincides with the change in mechanism of recrystallization.

As the stress decreases to either side of the discontinuity, it follows from the above assumption that the switchover on mechanism is not related to stress, but must be due to a change in temperature with the granulite side being hotter than the amphibolite side. The postulated temperature profile (Fig. 5.19) is exactly what is expected to result from the effect of thrusting on a set of initially horizontal isotherms.

That is, as long as the displacement-rate on the thrust is faster than the rate of re-equilibrium of the isotherms, a horizontal section across the mylonite zone at the present erosion level will pass through rocks that were deformed at increasingly higher temperatures, going from amphibolite side to the granulite side.

The very high stress indicated by the new grains associated with micro-shears at stages G1 and G2 are consistent with quartz being deformed at about the brittle/ductile transition. This deformation is thought, therefore, to be related to the late faulting event associated with the formation of pseudotachylyte; these stress values have not been included in the profile.

The above interpretation is based completely on the observations of Bell and Etheridge (op.cit.). In 1979 Etheridge and Wilkie published a survey of grain size variations across a series of mylonite zones. This included a set of values from the Woodroffe Thrust, along the same traverse,

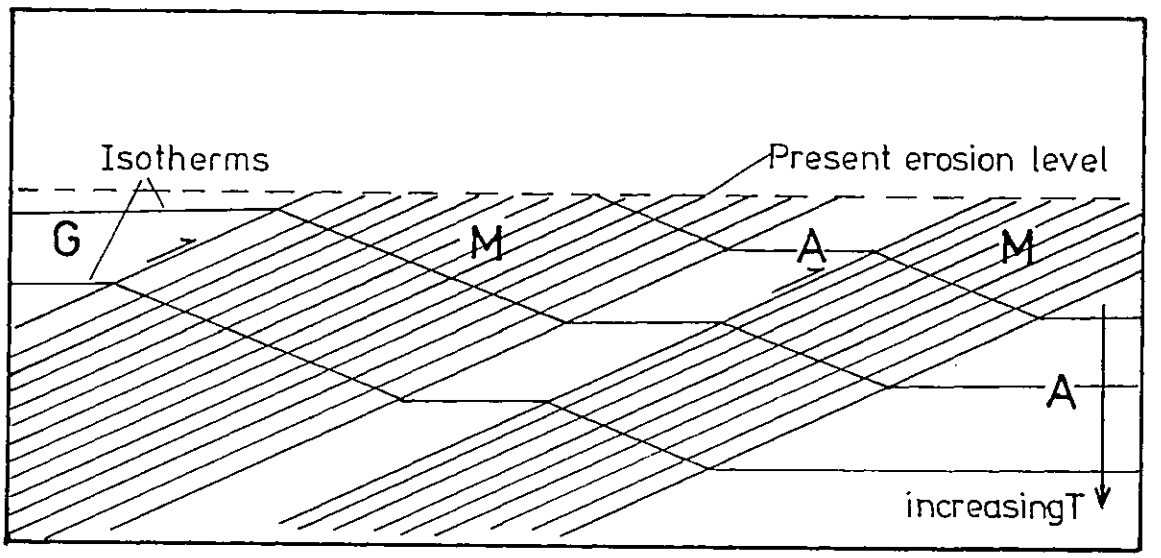


Fig. 5.19 The effect of thrusting on a set of initially horizontal isotherms, related to a vertical section along the traverse A — A across the Woodroffe thrust. (G = granulite facies gneiss, A= amphibolite facies gneiss, M = mylonite)

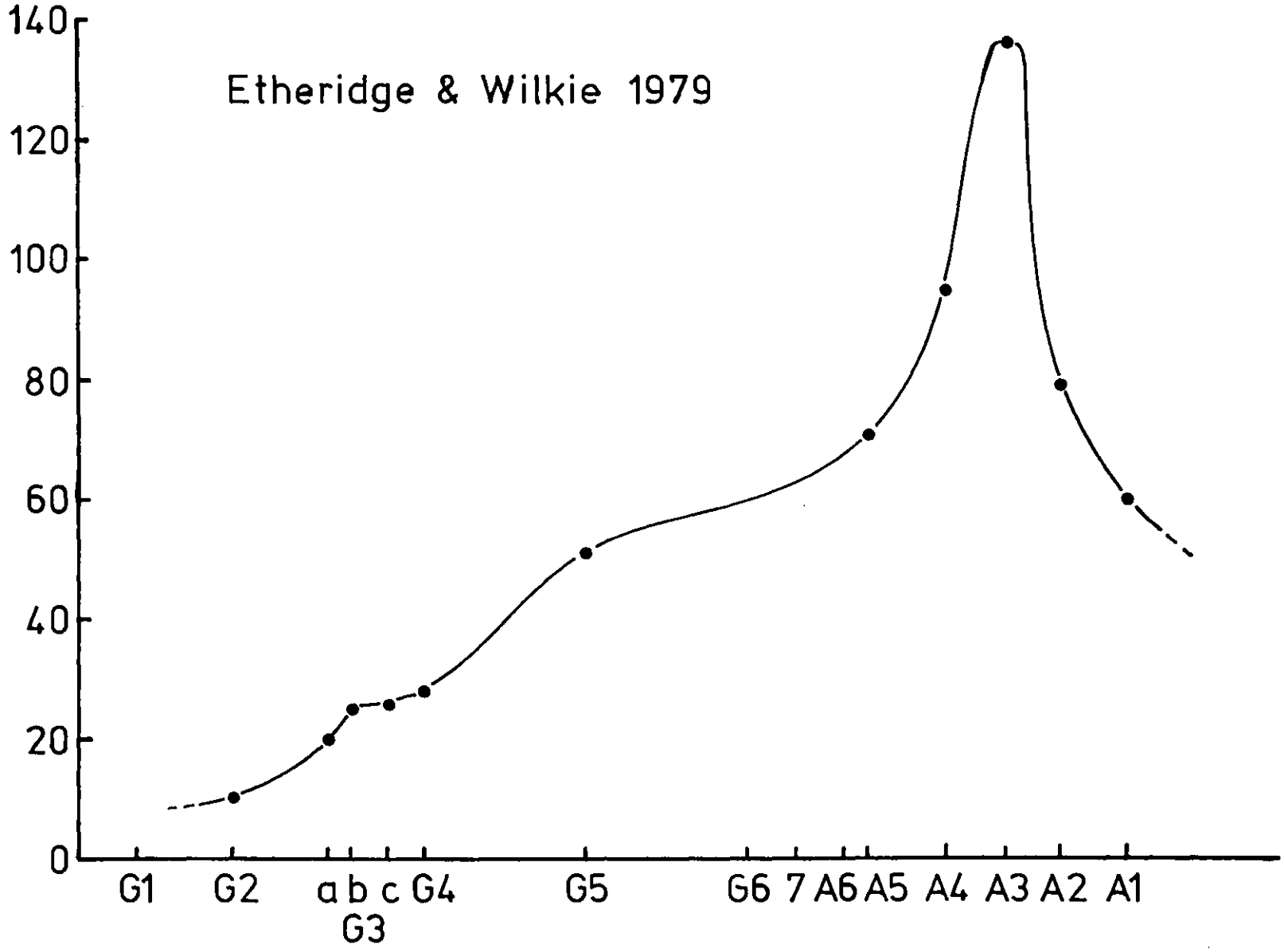


Fig. 5.20 Variation of quartz recrystallized grain size across the Woodroffe thrust (from Etheridge and Wilkie, 1979) to illustrate the changes in grain size from those reported in Bell and Etheridge, 1976 (see Fig. 5.16 for comparison).

but remeasured for the purposes of the new study. This variation in grain size is shown in Fig. 5.20. Major differences include a reversal of the trend for samples G3(a), (b), (c), thus removing the discontinuity between G3(c) and G4. It should be emphasized, therefore, that the interpretation presented here is not intended as a contribution to the study of the Woodroffe Thrust but merely as an example of how the methods previously outlined may be used in practice.

In the study of this mylonite zone, the measurement of even a few sub-grain sizes and dislocation densities would greatly aid the interpretation.

5.5 Observations from Cap de Creus

A series of quartz samples have been studied to obtain the parameters, dislocation density, sub-grain size, and recrystallized grain size. Dislocation densities were measured by counting the number of etchpits within a certain area on SEM micrographs of etched polished sections (e.g. Plate 5.1). Unfortunately, the specimen preparation was in many cases not good enough to allow the accurate measurement of the density, as can be seen in Plate 5.2. However, as dislocation densities seem to be the most ephemeral of the microstructures, it was not considered worth using the only other available technique, T.E.M., which seems wasteful of microscope time as well as time-consuming in the measurement, if a statistically valid result is to be obtained. Dislocation densities are therefore quoted only for a few of the specimens.

Sub-grain sizes in the samples studied are in the range 10-40μm, and were, therefore, measured from etched polished sections by reflected light microscopy, using a Nomarski interference attachment to give good contrast (Ball and White, 1977). For only about 30% of the samples studied was the surface preparation good enough to allow the measurement of the sub-grain size.

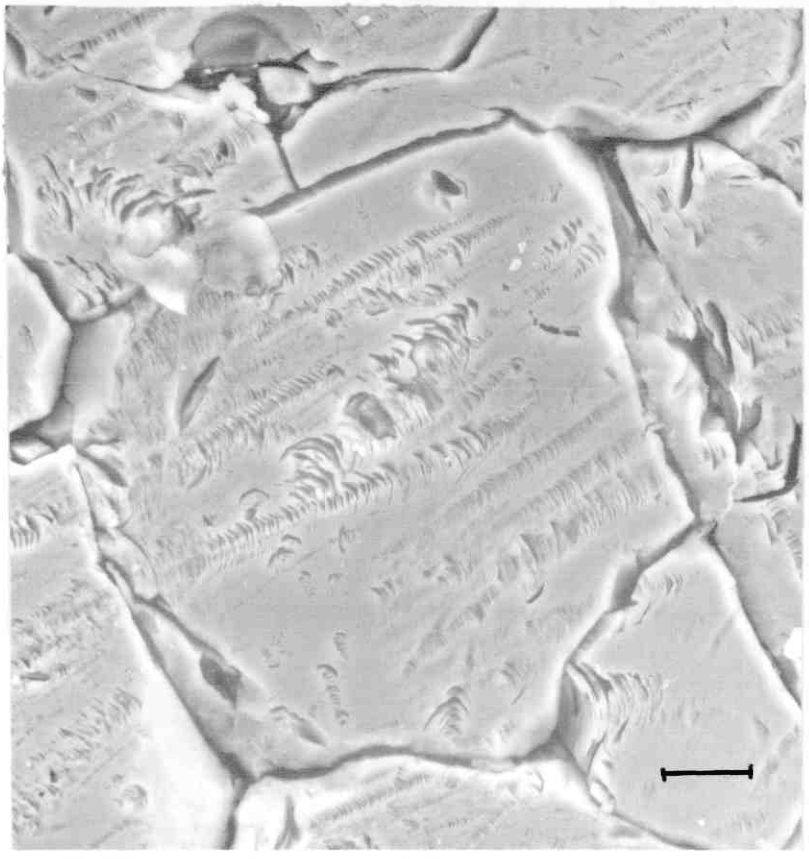


Plate 5.1 A typical example of poor specimen preparation in an etched polished section of quartz, showing development of "chatter tracks". Scale bar = 25μm.

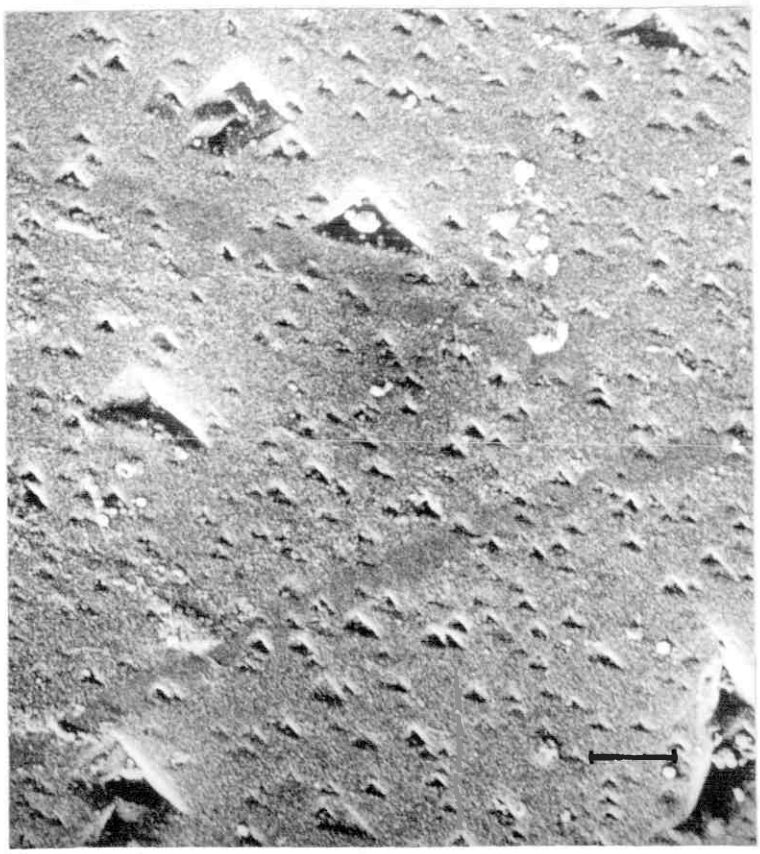


Plate 5.2 A well etched quartz polished section showing the individual dislocation etch-pits. Scale bar = 2.5μm.

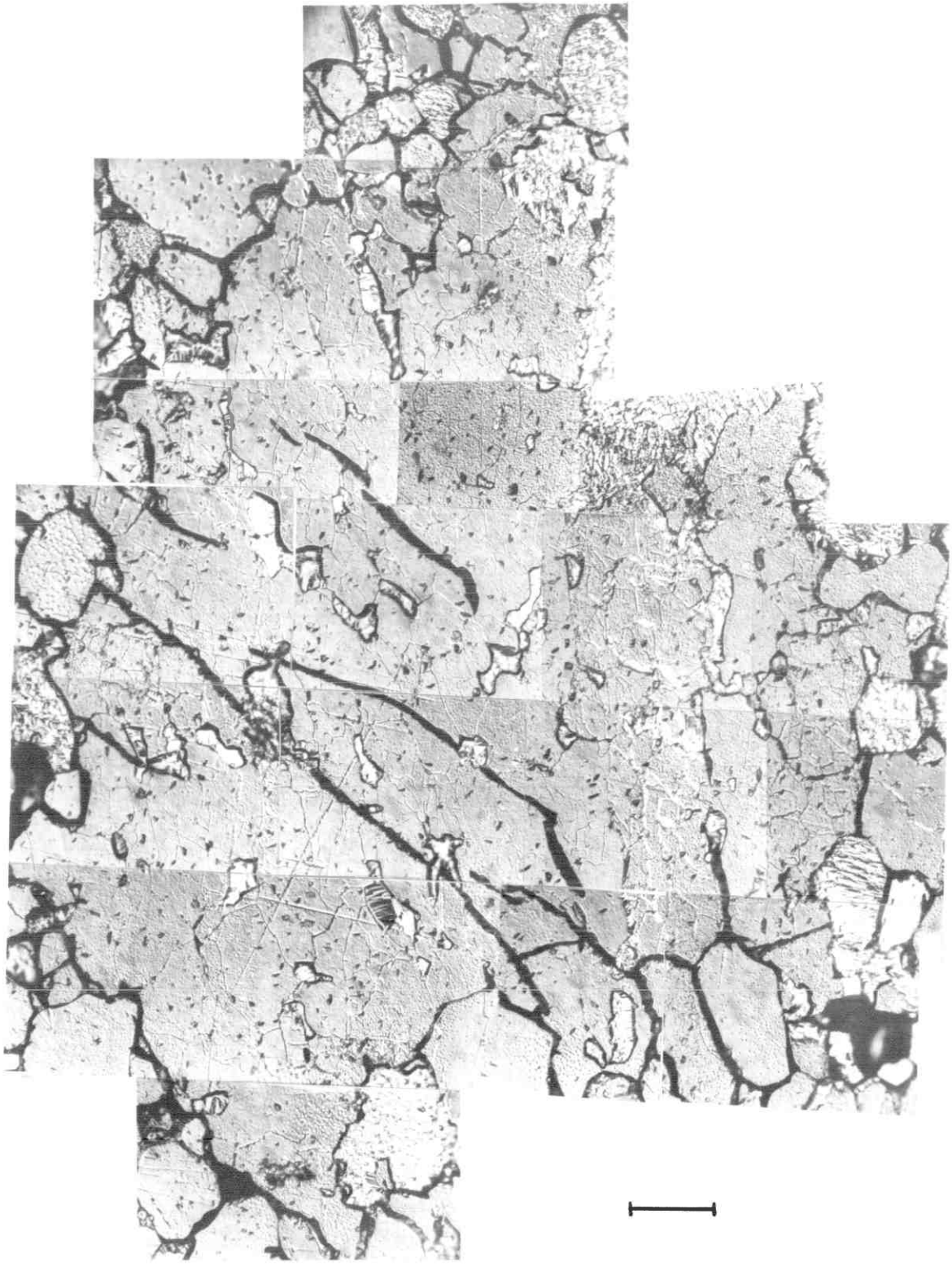
In two samples, relict quartz grains with well-etched sub-grain networks were used to study sub-grain size distributions. Plate 5.3 and Fig. 5.21 show the complete pattern of sub-grains found by etching a remnant grain in one of the mylonites. Only two sub-grains are present of sufficient misorientation (estimated from the depth of the etching of the sub-boundary and the change in etching-intensity across them) to be visible optically, i.e. this grain in this section would appear to contain just three sub-grains whereas by etching some 1,800 are revealed. By measuring all the sub-grains defined by the etched low-angle sub-boundaries in particular sub-areas it is possible to show that sub-grain sizes are uni-modally distributed (e.g. Fig. 5.22.).

Grain sizes and sub-grain sizes were measured from optical micrographs of known magnification using a sonic digitizer. This enabled all the grains within the field of the micrograph to be measured quickly and accurately. The digitizer outputs the apparent grain areas into a text file, and this data is then processed using the program GSIZE (see Appendix 1). This program works out circle equivalent diameters to the measured areas (i.e. equant grain shapes are assumed), sorts them into classes with a module of $\alpha=\sqrt{2}$, works out the true distribution by correcting for the effect of sectioning, and finally outputs this distribution, with the mean and standard deviation.

The correction for the effect of sectioning is carried out using the recursive equations of Exner (1972), slightly altered for use with a single-phase material. Another equation that has commonly been used to correct for sectioning is $\bar{d}_{true} = \bar{l}_{measured} \cdot 1.5$ (where $\bar{l}$ is the mean linear intercept) (e.g. Etheridge and Wilkie, 1979), but this assumes that all the grains are the same size, and does not take account of a continuous size distribution.

In a few of the quartz mylonites (especially the type 1, section 4.1.2.3) elongate grains are present, and on all samples many of the sub-grains are

Plate 5.3 Mosaic of reflected light micrographs of the complete sub-grain network in a remnant quartz grain in the mylonite CSA 18 revealed using a Nomarski interference attachment. Scale bar = 100μm.



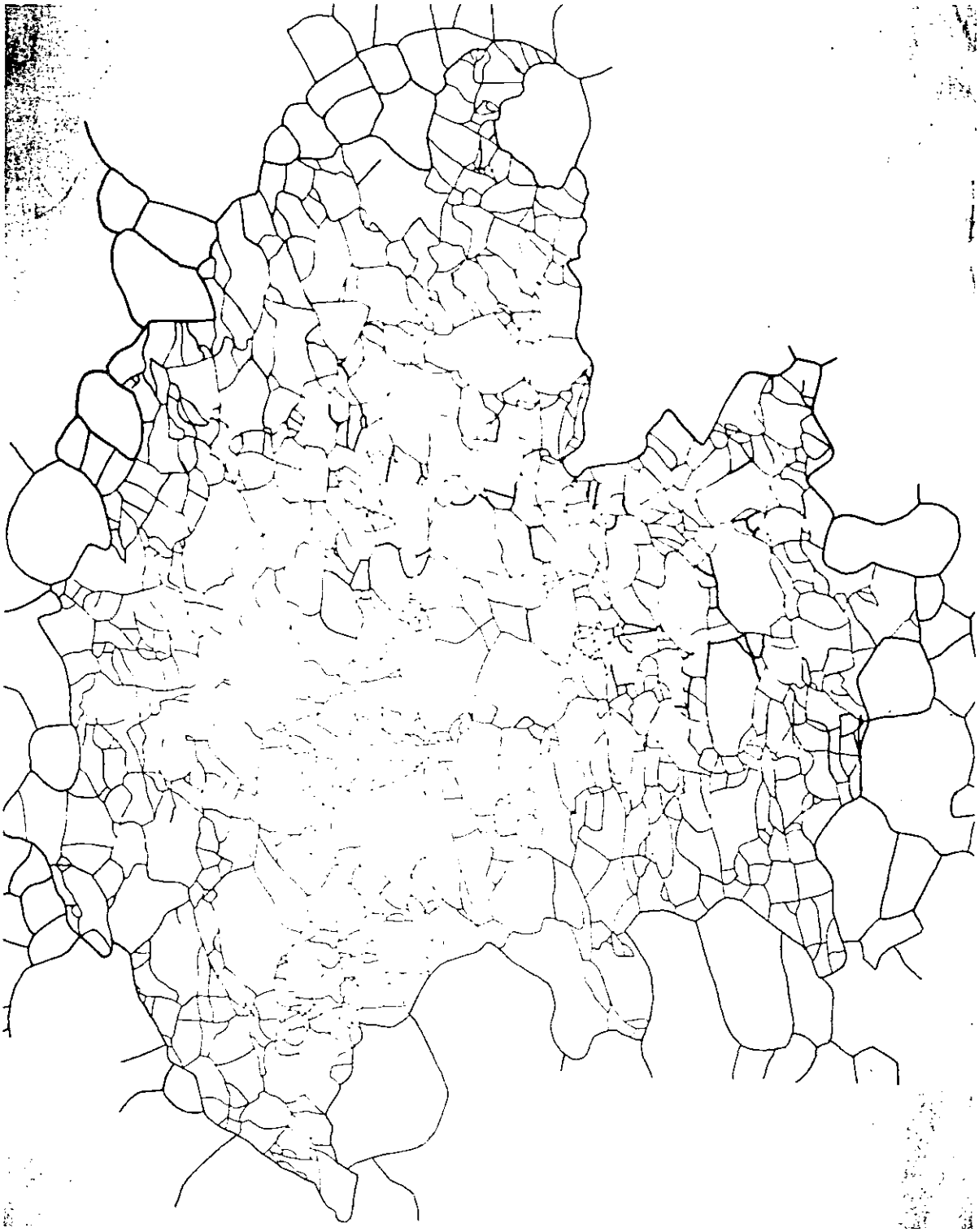


Fig. 5.21 Complete network of sub-grain boundaries from a remnant grain in a mylonite (sample CSA 18, tracing of Plate 5.3)

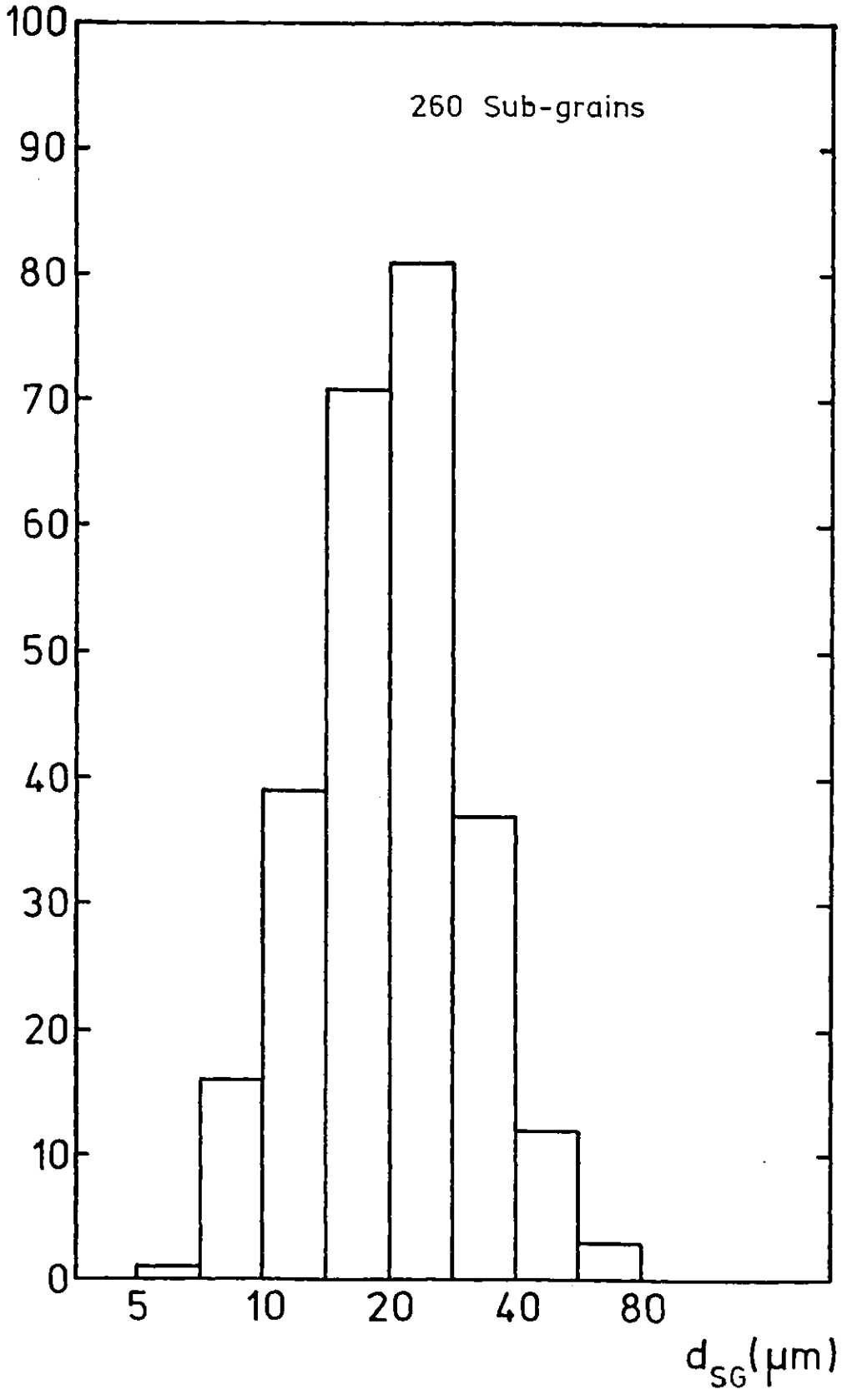


Fig. 5.22 Frequency distribution of sub-grain size from a sub-area within the relict grain shown in Fig. 5.21, Plate 5.3.

quite inequant. Measurements of these were made with the digitizer, but instead of using the whole grain area, an equant area is measured, as depicted in Fig. 5.23, the circle equivalent diameter giving in this case the short dimension of the grain or sub-grain. The short dimensions of inequant grains or subgrains are normally used when combining data from equant and elongate types.

Table 5.2 shows all the measurements of the three parameters obtained for quartz in this study. The grain and sub-grain sizes were measured using at least 100 observations (usually ∿200) except where noted. Dislocation densities were measured from several grains or areas within quartz to give a total area $\sim 10^4 \mu m^2$.

5.6 Stresses associated with the shear zones at Cap de Creus

Table 5.3 shows the stress estimated for the various parameters from each sample. As grain sizes were determined for all of the samples, much of the interpretation must rest on these results. The other parameters particularly sub-grain size should, however, contain some useful information.

The few dislocation densities indicate stresses that vary widely between 18 and 76MPa. The highest values of stress are greater than any indicated by grain or sub-grain size and inspection of Fig. 5.6 shows that both this data, and that from Atkinson et al. (1979) for the Cap de Creus fall away from the 'equilibrium' line suggesting that the dislocation densities have been reset, to higher stresses, probably during uplift. Carreras et al. (1977) have proposed that the populations of dislocation of $\langle 11\bar{2}0 \rangle$ (0001) type which are commonly straight and pinned in the quartz mylonites from Cap de Creus were introduced during uplift.

Including the data from Atkinson et al. (1979) it can be seen from Fig. 5.10 that the grain and sub-grain sizes from the Cap de Creus give a spread to both sides of the assumed 'equilibrium' line. Part of this

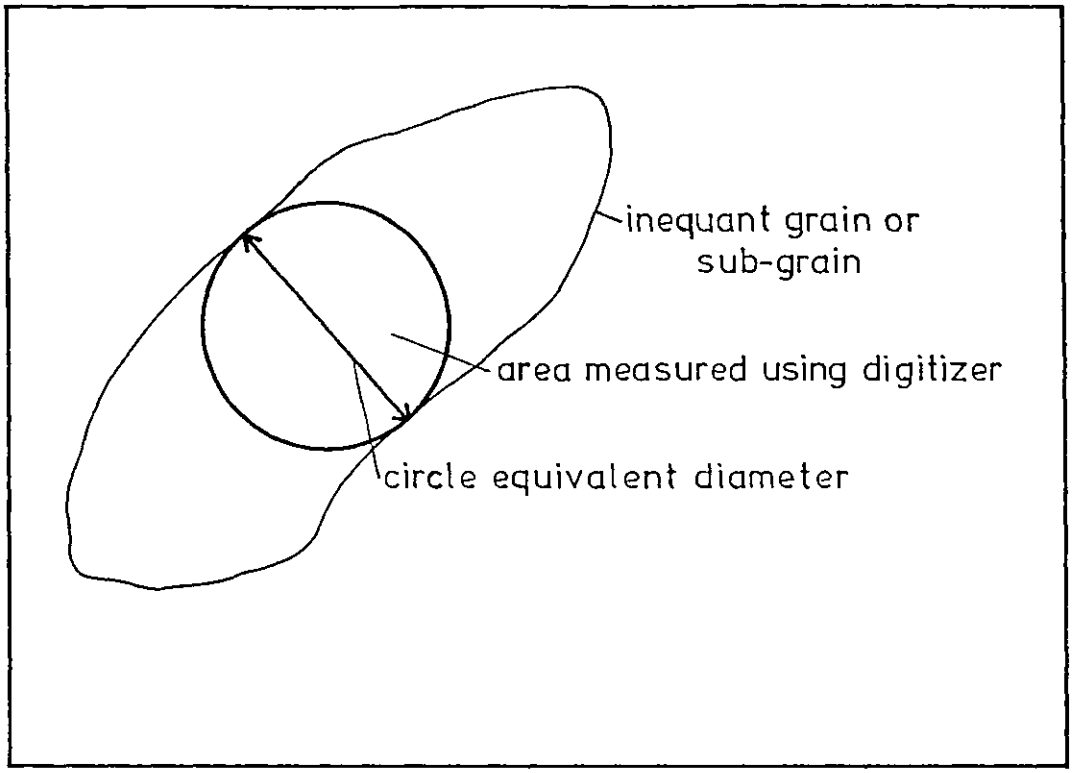


Fig. 5.23 Diagram to illustrate the method used to measure the diameter of inequant grains or sub-grains in this study.

Table 5.2

Summary of observations of microstructural parameters in quartz, this study

	Grain Size				
	Sample type	Sample No.	Mean(μm)	Standard Deviation(μm)	
P/M	Microgranite	PDM 02	102.4	48.1	
M	Microgranite	PDM 03	97.8	40.5	
P/M	Quartz vein	PDM 04	155.2	64.3	
M	Quartz vein	PDM 05	135.3	41.6	
M	Quartz vein	RDS 04	82.9	26.2	
M	Quartz vein	CSE 04	63.0	15.4	
P/M	Quartz vein	CSE 04(a)	54.6	16.4	
P/M	Quartz vein	CSE 08(b)	52.6	12.4	(84)
M	Quartz vein	CSE 15(a)	144.4	60.0	
P/M	Quartz vein	CSE 20	94.7	31.9	
M	Quartz vein	CSE 23(a)	100.5	36.0	
M	Quartz vein	CSE 25	75.8	23.1	
P/M	Quartz vein	CSE 27	70.2	32.8	
M	Quartz vein	CSC 04(b)	52.3	14.7	
M	Quartz vein	CSA 10	57.1	19.4	
M	Quartz vein	CSA 15	353.5	102.4	
P/M	Quartz vein	CSA 16	357.7	136.0	
M	Quartz vein	CSA 17	266.0	75.0	
M	Quartz vein	CSA 18	128.0	35.5	
M	Quartz vein	CSA 19	393.5	197.8	
M	Quartz vein	CSA 20	216.4	76.1	
M	Quartz vein	CSA 21	432.1	163.0	
M	Quartz vein	CSA 22	490.1	216.9	
M	Quartz vein	CSA 23	386.0	144.2	
M	Quartz vein	CSA 24	380.1	136.1	
M	Quartz vein	CSA 25	426.3	130.1	
M	Quartz vein	CSA 26	349.6	144.1	
P/M	Quartz vein	CSA 27	338.3	144.7	
M	Quartz vein	CSA 28	231.5	87.5	(99)

Table 5.2 (Continued)

Sub-grain Size			Mean(μm)	Standard Deviation(μm)
P/M	Quartz vein	CSE 04(a)	19.2	7.5
M	Quartz vein	CSE 15(a)	20.6	11.5
P/M	Quartz vein	CSE 20	28.6	14.1
P/M	Quartz vein	CSA 16	30.7	15.7
P/M	Quartz vein	CSA 17(a)	26.6	12.5
M	Quartz vein	CSA 18	20.9	9.9
M	Quartz vein	CSA 21	29.6	15.4
M	Quartz vein	CSA 22	73.2	25.7
M	Quartz vein	CSA 24	76.2	27.2

Dislocation Density			Mean(m^{-2})
M	Quartz vein	CSE 15(a)	1.3×10^{12}
P/M	Quartz vein	CSA 16	1.5×10^{11}
M	Quartz vein	CSA 18	5.0×10^{11}
M	Quartz vein	CSA 21	1.3×10^{12}

P/M = Protomylonite
M = Mylonite

Figures in brackets indicate number of grains measured if less than 100.

TABLE 5.3

Sample	Grain Size	Sub-Grain Size	Dislocation Density
PDM 02	35.9		
PDM 03	37.3		
PDM 04	25.3		
PDM 05	28.4		
RDS 04	42.9		
CSE 04	54.0		
CSE 04(a)	60.9	32.2	
CSE 08(b)	62.9		
CSE 15(a)	26.9	30.0	76.2
CSE 25	46.3		
CSE 27	49.3		
CSA 10	58.7		
CSA 15	12.7		
CSA 16	12.6	20.1	18.3
CSA 17	16.1	23.2	
CSA 18	29.8	29.5	40.5
CSA 19	11.6		
CSA 20	19.2		
CSA 21	10.7	20.8	76.2
CSA 22	9.6	8.4	
CSA 23	11.8		
CSA 24	11.9	8.1	
CSA 25	10.8		
CSA 26	12.8		
CSA 27	13.2		
CSA 28	18.1		
CSE 20	38.4	21.6	
CSE 23	36.5		
CSC 04(b)	63.2		

Table 5.3 Stresses estimated from the data shown in Table 5.2 using equations (3), (15), (19). (MPa).

scatter may be due to errors in measurement, but, as the values of both parameters represent at least 100 measurements, errors should be no greater than 10%, and this is insufficient to explain the observed variation.

Two data points (for specimens CSE04(a), CSE20) fall distinctly below the line, i.e. the stresses indicated by the grain size are higher than those indicated by the sub-grain size (N.B. for sample localities see Section 3.3, Figs. 3.15 and 3.16 and Maps 1 and 2(c)). All the sub-grains measured in these samples are from remnant grains and should theoretically represent the highest stress to which they have been subjected.

Although annealing cannot be entirely ruled out it would be difficult to explain why only these two samples were affected. As both of these specimens are only partially recrystallized it is possible that the grain size measurements were taken in areas where the new grains had not quite established their equilibrium size, leading to an overestimate on the stress. It is interesting to note that both give grain sizes slightly smaller than adjacent mylonites. It has been a general observation (e.g. White 1979(b)) that recrystallized grain sizes decrease into mylonite zones; in this study grain sizes vary from showing a considerable decrease (PDM04/05, CSA17(a)/18) to a very small increase (CSE04/04(a), CSE20/23, CSE25/27). As all grain sizes away from high-strain mylonites indicate low stresses $\sim$ 10-15 MPa it is assumed that stress should show a continuous increase, and grain size a continuous decrease into the zones, and that samples for which there is a small increase in grain size from protomylonite to adjacent mylonite have failed to reach their equilibrium sizes.

The data points from this study that fall to the other side of the line are all from what have been termed low-strain mylonites (Section 3.3.1.2.1) The most likely explanation for the sub-grain size indicating a higher stress is that they reflect the differential stress at a different time to that indicated by the grain size, probably during the propagation event. All

of these low-strain mylonites (CSA 16, CSA 17(a), and CSA 21) are adjacent to high strain zones, while the data from the other two low strain mylonite samples (CSA 22, CSA 24), which are further from such zones, fit close to the equilibrium line, as do the two high-strain mylonites (CSE 15(a), CSA 18).

No sub-grain size measurements were possible from completely re-crystallized samples due to a paucity of correctly etched grains showing any sub-grain structure. This may reflect the reworking of the micro-structure caused by continuous dynamic recrystallization. However, evidence is presented elsewhere (Chapter 3.) that some of the mylonites deformed with a large contribution from grain-boundary sliding which should tend to preserve earlier structures. As the new grains were formed by a GBM mechanism they would start without an inherited, sub-grain structure but should develop one after even a small amount of further strain. The lack of sub-grain boundaries observed in new grains may simply reflect the overall relaxation of stresses, following mylonitization, to the background level. Clearly if the largest observed sub-grains ($\sim$75μm) represent this background level only grains $\geq$ 100μm will show any sub-grain boundaries at all.

All further interpretation will be based on variations in the re-crystallized grain size. Table 5.4 shows a breakdown of estimated stress levels for different ranges of shear strain, both for mylonite and proto-mylonites. The strains measured are only approximate but allow the samples to be fitted into the broad categories shown.

Stresses in the mylonites increase with increasing strain, but as the protomylonites (all at approximately the same strain) show a large range of stress, strain cannot be the controlling factor. The observed variation probably reflects the degree of strain-softening (i.e. the greater the strain-softening, the higher the resultant strain-rate) due to the effect of grain size on the deformation mechanism (see Section 4.1.1.3).

TABLE 5.4

	PROTOMYLONITES		MYLONITES					
Approx. Shear Strain	$2 \geqslant \gamma \geqslant 1$		$20 > \gamma > 2$		$50 > \gamma \geqslant 20$		$\gamma \geqslant 50$	
	Sample	Stress (MPa)	Sample	Stress (MPa)	Sample	Stress (MPa)	Sample	Stress (MPa)
	PDM 02	35.9	PDM 05	28.4	CSE 25	46.3	RDS 04	42.9
	PDM 04	25.3	PDM 03	37.3	CSE 23	36.5	CSE 04	54.0
	CSE 04(a)	60.9	CSE 15(a)	26.9	CSA 18	29.8	CSA 10	58.7
	CSE 08(b)	62.9	CSA 15	12.7			CSC 04(b)	63.2
	CSE 27	49.3	CSA 17	16.1				
	CSE 20	38.4	CSA 19	11.6				
	CSA 16	12.6	CSA 20	19.2				
	CSA 27	13.2	CSA 21	10.7				
			CSA 22	9.6				
			CSA 23	11.8				
			CSA 24	11.9				
			CSA 25	10.8				
			CSA 26	12.8				
			CSA 28	18.1				

Table 4.4 . Variation of stress with strain in both mylonites and protomylonites .

In Section 3.3.1 it was noted that certain of the low strain mylonites had distinctive boundaries with the country-rock schists that were not marked by a high-strain zone, and had lineations plunging straight down-of the foliation. Samples were taken from either side of two of these boundaries (CSA 15/16, CSA 26/27); the stresses given by all four samples are virtually identical. All the low strain mylonites indicate stresses in the range 10-15 MPa and it is suggested that this represents the 'background' stress level. It therefore follows that the stress intensification during shear zone formation varied in the range x2 to x5.

Fig. 5.24 shows stress profiles across two parts of the Cala Sardina zone, with sketch maps to show the positions of the sampling points. Fig. 5.24(a),(c) is a profile across the large area of low strain mylonite between the major dextral zone and a minor sinistral zone (for locality, see Fig. 3. and for discussion of field relationships see Section 3.3.1) The two high-strain zones give stress ~19MPa while all the samples between them give stresses ~11MPa, which indicates that the stresses associated with the formation of the two high-strain zones did not affect the adjacent country.rock for more than a few metres away; as previously argued the sub-grain size from CSA 21 suggests that this influence did extend a little further than as indicated by the grain size. The other profile (Fig. 5.24(b), (d)) serves to emphasise the difference between a country rock/high-strain mylonite boundary and a country-rock/low-strain mylonite boundary.

The samples PDM 02/03 were measured for comparison with PDM 04/05 to see if there was any difference in grain size between recrystallized quartz from a microgranite, and adjacent quartz vein at two levels of strain. PDM 02/03 show exactly the same trend as 04/05, viz. a small decrease from protomylonite to mylonite, but give stresses that are C.30% higher. Originally it was suspected that the difference in grain size was caused by the presence of other phases (see Section 5.13) but careful inspection

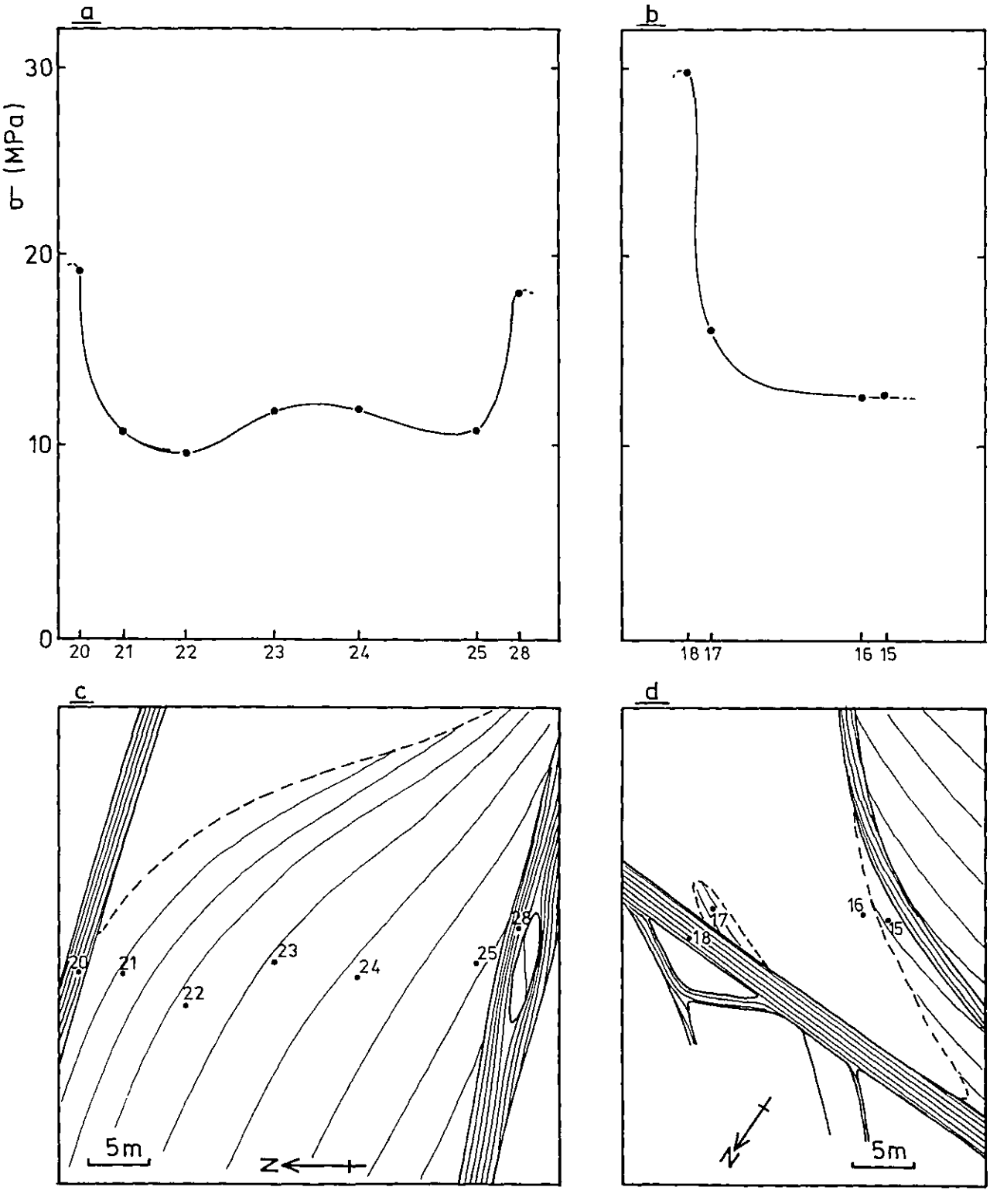


Fig. 5.24 Stress profiles across zones at Cala Cardina estimated using quartz recrystallized grain sizes.

(a), (c) Stress profile and accompanying sketch map from a low-strain mylonite between two high-strain mylonites.

(b), (d) Stress profile and accompanying sketch map to illustrate the difference between a high-strain mylonite/country-rock boundary, and a low-strain mylonite/country-rock boundary.

of the specimens in thin section suggests that this is not the case. The conclusion is that the stresses in the microgranites were higher, due presumably to the greater resistance to deformation presented by the feldspars.

CHAPTER 6 SHEAR ZONE DEVELOPMENT

In this chapter a physical model of a shear zone is presented and this is used to predict certain aspects of the development of individual shear zones, and shear zone networks. These results are then compared with the field and microstructural observations from Cap de Creus. The relative importance of the possible softening mechanisms in the formations of these zones is also considered.

6.1 The Physical Model

At a particular time during its propagation a shear zone may be approximated to a disc-like volume of softened rock with strain and stress concentrations at its edges, forming a toroidal volume of concentrated deformation, Fig. 6.1 (see also Ball, 1980). It may be likened to an expanding dislocation loop, with the type of displacement at the edges varying from pure edge to pure screw (e.g. Hull, 1975). Alternatively, this model is more closely allied to that of a discoid shear-crack with crack-tip displacements varying from pure mode II (in-plane shear) to pure mode III (anti-plane shear), and a zone of plastic deformation at the leading edge (Lawn and Wilshaw, 1975).

The main reason that a ductile shear-crack analysis is unsuitable for modelling a shear zone is that the deformation on a crack is necessarily discontinuous, whatever the nature of the deformation at the leading edge, while in a shear zone strain continuity is maintained from one side of the zone to the other. The closest approach to a model capable of dealing with the continuous nature of deformation in a shear zone is that due to Palmer and Rice (1973), developed for shear bands in clay. However, although the analysis includes the effect of stress transmitted across the band, the strain across the band is not continuous.

I will now look at the area around the top of a propagating zone, choosing

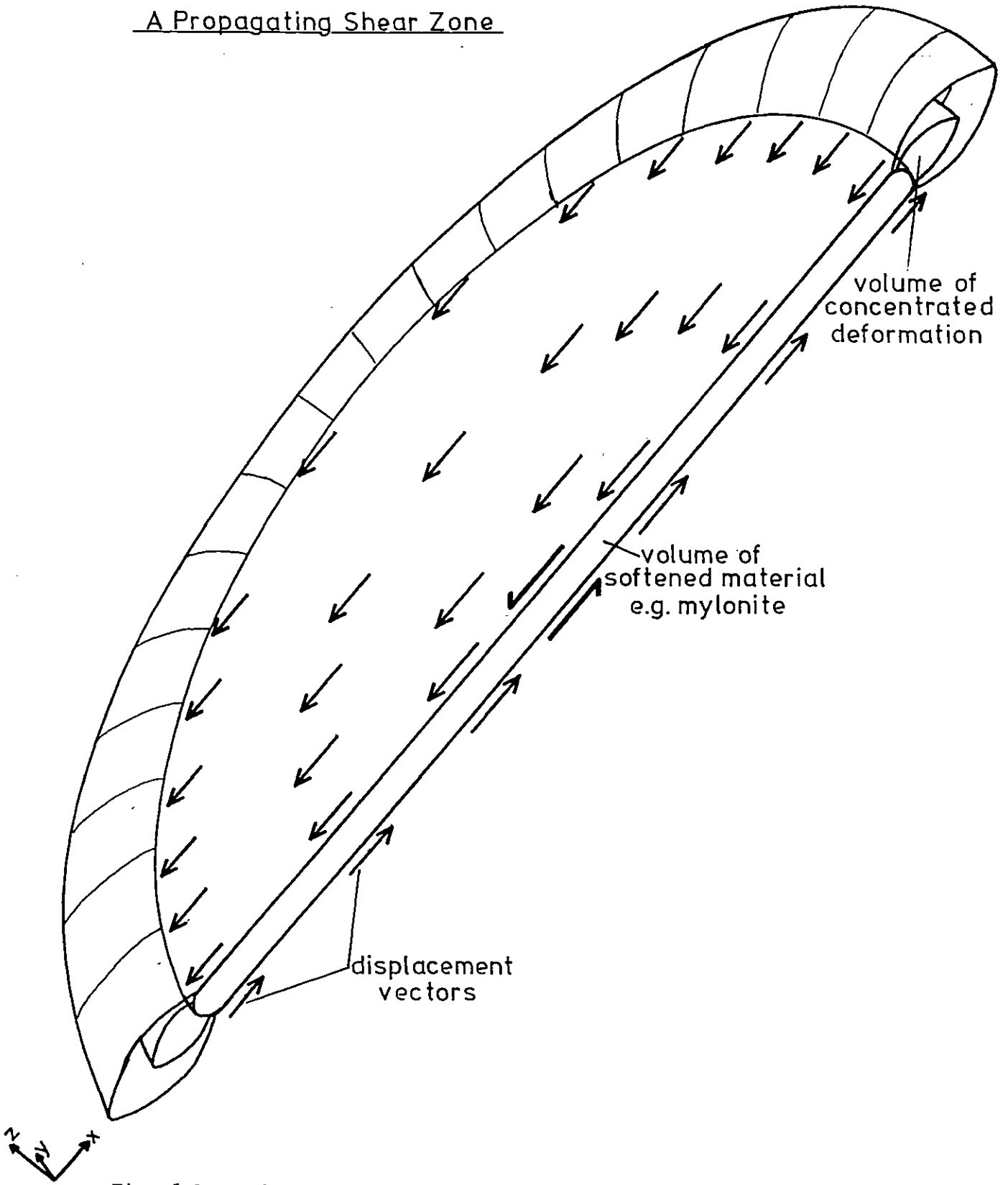


Fig. 6.1 Schematic diagram of a shear zone during propagation, showing the concentrated volume of deformation at the leading edge.

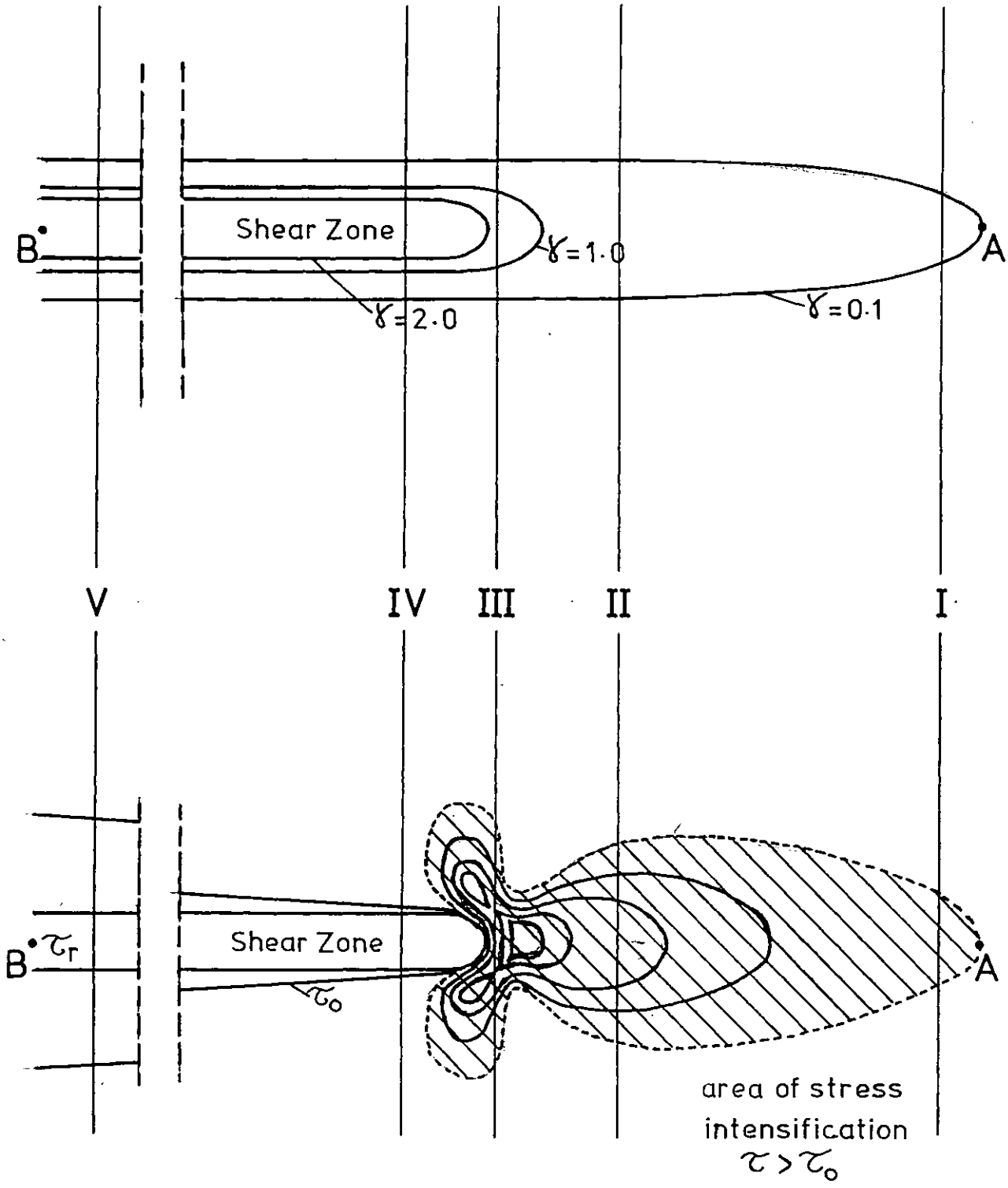


Fig. 6.2 The distribution around the tip of a propagating shear zone of (a) strain, and (b) stress.

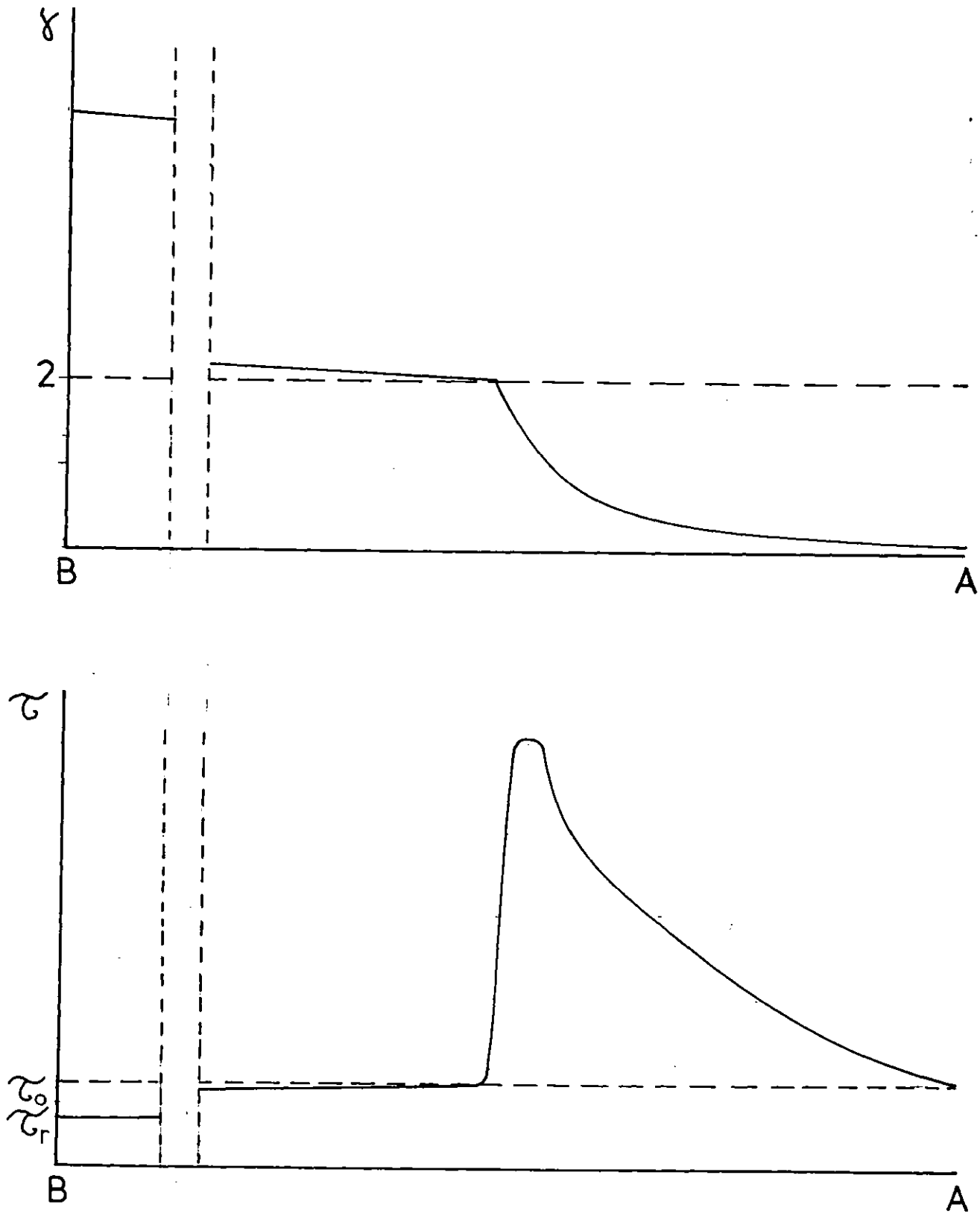


Fig. 6.3 Profiles along line AB in Fig. 6.2 of (a) strain, and (b) stress.

a section for which the direction of propagation is parallel to the displacement vector, so that it may be represented in two dimensions. Fig. 6.2 (a)(b) show the distributions of strain and stress around the tip of the zone; these have been obtained, respectively, from (a) the observation of shear zone terminations in the field, and (b) the calculated stress field around a shear crack (Chinnery, 1966; Paris and Shi, 1967) modified to take account of the observation that strain-softening in mylonites is not instantaneous (as bond rupture is in crack propagation) by reducing the stress gradients in the area just around the tip (N.B. the degree of stress intensification shown is obtained from the shear zone at Cap de Creus in this study, section 5.5).

Fig. 6.3(a)(b) show strain and stress profiles along the line A-B in Fig. 6.2. If the shear zone is propagating at constant speed these profiles will also illustrate the variation of strain and stress with time, going from right to left, for a point in the direct path of the advancing zone. Fig. 6.4 shows strain and stress profiles along the lines marked (I-V) on Fig. 6.2.

Along the line (I) that just falls within the zone affected by the deformation around the tip, the strain shows a marginal increase over its initial level, while the stress is already significantly higher than the initial background level. Along the second line the strain now shows a smoothly varying profile, reaching a maximum of just under $\gamma = 1$. At this level of strain, some strain-softening will already have occurred and all further strain profiles will show sharp strain gradients as the strain localizes within the softened region. At this point the stress has already built up to almost four times the initial level.

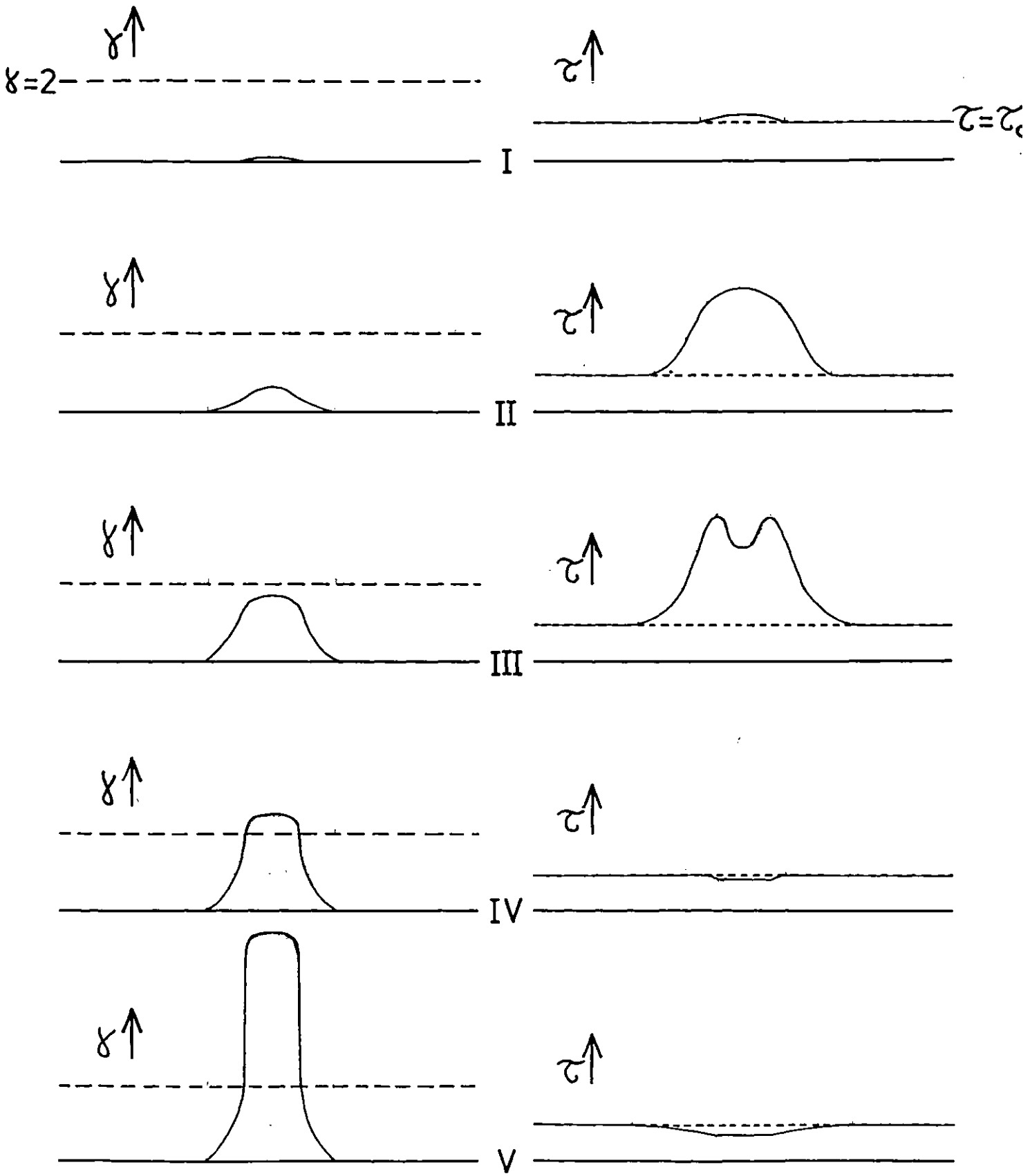


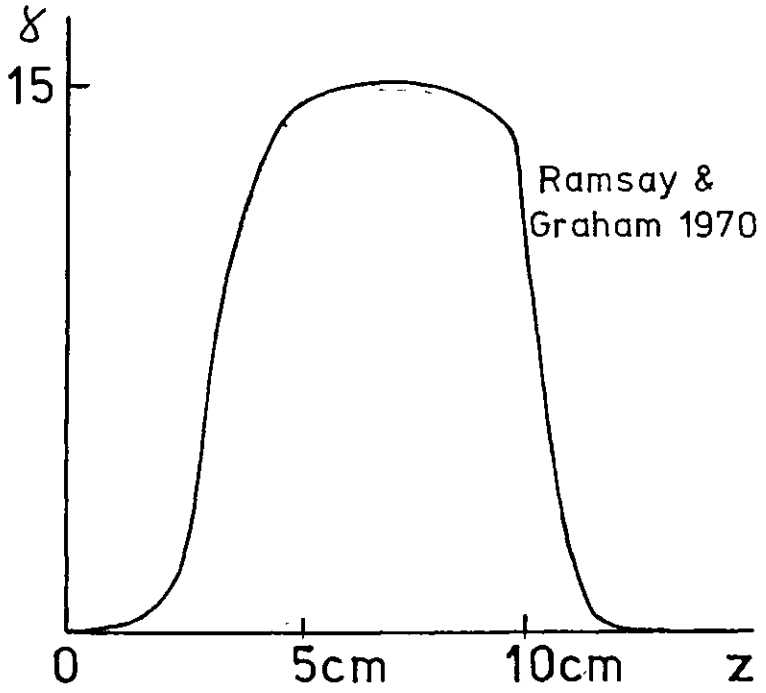
Fig. 6.4 Strain and stress profiles along the lines (I-V) perpendicular to the direction of propagation.

At the point at which the shear zone proper starts (IV) the strain profile already shows the sharp strain gradients mentioned above; virtually all the later deformation will now be concentrated within the shear zone itself. The stress profile demonstrates the effects of the secondary stress lobes shown in Fig. 6.3(b); the stress in the zone itself has very nearly relaxed to the background level.

Strain profile No. IV shows virtually no change from No. III, just a slight increase in the strain within the zone, the stress having now relaxed to its original level with a slight relaxation below that in the zone itself. Some distance from the top (V) the strain within the zone has increased markedly while the deformation outside has been negligible, and the stress is now relaxed to below its original level over a large area. This is due to the shear zone allowing a volume of rock much larger than itself to meet the regional constraints at a stress lower than the initial stress.

It should be noted that this model predicts that variations in strain within a shear zone should be very much smaller than those across the boundaries. At high shear strains the strain profile will approximate very closely to 'flat-topped'. Ramsay (1979) has suggested that such profiles indicate the onset of secondary strain-hardening within the centre of the zone, associated with lateral propagation of the zone boundaries. In the case of twins, or kink bands, both of which have a characteristic amount of rotation associated, this is clearly so, but ductile shear zones develop with a very large range of shear strains (e.g. this study section 3.3.4) and it is difficult to understand why strain-hardening should appear at $\gamma \sim 50$ when the microstructures indicate a steady-state from $\gamma \sim 2$ onwards, without changes in external parameters.

Fig. 6.5 shows two shear strain profiles from shear zones taken from the literature (Ramsay and Graham, 1970; Watterson, 1979). Both profiles are similar in form to that predicted in Fig. 6.4.



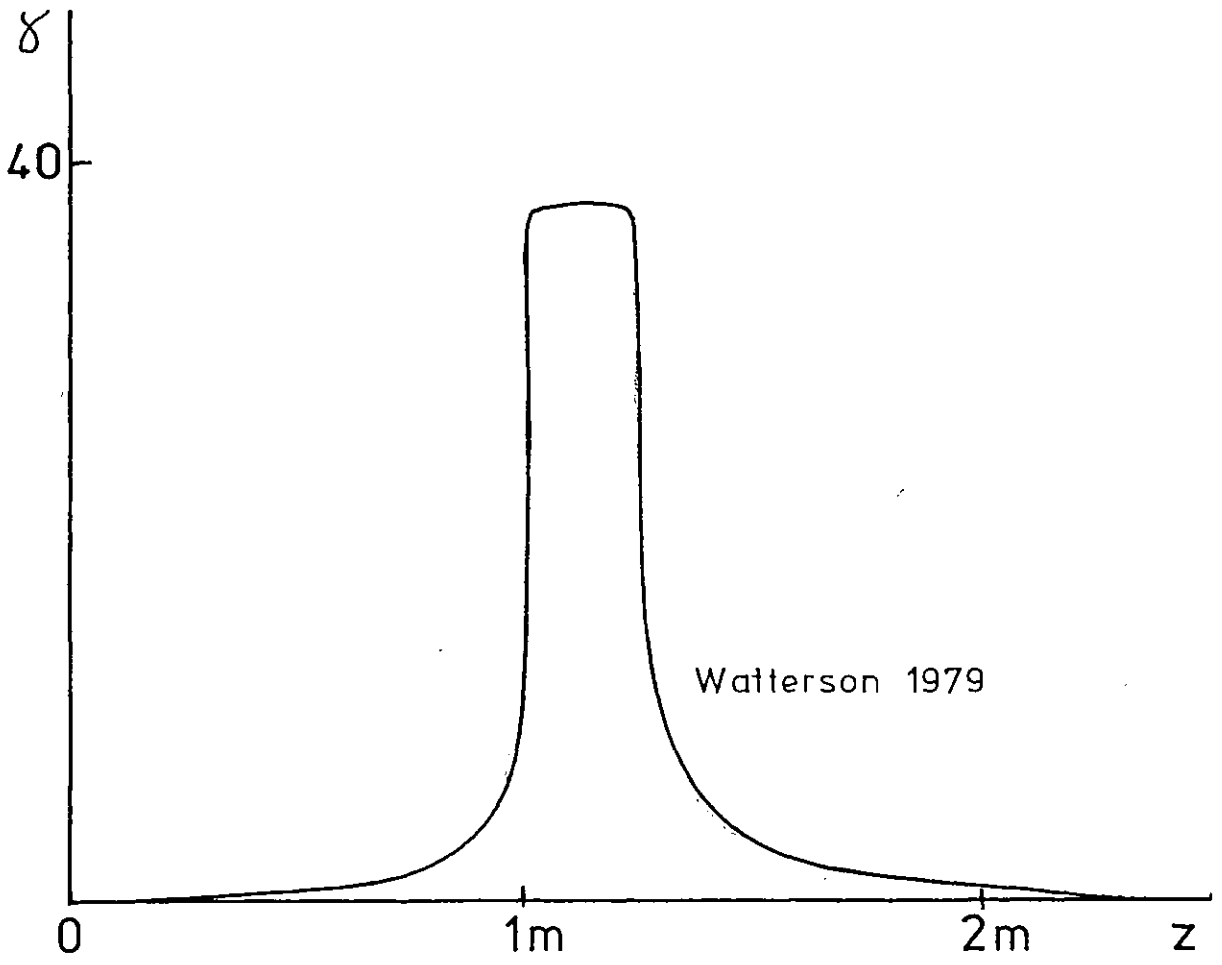


Fig. 6.5 Two published shear strain profiles.

(a) A zone developed in metagabbro, Castell O"Dair, Outer Hebrides. (Ramsay and Graham,1970)

(b) A zone developed in trondjhemitic gneiss, West Greenland. (Watterson,1979)

6.2 Shear zone propagation rates

In the development of a shear zone network it is important to have some idea as to the rates of propagation of individual shear zones when compared with strain-rates within the country-rock and the shear zones themselves (Coward, 1976). In this section a simple analysis is developed from the physical model presented in Section 6.1 using experimentally-determined flow-laws and parameters derived from both field and micro-structural observations.

6.2.1 Assumptions of the analysis

The main assumptions made in the following analysis may be summarized as:-

1. Shear zones propagate at a constant speed, u_x.

2. The stress distribution along the direction of propagation may be approximated to a 'saw-toothed' form, i.e.

$$\sigma_t = \sigma_0(1 + \{r-1\}\, {}^{t}/_{t_1}) \qquad (6.1)$$

where $r = \sigma max/\sigma_0$ the maximum stress intensification; $t = 0$ is the time at which a material point in the path of the propagating zone just comes under the influence of the zone of stress concentration, e.g. at point A in Fig. 6.2.

3. An area within the country-rock becomes part of the shear zone at a critical strain γ_c.

4. The material obeys a flow law of the form

$$\dot{\epsilon} = A\sigma^n \exp({}^{-Q}/_{RT}) \qquad (6.2)$$

5. The strain softening obeys a parabolic law of the form

$$A_t = A_0(1 + B\{{}^{t}/_{t_1}\}^2) \qquad (6.3)$$

where B represents the final degree of strain softening, i.e. at $t = t_1$

$$A_{t_1}/A_{t_o} = B + 1$$

The first assumption is perhaps the most difficult to justify but, if as suggested by Ball (1980), shear zones accelerate we would expect major variations in style along the length of a zone, something that is not observed.

Assumption (2) is taken from the stress distribution figured in Fig.6.2(b) approximated to simple linear form to make the later manipulation tractable.

Assumption (3) follows from the common observation that in any one area, all the shear zones show a sharp change in strain gradient above a certain constant strain. From microstructural studies this is seen to coincide with the establishment of a 'steady-state', both in fabric and texture.

The flow-law in assumption (4) is a type commonly assumed for the steady-state deformation of a material by dislocation creep (see also Section 4.1.1.3)

Strain-softening does not occur instantaneously but over a range of strains, and the relationship used in the final assumption gives the correct general form. Other types of polynomials may fit the actual behaviour better, but in the absence of any data on the detailed strain softening behaviour of geological material, this simple form will be used.

6.2.2 Analysis

For a material point in the path of a propagating zone, under the influence of the stress concentration, the strain-rate at time t, is given by

$$\dot{\varepsilon}_t = A_t \sigma_t^n \exp(^{-Q}/RT)$$

which from 6.1, 6.3 gives

$$\dot{\varepsilon}_t = A_o \sigma_o^n \exp(^{-Q}/RT).(1+\{r-1\}^{t}/t_1)^n(1+B\{^{t}/t_1\}^2) \qquad (6.4)$$

to obtain the total strain at the point, at time t, we integrate the above expression with respect to time

$$\varepsilon_t = A_o\sigma_o^n \exp(^{-Q}/RT) \int_o^t (1+\{r-1\}^t/t_1)^n.(1+B\{^t/t_1\}^2).\ dt$$

at $t = t_1$ $\gamma_t = \gamma_{t_1}$ but also $= \gamma_c$

$$\therefore\ \dot{\varepsilon}_c = A_o\sigma_o^n \exp(^{-Q}/RT) \int_o^{t_1} (1+\{r-1\}^t/t_1)^n.(1+B\{^t/t_1\}^2).dt \qquad (6.5)$$

after integration and manipulation this gives

$$\varepsilon_c = A_o\sigma_o^n\exp(^{-Q}/RT) \left[\frac{(1+B)t_1r^{(n+1)}}{(r-1)(n+1)} - \frac{2Bt_1r^{(n+2)}}{(r-1)^2(n+1)(n+2)} + \frac{2Bt_1r^{(n+3)}}{(r-1)^3(n+1)(n+2)(n+3)}\right.$$

$$\left. - \frac{t_1}{(r-1)(n+1)} - \frac{2Bt_1}{(r-1)^3(n+1)(n+2)(n+3)}\right] \qquad (6.6)$$

for a particular flow law and values of ε_c, r, B we may obtain t_1. The propagation rate is then obtained from

$$\dot{u}_x = {}^{x_1}/t_1 \qquad (6.7)$$

where x_1 is the extent of the zone of stress intensification in the x-direction. This extent is taken to be directly proportional to the shear zone width (w) as $x_1 = 1.w$

$$\therefore\ \dot{u}_x = {}^{1.w}/t_1 \qquad (6.8)$$

6.2.3 Results

The flow-law used in the calculation is taken from Koch et al. (1981) obtained from the experimental deformation of a wet quartzite. This flow-law predicts crustal behaviour that seems to be in accord with observations such as the brittle-ductile transition as determined from the depth distribution of microearthquakes (Sibson, 1981). The question must arise as to whether a quartzite flow-law is suitable for modelling crustal processes. A very recent paper by Carter et al. (1981) has provided a flow-law for granite.

This is very similar to that found by Koch et al. (1981) for quartzite, leading the authors to suggest that the deformation of quartz is rate-controlling in the deformation of granite.

From Koch et al. we obtain values of n = 2.44 and

$A_o \exp(^{-Q}/_{RT}) = 1.5 \times 10^{-12}$ at 400^oC

$= 1.1 \times 10^{-11}$ at 450^oC.

The critical strain value is taken as $\gamma_c = 2$ for observation of the development of a steady-state microstructure during mylonitization at Cap de Creus (Carreras et al. 1977), the equivalent logarithmic strain is $\varepsilon_c = 0.88$.

The maximum stress intensification is taken in the range $2 \leqslant r \leqslant 5$ from the interpretation of stress estimates derived from quartz microstructures (see section 4) from the Cap de Creus. The background stress level of 10MPa is also derived in this way.

The degree of strain-softening is taken as being

$A_{t_1}/A_o = 100$ i.e. B = 99

this follows from comparison of the finite shear strain observed in shear zones compared with those in the country-rock. In the zones shear strains of $\gamma_{sz} \sim 50$ are common (see Section 3.34) while the country-rock schists show strains of no greater than $\gamma_{CR} \sim 0.5$. Assuming that these strains have been accumulated over the same period of time, then two orders of magnitude of softening are indicated.

The ratio of extent of the zone of stress intensification to shear zone width is taken as $\ell = 10$ from field observations, see e.g. Fig.3.18

The results are presented in Table 6.1, giving propagation rates for values of r = 2 and 5, temperature at 400°C and 450°C, and for shear zones of w = 1cm, 1m, 100m and 10km.

6.2.4 Discussion

To compare the rate of displacement on a shear zone with its rate of propagation we will take the example of a 1m wide zone, for a stress intensification of x5 at 400°C.

From Table 6.1

$$\dot{u}_x = 6.5 \times 10^{-11} ms^{-1}$$

now, using the softened value of A = At, in the flow-law (6.2) we obtain for the strain-rate in the shear zone

$$\dot{\gamma}_{sz} = 9.5 \times 10^{-13} s^{-1}$$

but for the 1m zone the displacement rate is equal to the strain rate

i.e. $\dot{d}_{sz} = 9.5 \times 10^{-13} ms^{-1}$

nearly two orders of magnitude slower than the propagation rate. For r = 2 the propagation rate is still ten times faster than the displacement rate.

At the very much higher speeds of seismic faulting an even larger disparity exists (a factor $\sim 10^3$- 10^4) between rupture velocity, and sliding velocity (Johnson and Scholz, 1976).

Coward (1976) has suggested that strongly curving shear zones that form anastomosing networks may be formed when the rate of propagation is similar to the rate of displacement (see Section 5.82). It would appear from the above results that the curvature, and anastomosing nature of the shear zones at Cap de Creus cannot be explained in this way.

One implication of the analysis is that the rate of propagation of a

TABLE 6.1

PROPAGATION RATES (ms^{-1}).

			W = 1cm	W = 1m	W = 100m	W = 10km
B=9	r=2	T=400°C	9.50×10^{-15}	9.50×10^{-13}	9.50×10^{-11}	9.50×10^{-9}
		T=450°C	6.95×10^{-14}	6.95×10^{-12}	6.95×10^{-10}	6.95×10^{-8}
	r=5	T=400°C	6.95×10^{-14}	6.95×10^{-12}	6.95×10^{-10}	6.95×10^{-8}
		T=450°C	5.10×10^{-13}	5.10×10^{-11}	5.10×10^{-9}	5.10×10^{-7}
B=99	r=2	T=400°C	1.20×10^{-13}	1.20×10^{-11}	1.20×10^{-9}	1.20×10^{-7}
		T=450°C	9.00×10^{-13}	9.00×10^{-11}	9.00×10^{-9}	9.00×10^{-7}
	r=5	T=400°C	6.50×10^{-13}	6.50×10^{-11}	6.50×10^{-9}	6.50×10^{-7}
		T=450°C	4.75×10^{-12}	4.75×10^{-10}	4.75×10^{-8}	4.75×10^{-6}

W = Width of zone

B = Degree of structural softening

r = Degree of stress intensification

Table 6.1 Propagation rates of shear zones of varying width, degree of structural softening, and degree of stress intensification.

TABLE 6.2

		tp		γ_{tp}
B = 9	r = 2	T = 400°C	2.8×10^{14}	27.9
		T = 450°C	2.3×10^{13}	
	r = 5	T = 400°C	3.5×10^{13}	5.3
		T = 450°C	5.0×10^{12}	
B = 99	r = 2	T = 400°C	2.0×10^{13}	21.0
		T = 450°C	2.8×10^{12}	
	r = 5	T = 400°C	3.8×10^{12}	5.5
		T = 450°C	5.3×10^{11}	

Table 6.2 Time taken to reach final aspect ratio (tp, secs) shear strain accumulated at point of initiation at $t = tp(\gamma_{tp})$ for various values of B (the degree of structural softening) and the degree of stress intensification (r).

shear zone is directly proportional to the width. Evidence for this is difficult to obtain, but one observation at Cap de Creus is of interest. The aspect ratio (i.e. length : width) of the Cap de Creus shear zone is c. 500 : 1, independent of shear zone width. Assuming most shear zones to have been propagating for about the same amount of time, this indicates that the wider shear zones did indeed propagate faster than the narrower zones.

The time taken for propagation to the final aspect ratio (t_p) is therefore the same for all shear zones at constant r and T (Table 6.2). Also included in this table are the shear strains reached at the point of shear zone initiation at time t_p, to see if any variations in shear are predicted along the length of the shear zones.

For r = 2 the shear strain will be of the same order as the total value, while for r = 5 the strain accumulated at time t_1 will represent a relatively small fraction of the final strain. The first case would predict significant systematic strain variations along the length of a shear zone, while in the second the variation would be insufficient to be detected. Field observations indicate that shear strains do not vary systematically except in the region of their terminations.

In Table 6.3 the time taken for propagation to the final aspect ratio (t_T) is compared with the active life of the shear zone (t_L), taking an average final shear strain of $\gamma_{sz} \sim 50$.

It seems from these figures that the development and entire life of a shear zone network similar to that at Cap de Creus represents a considerable proportion of the time during an orogenic episode.

TABLE 6.3

B	r	T	t_p(years)	t_L(years)
9	2	400	8.8×10^6	17×10^6
		450	1.1×10^6	2.3×10^6
	5	400	1.1×10^6	17×10^6
		450	1.5×10^5	2.3×10^6
99	2	400	6.5×10^5	1.7×10^6
		450	8.8×10^4	2.3×10^5
	5	400	1.2×10^5	1.7×10^6
		450	1.6×10^4	2.3×10^5

Table 6.3 Propagation time (t_p) compared to active life (t_L) for various values of B (the degree of structural softening and r (the degree of stress intensification).

6.3 The development of shear zones within a system subject to constraints

We will now move up in scale from an individual shear zone to the development of a network of zones within a system representing a volume of rock subjected to certain constraints, and to what effect this localization has on the deformation of the system as a whole.

6.3.1 Approach adopted

Structural geologists have tended to model the development of structures by taking a system, applying a stress and observing the resultant strains. A more rewarding approach involves the application of particular geometric and kinematic constraints at the boundary of a system. Geological examples of this type of system are very common but a few examples will suffice. On a small scale, in the buckling of a multilayer consisting of alternating sandstone/shale units, the buckling is governed principally by the behaviour of the relatively 'competent' sandstone units while the shale units are constrained to take up the geometry of these layers, at the strain-rate imposed. On a larger scale, for a continental type transform plate margin, the deformation of the boundary zone (e.g. the Alpine Fault, New Zealand) is constrained by the relative motion of the plates.

6.3.2 The System

The system is a volume of isotropic, relatively homogeneous rock, such as a granitic intrusion. At the pressures and temperatures considered (i.e. mid to upper greenschist) the rocks deform ductilely except at high strain-rate. Until constraints are applied the system is in a state of hydrostatic stress.

Once constraints are applied the system may respond in a number of different ways, depending on the applied strain-rate, which are shown schematically in Fig. 6.6. At a fast strain-rate (curve (1)) recovery mechanisms are always insufficient to keep up with the increase in stored

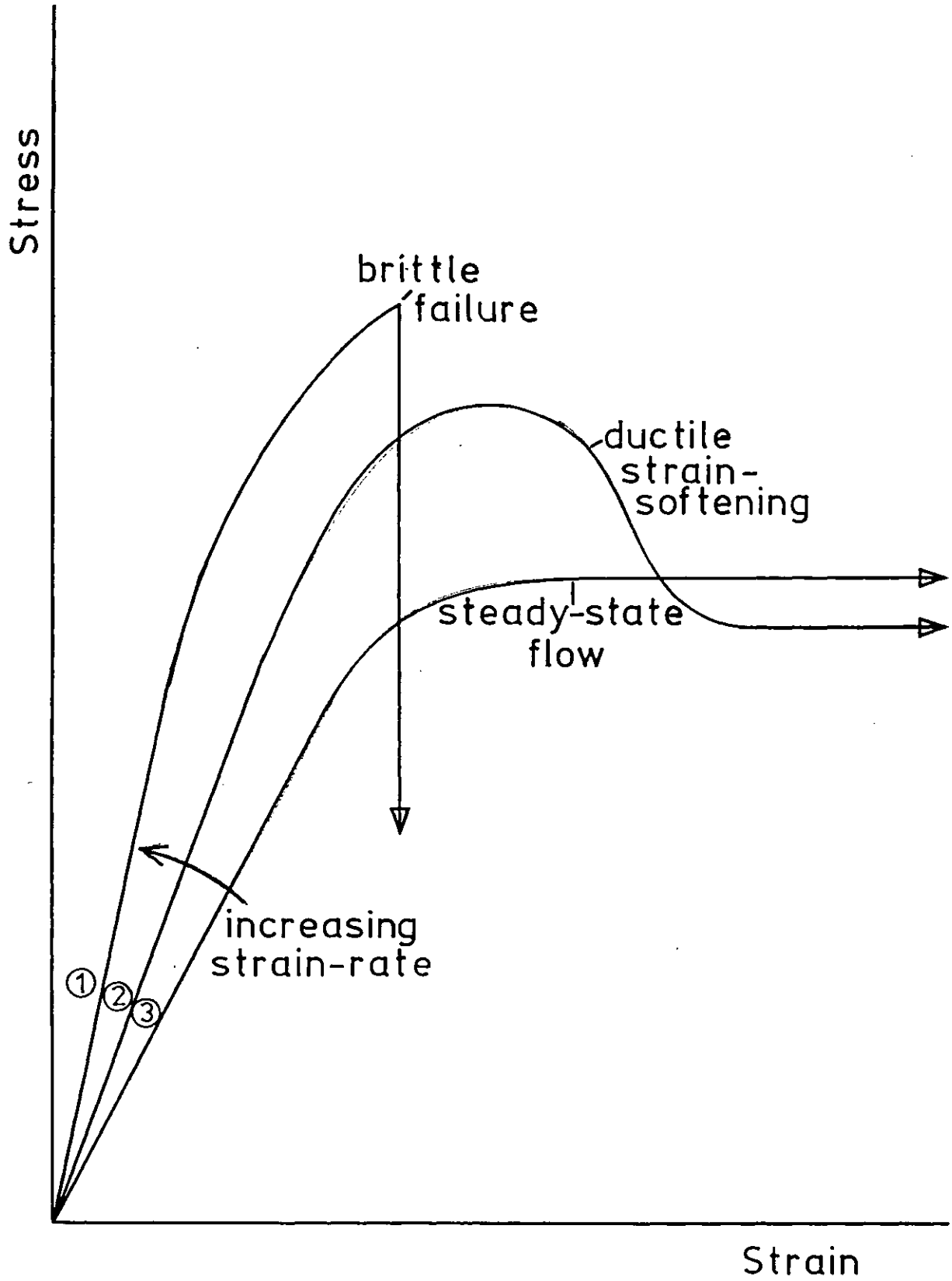


Fig. 6.6 Response of a system to applied constraints at; fast, intermediate, and slow strain-rates.

elastic strain energy, and with strain the stress continues to rise until catastrophic brittle failure occurs, relaxing the stored energy. Alternatively at slow strain-rates (curve (3)) the stress increases until that time at which the rate of increase of stored elastic strain energy is exactly balanced by the rate of energy dissipation through recovery, leading to a steady-state flow at a constant stress.

At intermediate strain rates (curve (2)), the stress continues to rise with strain until a change in structure occurs that allows reduction in the stored strain energy, either by decreasing the rate of accumulation of stored elastic strain energy or by enhancing recovery, i.e. the process known as strain-softening (s.l.).

For a completely homogeneous system strain-softening would happen everywhere simultaneously. However, it is more realistic to assume the presence of a large number of heterogeneities due to compositional variations, grain size variations, etc., that may be regarded as strength defects. These defects may be either 'stronger' or 'softer' than the matrix, and vary in scale from individual grains (where the rock is truly heterogeneous) up to regions $\sim$ 100m e.g. minor intrusions in an igneous body.

6.3.3 The effect of progressive strain on the system

Fig. 6.7 shows the variation of stress with strain for the system as a whole, measured at its boundaries. For the first few increments of strain this response will be mainly elastic, but with further strain an increasing amount of the deformation is ductile in nature. At a certain point (marked A) that heterogeneity in the system which leads to the greatest stress concentration will have reached the stage at which the propagation of a shear zone may begin. The effect on the system is, however, purely local at this stage of the development, and with further strain the system stress will

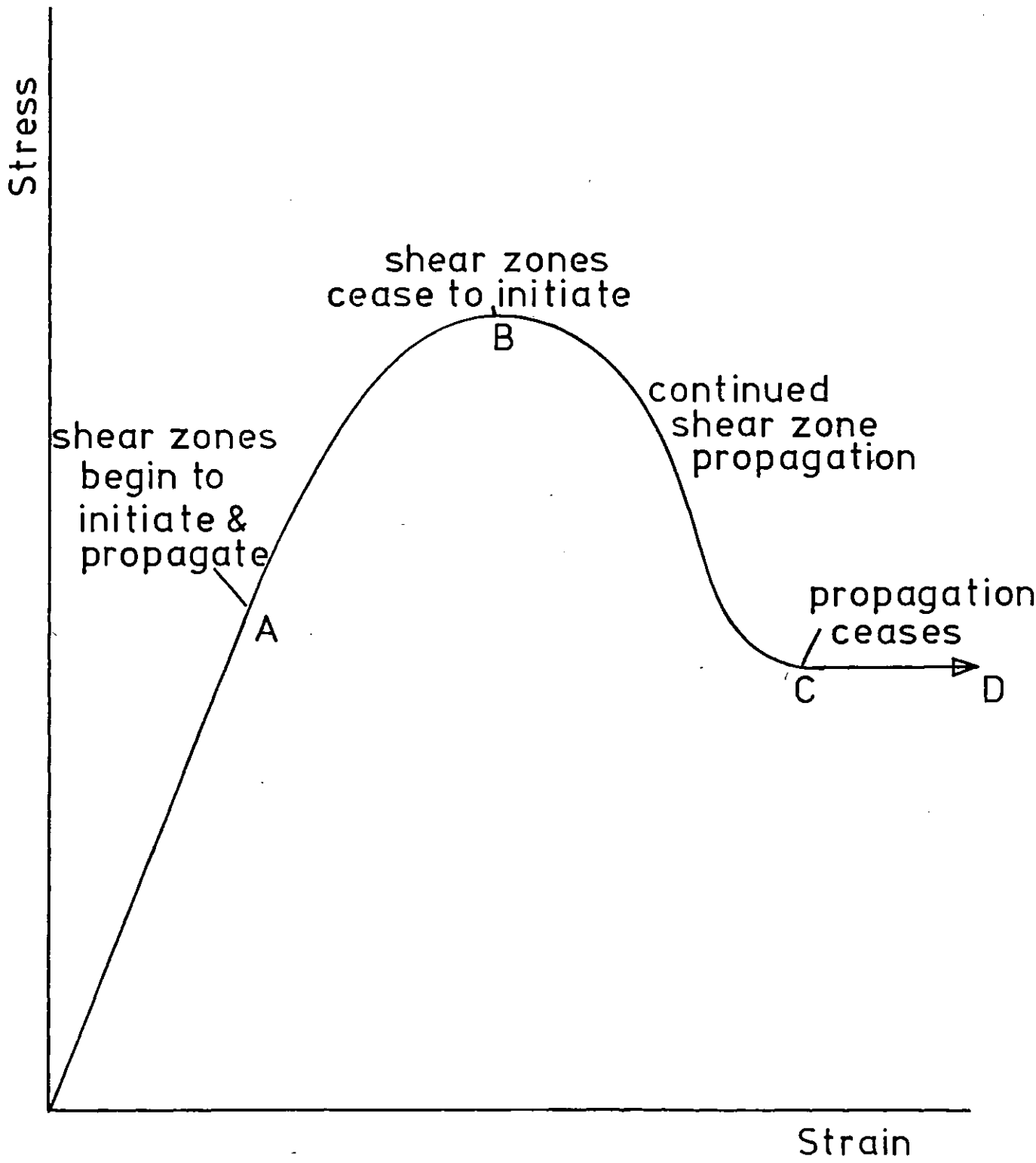


Fig. 6.7 Stress-strain curve for the system measured at its boundaries. N.B. As the displacement-rate at the boundaries is taken as constant, the strain axis also represents time.

continue to rise, but at an increasingly slower rate.

There is an important difference between this model and that presented by Bowden (1970) (see Section 2.7.1). In his analysis Bowden assumed that all localization of deformation occurred after the peak stress, in the region of negative slope of the stress-strain curve, i.e. while the deformation in the system was formally unstable (see Section 2.7). He also assumes that strain-softening is purely a function of the amount of strain accumulated at any point, thus ignoring the effects of the orientation of the finite strain ellipsoid with respect to external strain axes. Clearly such softening mechanisms as dynamic recrystallization will not be affected, but if fabric softening is important, a finite strain state that leads to softening in one part of the system may lead to hardening in another part, due to differences in their orientation. In the case of a shear zone network in any regional deformation other than simple shear the effect of geometric softening will be to reinforce the difference between the shear zones and their matrix; further strain in the matrix will not lead to the same degree of strain softening as found in the shear zones and in some cases may even produce hardening instead. Fig. 6.8 illustrates the effect for the case of a simple network formed during regional pure shear at plane strain.

As the stress rises, more shear zones will initiate and start to propagate from heterogeneities. With time, the position will be reached where sufficient volume of shear zones is present for the system to meet the applied constraints at the regional stress (Bowden op cit.). This point (B) (Fig. 6.7) marks both the maximum level of stress (as detected at the system boundaries) and the cessation of shear zone initiation. Stresses around heterogeneities will now have reached their maximum values, and unless a shear zone initiates at this point it is unlikely ever to do so.

Although shear zone initiation has by now ceased, propagation still continues as quickly as ever. Thus the volume fraction of shear zones in

Fig. 6.8 Schematic diagram of incipient p- and s-bands to illustrate the development of prefered orientation of dominant slip-planes (insets), progressive strain in the s-band will lead to a relative softening while in the p-band it will lead to relative hardening.

Fig. 6.9 Networks of shear zones associated with (a) simple shear (b) pure shear, for plane strain.

FIG. 6·8

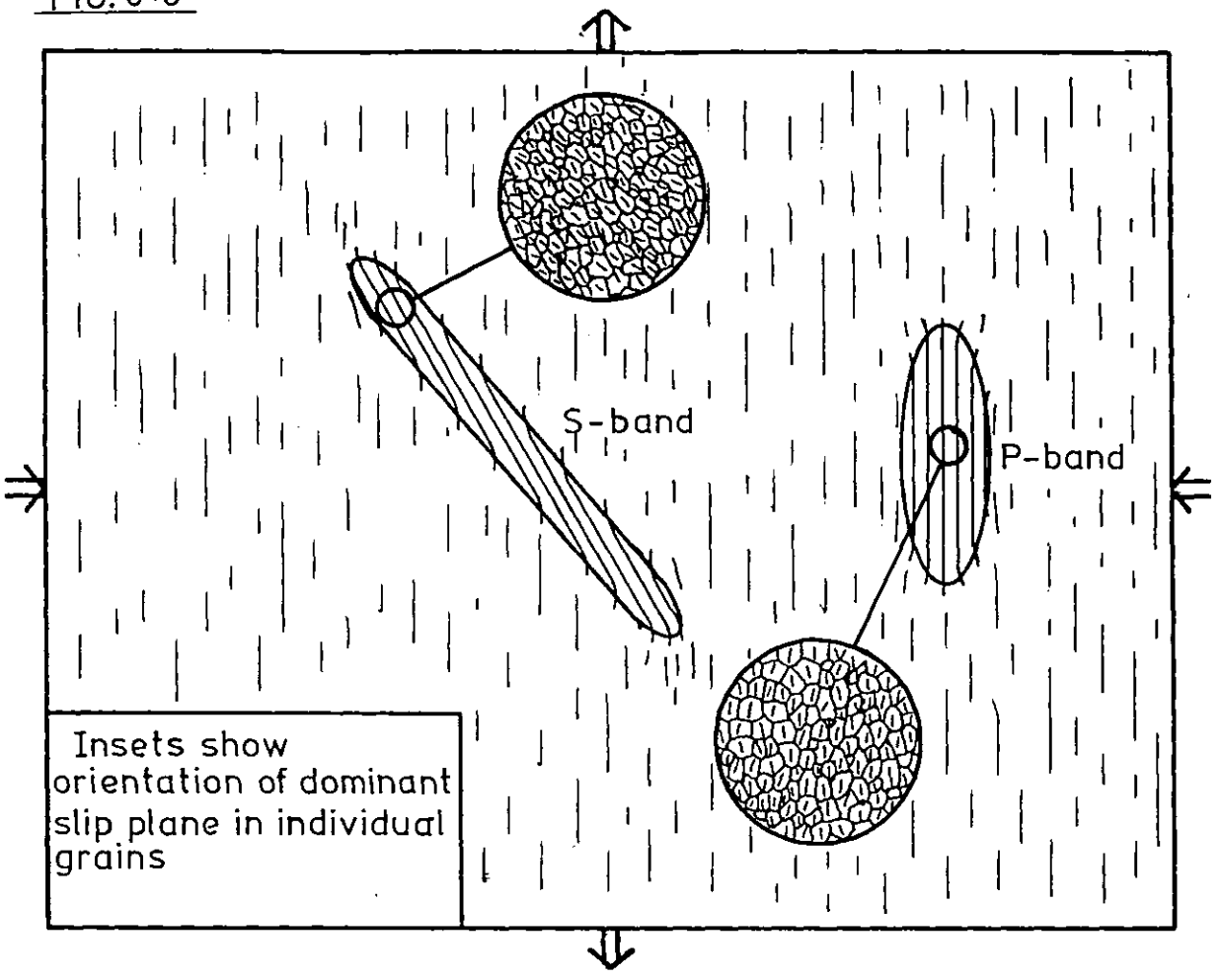
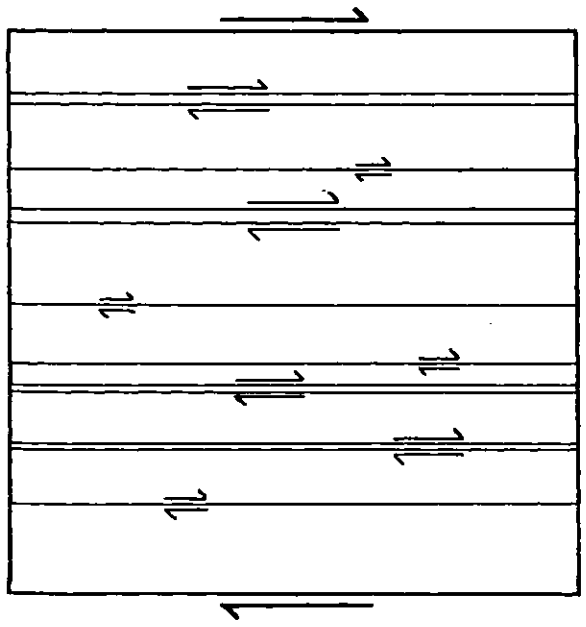
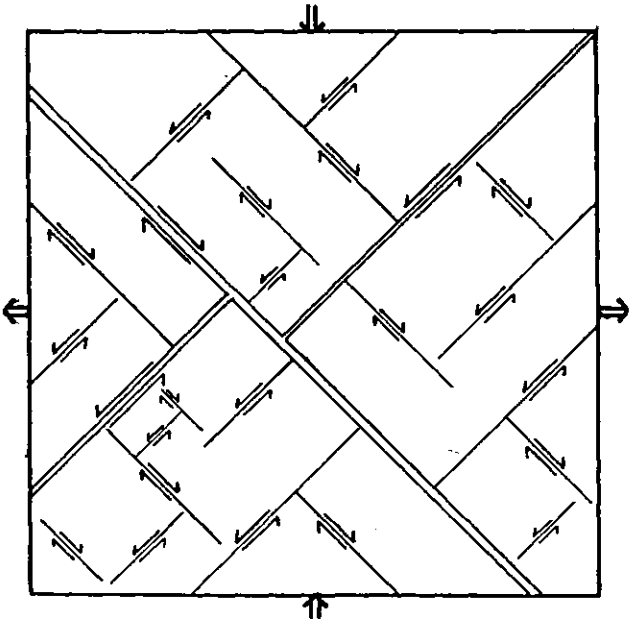

S-band
P-band
Insets show orientation of dominant slip plane in individual grains

FIG. 6·9





the system continues to increase, and the regional stress begins to fall. The stress will continue to fall until it has reached a level at which even those shear zones with the highest stress intensification are unable to propagate further (point C). Once propagation has ceased the system will deform, at a constant stress, as long as the same constraints continue to be applied (point D).

It should be mentioned here that this model of the development of a system with shear zones ignores one important problem; the interaction between the shear zones during their propagation, and during later deformation of the network formed; this will be considered in the next section.

As the strain-rate constraint on the system boundary is taken as constant, the abscissa in Fig. 6.7 also represents the variation with time. From the calculations presented in section 6.24 we may get some idea of the time-scale involved. The time taken to reach point A is indeterminate but at $400^{o}C$ the time between points A and C must be $\sim 10^{6}$ years, while the steady-state deformation continues for a further 2×10^{6} years.

6.4 Shear zone terminations

The use of sequential sampling across the boundaries of a shear zone in order to establish a sequence of progressive deformation has been criticized on the grounds that the deformation paths are not the same (this is clear from the strain profile development portrayed in Fig. 6.3(a). An alternative approach would be to study shear zone terminations, making the assumption that the 'frozen-in' strain field would be similar to that during propagation at any one time.

However, it is necessary to consider why the shear zone terminated. The simplest answer is that the regional stress level fell below that required to promote continued propagation (i.e. as suggested in previous section). If we now look at the types of shear zone terminations observed

at Cap de Creus (see Fig. 3.7) the above reason for termination is consistent with the type described as 'simple.'

All further types of termination involve interactions with other zones. In the type termed 'failed branch', it appears that a second shear zone has begun propagating under the influence of the stress field of the original zone. This effect may be likened to the mechanism proposed by Johnson and Holloway (1966) for the bifurcation of a brittle crack. However the original zone in such a case is always the larger, and will therefore propagate faster than the branch zone. The effect of the main zone is then to relax the stress in the region into which the branched zone is propagating, finally causing it to stop.

In the types of termination termed 'like and opposite-sense cancellation', further propagation of the zone involved seems to have been prevented by the interaction between the stress and strain fields around the shear zone tips. This sort of interaction has been studied analytically for the case of shear cracks (Segall and Pollard, 1980). Cancellation only seems to occur if the two shear zones are of similar width, otherwise it is presumed that the larger one will continue to propagate, whilst the smaller one stops.

The final unnamed type of termination (6), a small shear zone dies out having apparently encountered a larger established and active shear zone during its propagation. Such an established zone will be surrounded by a volume of rock in which the stress is relaxed (section 6.1) to below the regional level. A second zone which encounters the volume during propagation may therefore be stopped at that point. A sufficiently large zone may be able to intersect the original zone if the zone of relaxation is small, producing a junction. If the original zone had been the smaller

of the two it would be cut by the second zone.

Many shear zones, irrespective of the cause of propagation cessation, have complex areas of minor splays at their terminations. It is considered that these secondary zones are caused by the effects of continued displacement on a zone that has stopped propagating. Further displacement will lead to a continual accumulation of strain in the region of the tip. If the rock in this region is unable to dissipate this strain without strain hardening, heterogeneities within the resulting zone of stress intensification may lead to the initiation and propagation of minor shear zones. These zones will only extend as far as the zone of intensified stress. The splays at the ends of shear zones are thus explained in the same way as the splays at the end of brittle fault zones (e.g. Chinnery, 1966).

The final way in which a shear zone may terminate is by encountering a change in lithology during propagation. If the mechanical properties of the other lithology are significantly different to those of the lithology in which the zone started, then the propagation will be affected. If a weaker volume of rock is encountered the region just across the lithological boundary may be able to dissipate the strain concentration at the shear zone tip without strain-hardening, leading both to the relaxation of the stress concentration, and the cessation of propagation. If a stronger volume of rock is encountered the stress concentration may be insufficient to promote continued propagation.

It is clear that in none of the above cases will the macro- or microstructural variations around a shear zone termination represent the state developed during propagation. The distribution of stress, strain and microstructural changes around the tip of a propagating zone cannot be directly observed, either by sampling at the edges, or at a termination; such observations may, however, provide strong, indirect evidence.

6.5 The shear zone networks at Cap de Creus

In the previous section some of the field observations from Cap de Creus have already been interpreted in the light of the shear zone model presented in Section 6.1. In this section the other field observations and the microstructures from this area will be discussed.

6.5.1 The Cala Sardina network

In Section 6.3.3 no attempt was made to consider the type of shear zone network that might be produced in the system. The network should fully reflect the type of strain-field applied and, therefore, interpretation of shear zone networks may lead to an understanding of the nature of the regional strain field. The complexity of networks that may be produced will be directly related to the complexity of the applied strain field.

Figs. 6.9 shows the two simplest types of network, due to plane strain pure shear, and simple shear respectively. However, as already implied in Section 3.3.1.4 , the overall deformation at Cala Sardina departed significantly from plane strain, and the effects of a more general type of deformation must be considered.

We will now look at the networks likely to arise from co-axial deformation (i.e. one in which the axes of bulk regional finite and strain coincide) for various types of bulk strain ellipsoid. It is most convenient to discuss these in terms of their 'k' values (Flinn, 1962). Fig. 6.10 shows the expected orientation of lineations (assumed approx. parallel to movement direction) and poles to shear zone planes for the case of prolate ($k = \infty$), plane strain ($k = 1$) and oblate ($k = 0$) ellipsoids, for three different orientations of the ellipsoid. The dihedral angles of the shear zone sets are taken to vary with k-value. The angles used are

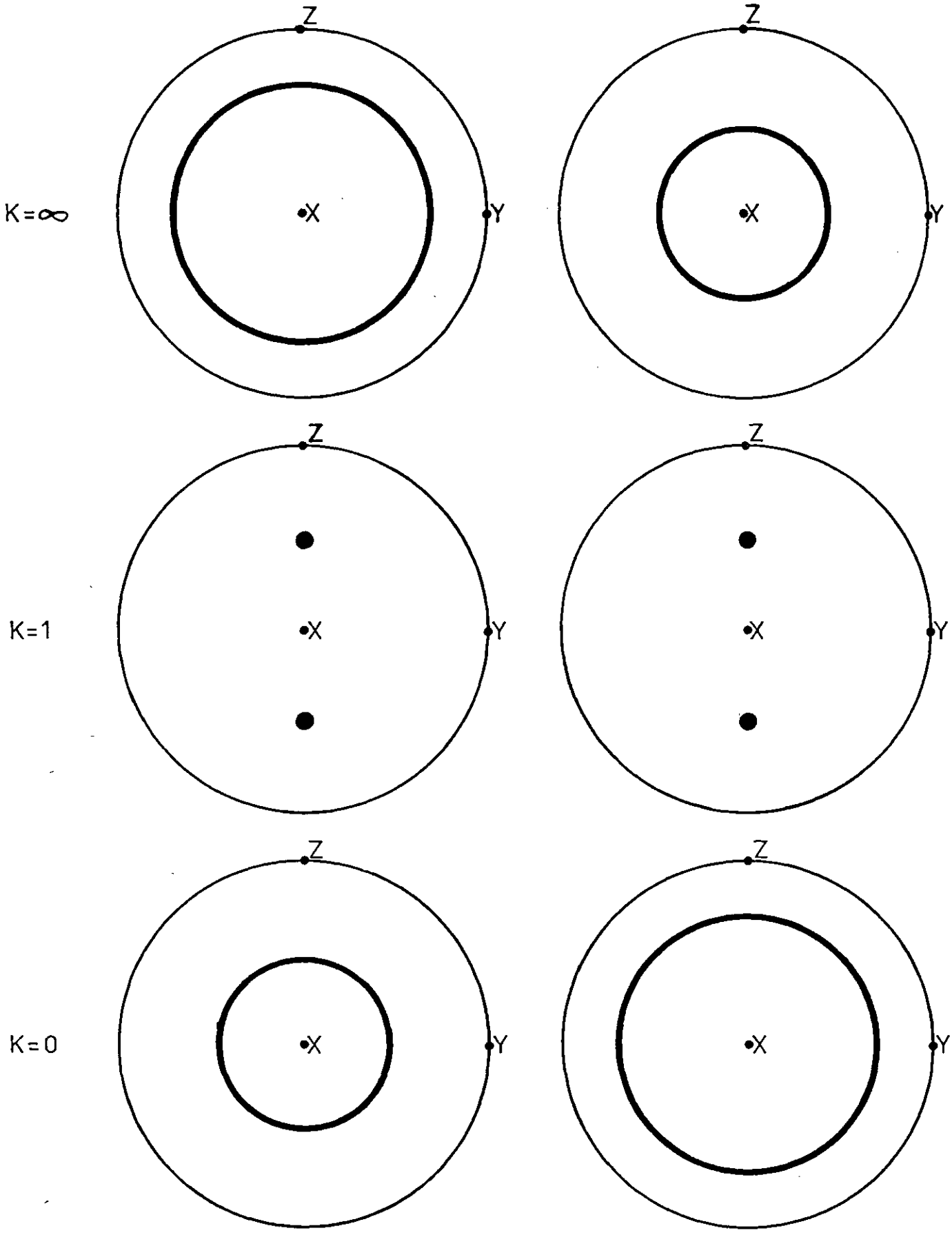


Fig. 6.10 Stereoplots of expected orientation of shear zones and associated lineations resulting from coaxial deformation for three types of bulk strain ellipsoid; perfectly prolate (k=∞), plane strain (k=1), and perfectly oblate (k=0).

FIG. 6.11

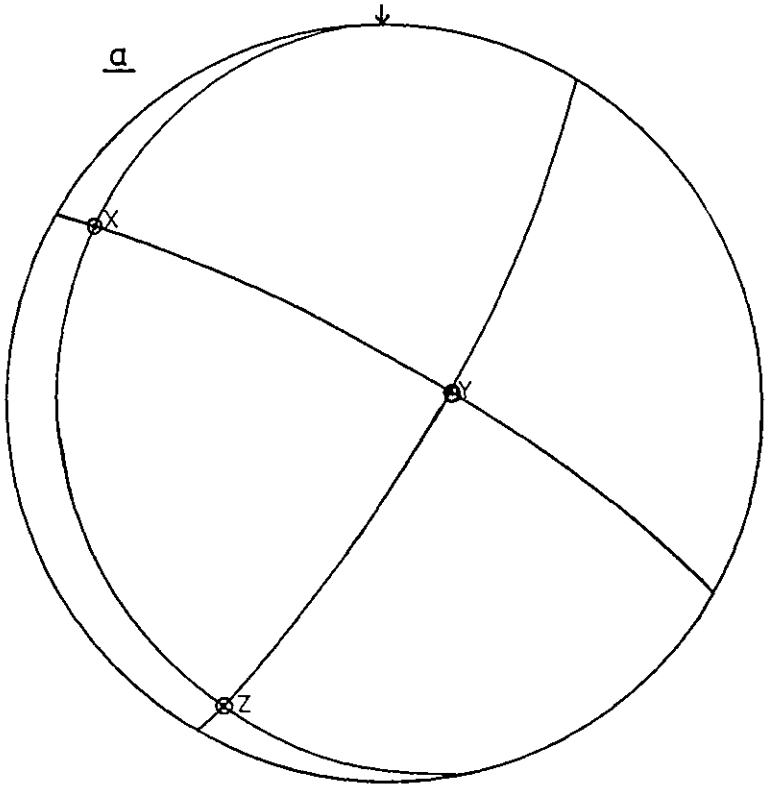


Fig. 6.11

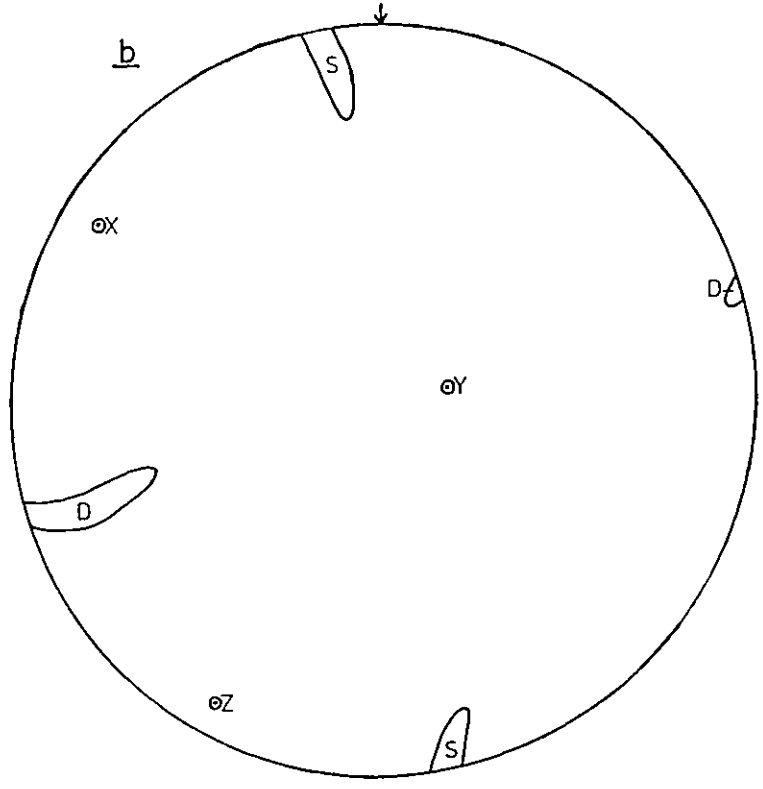
(a) Bulk strain axes for the Cala Sardina area derived from shear zone orientations.

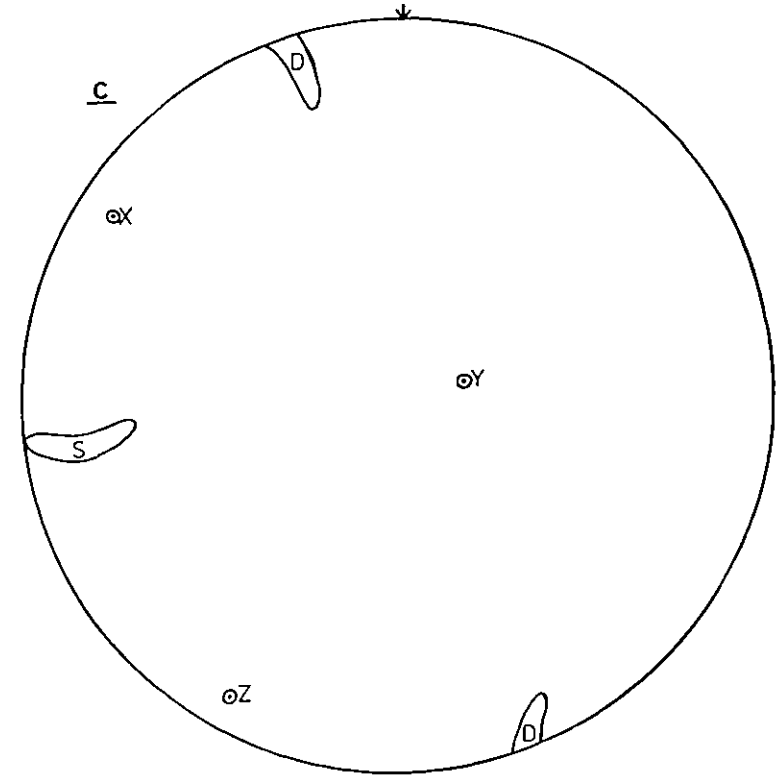
(b) Orientations of shear zones expected for a (O<k<1) ellipsoid (π-poles), as indicated by the geometry of the observed network.

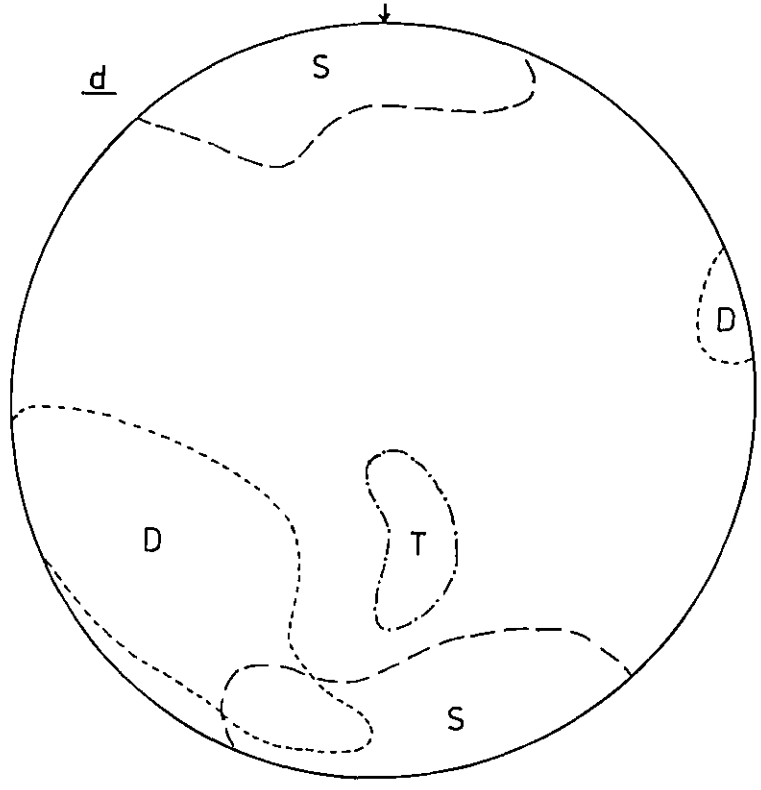
(c) Lineations expected for shear zone network due to a (O<k<1) ellipsoid.

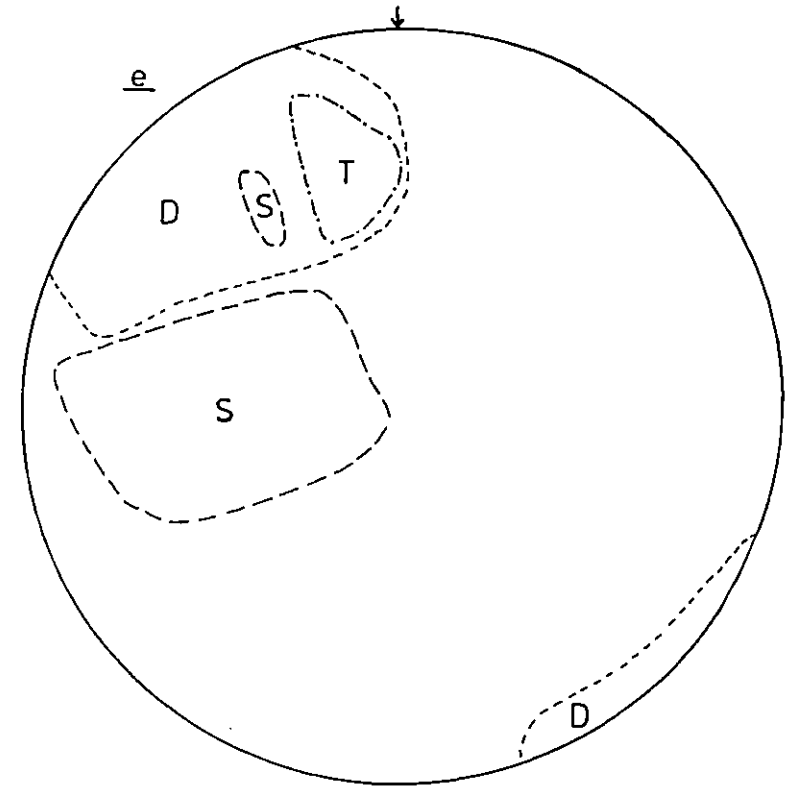
(d) Observed orientations of shear zones in the Cala Sardina network showing fields of data from each of the three types; S sinistral, D dextral, T thrust. (π-poles)

(e) Observed lineations from shear zones in the Cala Sardina network, showing fields of data from each type (as (d)).


b
S
X
D
Y
D
Z
S


c
D
X
Y
S
Z
D


d
S
D
D
T
S


e
T
D
S
S
D

taken from Watterson (in prep.) who derived them from a consideration of the minimization of stored elastic strain energy for shear zones of various orientations.

The effect of a non-coaxial strain history is principally to alter the relative degree of development of the conjugate sets, the angle involved will remain the same for constant k (e.g. for k = 1, see Figs. 6.9).

The approximate k-value for the bulk strain represented by the minor shear zone network at Cala Sardina may be estimated by a consideration of the effects of the three types of zone acting together. The two best-developed sets, dextral and sinistral, together indicate a sub-horizontal (SSW-NNE) direction of principal shortening (Z) with principal extension also sub-horizontal (WNW-ESE). The thrust sense zones indicate the same Z-direction but with sub-vertical principal extension. The overall strain therefore, is characterized by a sub-horizontal direction of principal shortening (SSW-NNE) with extension in both of the two orthogonal directions, although by different amounts, i.e. $0 < k < 1$.

Fig. 6.11(a) is a stereogram showing the principal strain axes as derived above for the Cala Sardina network. Fig. 6.11(b)(c) show the expected spread of shear zone orientation, and associated lineations for a bulk strain of $0 < k < 1$ for the strain orientation in 6.11(a). Fig. 6.11 (d)(e) summarize the observed shear zone orientations and lineation from Cala Sardina. Comparing the observed distributions with the predicted, it can be seen that the lineations show very good agreement, while the shear zone orientations are only in fair agreement. Part of the observed discrepancies are thought to be due to re-orientation of the minor shear zones in the vicinity of the major zone, or in areas where considerable flattening strains have developed in the matrix between the minor zones.

The observed network is, therefore, consistent with a bulk $0 < k < 1$

strain ellipsoid for the area of minor shear zones, and because the sinistral and dextral zones are equally well developed the strain must be essentially coaxial.

It is clear that in this area there are domains of essentially simple shear, that is the major shear zones, with domains of pure shear deformation between them accommodated in minor shear zone networks. From the considerations presented at the beginning of this section, any general deformation can be taken up a single network and the domainal nature of the regional strain must be explained.

The most likely cause of the domainal structure of the Cala Sardina area is control of the main shear zone orientation by a preexisting structure (N.B. such control is also suspected in the area marked C on Map 1, Section 3.1.1.3). As indicated in the review of the general geology of Cap de Creus (Section 3.2), the final fold phase has a similar axial plane orientation to the main set of dextral shear zones. That such a control is possible is shown by the shear zone localized in a minor fold at Portixol (section 3.3.2.3)

The result of such control is indicated schematically in Fig. 6.12. A general type of deformation, with components of both pure and simple shear is applied to a system containing earlier structures that control the orientation of the major shear zones. The main zones, therefore, take up the non-co-axial deformation leaving the pure shear component to be taken up by the area between the major zones on a minor shear zone network. The similarity of this pattern to that observed at Cala Sardina is apparent.

6.5.1.1 Low-strain mylonites

The main features of these areas developed at the edges of the Cala Sardina main zone were described in Section 3.3.1.2.1 ; lineation plunging down foliation, comparatively low shear strains, and partial bounding by other shear zones. In Section 5.6 evidence was presented from recrystallized

Fig. 6.12 The effects of prior structural control on the resultant network of shear zones in system subject to components of both pure and simple shear. Incipient weak zones control the localization of the dominant set of shear zones leaving a component of pure shear to be accommodated by a secondary network of zones leading to a domainal structure.

Fig. 6.13 Schematic diagram to illustrate the effect of the overlap of strain fields from two adjacent shear zones.

FIG. 6-12

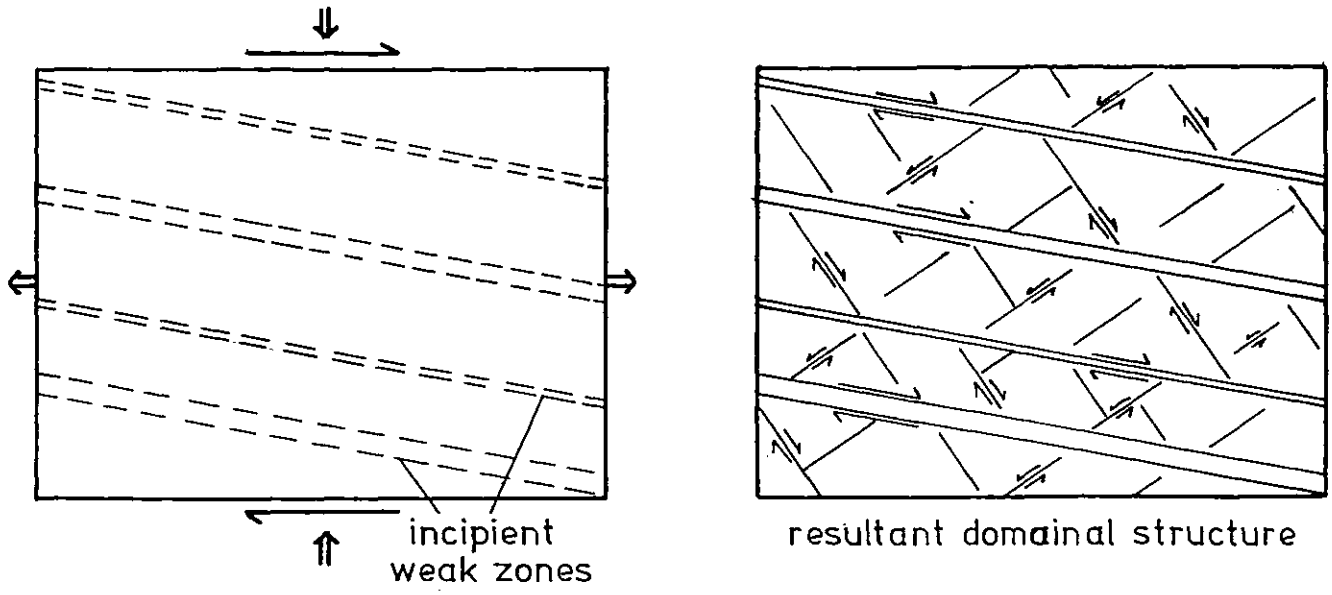
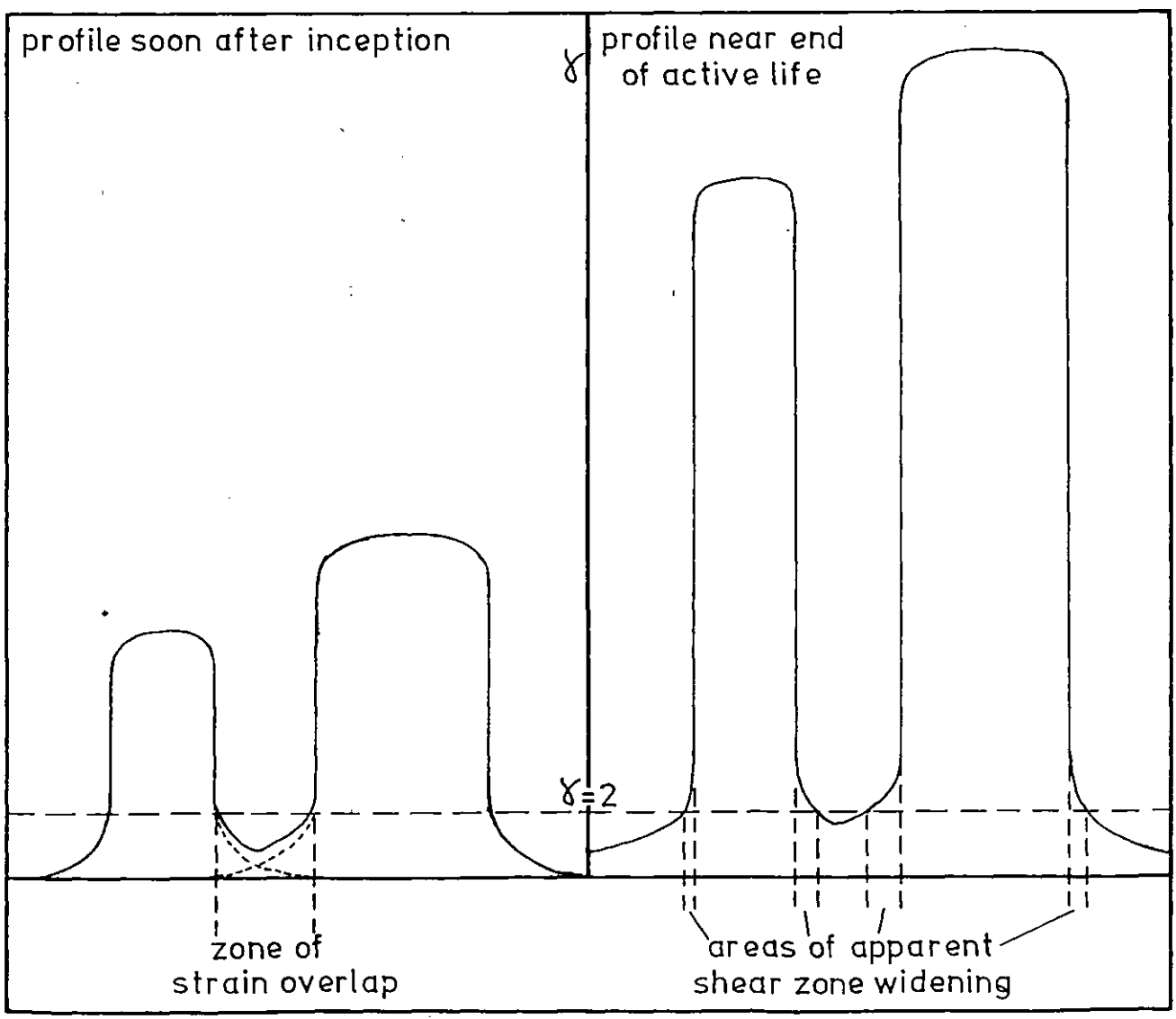


FIG. 6.13



grain sizes and sub-grain sizes that most of these mylonites were never subject to the higher stresses associated with shear zone formation. Also sampling across country-rock - low strain mylonite boundaries showed no change in stress, indicating a gradational boundary.

Fig. 6.13 shows the result of overlap of strain fields from two adjacent shear zones, on the developing strain profiles. As the strain continues to accumulate in the areas between shear zones the areas of strain overlap may reach the critical strain required for strain softening, and mylonite formation. Fig. 6.14 shows schematically a junction between a major and a minor shear zone with strain contours marked to illustrate how the characteristic form of the low-strain mylonites could have been developed. Such an area is found in Cala Sardina, marked (E) on Map (1), but the outcrop pattern is unusual as the line of intersection between the two zones is nearly in the plane of the outcrop.

The area around the junction between the main dextral zone and a minor sinistral zone has been described in detail (section 3.3.1.2.1 , area (D) in Map (1)). A possible mode of evolution of this junction is outlined in Fig. 6.15. This is a particular example of the strain compatibility problems that occur at shear zone junctions during the progressive deformation of a shear zone network.

6.5.2 The Portixol (Cala Serena) area

As described in Section 3.3.2.1 , the lineation and orientations of the minor shear zones at Portixol display a curious angular relationship; the lines of intersection of conjugate pairs are almost parallel to the lineation measured in both sets. This type of relationship runs contrary to all existing theory, no matter what the bulk strain. Such a relationship requires there to have been a major change in the bulk incremental strain state during deformation.

Fig. 6.14 Schematic diagram of a junction between a major shear zone and a minor shear zone, showing the expected strain distribution.

Fig. 6.15 A model for the evoutiom of the complex junction in the area marked (D) on Map 1.

(1) Initial geometry of shear zones with minor sinistral zone and branched major dextral zone.

(2) Areas of strain overlap at junctions become low-strain mylonites with progressive strain.

(3) This process continues particularly in the augen between the two dextral zones.

(4) Final configuration showing the distribution of mylonite types.

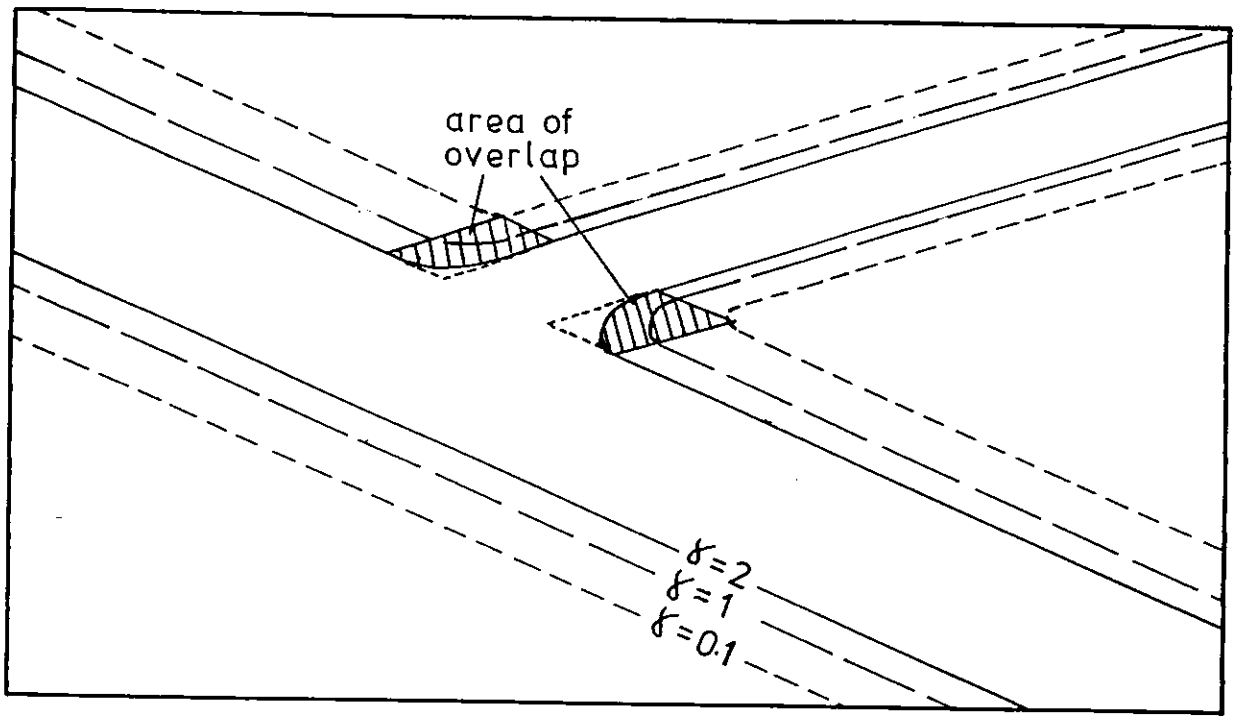
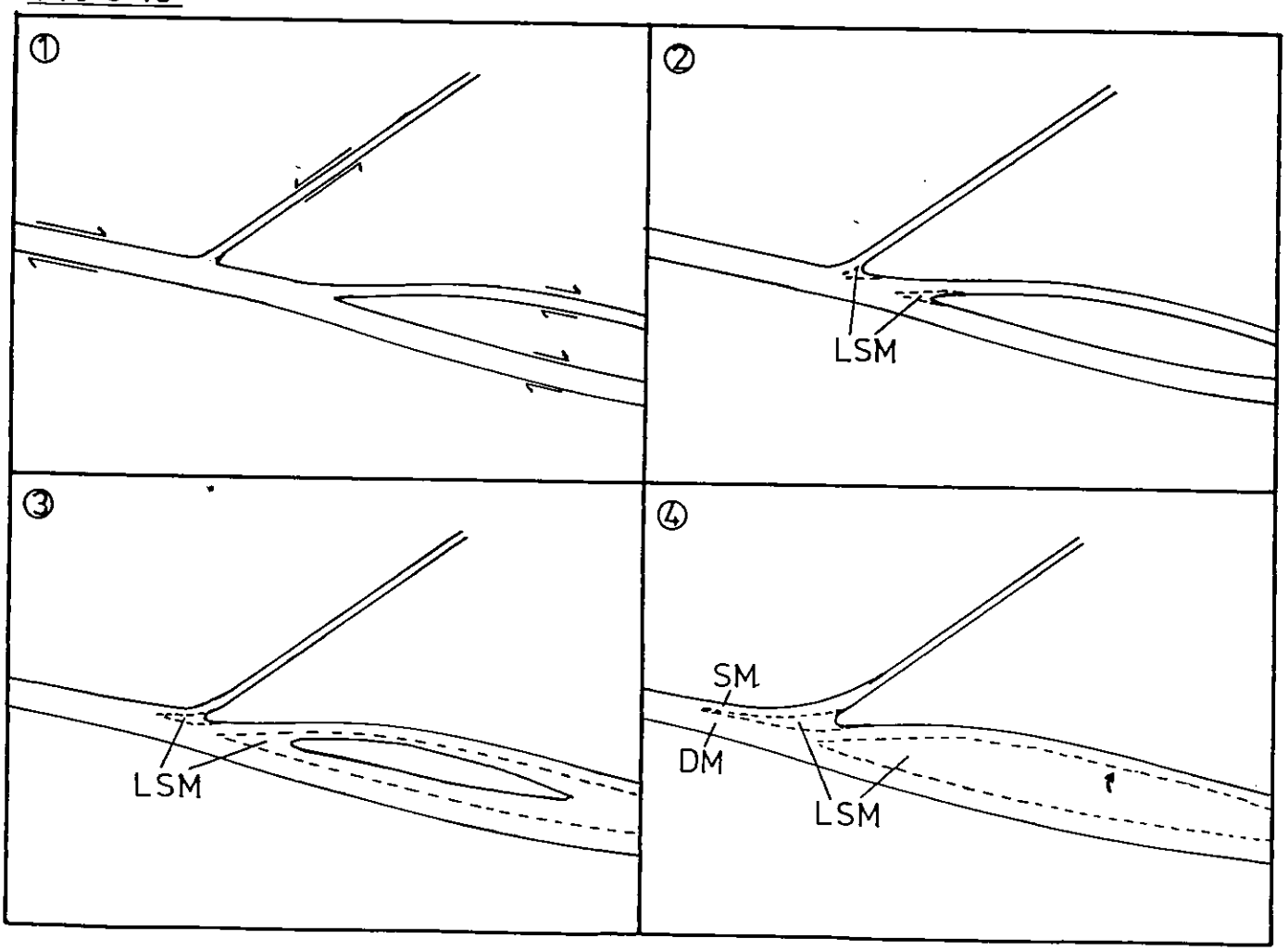


FIG. 6.15



LSM low-strain mylonite

SM sinistral sense mylonite

DM dextral sense mylonite

From the dihedral angles of the two shear zone sets (i.e. obtuse angle bisector sub-horizontal (NW-SE) assuming $0< k< 1$ bulk strain) it is assumed that the zones started life as reverse sense, but became modified later, taking up further deformation along the two sets by a form of pencil glide. Such a major change in the local bulk deformation may be correlated with the enforced reorientation of the shear zone in this area due to the postulated rotation of the more 'competent' quartz-diorite and migmatite block (section 3.3.2.3.).

6.6 Strain-softening in the shear zones at Cap de Creus

In this section the possible mechanisms contributing to strain-softening in the shear zones at Cap de Creus will be considered, under the headings used in section 2.7.2

6.6.1 Geometrical softening

As described in section 2.7.2.1 two types of geometric softening may be considered, rotation softening due to a bulk anisotropy or fabric softening related to the development of a crystallographic preferred orientation. At Cap de Creus, shear zones are developed both in areas of strong bulk anisotropy (e.g. the Portixol area) and in areas where the rock is effectively isotropic, except on the small scale, due to the effects of polyphase folding (e.g. the Cala Sardina area). As already argued in Section 3.3.2.3. the shear zones at Portixol are thought to have localized within an earlier kink-like structure, itself the result of the strong bulk anisotropy.

In some sense at least, the rotation softening associated with the formation of the kink-like structures has contributed to the shear zone formation. From observation in the Cala Sardina area, rotation softening is clearly not a prerequisite for shear zone formation and, even when it may be involved it must be insignificant relative to other effects.

Fabric softening, in contrast, seems to be very important in the formation

of many mylonites (White et al., 1980). The very strong preferred orientation in the quartz, particularly the a-axis point maximum (Schmid et al., 1981), developed in the mylonite of Cap de Creus, suggest this was a major, and possibly the controlling factor in the strain-softening process.

6.6.2. Structural softening

The effects of structural softening will be discussed separately for each mineral. Quartz is not involved in any phase transformation and the only change in structure, apart from possible effect due to variations in P_{H_2O} which are not quantifiable, is due to recrystallization. The small recrystallized grains are all formed by a mechanism which involves grain boundary migration, and the new grains are, therefore, strain-free and more deformable than the old grains from which they are derived. This more deformable state would, however, be relatively short-lived as the dislocation density rose steadily to its equilibrium level, unless continuous, cyclic, recrystallization occurred.

The other permanent strain-softening effect due to recrystallization is that caused by grain-size reduction. Initial grain sizes in the Cap de Creus schists, pegmatite, microgranites and quartz-diorites are of the order of mm's to cm's while the recrystallized grains vary from 50μm to 400μm. That this size reduction has affected the rheology of the rock is confirmed by the observed relationship between mylonitic microstructure (Section 4.1.4), and that between grain size and strain (Section 5.5) in a particular shear zone.

These may be summarized (and simplified) as follows. Fine-grained (Type III, $d_{RG} \sim 50\mu m$) quartz mylonites are thought to deform by dominant grain-boundary sliding processes due to their blocky grain shapes, and are found in shear zones of strain $\gamma \geqslant 100$. The coarser (Type I, $d_{RG} \geqslant 150\mu m$)

mylonites have textures consistent with dominant continuous dynamic recrystallization, and are characterized by shear strains of $2 \leqslant \gamma \leqslant 20$. Intermediate (Type II) mylonites show texture indicating contributions from both dynamic recrystallization and grain boundary sliding, and develop intermediate strains.

In the coarser-grained mylonites the comparatively low strains indicate less strain-softening than in the finer-grained types. It is thought that in the former type, grain-size reduction has had little or no softening effect, while with decreasing grain sizes the mylonites reflect an increasing degree of softening due to a consequent increase in the amount of grain-boundary sliding.

Feldspars recrystallize to fine-grained aggregates, or are broken down to form masses of fine-grained white mica. The effect of recrystallization is in many cases not to increase the intrinsic deformability, as the mechanism involved is one of sub-grain rotation and only those formed by nucleation will be strain free. Recrystallization in some of the feldspar-bearing mylonites is very restricted and, presumably, the effect on the rock as a whole is minimal. In some, however, almost 100% recrystallization takes place, giving rise to bands of very small ($\sim$ 5μm) feldspar grains which may deform by dominant grain boundary sliding, possibly leading to significant softening.

Fine-grained white micas are produced from the breakdown of biotite, and feldspar and also appear to grow in the mylonite foliation. The deformation mechanism of this fine-grained aggregate is not known, but the general lack of internal deformation features suggest that grain-boundary sliding was important. The largest effect is probably due to the inhibition of grain growth during steady-state deformation of the mylonite.

6.6.3 Strain and Strain-rate softening?

As discussed in Chapter 2, the effect of strain is likely to be negligible, and the effect of increasing strain-rate will be to harden the material; it is therefore this last term against which all the other effects must be balanced.

6.6.4 Shear Heating

The possibility that shear heating was responsible for strain softening in the shear zones at Cap de Creus was investigated using the equations of Carlslaw and Jaeger (1959), assuming a constant rate of heat production per unit volume and, therefore, linear viscous rheology (for a review of the possible methods see Section 2.7.2.5). This study was carried out using a 'worst case' analysis, that is with all the parameters set so as to produce the maximum possible shear heating effect. If significant heating had been predicted, a more exact analysis, taking account of non-Newtonian behaviour, and positive thermal feedback would have been undertaken. However, in the light of the results described below, no further study was carried out.

The equations used are for the increase in temperature (T), at time (t) at a distance (x) from centre of a zone of heat product rate (A_o) of half width (l).

$$T = \frac{kA_o t}{K}\left[1 - 2i^2\mathrm{erfc}\ \frac{l-x}{\sqrt{kt}} - 2i^2\mathrm{erfc}\ \frac{x+l}{\sqrt{kt}}\right] \qquad (6.1(a))$$

for $0 \leqslant x \leqslant l$.

$$T = \frac{kA_o t}{K}\left[2i^2\mathrm{erfc}\ \frac{x-l}{\sqrt{kt}} - 2i^2\mathrm{erfc}\ \frac{x+l}{\sqrt{kt}}\right] \qquad (6.1(b))$$

for $x \geqslant l$.

where k is the thermal diffusivity, K is the thermal conductivity, i^2erfc is the integral of the complement of the error function as tabulated by Carslaw and Jaeger.

The heat production as described in Section 2.7.2.5 is given by

$A_o = c.\sigma_{ij}\,\dot{\varepsilon}_{ij}$ where c_1 the efficiency is taken to be $\sim$1.

To model the decay, with time, of an initial heat pulse associated with the propagation event another equation due to Carslaw and Jaeger was used,

$$T = \tfrac{1}{2}To\left[\text{erf}\ \frac{a-x}{\sqrt{kt}} + \text{erf}\ \frac{a+x}{\sqrt{kt}}\right] \qquad (6.2)$$

where T is the temperature at time t at a distance x from the centre of a zone of half-width a initially at a temperature To above its surroundings and erf is the error function, as tabulated by Carslaw and Jaeger.

The effects of varying the parameters in equation 6.1(a)(b) are illustrated by two graphs Figs. 6.16, 6.17. The first shows the effect of varying the width of a shear zone for constant values of stress, strain-rate and time. The second illustrates the effects of altering the strain-rate for a zone of constant width, at constant stress and strain. It is clear that only for strain-rates of $\gamma > 10^{-10}$ and shear zones wider than 20m are temperature rises of more than a few degrees expected.

To instigate the thermal history of a shear zone, a simple two-stage model was chosen, with a propagation event at a high stress followed by steady-state flow at a low stress. Fig. 6.18 shows the sort of values of strain-rate and stress required in order to produce a temperature rise of $T \sim 50^{o}$, which is required to cause an order of magnitude increase in the strain rate (from the flow-law of Koch et al., 1981, see Section 6.23), in a 20m wide zone.

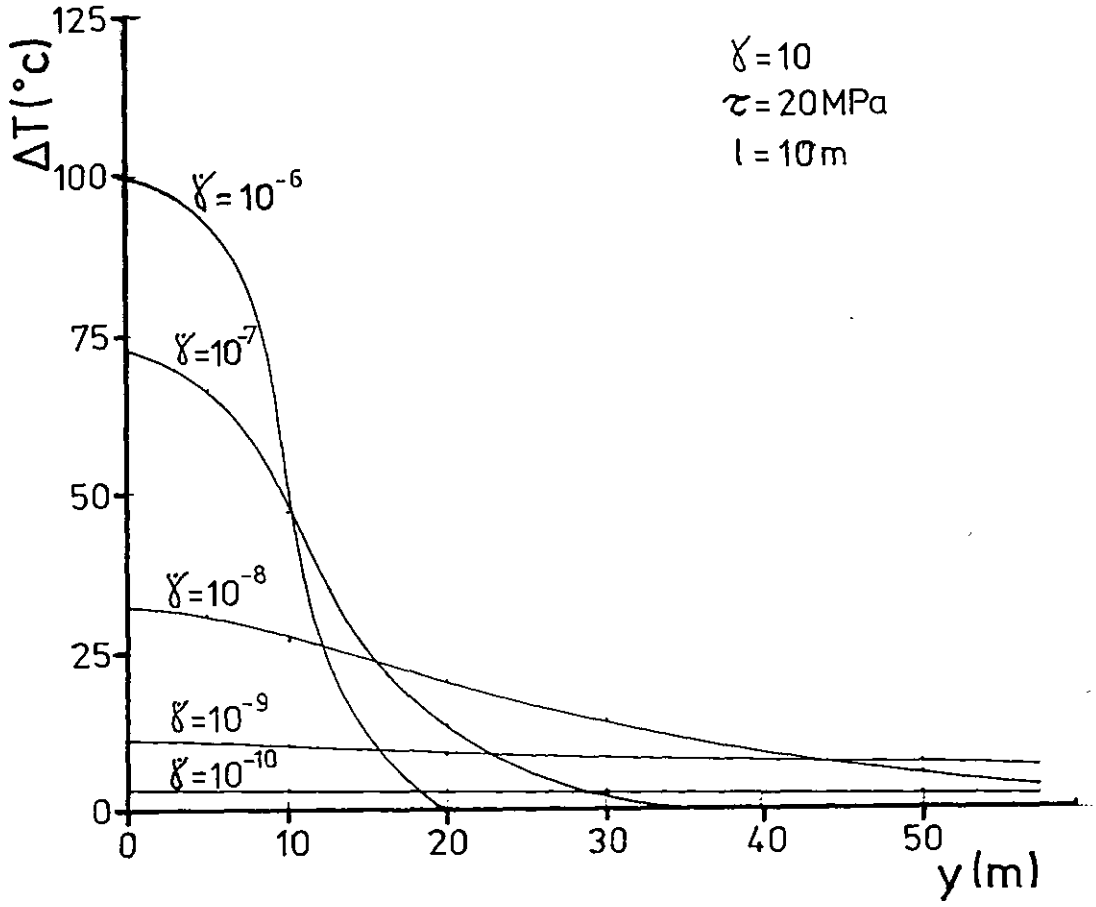


Fig. 6.16 Temperature profiles for a 20m wide zone at constant strain and stress, for varying strain-rate.

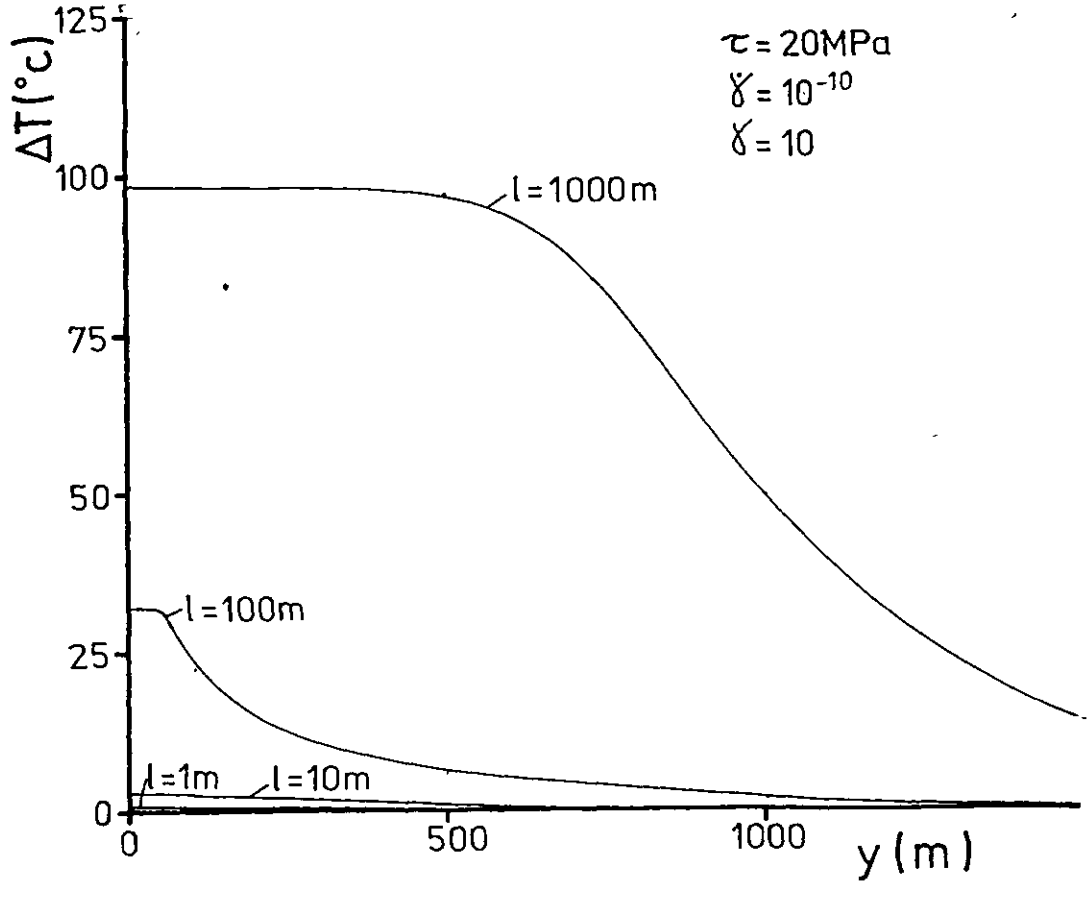


Fig. 6.17 Temperature profiles for zones of various widths at constant stress, strain and strain-rate.

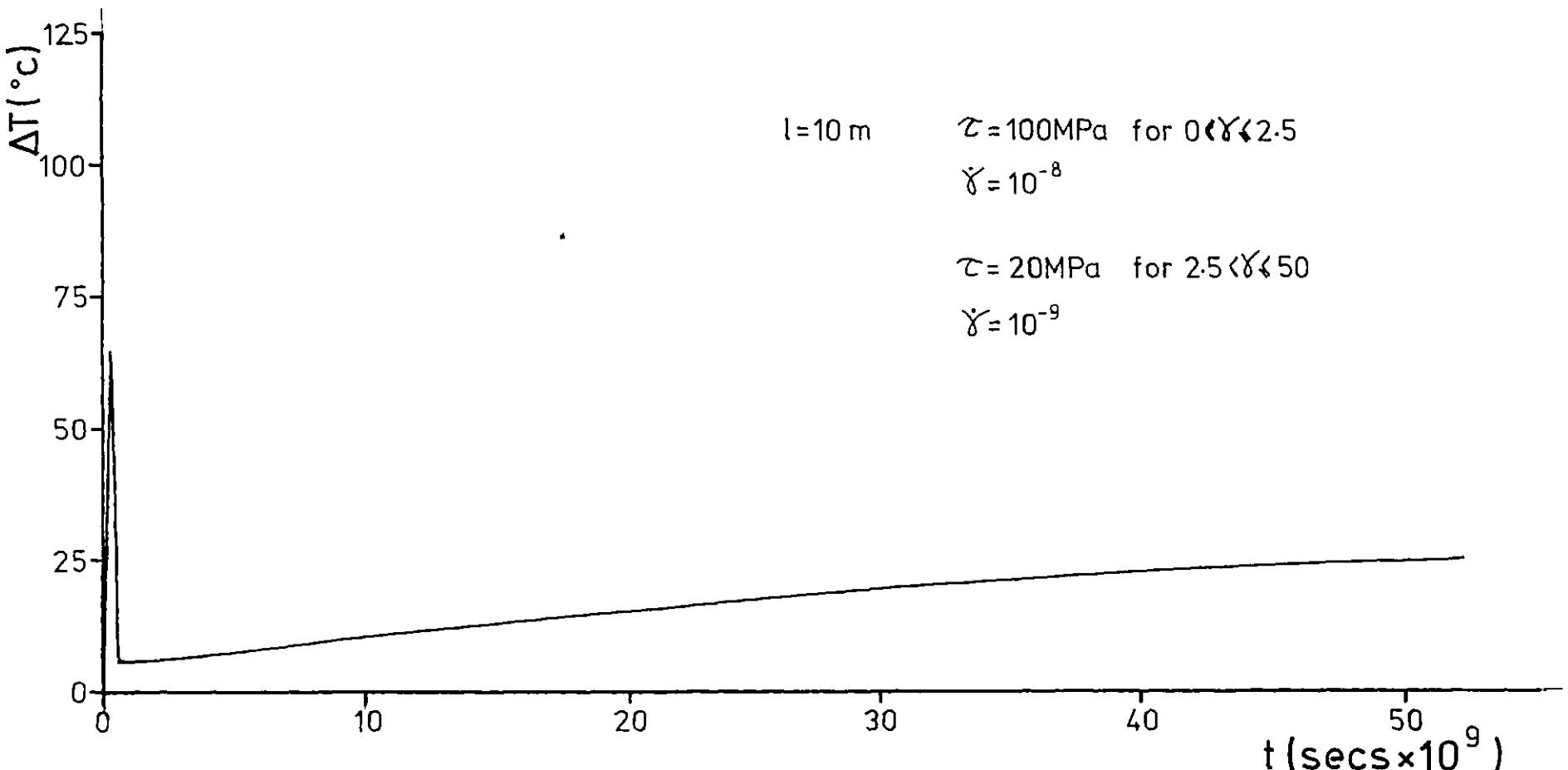


Fig. 6.18 Temperature rise at the centre of a zone of 10m half-width using a two-stage model of shear zone evolution. An initial high stress level during the propagation event gives rise to a short lived temperature pulse. The steady-state flow at lower stress then leads to a slow increase in temperature.

The stresses are double those estimated from microstructures, and the strain-rate required are two to three orders of magnitude faster than the flow-laws would predict at those stresses. The conclusion is that shear-heating has had no significant effect on the development of shear zones at Cap de Creus.

6.6.5 Relative importance of softening mechanisms at Cap de Creus

No matter what the steady-state deformation mechanism, fabric softening of quartz will lead to a large and relatively constant contribution to the overall softening. To this will be added a variable effect due to continuous dynamic recrystallization or grain boundary sliding, depending on the grain size. Feldspar recrystallization will only be important in the high strain zones in which a large percentage of the grains are recrystallized. The fine white micas will lead to a considerable additional softening through the promotion of grain boundary sliding. The various contributions are summarized in Table 6.4.

6.7 A history of part of the shear zone network at Cap de Creus

Fig. 6.19 shows a schematic block diagram depicting the distribution of rock-types prior to shear zone formation for a portion of the Cap de Creus area as deduced by removing the effects of the shear zones (N.B. there is little control as to the three-dimensional structures at Cap de Creus).

The degree of bulk anisotropy, that is the relative consistency of the orientation of the schistosity, varies from strong in the south-west to almost non-existent in the north-east. Also indicated are zones of incipient weakness, sub-planar regions that will affect the localization of deformation in shear zones. These possibly represent gross lithological variations whose exact nature has been obscured during the ensuing shear zone formation. They

TABLE 6.4

Total shear strain	Fabric Softening	Structural Softening			
		Quartz Dynamic Recrystallization	GBS	Feldspar - dynamic recrystallization	Micas - neomineralizatior and GBS
Low	H	M	L	-	H
Medium	H	L	M	L	H
High	H	-	H	M	H

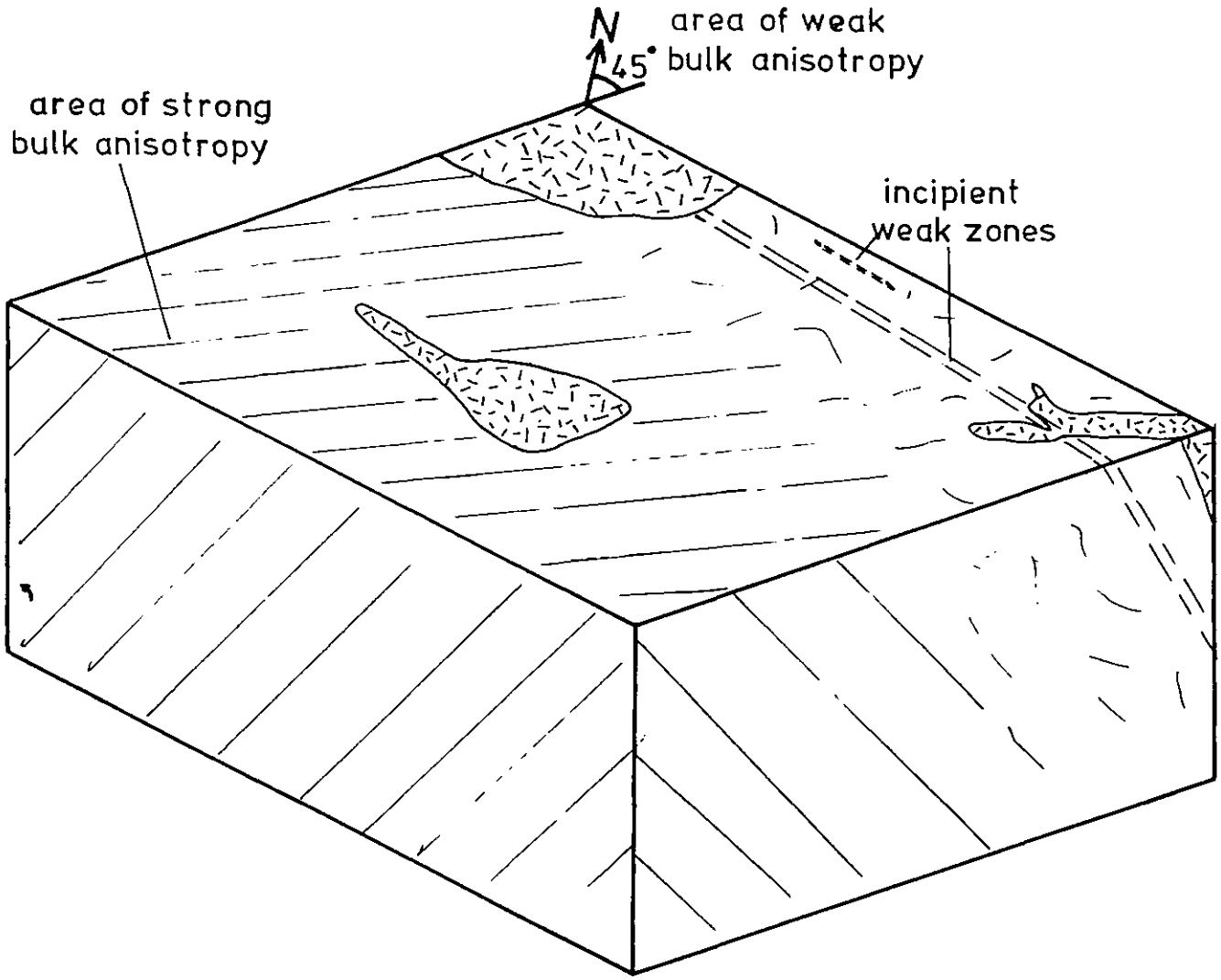
H = High

M = Medium

L = Low

- = No effect

Table 6.4 Qualitative estimate of relative contributions of softening mechanisms in the mylonites developed in the shear zones at Cap de Creus and their variation with total shear strain.



Quartz-diorite, Migmatite & Pegmatite

Country-rock Schists

Fig. 6.19 Schematic block diagram of part of the Cap de Creus area between Portixol and Cala Sardina, just prior to the formation of shear zones, as deduced by removing the effects of the zones.

might be zones in which deformation has already become concentrated, such as a thinned fold-limb due to an earlier fold phase. Some of the larger pegmatite and quartz-diorite/migmatite bodies are also shown.

In Fig. 6.20(a) the block is initially subjected to dominant dextral sense, simple shear, with components of flattening. The only response at this stage is to form angular folds similar to kink-bands on those parts of the area where a strong bulk anisotropy is present. With further strain the regional stress level increases such that shear zones initiate in certain areas, e.g. within the angular folds on the rotated limb, or within the incipient weaker zones (Fig. 6.20(b)).

Localization of deformation within the kink-band structures leads to the development of several parallel, smaller, shear zones separated by septa of less-deformed country-rock schist. The fact that so many parallel shear zones could form with such small spacings between them without relaxing the local stress level, suggests that they developed during the early stage of regional stress increase.

The large incipient weaker zone towards the north-west controls the propagation of a major shear zone developed within it, and causes it to impinge upon a major pegmatite body. Propagation is then stopped, until sufficient strain has built up within the pegmatite to produce strain softening; the more 'competent' material giving rise to a greater degree of strain softening and thereby a narrower shear zone. This propagates quickly through the rest of the pegmatite and then back into the schists where it resumes its former width, as the less 'competent' material relaxes the intensified stress field.

As the main set of dextral shear zones begin to take up the dextral sense, simple shear part of the applied deformation the volumes of rock

Fig. 6.20 Stages in the formation of the area between Portixol and Cala Sardina.

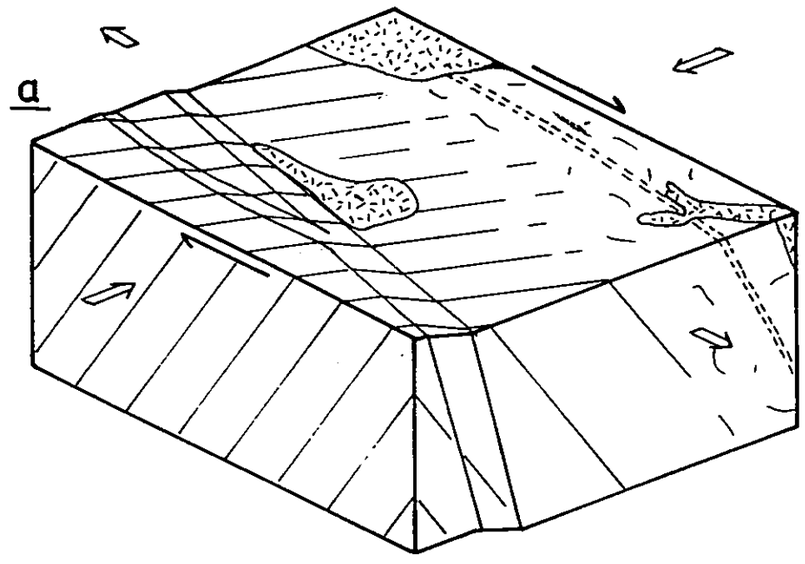
(a) Formation of kink-like structures.

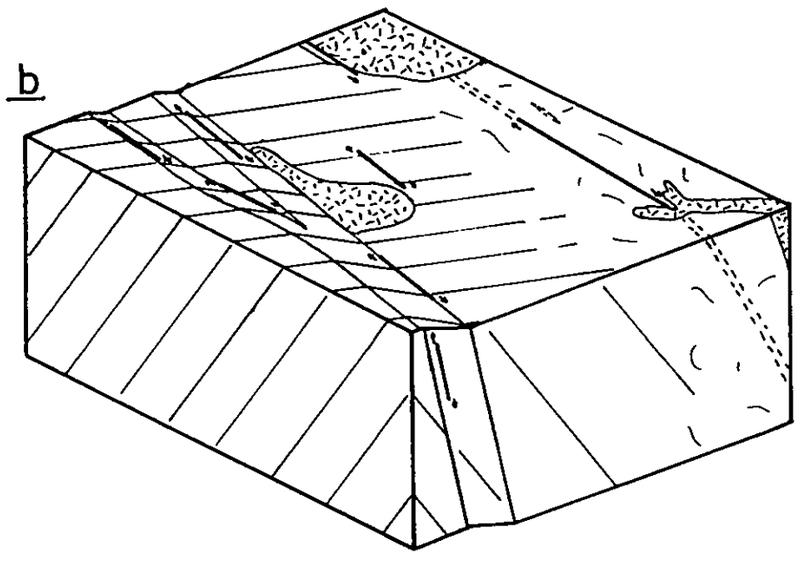
(b) Initiation and propagation of shear zones of the main set, during regional stress rise.

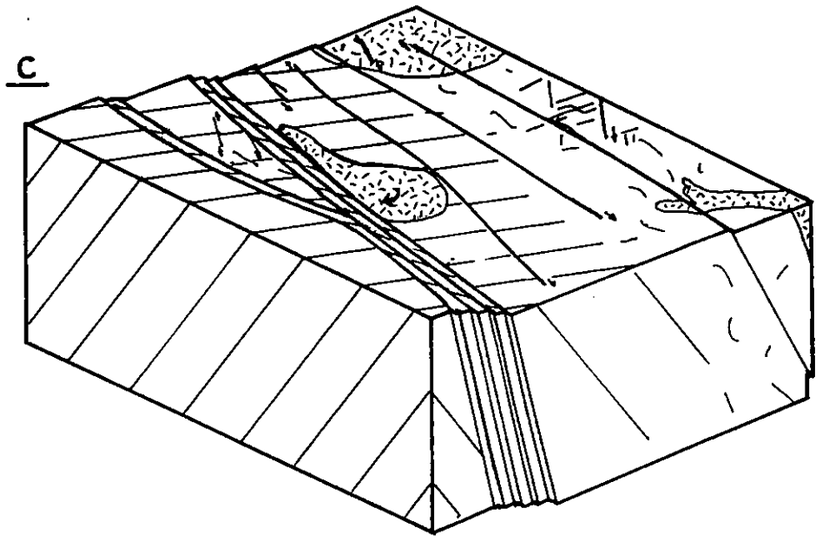
(c) Continuing propagation of main set, initiation and propagation of minor shear zones in areas of country rock between main shear zones during the period around peak regional stress; rotation induced in migmatite block.

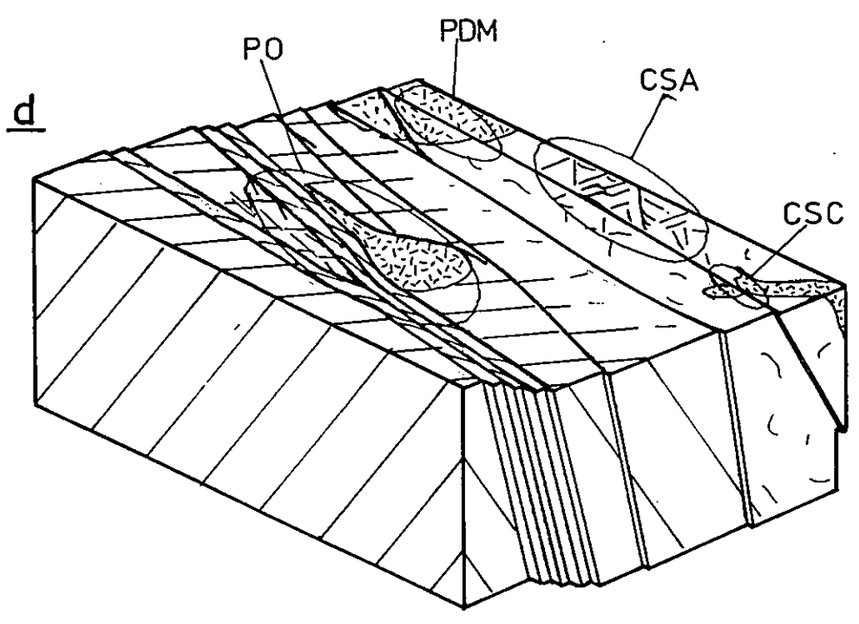
(d) Continuing displacement on the shear zone networks with further rotation of migmatite block and attendant rotation of adjacent shear zones; sinistral zone formed on the northern margin.

FIG. 6.20









PO Portixol (Cala Serena)

PDM Punta del Moli

CSA Cala Sardina

CSC Cala sa Caixa

between them are subject to the remaining flattening component. Fig. 6.20(c) shows the varied response to this with the initiation of many minor shear zones, locally in conjugate sets, reflecting the bulk strain ellipsoid. Some of these shear zones in the north-eastern area encounter a small zone of incipient weakness causing them to divert along it. The response of the quartz-diorite/migmatite block is to rotate towards a more stable configuration with respect to the flattening, causing also the rotation of adjacent shear zones, and locally the development of a sinistral zone, to maintain strain compatibility between the block and the surrounding schists.

During this period, roughly equivalent to the peak regional stress, local stress relaxation around established shear zones becomes sufficient to affect the propagation of other minor zones, e.g. a shear zone of the main set propagating towards the south-east starts a branch, which fails to become established. Other shear zones in the minor zone networks start to interact and stop; propagation in general continues even as the regional stress begins to fall.

Finally in Fig. 6.20(d) the regional stress has fallen sufficiently such that almost all shear zone propagation has ceased, and most of the strain is taken up on the existing networks. The only shear zone initiation and propagation at this stage is caused by the strain accumulation at shear zone terminations as displacements on them continue. Locally these strain fields are relieved by the formation of splays, minor zones may also be initiated where high compatability strains are caused at shear zone junctions. At the same time a minor amount of shear zone widening is taking place as strains build up within the volumes of rock adjacent to shear zones.

Shear zone activity will continue until such time as the regional constraints cease to be applied, or uplift reduces the ambient temperature

leading to either a reduction in deformabability of the feldspar or more likely a change from dominant prism <a> slip activity in quartz to dominant basal <a>.

This model for the history of part of the network at Cap de Creus is intended to draw together the field data with the theoretical predictions on shear zone development. The history presented is consistent with that due to Carreras et al. (1980) on the larger scale for the whole of Cap de Creus and similar areas throughout the axial zone of the Pyrenees.

CHAPTER 7 Conclusions

The conclusions of this study are presented approximately in the same order in which they are to be found in the thesis.

1. The observed relationship between texture, and strain, or grain size in quartz mylonites is due to a variation in the contribution of grain boundary sliding to the bulk deformation.

2. Peristerite exsolution in sodic plagioclases is significantly enhanced by deformation allowing lamellar exsolution in plagioclases in the compositional range An_{17-23} for which this has not previously been reported.

3. In the Cap de Creus mylonites fine-grained feldspars are formed by two recrystallization mechanisms, while fine-grained micas are formed by neocrystallization and recrystallization, and grain sizes in these minerals are not suitable for use in the estimation of palaeostresses.

4. Observations of naturally deformed minerals are consistent with the theoretical and empirical laws relating recrystallized grain size, sub-grain size, and dislocation density, to the differential stress.

5. Log-log plots of dislocation density against sub-grain size, and sub-grain size against recrystallized grain size, may be used to check if parameters were set in response to the same differential stress.

6. The Cap de Creus shear zones propagated at least an order of magnitude faster than the rate of displacement across them. The

history of a shear zone network such as that at Cap de Creus may be divided into a relatively short propagation stage, followed by steady-state deformation on the established network.

7. The Cala Sardina shear zone network may be explained in terms of alternating domains of dominant pure, and dominant simple shear.

7.1 Suggestions for further work

Suggested topics for further work arising from this study are as follows:-

1. The study of other shear zone networks to find further evidence for the relationship between the bulk strain state and the resultant network.

2. The development of a more exact mathematical model of a propagating shear zone, allowing the use of finite element methods to study all stages of shear zone development and the interaction between shear zones.

3. Observation of feldspars deformed in a variety of metamorphic environments to seek further evidence for the interrelationship between strain, exsolution and ordering.

4. The measurement of microstructural parameters of geological materials from a wide range of tectonic environments so that equilibrium relationship between these parameters may be better defined, and that the effects of changes in recrystallization mechanisms may be observed.

5. An attempt to quantify the effect of extrinsic variables such as temperature and P_{H_2O} on the relationship between microstructural parameters and stress, through the experimental deformation of suitable analogues for geological materials.

Acknowledgements

I would like to thank Stan White my supervisor for suggesting the area of my research and for his continual support especially during the prolonged gestation of this thesis. I would also like to thank Jordi Carreras for introducing me to the shear zones of Cap de Creus, Dave Johnston for his help with microanalysis on both probe and STEM, and Chris Spiers, Colin Leach, J.P. Latham, Joe White, Paul Tungatt, Martyn Drury, Steve Hall for many fruitful discussions. Finally I would like to thank Carolyn Holloway for speedy and accurate typing and the staff of Photography section for all their help. I acknowledge financial support from N.E.R.C. in the form of a research studentship.

REFERENCES

Ager, D.V. 1980. The Geology of Europe. McGraw-Hill, London.

Akizuki, M. 1972. Electron-microscopic investigation of microcline twinning. Am. Mineral. 57, 797-808.

Allison, I., Barnett, R.L. and Kerrich, R. 1979. Superplastic flow and changes in crystal chemistry of feldspars. Tectonophysics 53, T41-T46.

Ardell, A.J., Christie, J.M. and Tullis, J.A. 1973. Dislocation substructures in deformed quartz rocks, Cryst. Lattice Defects. 4, 275-285.

Argon, A.S. 1973. Stability of plastic deformation. In: The inhomogeneity of plastic deformation. ASM Publication.

Atkinson, B.K., Rutter, E.H., Sibson, R.H., White, S.H. 1979. Some specific experimental and field studies pertaining directly to the mechanisms of seismic and aseismic faulting. Final technical report for FY1979 to the manager U.S. National Earthquake Hazards Reduction Program.

Bak, J., Korstgård, J.A. and Sørensen, K. 1975. A major shear zone in the Nagssuqtoqidian of west Greenland. Tectonophysics 27, 191-209.

Ball, A. 1980. A theory of geological faults and shear zones. Tectonophysics. 61, T1-T6.

Ball, A. and White, S. 1977. An etching technique for revealing dislocation structure in deformed quartz grains. Tectonophysics, 37, T9-T14.

Ball, A. and White, S. 1978. On the deformation of quartzite. Phys.Chem. Min. 3, 163-172.

Beach, A. 1973. The mineralogy of high temperature shear zones at Scourie, N.W. Scotland. J. Petrol. 14, 231-248.

Beach, A. 1975. The geometry of en-echelon vein arrays. Tectonophysics 28, 245-263.

Beach, A. 1976. The interrelations of fluid transport, deformation, geochemistry and heat flow in early Proterozoic shear zones in the Lewisian complex. Phil.Trans.R.Soc. A280, 569-604.

Beach, A. 1980. Retrogressive metamorphic processes in shear zones with special reference to the Lewisian complex. J.Struct.Geol. 2, 257-264.

Beach, A. and Fyfe, W.S. 1972. Fluid transport and shear zones at Scourie, Sutherland: evidence of overthrusting? Con.Min.Pet. 36, 175-180.

Beach, A., Coward, M.P. and Graham, R.H. 1973. An interpretation of the structural evolution of the Laxford Front. Scot. J. Geol. 9, 294-308.

Belkin, E.G., Demikhovskaya, N.N., Kurov, I.E. and Myshlyaev, T. 1973. Kinetics of substructure formation during creep in aluminium. Phys. Stat. Sol. (a) 16, 425.

Bell, T.H. 1978. Syntectonic nucleation of new grains in deformed mica. Tectonophysics 61, T31-T37.

Bell, T.H. 1979. The deformation and recrystallization of biotite in the Woodroffe Thrust. Tectonophysics 58, 139-158.

Bell, T.H. 1981. Foliation development - the contribution, geometry and significance of progressive, bulk, inhomogeneous shortening. Tectonophysics 75, 257-272.

Bell, T.H. and Etheridge, M.A. 1973. Microstructures of mylonite and their descriptive terminology. Lithos 6, 337-348.

Bell, T.H. and Etheridge, M.A. 1976. The deformation and recrystallization of quartz in a mylonite zone, Central Australia. Tectonophysics 32, 235-267.

Berthé, D., Choukroune, P. and Jegouzo, P. 1979. Orthogneiss, mylonite and non-coaxial deformation of granites: the example of the South American shear zone. J.Struct.Geol. 1, 31-42.

Biot, M.A. 1965. Mechanics of incremental deformations. Wiley, New York.

Bishop, J.F.W. and Hill, R. 1951. A theory of the plastic distortion of a polycrystalline aggregate under combined stress. Phil.Mag. 42, 414-427.

Boland, J.N., McLaren, A.C. and Hobbs, B.E. 1971. Dislocations associated with optical features in naturally deformed olivine. Con.Min. Pet. 30, 53-63.

Boland, J.N. and Buiskool-Toxopeus, J.M.A. 1977. Dislocation deformation mechanisms in peridotite xenoliths in kimberlites. Con.Min.Pet. 60, 17-30.

Borg, I.Y. and Heard, H.C. 1969. Mechanical twinning and slip in experimentally deformed plagioclases. Con.Min.Pet. 23, 128-135.

Borg, I.Y. and Heard, H.C. 1970. Experimental deformation of plagioclases. In: Experimental and natural rock deformation. Springer Berlin.

Borges, F.P.B.S. 1978. Chemical changes associated with the deformation of intermediate plagioclase. Unpublished Ph.D. thesis, London.

Bossière, G. and Vauchez, A. 1978. Deformation naturelle par cisaillement ductile d'un granite de Grande Kabylie occidental (Algérie). Tectonophysics 51, 57-81.

Bouchez, J-L. and Pecher, A. 1976. Plasticité du quartz et sens de cisaillement dans les quartzites du Grand Chevauchement Central Himalayen. Bull.Soc. Géol.Fr.18, 1354-1357.

Boullier, A.M. and Gueguen, Y. 1975. S-P Mylonites: Origin of some mylonites by superplastic flow. Con.Min.Pet. 50, 93-104.

Bowden, P.B. 1970. A criterion for inhomogeneous plastic deformation. Phil.Mag. 22, 455-462.

Boyle, R.W. 1961. The geology, geochemistry and origin of the gold deposits of the Yellowknife district. Geol.Survey.Can.Mem. 310.

Bøggild, O.B. 1924. On the labradorization of the feldspars. K.danske vidensk. selsk. Mat.-Fys.Meddel. 6, 1-79.

Bridgewater, D. 1979. Chemical and isotopic redistribution in zones of ductile deformation in a deeply eroded mobile belt. In: Analysis of actual fault zones in bedrock. USGS Open File Report 79-1239, 505-526.

Briegel, U. and Goetze, C. 1978. Estimates of differential stress recorded in the dislocation structure of Lochseiten Limestone (Switzerland). Tectonophysics 48, 61-76.

Brodie, K.H. 1981. Variations in amphibole and plagioclase composition with deformation. Tectonophysics 78, 385-402.

Brodie, K.H. and White, S.H. 1982. (in prep).

Brown, W.L. 1960. Xray studies in the plagioclases. Part 2. The crystallographic and petrologic significance of peristerite unmixing in the acid plagioclases. Zeit. Krist. 113, 297-344.

Brown, W.L. and Williame, C. 1974. An explanation of exsolution orientations and residual strain in cryptoperthite. In: The Feldspars (ed. Mackenzie, W.S. and Zussman, J.) Manchester University Press, New York.

Brun, J.P. and Cobbold, P.R. 1980. Strain heating and thermal softening in continental shear zones: a review. J.Struct.Geol. 2, 149-158.

Burg, J.P. and Laurent, Ph. 1978. Strain analysis of a shear zone in a granodiorite. Tectonophysics 47, 15-42.

Carpenter, M.A. 1981. A 'conditional spinodal' within the peristerite miscibility gap of plagioclase feldspars. Am.Mineral. 66, 553-560.

Carreras, J. 1974. Progressive mylonitization in quartzitic and quartzofeldspathic rocks in the shear belts of the Cabo de Creus (E.Pyrenees, Spain). Unpublished MSc. thesis, London.

Carreras, J. 1975(a). Las deformaciones tardi-hercínicas en el litoral septentrional de la península del Cabo de Creus (prov. de Gerona, España): La génesis de las bandas milonítticas. Acta.geol.Hispanica, 10, 109-115.

Carreras, J. 1975(b). Determinición de las relaciones angulares y de la deformación par cizalla, para cizallamientos en materiales con un heterogeneidad planar. Acta. geol. Hispanica 10, 141-145.

Carreras, J. 1979. Guide to the Cap de Creus shear zones. University of Barcelona, Barcelona.

Carreras, J., Estrada, A. and White, S.H. 1977. The effects of folding on the c-axis fabrics of a quartz mylonite. Tectonophysics 39, 3-24.

Carreras, J., Julivert, M. and Santanach, P. 1980. Hercynian mylonite belts in the eastern Pyrenees: an example of shear zones associated with late folding. J.Struct.Geol. 2, 5-10.

Carreras, J., Orta, J.M. and SanMiguel, A. 1975. El area pegmatítica del litoral N. de la península del Cabo de Creus y su contexto metamórfico y estructural. Inst.Inv.Geol.Barcelona. 30, 11-34.

Carreras, J. and Santanach, P. 1975. Micropliegues y movimiento en los cizallamientos profundos del Cabo de Creus (prov. de Gerona, Espana). Est.Geol. 29, 439-450.

Carslaw, H.S. and Jaeger, J.C. 1959. Conduction of Heat in Solids. Oxford University Press, Oxford.

Carter, S., Champness, P.E. and Lorimer, G.W. 1980. Exsolution in sodium-rich plagioclases. Inst.Phys.Conf.Ser. 52, 117-120.

Casey, M. 1980. Mechanics of shear zones in isotropic dilatant materials. J.Struct.Geol. 2, 143-147.

Champness, P.E. and Lorimer, G.W. 1976. Exsolution in silicates. In: Electron Microscopy in Mineralogy (Ed. Wenk, H.R.) Springer-Verlag, Berlin.

Chessex, R., Delaloye, M., Krummenacher, D. and Vaugnat, M. 1965. Sur l'âge des roches granitiques de la région Palamós - Palafrugell (Costa Brava, Espagne). Schweiz Miner.Petrogr.Mitt. 45, 15-17.

Chinnery, M.A. 1966. Secondary faulting I. Theoretical aspects. Can.J. Earth Sci. 3, 163-190.

Christie, J.M. 1963. The Moine Thrust zone in the Assynt region, Northwest Scotland. Univ.Calif.Pubs. geol.Sci. 40, 345-440.

Christie, J.M. and Ardell, A.J. 1974. Substructures of deformation lamellae in quartz. Geology 2, 405-408.

Christie, J.M. and Ord, A. 1980. Flow stresses from microstructures of mylonites, example and current assessment. In: Magnitude of deviatoric stresses in the earth's crust and upper mantle. USGS Open File Report 80-625, 684-705.

Christie, J.M., Ord, A. and Koch, P.S. 1980. Relationship between recrystallized grain size and flow stress in experimentally deformed quartzite. Trans.Am.Geophys.Union. 61, 377.

Clark, G.K.C., Nitsan, U. and Paterson, W.S.B. 1977. Strain heating and creep instability in glaciers and ice sheets. Rev.Geophys. & Space Phys. 15, 235-247.

Cobbold, P.R. 1977(a). Description and origin of banded deformation structures. I. Regional strain, local perturbations, and deformation bands. Can. J. Earth Sci. 14, 1721-1731.

Cobbold, P.R. 1977(b). Description and origin of banded deformation structures. II. Rheology and growth of banded perturbations. Can. J. Earth Sci. 14, 2510-2523.

Cohen, M. 1970. Self-diffusion during plastic deformation. Trans.Jpn.Inst. Met. 11, 145-151.

Cooper, R.F., Kohlstedt, D.L., Weathers, M.S. and Bird, J.M. 1978. Dislocation structure in deformed quartz grains from the Moine Thrust Fault, Scotland (Abstr.). Trans.Am.Geophys.Un. 60, 370.

Coward, M.P. 1976. Strain within ductile shear zones. Tectonophysics. 34, 181-197.

Dalziel, I.W.D. and Bailey, S.W. 1968. Deformed garnets in a mylonitic rock from the Grenville front and their tectonic significance. Am. J.Sci. 266, 542-562.

Debat, P., Soula, J.C., Kubin, L. and Vidal, J.L. 1978. Optical studies of natural deformation microstructures in feldspars (gneiss and pegmatites from Occitania Southern France) Lithos 11, 133-145.

Dillamore, I.L., Roberts, J.G. and Bush, A.C. 1979. Occurrence of shear bands in heavily rolled cubic metals. Metal.Sci.J. 13, 73-77.

Dostal, J., Strong, D.F. and Jamieson, R.A. 1980. Trace element mobility in the mylonite zone within the ophiolite aureole, St. Anthony Complex, Newfoundland, Earth Planet.Sci. Lett. 49, 188-192.

Durham, W.B., Goetze, C. and Blake, B. 1977. Plastic flow in oriented single crystals of olivine, Part 2. Observations and interpretations of the dislocation structure. J.Geophys.Res. 82, 5755-5770.

Eisbacher, G.H. 1970. Deformation mechanisms of mylonitic rocks and fractured granite in Cobequod Mountains, Nova Scotia, Canada. Bull. Geol.Soc.Amer. 81, 2009-2020.

Escher, A., Escher, J. and Watterson, J. 1975. The reorientation of the Kangâmiut dyke swarm, west Greenland. Can.J.Earth Sci. 12, 158-173.

Etheridge, M.A. and Wilkie, J.C. 1979(a). Grain size reduction, grain boundary sliding and the flow strength of mylonites. Tectonophysics 58, 159-178.

Etheridge, M.A. and Wilkie, J.C. 1979(b). The geometry and microstructure of a range of Q.P. mylonite zones - a field test of the recrystallized grain size palaeopiezometer. In: Analysis of actual fault zones in bedrock. USGS Open File Report 79-1239, 448-504.

Evans, B., Rowen, M. and Brace, W.F. 1980. Grain-size sensitive deformation of a stretched conglomerate from Plymouth, Vermont. J.Struct.Geol. 2, 411-424.

Exner, H.E. 1972. Analysis of grain and particle-size distributions in metallic materials. Int.Met.Rev. 159, 25-42.

Fleet, S.G. and Ribbe, P.H. 1965. An electron-microscope study of peristerite plagioclases. Min.Mag. 35, 165-176.

Fleitout, L. and Froidevaux, C. 1980. Thermal and mechanical evolution of shear zones. J.Struct.Geol. 2, 159-164.

Flinn, D. 1962. On folding during three-dimensional progressive deformation. Q.J.Geol.Soc.Lond. 118, 385-433.

Gapais, D. and White, S.H. 1982. Ductile shear bands in a naturally deformed quartzite. Textures and Microstructures 5 (in press).

Gavis, J. and Laurence, R.L. 1968. Viscous heating in plane and circular flow between moving surfaces. Ind. & Eng.Chem.Fundam. 7, 232-239.

Gifkins, R.C. 1976. Grain boundary sliding and its accommodation during creep and superplasticity. Metall.Trans.Ser. A, 7, 1225-1232.

Goetze, C. 1971. High temperature rheology of Westerly granite. J.Geophys. Res. 76, 1223-1230.

Goetze, C. 1975. Sheared Lherzolites: from the point of view of rock mechanics. Geology 3, 172-173.

Goetze, C. and Brace, W.F. 1972. Laboratory observations of high temperature rheology of rocks. Tectonophysics 13, 583-600.

Goetze, C. and Kohlstedt, D.L. 1973. Laboratory study of dislocation climb and diffusion in olivine. J.Geophys.Res. 78, 5961-5971.

Goldstein, A.G. 1980. Magnetic susceptibility anisotropy of mylonites from the Lake Char mylonite zone, southeastern New England. Tectonophysics 66, 197-212.

Green, H.W. and Radcliffe, S.V. 1972(a) Dislocation mechanisms in olivine and flow in the upper mantle. Earth Planet Sci.Lett. 15, 239-247.

Green, H.W. and Radcliffe, S.V. 1972(b). Deformation processes in the upper mantle. Am.Geophys.Union Mono. 16, 139-156.

Grocott, J. and Watterson, J. 1980. Strain profile of a boundary within a large ductile shear zone. J.Struct.Geol. 2, 111-118.

Gueguen, Y. 1977. Dislocations in mantle peridotite nodules. Tectonophysics 39, 231-251.

Gueguen, Y. and Nicolas, A. 1980. Deformation of mantle rocks. An.Rev. Earth Planet.Sci. 8, 119-144.

Guillopé, M. and Poirier, J.P. 1979. Dynamic recrystallization during creep of single-crystalline halite: an experimental study. J.Geophys. Res. 84.

Hall, S.H. and Rutter, E.H. 1981. Post-alpine tectonic evolution of south-east Spain and the structure and microstructure of fault rocks. (Abstr.). J.Struct.Geol. 3, 187.

Harker, A. 1895. Petrology for Students. Cambridge University Press, Cambs.

Hill, R. 1950. The Mathematical Theory of Plasticity, Oxford University Press, London.

Hirsch, P.B., Howie, A., Nicholson, R.B., Pashley, D.W. and Whelan, M.J. 1967. Electron Microscopy of Thin Crystals. Butterworths, London.

Hobbs, B.E. 1968. Recrystallization of single crystals of quartz. Tectonophysics 6, 353-401.

Hobbs, B.E., Means, W.D. and Williams, P.F. 1976. An Outline of Structural Geology. Wiley.

Holt, D.L. 1970. Dislocation cell formation in metals. J.Appl.Phys.41, 3192.

Hull, D. 1975. Introduction to Dislocations. Pergamon. Oxford.

Jamison, W.R. and Spang, J.H. 1976. Use of calcite twin lamellae to infer differential stress. Bull.Geol.Soc.Amer. 87, 868-872.

Johnson, J.N. and Holloway, D.G. 1966. On the shape and size of fracture zones on glass fracture surfaces. Phil.Mag. 14, 731-743.

Johnson, M.R.W. 1967. Mylonite zones and Mylonite banding. Nature. Lond. 213, 246-247.

Johnson, T.L. and Scholz, C.H. 1976. Dynamic properties of stick-slip friction of rock. J.Geophys.Res. 81, 881-888.

Karato, S., Toriumi, M. and Fujii, T. 1980. Dynamic recrystallization of olivine single crystals during high temperature creep. Geophys. Res.Lett. 7, 649-652.

Kehlenbeck, M.M. 1972. Deformation textures in the Lac Rouvray anorthosite mass. Can.J.Earth Sci. 9, 1087-1098.

Kerrich, R., Allison, I., Barnett, R.L., Moss, S. and Starkey, J. 1980. Microstructural and chemical transformations accompanying deformation of granite in a shear zone at Miéville, Switzerland; with implications for stress corrosion cracking and superplastic flow. Con.Min.Pet. 73, 221-242.

Kerrich, R., Fyfe, W.S., Gorman, B.E. and Allison, I. 1977. Local modification of rock chemistry by deformation. Con.Min.Pet. 65, 183-190.

Kirby, S.H. 1980. Tectonic stresses in the lithosphere; constraints provided by the experimental deformation of rocks. In: Magnitude of deviatoric stresses in the earth's crust and upper mantle. USGS Open File Report 80-625, 727-770.

Kirby, S.H. and Green, H.W.II. 1980. Dunite xenoliths from Hualalai Volcano: evidence for mantle diapiric flow beneath the Island of Hawaii. Am.J.Sci. 280, 550-575.

Knipe, R.J. and White, S.H. 1979. Deformation in low grade shear zones in the Old Red Sandstone, S.W. Wales. J.Struct.Geol. 1, 53-66.

Koch, P.S., Christie, J.M., and George, R.P. 1980. Flow law of 'wet' quartzite in the α-quartz field. Trans.Am.Geophys.Un. 61, 376.

Kohlstedt, D.L. 1980. Palaeostress levels in deeply eroded fault zones based on analyses of deformation-induced microstructures. In: Magnitude of deviatoric stresses in the earth's crust and upper mantle. U.S.G.S. Open File Report, 80-625, 648-664.

Kohlstedt, D.L., Cooper, R.F., Weathers, M.S. and Bird, J.M. 1979. Palaeostress analysis of deformation induced microstructures: Moine thrust zone and Ikertoq shear zone. In: Analysis of actual fault zones in bedrock. USGS Open File Report 79-1239, 394-425.

Kohlstedt, D.L., Goetze, C. and Durham, W.B. 1976. Experimental deformation of olivine single crystals with application to mantle flow. In: The Physics and Chemistry of Minerals (Ed. Streus, R.G.J.). Wiley, New York.

Korekawa, M., Nissen, H-U., and Phillipp, D. 1970. X-ray and electron microscopic studies of a sodium rich low plagioclase. Zeit.Krist. 131, 418-436.

Lapworth, C. 1885. The Highland controversy in British geology: its causes, course and consequences. Nature.Lond. 32, 558-559.

Laurent, Ph. and Etchecopar, A. 1976. Mise en évidence à l'aide de la fabrique du quartz d'un cisaillement simple à deversement ouest dans le Massif de Dora Maira (Alpes Occidentales). Bull.Soc.géol.Fr. 18, 1387-1393.

Laves, F. 1950. The lattice and twinning of microcline and other potash feldspars. J.Geol. 58, 548-571.

Laves, F. 1960. The feldspars, their polysynthetic twinning and their phase relations. Rend.soc.mineral.ital. 16, 37-100.

Lawn, B.R. and Wilshaw, T.R. 1975. Fracture of Brittle Solids. Cambridge University Press, Cambridge.

Leach, C.A., White, S.H. and Suddaby, P. 1982. Possible end member compositions for Bøggild exsolution lamellae. (In prep.).

Lister, G.S., Paterson, M.S. and Hobbs, B.E. 1978. The simulation of fabric development in plastic deformation and its application to quartzite: the model. Tectonophysics 45, 107-158.

Lister, G.S. and Williams, P.F. 1979. Fabric development in shear zones theoretical controls and observed phenomena. J.Struct.Geol. 1, 283-298.

Logan, J.M., Higgs, N.G. and Friedman, M. 1981. Laboratory studies on natural gouge from the U.S. Geological Survey Dry Lake Valley, no.1 well, San Andreas fault zone. A.G.U. geophysical Monograph 24, 121-134.

Lor imer, G.W., Nissen, H-U. and Champness, P.E. 1972. High voltage electron microscopy of deformed sodic plagioclase from an alpine gneiss. Schweiz. miner.petrogr.mitt. 54, 707-715.

Lücke, K. and Stüwe, H.P. 1971. On the theory of impurity controlled grain boundary motion. Acta.Met. 19, 1087-1099.

McConnell, J.D.C. 1969. Electron-optical study of incipient exsolution and inversion phenomena in the system $NaAlSi_3O_8$ - $KAlSi_3O_8$. Phil. Mag. 19, 221-229.

McConnell, J.D.C. 1971. Electron optical study of phase transformations. Min.Mag. 38, 1-20.

McConnell, J.D.C. 1974. Analysis of the time-temperature-transformation behaviour of the plagioclase feldspars. In: The Feldspars (eds. Mackenzie, W.S., Zussman, J.) Manchester University Press, Manchester.

McCormick, J.W. 1977. Transmission electron microscopy of experimentally deformed synthetic quartz. PhD. Thesis, Univ.Calif., Los Angeles.

McLaren, A.C. 1978. Defects and Microstructures in Feldspars. Chemical physics of Solids and their surfaces, 7, 1-28.

McLaren, A.C., Retchford, J.A., Griggs, D.T. and Christie, J.M. 1967. Transmission electron microscope study of Brazil twins and dislocations experimentally produced in natural quartz. Phys.Stat.Solidi. 19, 631-644.

Marshall, D.B. and McLaren, A.C. 1977(a). The direct observation and analysis of dislocations in experimentally deformed plagioclase feldspars. J.Mat.Sci. 12, 893-903.

Marshall, D.B. and McLaren, A.C. 1977(b) Deformation mechanisms in experimentally deformed plagioclase feldspars. Phys.Chem.Min. 1, 351-370.

Marshall, D.B. and Wilson, C.J.L. 1976. Recrystallization and peristerite formation in albite. Con.Min.Pet. 57, 55-69.

Marshall, D.B., Vernon, R.H. and Hobbs, B.E. 1976. Experimental deformation and recrystallization of a peristerite. Con.Min.Pet. 57, 49-54.

Matsui, T., Karato, S. and Yokokura, T. 1980. Dislocation structures from Pallasite meteorites. Geophys.Res.Lett. 7, 1007-1010.

Means, W.D. 1981. The concept of steady-state foliation. Tectonophysics, 78, 179-200.

Melosh, H.J. 1976. Plate motion and thermal instability in the asthenosphere. Tectonophysics 35, 363-390.

Mercier, J-C. C. 1976. Natural peridotites: chemical and rheological heterogeneity of the upper mantle. PhD. thesis, S.U.N.Y., New York.

Mercier, J-C. C. 1980. Magnitude of the continental lithospheric stresses inferred from rheomorphic petrology. In: Magnitude of deviatoric stresses in the earth's crust and upper mantle. USGS Open File Report 80-625, 771-802.

Mercier, J-C. C., Anderson, D.A. and Carter, N.L. 1977. Stress in the lithosphere: inferences from steady state flow of rocks. Pageophys. 115, 199-226.

Mitra, G. 1979. Ductile deformation zones in Blue Ridge basement rocks and estimation of finite strains. Bull.geol.Soc.Am. 90, 935-951.

Morrison-Smith, D.J., Paterson, M.S. and Hobbs, B.E. 1976. An electron microscope study of plastic deformation in single crystals of synthetic quartz. Tectonophysics 33, 43-50.

Nicolas, A., Bouchez, J.L., Boudier, F. and Mercier, J.C. 1971. Textures, structures and fabrics due to solid state flow in some European lherzolites. Tectonophysics 12, 55-85.

Nicolas, A. and Poirier, J.P. 1976. Crystalline Plasticity and Solid State Flow in Metamorphic Rocks. Wiley - Interscience, New York.

Olsen, A. 1974. Schiller effects and exsolution in sodium-rich plagioclases. Con.Min.Pet. 47, 141-152.

Owen, D.C. and McConnell, J.D.C. 1974. Spinodal unmixing in an alkali feldspar. In: The Feldspars (Eds. MacKenzie, W.S., Zussman, J.) Manchester University Press, Manchester.

Palmer, A.C. and Rice, J.R. 1973. The growth of slip surfaces in the progressive failure of overconsolidated clay. Proc. R.Soc. A332, 527-548.

Paris, P.C. and Sih, G.C. 1965. Stress analysis of cracks. In: Fracture toughness testing and its applications. A.S.T.M. Spec.Tech.Publ. 381, 30.

Poirier, J.P. 1980. Shear localization and shear instability in materials in the ductile field. J.Struct.Geol. 2, 135-142.

Poirier, J.P., Bouchez, J.L. and Jonas, J.J. 1979. A dynamic model for aseismic ductile shear zones. Earth Planet Sci.Lett. 43, 441-453.

Poirier, J.P. and Nicolas, A. 1975. Deformation-induced recrystallization due to progressive misorientation of sub-grains with special reference to mantle peridotites. J.Geol. 83, 707-720.

Pontikis, V. and Poirier, J.P. 1975. Phenomenological and structural analysis of recovery controlled creep, with special reference to the creep of single crystal silver chloride. Phil.Mag. 32, 577-592.

Post, R.L.Jr. 1973. The flow laws of Mt. Burnet dunite. PhD. thesis, Univ. Calif., Los Angeles.

Putnis, A. and McConnell, J.D.C. 1980. Principles of Mineral Behaviour, Blackwell, Oxford.

Raleigh, C.B. and Kirby, S.H. 1970. Creep in the upper mantle. Min.Soc. Am.Spec.Pap. 3, 113-121.

Ramsauer, H. 1941. Achsenverteilungsanalysen an Quartztektoniten. Inst. Min.Pet.Innsbruck.

Ramsay, J.G. 1979. Shear zones. In: Analysis of actual fault zones in bedrock. USGS Open File Report, 79-1239, 2-35.

Ramsay, J.G. 1980. Shear zone geometry: a review. J.Struct.Geol. 2, 83-100.

Ramsay, J.G. and Allison, I. 1979. Structural analysis of shear zones in an alpinised Hercynian granite (Maggia Lappen, Pennine Zone, Central Alps). Schweiz.miner.petrogr.Mitt. 59, 251-280.

Ramsay, J.G. and Graham, R.H. 1970. Strain variation in shear belts. Can. J.Earth Sci. 7, 786-813.

Read, H.H. and Watson, J.V. 1975. Introduction to Geology. Vol. I. Earth History. Part II, Later Stages. Macmillan, London.

Reid, C.N. 1973. Deformation Geometry for Material Scientists, Pergamon Press, Oxford.

Ribbe, P.H. 1962. Observations on the nature of unmixing in peristerite plagioclases. Norsk.geol.Tiddskr. 42, 138-151.

Ribbe, P.H. 1975. Exsolution textures and interference colors in feldspars. In: Feldspar Mineralogy Am.Min.Soc. Short course Notes.

Rice, J.R. 1968(a). A path independent integral and the approximate analysis of strain concentration by notches and cracks. J.Appl.Mech. 35, 379

Rice, J.R. 1968(b). Mathematical analyses on the mechanics of fracture. In: Fracture (ed. Liebowitz, H.) Academic Press, New York.

Rice, J.R. 1973. The initiation and growth of shear bands. In: Plasticity and Soil Mechanics, edited by Palmer, A.C., pp. 263-274. Cambridge.

Riley, N.A. 1947. Structural petrology of the Baraboo quartzite. J.Geol. 55, 453-475.

Roberts, W. and Ahlblom, B. 1978. A nucleation criterion for dynamic recrystallization during hot working. Acta.Metall. 26, 801-813.

Rosenbuch, (translated Iddings) 1888. Microscopic Physiography of the Rock-forming Minerals, London.

Ross, J.V. 1973. Mylonitic rocks and flattened garnets in the southern Okanagan of British Columbia. Can.J.Earth Sci. 10, 1-17.

Ross, J.V., Ave Lallement, H.G. and Carter, N.L. 1980. Stress dependence of recrystallized grain and subgrain size in olivine. Tectonophysics 70, 39-61.

Rudnicki, J.W. 1979. The inception of faulting in a rock mass with a weakened zone. J.Geophys.Res. 82, 844-854.

Sacerdoti, M., Labernardière, H. and Gandais, M. 1980. Transmission electron microscope (TEM) study of geologically deformed feldspars. Bull.Minéral. 103, 148-155.

Sander, B. 1930. Gefügekunde der Gesteine mit besonderer berücksichtig der Tektonite. Springer, Vienna.

Sander, B. 1970. An Introduction to the Study of Fabrics of Geological Bodies. Translated by F.C. Phillips and G. Windsor, Pergamon, N.York.

Schmid, S.M., Casey, M. and Starkey, J. 1981. An illustration of the advantages of a complete texture analysis described by the orientation distribution function (ODF) using quartz pole figure data. Tectonophysics 78, 101-118.

Schmid, S.M., Paterson, M.S. and Boland, J.N. 1980. High temperature flow and dynamic recrystallization in Carrara marble. Tectonophysics 65 245-280.

Schubert, G. and Yuen, D.A. 1978. Shear heating instability in the earth's upper mantle. Tectonophysics 50, 197-205.

Segall, P. and Pollard, D.D. 1980. Mechanics of discontinuous faults. J. Geophys.Res. 85, 4337-4350.

Seifert, K.E. 1965. Deformation bands in albite. Am.Mineral. 50, 1469-1472.

Sellars, C.M. 1978. Recrystallization of metals during hot deformation. Phil.Trans.R.Soc.Lond. A288, 147-158.

Shelton, K.L. and Orville, P.M. 1980. Formation of synthetic fluid inclusions in natural quartz. Am.Mineral. 65, 1233-1236.

Sibson, R.H. 1977. Fault rocks and fault mechanisms. J.Geol.Soc.Lond. 133, 191-213.

Sibson, R.H. 1979. Fault rocks and structures as indicators of shallow earthquake source processes in Proc.Conf. "Analysis of actual fault zones in bedrock" USGS Open File Report 79-1239, 296-303.

Sibson, R.H. 1982 (In Prep.)

Simpson, C. 1980. Oblique girdle orientation patterns of quartz c-axes from a shear zone in the basement core of the Maggia Nappe, Ticino, Switzerland. J.Struct.Geol. 2, 243-248.

Smith, J.V. and Stenstrom, R.C. 1965. Electron-excited luminescence as a petrologic tool. J.Geol. 73, 627-635.

Smith, J.V. 1974. Feldspar Minerals. I. Crystal Structure and Physical Properties. Springer Verlag, Berlin.

Smith, J.V. 1974. Feldspar Minerals II. Chemical and Textural Properties. Springer Verlag, Berlin.

Spiers, C.J. 1982. The development of deformation textures in calcite rocks. Unpublished PhD. thesis, London.

Spry, A. 1969. Metamorphic Textures. Pergamon, Oxford.

Starkey, J. 1967. On the relationship of pericline and albite twinning to the composition and structural state of plagioclase feldspars. Schweiz.miner.petrogr.Mitt. 47, 257-268.

Streb, G.& Reppich,B. 1973.Steady state deformation and dislocation structure of pure and Mg-doped LiF single crystals II Etch pit studies of dislocation structure. Phys.Stat.Sol. a16, 493.

Sukanek, P.C. and Laurence, R.L. 1974. An experimental investigation of viscous heating in some simple shear flows. A.I.ChE.J. 20, 479-484.

Summers, J. 1979. An experimental and theoretical investigation of multi-layer fold development. Unpublished PhD. thesis, London.

Takeuchi, S. and Argon, A.S. 1976. Steady-state creep of single phase crystalline matter at high temperature. J.Mat.Sci. 11, 1542-1566.

Taylor, G.I. 1938. Plastic strain in metals. J.Inst.Metals. 62, 307-324.

Teall, J.J.H. 1885. The metamorphism of dolerite into hornblende schist. Q.J.geol.Soc.Lond. 41, 133-145.

Teall, J.J.H. 1888. British Petrography.

Toriumi, M. 1979. Relation between dislocation density and subgrain size of naturally deformed olivine in peridotites. Con.Min.Pet. 68, 181-186.

Toxopeus, J.M.A.B. 1976. Petrofabrics, microtextures and dislocation structures of olivine in a peridotite mylonite (Alpe Arami, Switzerland). Leidse.Geol.Med. 51, 1-36.

Toxopeus, J.M.A.B. and Boland, J.N. 1976. Several types of natural deformation in olivine, an electron microscope study. Tectonophysics.32, 209-233.

Tullis, T.E. 1980. The use of mechanical twinning in minerals as a measure of shear stress magnitudes. In: Magnitude of deviatoric stresses in the earth's crust and upper mantle. U.S.G.S. Open File Report, 80-625, 706-726.

Tuttle, O.F. and Bowen, N.L. 1950. High temperature albite and contiguous feldspars. J.Geol. 58, 572-583.

Twiss, R.J. 1977. Theory and applicability of a recrystallized grain size paleopiezometer. Pageophys. 115, 227-244.

Twiss, R.J. 1980. Static theory of size variation with stress for subgrains and dynamically recrystallized grains. In: Magnitude of deviatoric stresses in the earth's crust and upper mantle. USGS Open File Report 80-625, 665-683.

Vance. K.A. 1961. Polysynthetic twinning in plagioclase. Am.Mineral. 46, 1097-1119.

Vernon, R.H. 1965. Plagioclase twins in some mafic gneisses from Broken Hill, Australia. Min.Mag. 35, 488-507.

Vernon, R.H. 1975. Deformation and recrystallization of a plagioclase grain. Am.Mineral. 60, 884-888.

Vidal, J.L., Kubin, L., Debat, P. and Soula, J.C. 1980. Deformation and dynamic recrystallization of K feldspar augen in orthogneiss from Montagne Noire, Occitania, Southern France. Lithos. 13, 247-256.

Voll, G. 1960. New work on petrofabrics. Lpool.Manch.geol.J. 2, 503.

Voll, G. 1976. Recrystallization of quartz biotite and feldspars from Erstfeld to the Leventina Nappe, Swiss Alps, and its geological significance. Schweiz.mineral.petrogr.Mitt. 56, 641-647.

Watterson, J. 1979. Strain and strain rate gradients at the ductile levels of fault displacements. In: Analysis of actual fault zones in bedrock. USGS Open File Report 79-1239, 235-257.

Watterson, J. 1982 (In Prep.)

Watts, M.J. and Williams, G.D. 1979. Fault rocks as indicators of progressive shear deformation in the Guingamp region, Brittany. J.Struct. Geol. 1, 323-332.

Weathers, M.S., Bird, J.M., Cooper, R.F. and Kohlstedt, D.L. 1979. Microstructure and stress analysis of the Mullen Creek - Nash Fork shear zone, Wyoming. In: Analysis of actual fault zones in bedrock. USGS Open File Report 79-1239, 428-447.

Wegner, M.W. and Christie, J.M. 1979. Preferential chemical etching of terrestrial and lunar olivines. Con.Min.Pet. 43, 196-212.

White, J.C. 1982 (In Press).

White, J.C. and White, S.H. 1981. On the structure of grain boundaries in tectonites. Tectonophysics 78, 613-628.

White, S. 1970. Defect and diffusion studies of quartz. Unpublished PhD. thesis, University of Melbourne.

White, S. 1971. Natural creep deformation of quartzites. Nature Physical Science, 234, 175-177.

White, S. 1973(a) Dislocation structures responsible for the optical effects in some naturally deformed quartzites. J.Mat.Sci. 8, 490-499.

White, S. 1973(b) Syntectonic recrystallization and texture development in quartz. Nature, 244, 276-278.

White, S. 1974. Inter-relationship between chemistry and deformation in tectonically deformed minerals. In: Electron microscopy in 1974 (Eds. Sanders, J.V., Goodchild, R.J.) Aust.Acad.Sci., Canberra.

White, S. 1975. Tectonic deformation and recrystallization of oligoclase. Con.Min.Pet. 50, 287-304.

White, S. 1976. The effects of strain on the microstructures, fabrics and deformation mechanisms in quartzites. Phil.Trans.R.Soc.Lond. A283, 69-86.

White, S. 1977. Geological significance of recovery and recrystallization processes in quartz. Tectonophysics 39, 143-170.

White, S.H. 1979(a) Difficulties associated with palaeostress estimates. Bull.Minéral. 102, 210-215.

White, S. 1979(b). Grain and sub-grain size variations across a mylonite zone. Con.Min.Pet. 70, 193-202.

White, S. 1979(c) Palaeo-stress estimates in the Moine Thrust Zone, Eriboll, Scotland. Nature 280, 222-223.

White, S.H. 1982. Fault rocks of the Moine Thrust Zone: a guide to their nomenclature. Textures and Microstructures (in press).

White, S.H. and Knipe, R.J. 1978. Transformation and reaction-enhanced ductility in rocks. J.Geol.Soc.Lond. 135, 513-516.

White, S.H., Burrows, S.E., Carreras, J., Shaw, N.D. and Humphreys, F.J. 1980. On mylonites in ductile shear zones. J.Struct.Geol. 2, 175-187.

Willaime, C., Brown, W.L. and Gandais, M. 1976. Physical aspects of exsolution in natural alkali feldspars. In: Electron microscopy in Mineralogy (ed. Wenk, H.V.) Springer-Verlag.

Willaime, C., Christie, J.M. and Kovacs, M-P. 1979. Experimental deformation of K feldspar single crystals. Bull. Minéral. 102, 168-177.

Willaime, C. and Gandais, M. 1972. Study of exsolution in alkali feldspars. Calculations of elastic stresses inducing periodic twinning. Phys.Stat.Solidi 9, 529-539.

Wilson, C.J.L. and Bell, I.A. 1979. Deformation of biotite and muscovite: optical microstructure. Tectonophysics 58, 179-200.

Yuen, D.A. and Schubert, G. 1977. Asthenospheric shear flow: thermally stable or unstable. Geophys.Res.Lett. 4, 503-506.

Yuen, D.A., Fleitout, L., Schubert, G. and Froidevaux, C. 1978. Shear deformation zones along major transform faults and subducting slabs. Geophys.J.R.astr.Soc. 59, 93-119.

Yund, R.A. 1975. Microstructures, kinetics, and mechanisms of alkali feldspar exsolution. In: Feldspar Mineralogy (Ed. Ribbe, P.H.) Min. Soc.Am. Short course Notes.

Yund, R.A., McLaren, A.C. and Hobbs, B.E. 1974. Coarsening kinetics of the exsolution microstructure in alkali feldspar. Con.Min.Pet. 48, 45-56.

Yund, R.A. and Tullis, J. 1980. The effect of water, pressure, and strain on Al/Si order-disorder kinetics in feldspar. Con.Min.Pet. 72, 297-302.

Zeuch, D.H. and Green, H.W. 1979. Experimental deformation in an 'anhydrous' synthetic dunite. Bull.Minéral. 102, 185-187.

Zwart, H.J. 1962. On the determination of polymetamorphic mineral associations, and its application to the Bosost area (Central Pyrenees). Geol. Rundschau 52, 38-65.

APPENDIX

Listing of program GSIZE with commentary

```
READY.
LIST

 82/01/17. 15.23.14.
PROGRAM   GSIZE
00100 PROGRAM GSIZE(INPUT,OUTPUT,TAPE1,TAPE2)
00110 DIMENSION CLASS(10),IFREQ(10),AMARK(10),BCOEFF(9),IFREQ(10),AREA(400)
00130 B=1.4142
00140 BCOEFF(1)=0.3178
00150 BCOEFF(2)=0.0670
00160 BCOEFF(3)=0.0193
00170 BCOEFF(4)=0.0063
00180 BCOEFF(5)=0.0022
00190 BCOEFF(6)=0.0008
00200 BCOEFF(7)=0.0003
00210 BCOEFF(8)=0.0001
00220 BCOEFF(9)=0.00005
00230 DATA PI/3.1415927/
00240 PRINT 5
00250 5 FORMAT(/,* ENTER MAG ON PRINT *)
00260 READ 11,AMAG
00270 11 FORMAT(F7.3)
00280 SCALE=(10000.0/AMAG)**2.0
00290 PRINT 25
00300 25 FORMAT(/,* ENTER UPPER LIMIT,LOWEST CLASS,F6.2*)
00310 READ 110,D
00320 110 FORMAT(F6.2)
00330 PRINT 75
00340 75 FORMAT(/,* ENTER CLASS MODULE,F6.4*)
00350 READ 220,ALPHA
00360 220 FORMAT(F6.4)
00410 E=D/ALPHA
00420 C=1.0
00430 DO 40 K=1,10
00440 CLASS(K)=E*ALPHA
00450 E=CLASS(K)
00460 AMARK(K)=SQRT(E*C)
00470 C=E
00480 IFREQ(K)=0
00490 40 CONTINUE
00500 NDATA=0
00530 DO 50 LL=1,400
00531 READ (1,330),AREA(LL)
00532 330 FORMAT(F8.3)
00533 IF(AREA(LL).EQ.0.00) GO TO 5000
00610 AREA(LL)=AREA(LL)*SCALE
00614 N=0
00616 NDATA=NDATA+1
```

Commentary

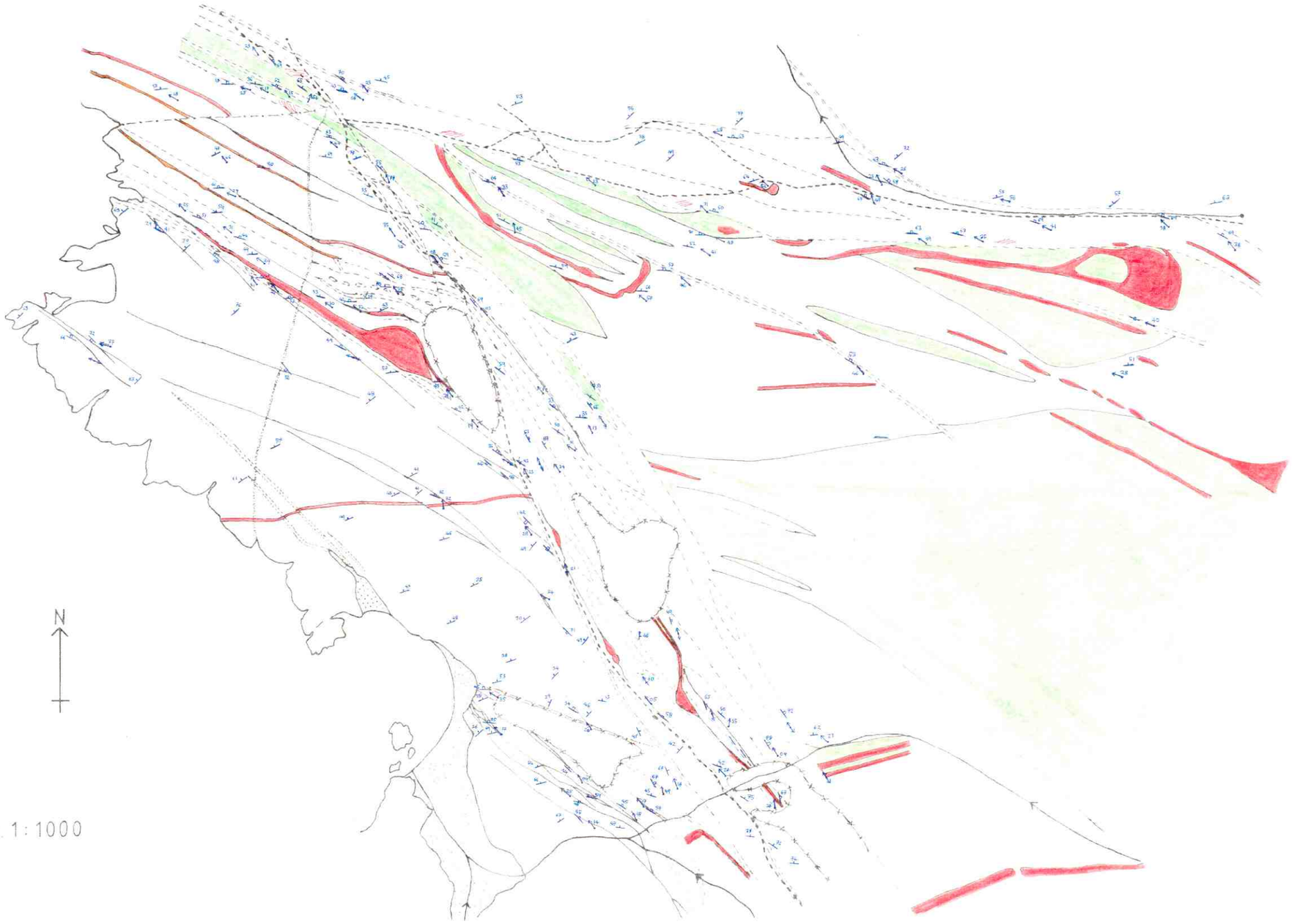
Interactive section , in which the print magnification , the required class module, and the estimated upper limit of the lowest class are inputted.

The upper and lower limits of each class are set

The data file is read in

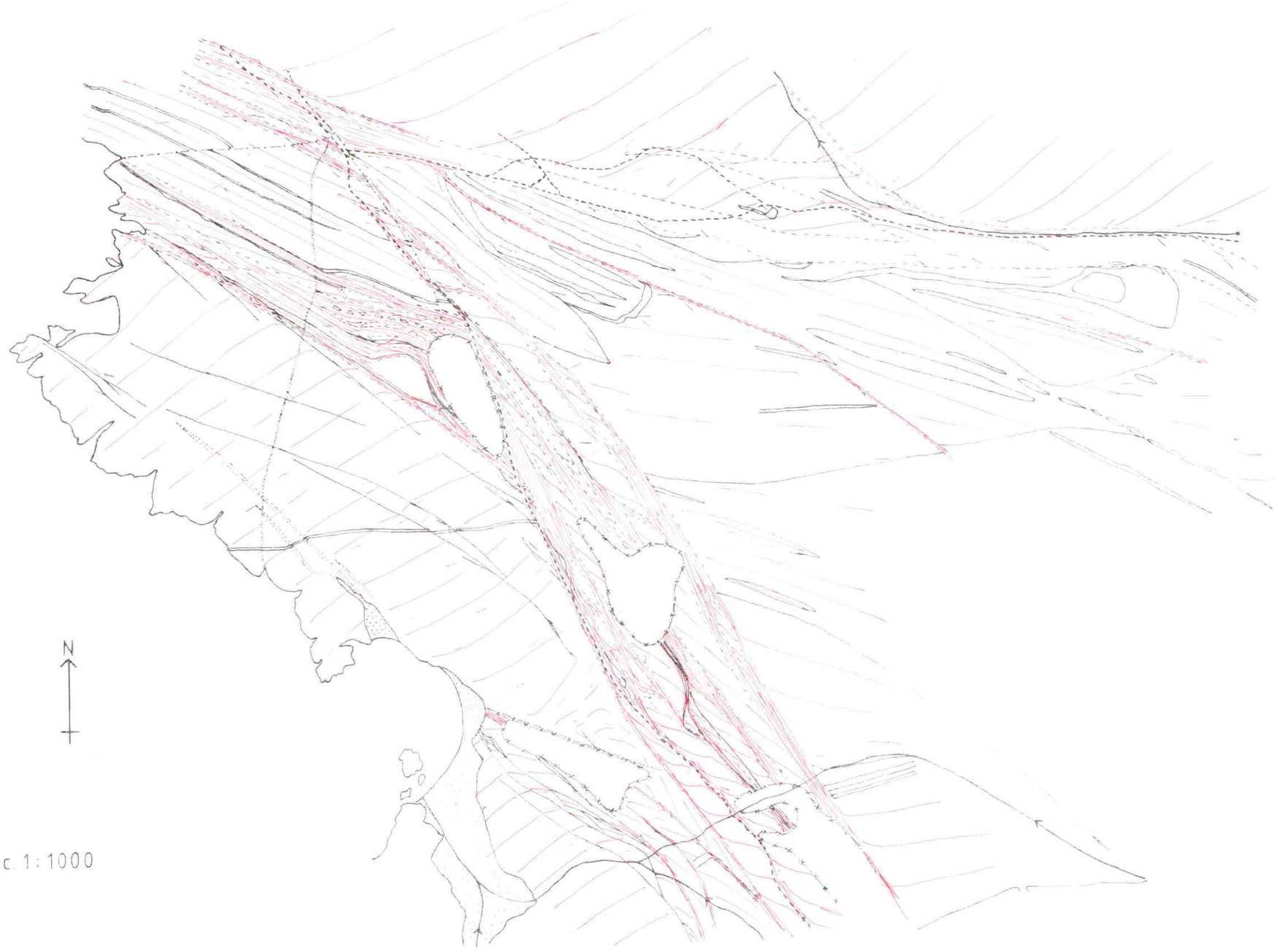
```
00620 SIZE=SQRT((4.0*AREA(LL))/PI)                    The circle equivalent diameter is calculated from the inputted area
00650 DO 60 I=1,10
00660 N=N+1
00670 A=CLASS(I)                                      This section sorts the diameters into classes
00680 IF (SIZE.LT.A) GO TO 4000
00690 60 CONTINUE
00700 4000 IFREQ(N)=IFREQ(N)+1
00710 50 CONTINUE
00720 5000 DO 70 II=1,10
00730 BLAT=0.0
00740 DO 80 KK=1,10                                   In this section the measured frequency distribution is corrected for the
00750 L=II+KK
00760 IF (L.EQ.11) GO TO 6000                         the effect of sectioning to give the true frequency distribution
00770 BLAT=BLAT+BCOEFF(KK)*FLOAT(IFREQ(L))
00780 80 CONTINUE
00790 6000 TFREQ(II)=(B*FLOAT(IFREQ(II)))-BLAT
00800 70 CONTINUE
00810 TCUM1=0.0
00820 TCUM2=0.0
00830 TNUM=0.0
00840 DO 90 J=1,10                                    In this final section the true mean and standard deviation of the
00850 F1=AMARK(J)*TFREQ(J)                            distribution are calculated
00860 F2=TFREQ(J)
00870 G1=F1*AMARK(J)
00880 TCUM1=TCUM1+F1
00890 TCUM2=TCUM2+G1
00900 TNUM=TNUM+F2
00910 90 CONTINUE
00920 AMEAN=TCUM1/TNUM
00930 STD=SQRT((TCUM2-((TCUM1**2.0)/TNUM))/TNUM)
00940 PRINT 550,AMEAN                                 The mean grain size, standard deviation and corrected distribution are
00950 550 FORMAT(/,24H THE MEAN GRAIN SIZE IS ,F6.2,8H MICRONS)   outputted
00960 PRINT 660,STD
00970 660 FORMAT(/,32H STANDARD DEVIATION OF GRAIN SIZE IS ,F6.2,8H MICRONS)
00980 PRINT 770,NDATA
00990 770 FORMAT(/,25H SIZE OF SAMPLE MEASURED ,I3,7H GRAINS)
00991 DO 73 IK=1,10
00994 PRINT 37,TFREQ(IK)
00995 37 FORMAT(F7.2)
00996 73 CONTINUE
01000 STOP
01010 END
READY.
```

MAP 2(a)



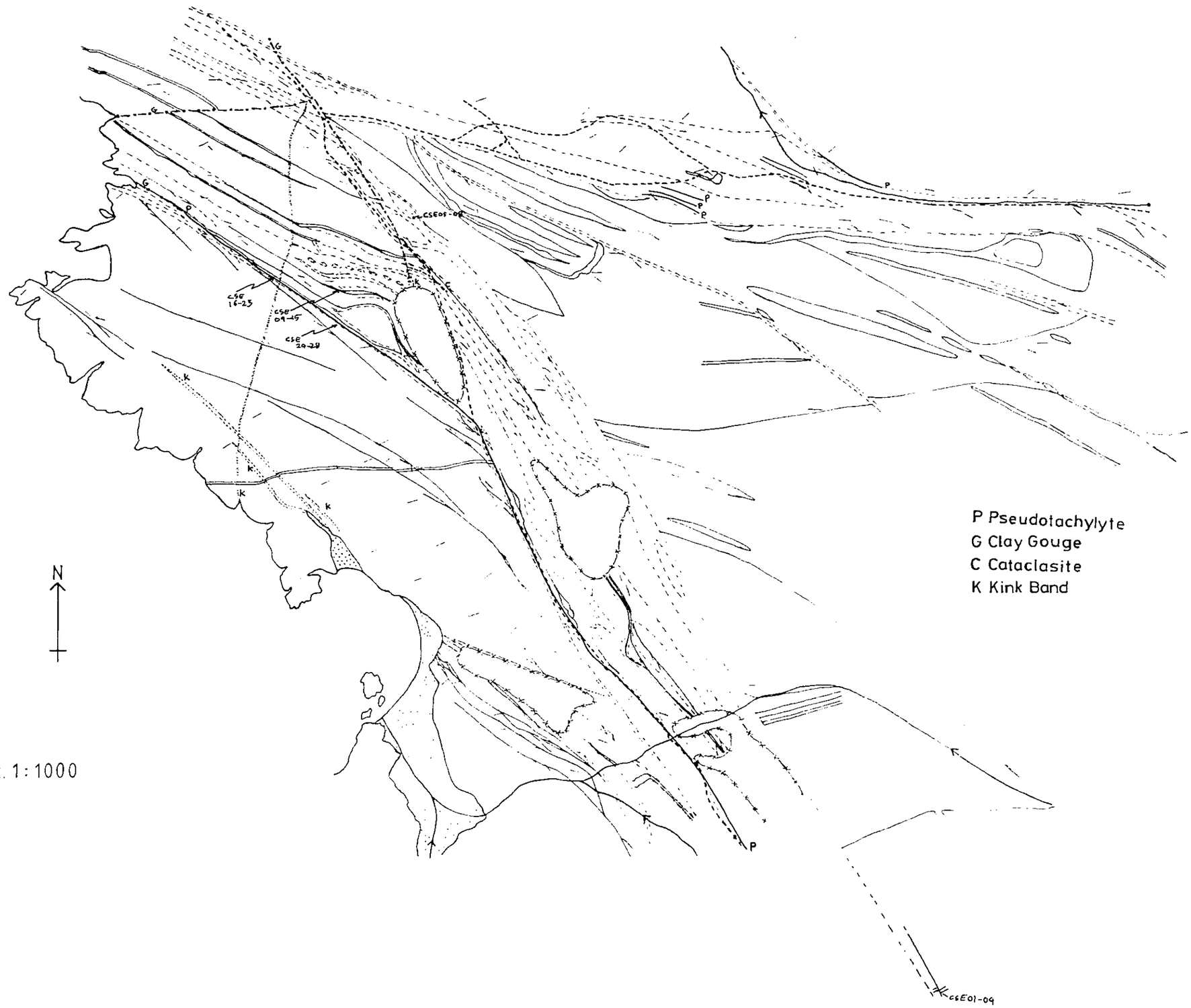
Scale : c. 1:1000

MAP 2(b)



Scale : c. 1:1000

MAP 2(c)

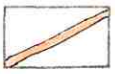


Scale : c. 1:1000

KEY


Undifferentiated Schist


Migmatitic Schist

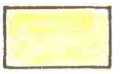

Garnetiferous Schist

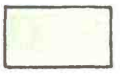

High-Strain


Low-Strain

} Mylonite

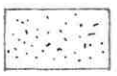

Pegmatite

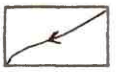

Microgranite

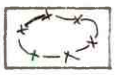

Quartz-Diorite


Foliation Trend


"Shear-Bands"


Sand


Stream


No Exposure



Schistosity



Mylonite Foliation



Quartz Elongation Lineation

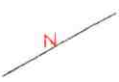


Fold Axis


Fault


Sinistral Shear-Zone


Dextral "



Normal "



Thrust "


Kink-Band

MAP1



Scale 1:500